

**UCLA**

**UCLA Electronic Theses and Dissertations**

**Title**

A Tale of Two Earths: Reconciling the Lunar and Terrestrial Hadean Records

**Permalink**

<https://escholarship.org/uc/item/02g3035s>

**Author**

Boehnke, Patrick

**Publication Date**

2016

Peer reviewed|Thesis/dissertation

UNIVERSITY OF CALIFORNIA

Los Angeles

A Tale of Two Earths: Reconciling the Lunar and Terrestrial Hadean Records

A dissertation submitted in partial satisfaction of the requirements for the degree Doctor of

Philosophy in Geochemistry

by

Patrick Boehnke

2016

© Copyright by

Patrick Boehnke

2016

## **ABSTRACT OF THE DISSERTATION**

A Tale of Two Earths: Reconciling the Lunar and Terrestrial Hadean Records

By

Patrick Boehnke

Doctor of Philosophy in Geochemistry

University of California, Los Angeles, 2016

Professor Timothy Mark Harrison, Chair

Studying early Earth history is complicated by the fact that the rock record doesn't extend past 4 Ga and our only record for the Hadean ( $>4$  Ga) comes to us from detrital zircons from the Jack Hills in Western Australia. The Hadean zircon record extends back to almost 4.4 Ga and has revealed that the early Earth may have had liquid water, a felsic crust, plate boundary interactions, and possibly a biosphere. On the other hand, analyses of lunar and meteoritic samples are used to argue for a hellish Hadean Earth where frequent, large impactors repeatedly destroyed the crust. Indeed, these two models stand in direct contradiction. The focus of this thesis is to examine the evidence for these two models and ultimately propose a reconciliation based on a new interpretation of the chronology of the lunar samples used to constrain the impact history into the early Earth-Moon system.

In order to improve the understanding of zircon crystallization in igneous settings, we undertook experimental studies of zircon saturation which were analyzed using a novel ion imaging approach by a secondary ion mass spectrometer. This study confirmed the original model for zircon saturation, that it is a function of only temperature, melt composition, and Zr content. Indeed, the primary implication for the early Earth from this work is that zircons are much more likely to crystallize in a felsic rather than mafic magma and therefore simply the existence of Hadean zircons suggests a high likelihood for felsic Hadean magmatism.

The majority of the thesis focuses on the interpretation of  $^{40}\text{Ar}/^{39}\text{Ar}$  ages of lunar and meteorite samples, specifically with regards to impact histories derived from compilations of such ages. The primary complication with lunar and meteorite  $^{40}\text{Ar}/^{39}\text{Ar}$  ages is that the vast majority show evidence for later disturbances due to diffusive loss of  $^{40}\text{Ar}$ . To try and extract meaningful thermal histories from these samples, we undertook investigations of samples from Apollo 16 and the Jilin chondrite. We then used an extension of the multi-domain diffusion model that can model samples containing multiple activation energies (i.e., whole rock samples with multiple K bearing minerals) to propose that the  $^{40}\text{Ar}/^{39}\text{Ar}$  system can be used to recover shock heating temperatures and durations.

Having shown the effects of diffusive  $^{40}\text{Ar}$  loss on the accuracy of  $^{40}\text{Ar}/^{39}\text{Ar}$  dating, we then explored the question as to whether or not compilations of disturbed  $^{40}\text{Ar}/^{39}\text{Ar}$  ages simply misestimate the timing of bombardment episodes or are fundamentally inaccurate. For this we created a simple numerical model that simulates a chosen impact history on a surface and then creates a histogram of  $^{40}\text{Ar}/^{39}\text{Ar}$  plateau ages. Our results show that rather than simply

misestimate timing, compilations of  $^{40}\text{Ar}/^{39}\text{Ar}$  ages can lead to inferences of illusory bombardment episodes.

Finally, we examine the  $^{40}\text{Ar}/^{39}\text{Ar}$  ages of suite of geochemically related Apollo 16 rocks to examine the effects of mixing and brecciation on the accuracy of inferred ages. By analyzing multiple rocks from each soil sample, we show that three out of six samples are not compatible with a single thermal history. That is to say, despite their close proximity during sampling and geochemical similarities, analyzed rocks in the soil sample have unique chronologies. Based on these findings, we developed a simple numerical model which shows that internal isochrons of mixed samples can yield erroneous ages while retaining a statistically acceptable mean squared weighted deviation (MSWD).

The dissertation of Patrick Boehnke is approved.

Edward Donald Young

Kevin D. McKeegan

Ioanna Kakoulli

David Shuster

Timothy Mark Harrison, Committee Chair

University of California, Los Angeles

2016

For my family and friends

## Table of Contents

Abstract of Dissertation.....	ii
Committee Page.....	v
Dedication.....	vi
Table of Contents.....	vii
Acknowledgments.....	viii
Vita.....	x
Chapter 1: Introduction – Impact Records and the Early Earth.....	1
Chapter 2: Zircon Saturation Re-revisited.....	16
Ch. 2 Figures and Tables.....	38
Chapter 3: A Model for Meteoritic and Lunar $^{40}\text{Ar}/^{39}\text{Ar}$ Age Spectra: Resolving the Effects of Multi-activation Energies.....	54
Ch. 3 Figures and Tables.....	73
Chapter 4: Illusory Late Heavy Bombardments.....	82
Ch. 4 Figures and Tables.....	94
Chapter 5: Impact Mixing and Brecciation: The Silent Killer of Chronologic Information.....	98
Ch. 5 Figures and Tables.....	110
Chapter 6: Conclusions.....	117
Appendix A: A meta-analysis of geochronologically relevant half-lives: What’s the best decay constant?.....	122
Appendix B: Zircon U/Th Model Ages in the Presence of Melt Heterogeneity.....	145
Appendix C: EPMA and $^{40}\text{Ar}/^{39}\text{Ar}$ Data for Chapter 3.....	167
Appendix D: Model Description for Chapter 4.....	173
Appendix E: $^{40}\text{Ar}/^{39}\text{Ar}$ Data for Chapter 5.....	186
References.....	203

## Acknowledgements

I am deeply grateful for discussions and exchange of ideas with Melanie Barboni, Beth Ann Bell, Rita Economos, Brenhin Keller, Robert Steele, Anke Watenphul, and Matthew Wielicki. Indeed, conversations with them greatly enriched my doctoral experience and I look forward to many future collaborations and scientific exchanges. Oscar Lovera was tremendously helpful in explaining and helping me to understand the Multi-Domain Diffusion model which was crucial to Ch. 3. All of the  $^{40}\text{Ar}/^{39}\text{Ar}$  data was acquired in the New Mexico Geochronology Research Laboratory with the help of Matt Heizler. Matt Heizler's detailed explanation of  $^{40}\text{Ar}/^{39}\text{Ar}$  analyses and willingness to let me participate permitted me to take an active part in collecting much of the data for this thesis. Kevin McKeegan and Axel Schmitt are thanked for teaching me how to use an ion microprobe as well as explaining its inner workings. Their tutelage allowed me to become an independent user of the UCLA ion microprobe facility.

I would like to thank Kevin McKeegan, Edward Young, Ioanna Kakoulli, and David Shuster for serving on my committee and providing insightful feedback that was invaluable for the writing of this dissertation and large parts of my doctoral research. Marc Caffee was the person who first introduced me to geochemistry while I was an undergraduate at Purdue University and I am grateful for our continued discussions and his advice.

I would like to thank my advisor Mark Harrison for his wisdom, skepticism, wide ranging conversations, and tremendous insight into Earth science. His skill as a supervisor and continual support ensured that my PhD experience was a great one and prepared me for career success.

Finally, I am deeply grateful for the love and support from my wife Elizabeth, my mother, my father, and my sister.

The ion microprobe facility at UCLA is partly supported by a grant from the Instrumentation and Facilities Program, Division of Earth Sciences, National Science Foundation. This research was conducted with support from a grant to T. Mark Harrison from NSF-EAR's Petrology/Geochemistry Program.

Ch. 2 was published in *Chemical Geology* as

Boehnke, P., Watson, E.B., Trail, D., Harrison, T.M. and Schmitt, A.K., 2013. Zircon saturation re-revisited. *Chemical Geology*, 351, 324-334.

Ch. 3 was published in *Earth and Planetary Science Letters* as

Boehnke, P., Harrison, T.M., Heizler, M.T. and Warren, P.H., 2016. A model for meteoritic and lunar  $^{40}\text{Ar}/^{39}\text{Ar}$  age spectra: Addressing the conundrum of multi-activation energies. *Earth Planet. Sci. Lett.*, 453, 267-275.

Ch. 4 was published in *Proceedings of the National Academy of Science* as

Boehnke, P. and Harrison, T. M., 2016. Illusory Late Heavy Bombardments. *Proc. Nat. Acad. Sci. U. S. A.*

Ch. 5 is based on a manuscript in preparation for submission:

Boehnke, P., Heizler, M. T., Warren, P. H. and Harrison, T. M., Impact Mixing and Brecciation: The Silent Killer of Chronologic Information. *In prep.*

## Vita

### Education

<b>University of California, Los Angeles, CA</b>	August 2014
Geochemistry	Candidate of Philosophy
<b>University of California, Los Angeles, CA</b>	May 2013
Geochemistry	Master of Science
<b>Purdue University, West Lafayette, IN</b>	May 2011
Physics	Bachelor of Science
Mathematics	Bachelor of Science

### Awards and Invited Talks:

- 2014 Eugene Shoemaker Impact Cratering Award, Geological Society of America
- 2014 Eugene B. Waggoner Scholarship for outstanding academic performance and original research, Department of Earth, Planetary, and Space Sciences, UCLA
- 2013 Harold and Mayla Sullwold Scholarship for excellence in graduate student research, Department of Earth, Planetary, and Space Sciences, UCLA
- Guest Lecturer at UCLA SIMS Workshop (2013-2016)
- Invited Talk: Lawrence Livermore National Lab (November 2013)
- Invited Talk: Challenges and Opportunities in Geochronology Workshop (Goldschmidt 2014)
- Invited Talk: Workshop on Decay Constants in Geochronology (Goldschmidt 2014)
- Invited Talk: University of Southern California (March 2015)
- Invited Talk: Caltech (March 2015)
- Invited Talk: University of Chicago (January 2016)
- Panelist: Special Session on Forensic Science Investigations in Art and Archaeology (ISA 2014)

### Peer Reviewed Publications

1. P. Boehnke, E. B. Watson, D. Trail, T. M. Harrison, and A. K. Schmitt, 2013 "Zircon Saturation Re-Revisited", *Chemical Geology*, 352, 324-334.
2. P. Boehnke and T. M. Harrison, 2014 "A meta-analysis of geochronologically relevant half-lives: What's the best decay constant?", *International Geology Review*, 56, 905-914.
3. O. M. Lovera, T. M. Harrison, and P. Boehnke, 2015 "Comment on "Systematic variations of argon diffusion in feldspars and implications for thermochronometry" by Cassata and Renne", *Geochimica et Cosmochimica Acta*, 151, 168-171.
4. R. C. J. Steele and P. Boehnke, 2015 "Titanium isotope source relations and the extent of mixing in the proto-Solar nebula examined by Independent Component Analysis", *The Astrophysical Journal*, 802, 80.
5. P. Boehnke, M. W. Caffee, and T. M. Harrison, 2015 "Xenon Isotopes in the MORB Source Are Not Distinctive of Early Global Degassing", *Geophysical Research Letters*, 42, 4367-4374.
6. E. A. Bell, P. Boehnke, M. D. Hopkins, and T. M. Harrison, 2015 "Distinguishing Primary

- and Secondary Inclusion Assemblages in Jack Hills Zircons", *Lithos*, 234, 15-26.
7. E.A. Bell, P. Boehnke, T.M. Harrison, and W. Mao, 2015 "Potentially Biogenic Carbon Preserved in a 4.1 Ga Zircon", *PNAS*, 112, 14518-14521.
  8. P. Boehnke, M. Barboni, and E. A. Bell, 2016 "Zircon U/Th Model Ages in the Presence of Melt Heterogeneity", *Quaternary Geochronology*, 34, 69-74.
  9. M. M. Wielicki, T. M. Harrison, A. K. Schmitt, P. Boehnke, and E. A. Bell, 2016 "Differentiated impact melt sheets may be a potential source of Hadean detrital zircons: COMMENT" *Geology*, 44, e398.
  10. P. Boehnke, T. M. Harrison, M. T. Heizler, and P. H. Warren, 2016 "<sup>40</sup>Ar/<sup>39</sup>Ar Dating of Meteoritic and Lunar Samples: The Paradox of Multi-activation Energies", *Earth and Planetary Science Letters*, 453, 267-275.
  11. E. A. Bell, P. Boehnke, and T. M. Harrison, 2016 "Recovering the primary geochemistry of Jack Hills zircons through quantitative estimates of chemical alteration", *Geochimica et Cosmochimica Acta*, 191, 187-202.
  12. P. Boehnke and T. M. Harrison, 2016 "Illusory Late Heavy Bombardments", *PNAS*, doi: 10.1073/pnas.1611535113.

#### Service and Professional Memberships

Reviewer for *Earth and Planetary Science Letters* and *Physics and Chemistry of Minerals*,  
*Proceedings of the National Academy of Science*, *NSF Proposals* and, *Geochimica et  
Cosmochimica Acta*  
Grand Award Judge for Earth Science at Intel International Science and Engineering Fair (2014)  
Docent at the UCLA Meteorite Museum  
American Geophysical Union  
Geological Society of America  
The Meteoritical Society  
The American Statistical Association

## **Chapter One: Introduction – Impact Records and the Early Earth**

The current views of Hadean (>4 billion years; Ga) Earth are evocative of the opening lines of Dicken’s *A Tale of Two Cities*: “It was the best of times, it was the worst of times”. Prior to the discovery of >4 Ga zircons (Froude et al., 1983), it was widely accepted that the Hadean crust, if any, was dry, hot, and mafic (Abe, 1993; Kaula, 1979; Wetherill, 1980). It was not until terrestrial samples older than 4 Ga became known that diverging views of early Earth developed. Broadly speaking, there are now two classes of models for early Earth, one which postulates felsic crust, liquid water, and possibly a clement climate, and the other of a desiccated world rendered sterile by impacts. The former is supported by data from terrestrial samples and the latter from material returned from the Moon.

### **1.1 The early Earth from the perspective of Hadean zircons**

#### **1.1.1 Geochemical Inferences**

Zircon is a highly robust mineral which generally incorporates significant U but rejects Pb (Watson et al., 1997) and is resistant to diffusive alteration of its constituent trace elements (e.g., Cherniak and Watson, 2003). While it is unsurprising that these characteristics have made zircon the most popular high temperature geochronometer (Schoene, 2014), the recognition that zircons could survive >4 Ga of tectonic processes and erosion to provide what is currently our only direct evidence of the Hadean Earth (Froude et al., 1983) surprised the geological community. In spite of its resistance to diffusive exchange, zircon is vulnerable to radiation damage and hydrothermal alteration (Hoskin, 2005) and thus care must be taken to assess secondary alteration effects (Bell et al., 2016). While Hadean zircons have now been reported from thirteen locations (see summary in Harrison et al., 2016), the present discussion is restricted to the Jack

Hills suite of Hadean zircons as they are the most numerous and best studied. Despite being a structurally simple mineral, zircon ( $\text{ZrSiO}_4$ ) incorporates a variety of trace elements including Rare Earth Elements (REEs), Hf, and Ti as well as inclusions of other minerals. These geochemical indicators can be used to infer the crystallization environment and possibly even surface conditions and the climate at the time of formation.

Analyses of the geochemistry of, and inclusions in, Hadean zircons have led to numerous revelations about early Earth. The first of these discoveries stems from the analysis of oxygen isotopes which revealed elevations in  $\delta^{18}\text{O}$  as high as 2-3‰ (Mojzsis et al., 2001; Wilde et al., 2001) over the mantle value of 5.3‰ (Valley et al., 1998), which was interpreted as evidence for liquid water at Earth's surface. This interpretation is based on the fact that sedimentary material which formed during low temperature aqueous alteration (e.g., clays) have elevated  $\delta^{18}\text{O}$  values ( $\geq 20\text{‰}$ ; Savin and Epstein, 1970). There is now widespread acceptance amongst investigators who study the early Earth through the terrestrial rock and mineral record that water was present at or nears Earth's surface during much of the Hadean (e.g., Harrison, 2009; Mojzsis et al., 2001; Rollinson, 2008; Shirey et al., 2008; Wilde et al., 2001).

In addition to oxygen isotopes, the abundant Hf in zircon provides another indicator of parental melt source materials. The usefulness of the Lu-Hf system stems from the decay of  $^{176}\text{Lu}$  to  $^{176}\text{Hf}$  ( $\tau_{1/2} = 37 \text{ Ga}$ ; Scherer et al., 2001) and the fact that variations in Lu/Hf are imposed by chemical differentiation. The depleted mantle retains a high Lu/Hf ( $\sim 0.04$ ; Vervoort and Blichert-Toft, 1999) following extraction of basalt (Lu/Hf  $\approx 0.02$ ). Further differentiation results in progressively lower values with typical continental crust characterized by a Lu/Hf  $\approx 0.015$ . Hafnium isotopes are amenable to study in individual zircons due to the high Hf contents of zircon ( $\sim 1\text{-}2$  weight percent) their very low Lu/Hf, and the fact that zircon can be precisely U-

Pb dated (Patchett, 1983). The first analysis of Hf isotopes from Archean and Hadean Jack Hills zircons showed evidence for an early (>4.3 Ga) crust-mantle differentiation event and the reworking of a previous crust into the Jack Hills zircons (Amelin et al., 1999).

Further analyses using both bulk solution and in-situ laser ablation analyses revealed the existence of zircons with Hf isotopes that are consistent with the formation of a felsic reservoir at >4.5 Ga (Bell et al., 2014; Harrison et al., 2008, 2005). Several zircons were found that lie near or above depleted mantle evolution and are thus consistent with a depletion event resulting from the formation of a widespread continental crust (Harrison et al., 2005), but were not subsequently replicated (Harrison et al., 2010). These findings are not without controversy and have been challenged by several works as either artifacts due to early Pb loss or analytical errors (Kemp et al., 2010). Kemp et al. (2010) propose instead that all of the Hf isotope evidence can be explained through the existence of a KREEP-like mafic crust, a claim that is at odds with several other lines of evidence as explained below.

While O and Hf isotopes provide information about the history and processing of the source material from which the Hadean zircons formed, other indicators such as Ti thermometry and petrogenetic information held in zircon inclusion assemblages provide direct constraints on the geophysical conditions of the host magmas. Watson and Harrison (2005), using a combination of experimental and natural samples, showed that [Ti] in a zircon is a simple function of temperature and  $\text{TiO}_2$  activity, and further argued that most terrestrial magmas have  $a_{\text{TiO}_2} \geq 0.7$ . Watson and Harrison (2005) also analyzed [Ti] of numerous Hadean zircons and found a peak centered at 680°C and argued that this represented near water saturated, minimum melting (e.g., Huang and Wyllie, 1981) as far back as 4.35 Ga. Subsequent development of the Ti-in-zircon thermometer shows that more mafic settings reliably produce higher temperature zircons (Carley

et al., 2014; Fu et al., 2008) and that [Ti] is elevated due to contamination by cracks (Harrison and Schmitt, 2007).

In addition to the chemistry of the source material and crystallization temperature, another significant question is the redox state of the magma from which the Hadean zircons crystallized. To address this question Trail et al. (2011) calibrated the size of the Ce anomaly, a proxy for  $Ce^{4+}/Ce^{3+}$  in the zircon, to allow inferences of the oxygen fugacity of the host magma. When applied to Hadean zircons, it reveals their origins in magmas ranging from close to the fayalite-magnetite-quartz buffer (similar to that of the modern upper mantle; e.g., Carmichael, 1991), to much more reduced values. Trail et al. (2011) further argued that the dominant gases degassing from volcanoes in the Hadean under these redox conditions would be  $H_2O$ ,  $CO_2$ ,  $SO_2$ , and  $N_2$ , implying perhaps surprisingly an oxidized atmosphere.

The last, and potentially most revealing, avenue of investigation is the study of mineral inclusions in the Hadean zircons. The dominant inclusions in the assemblage are quartz and muscovite with minor amounts of biotite, hornblende, apatite, REE oxides, Fe oxides, monazite, albite and, ilmenite (Bell et al., 2015b; Hopkins et al., 2010, 2008). Numerous inferences about the early Earth are permitted by examining the chemical composition of these inclusions. Amongst these are inferred crystallization pressures of >6 kbar, leading to the conclusion that they formed in a low heat flow environment which was interpreted as suggesting a plate boundary interactions (Hopkins et al., 2008).

However, the primary nature of these inclusions is controversial due to abundant cracks and crack-filling inclusions in the Hadean zircons (Rasmussen et al., 2011). Specifically, Rasmussen et al. (2011) argued that the muscovite crystallized from a fluid during metamorphism in a void

created by dissolving apatite. However, this interpretation does not explain the  $\text{Si}_{\text{ptu}}$  or morphology of the muscovite inclusions (Hopkins et al., 2012). Additionally, Bell et al. (2015b) found that there are significant differences between isolated, on-crack, and crack-filling inclusions supporting the interpretation that isolated inclusions are largely primary.

In summary, despite their insignificant mass, Hadean zircons have fundamentally changed our view of the early Earth. They provide evidence for liquid water in the near surface environment, an oxidized atmosphere, an evolved felsic crust, and potentially a biosphere.

### **1.1.2 The stability of zircon in magmas and its role as a tracer of Earth history**

Additional information about the evolution of the Earth can be gleaned merely from the existence of Hadean zircons. Zircons crystallize in a melt once the  $[\text{Zr}]$  exceeds that required for zircon saturation, which is dependent on temperature and melt composition (Watson and Harrison, 1983). This behavior is important in contexts beyond the early Earth. For example, interpreting crystallization ages of volcanic zircons is complicated by the fact that they crystallize at zircon saturation rather than at the time of eruption (Reid et al., 1997). However, despite the success of the Watson and Harrison (1983) model, over the intervening 30 years several challenges emerged such as proposed effects due to halogens (Baker et al., 2002) or pressure (Rubatto and Hermann, 2007). In order to address these potential complications, new experiments were undertaken and analyzed using a secondary ion mass spectrometer (SIMS) to avoid potential secondary fluorescence problems inherent to electron probe analyses (Boehnke et al., 2013). The results of Boehnke et al. (2013) confirm the form of the Watson and Harrison (1983) model with updated values for the parameters. That is to say, no effect due to pressure was found and the Baker et al. (2002) data were reconciled with the Boehnke et al. (2013) model

suggesting no effect due to halogens. This is further discussed in the chapter dedicated to zircon saturation, Chapter 2.

Inferences from zircon saturation systematics are A) that zircon is much more likely to crystallize in a felsic magma than a mafic one and B) the lower [Zr] of Archean rocks suggests that zircon saturation was more difficult to achieve earlier in Earth's history (Keller et al., 2016). Taken in combination, the mere presence of Hadean zircons increases the likelihood, over that of the canonical models (e.g., Kaula, 1979; Wetherill, 1980), of evolved melts in the Hadean. Additionally, changes in crustal [Zr] suggest that a shift of ~10 weight percent SiO<sub>2</sub> is necessary when using modern rocks as an analogue for the Hadean (Keller et al., 2016). That is to say, if the modern analogue has 50% SiO<sub>2</sub>, the Hadean analog must have had ~60% SiO<sub>2</sub> in order to have similar zircon crystallization systematics. This further burdens the formation of Hadean zircons in mafic magmas as several models for Hadean zircons propose (as discussed in the next section).

### **1.1.3 Geophysical Models for the Hadean Earth**

The models to explain the variety of evidence from the Hadean zircons fall into three major categories: 1) re-melting of an earlier mafic crust (Kemp et al., 2010), 2) formation in impact melts (Kenny et al., 2016; Marchi et al., 2014), and 3) possible plate boundary interactions (Harrison, 2009; Hopkins et al., 2008). Broadly speaking, the first two models are in agreement with the classical view of the Hadean Earth, one that is hot and had at most a mafic crust (e.g., Kaula, 1979; Wetherill, 1980). The plate boundary model however, has radical implications for both the evolution of the planet and the origins of plate tectonics. Each of these models makes different use of the geochemical evidence discussed in the previous section.

In the first model a thin, trace-element enriched layer forms at the end of the terrestrial magma ocean and is then buried by thick komatiitic flows from ubiquitous volcanic eruptions (Kemp et al., 2010). This layer is melted and differentiated to form small silicic melts from which the Hadean zircons crystallize. While Kemp et al. (2010) argue that their model explains their Lu-Hf data, the muscovite inclusions, and oxygen isotopes, it does not explain the 680°C Ti-in-zircon crystallization temperatures or the abundant quartz inclusions. Kemp et al. (2010) reference experiments from Ellis and Thompson (1986) in support of their model, however the lowest experimental runs with melt identified are at >770 °C which is incompatible with Ti-in-zircon temperatures of 680 °C. Ellis and Thompson (1986) also do not include alkalis in their experiments and therefore the relevance to natural systems is questionable. Additionally, Kemp et al. (2010) dismiss rather than explain the more primitive Hf isotope signatures reported by Harrison et al. (2008). Finally, while the Kemp et al. (2010) model requires water-saturated melting, they do not discuss the origin of the water and it appears unlikely that sufficient water could be delivered to a melt to achieve saturation.

The next major hypothesis is that Hadean zircons formed in impact melts (Kenny et al., 2016; Marchi et al., 2014), which comes about due to the presumed higher impact rates in the Hadean (See Section 1.2). The model of Marchi et al. (2014) attempts to explain the age distribution of Hadean zircons as resulting purely from impact processes. However, the impactors in the Marchi et al. (2014) model puncture the crust and the melt produced is derived from the mantle, and thus ultramafic. Indeed, in the model of Marchi et al. (2014) the Hadean Earth is covered in >18-km-thick flood basalts from which the Hadean zircons are expected to crystallize. This model is fundamentally incompatible with the geochemical signature of the Hadean zircons; zircons that would form under the conditions of the Marchi et al. (2014) model

would be much hotter ( $\gg 680$  °C), not include muscovite or quartz inclusions, and have Hf isotope signatures that plot on the depleted mantle evolution. On the other hand, Kenny et al. (2016) argued that the granophyres of the Sudbury impact melt had similar crystallization temperatures as the Hadean zircons and that therefore impact melts could be a source of Hadean zircons. However, the model of Kenny et al. (2016) cannot explain how this subset of zircons is removed from the higher temperature zircons in the Sudbury impact melt (Kenny et al., 2016; Wielicki et al., 2012) nor do they address any of the other geochemical observations found in Hadean zircons. The hypothesis of impacts generating the Hadean zircon suite was tested and rejected by Wielicki et al. (2012) on the basis that impact zircons yield significantly higher Ti-in-zircon temperatures than that observed in Hadean zircons.

The final model for the formation of the Hadean zircons is that they grew in water saturated magmas in plate boundary-like settings (Hopkins et al., 2008). That is to say in a low-heat flow environment, such as a modern convergent margin where a down going slab is continually fluxing water to the hanging wall. This explanation was first proposed based on combining muscovite inclusion barometry with Ti-in-zircon crystallization temperatures, which showed a formation at  $\geq 6$  kbar and  $\sim 680$  °C and leads to calculated near surface heat flows of  $\sim 75$  mW/m<sup>2</sup>. These calculated heat flows are substantially less than the inferred Hadean global heat flow of 160-400 mW/m<sup>2</sup> (Abe, 1993; Sleep, 2000; Smith, 1981). Based on the apparently lower heat flow in the Hadean zircons, Hopkins et al. (2008) suggested that they formed in a setting analogous to convergent margins. This is because the only regions of low heat flow undergoing magmatism on the modern Earth are found at subduction zones (Pollack et al., 1993). This model appears to explain all of the geochemical evidence from the Hadean, such as the inclusion assemblage, Ti-in-zircon temperatures, and Hf isotope signature. Indeed it is this last model

which suggests a clement, habitable, and in a sense modern planet evocative of “the best of times”.

#### **1.1.4 A Hadean Biosphere?**

Given that the microfossil record extends back to only ~3.5 Ga (Brasier et al., 2015) and the record of even highly metamorphosed rocks stops at 4.02 Ga (Bowring and Williams, 1999), the chances of finding microfossils at an earlier time in Earth’s history appear minimal. However, the carbon isotope record provides evidence for biogenic materials as far back as 3.8 Ga (Mojzsis et al., 1996; Rosing, 1999). Indeed, there has been a consistent offset between biogenic kerogens and carbonates throughout the past 3.4 Ga (Schopf and Kudryavtsev, 2014) due to isotope fractionation from the biologic fixation of carbon. Therefore, the Hadean zircon suite is the only presently viable mechanism to assess the possibility of life and the terrestrial C cycle prior to 4.0 Ga.

However, this idea is complicated by previous reports of diamond and abundant carbonaceous inclusions in Jack Hills zircons (Menneken et al., 2007). This was a surprising find because Hopkins et al. (2008), who examined >10 times as many Hadean zircons, did not observe these phases. Subsequent investigation showed unambiguously that the reported diamond, and likely the graphite inclusions as well, was due to contamination, introduced during sample polishing (Dobrzhinetskaya et al., 2014). This left the abundance and nature of carbonaceous inclusions in Hadean zircons unknown. A more recent study addressed the shortcomings in the Menneken et al. (2007) approach by using Raman spectroscopy to study only unexposed opaque inclusions. From the Raman spectra, two carbon inclusions were identified in a concordant 4.1 Ga zircon (Bell et al., 2015a). To further study these inclusions,

Bell et al. (2015a) used synchrotron transmission x-ray microscopy to generate a 3D computer tomography model of their inclusions and found no evidence for cracks. Subsequent C isotope analyses found a  $\delta^{13}\text{C}_{\text{PDB}} = -24 \pm 5\text{‰}$  which is consistent with a biogenic origin (Bell et al., 2015a). While this first report cannot be taken to confirm the existence of life in the Hadean, it shows a way towards to assessing the Hadean C cycle and may ultimately answer the question as to the timing of the origin of life.

## 1.2 The early Earth from lunar $^{40}\text{Ar}/^{39}\text{Ar}$ data

The combined processes of erosion and plate tectonics have erased most terrestrial craters. Indeed, less than 10% of all craters produced on Earth are expected to survive to present day (Johnson and Bowling, 2014). Therefore in order to establish an impact history into the early Earth it is necessary to examine impact craters on extra-terrestrial bodies (e.g., the Moon) which do not have active plate tectonics or high erosion rates and therefore preserve old craters. However, the inaccessibility of extra-terrestrial bodies means that the sample set is limited to that returned by missions or delivered to us as meteorites. This limitation first and foremost means that we cannot easily replace samples which are not ideal due to later thermal disturbances (Boehnke et al., 2014) and brecciation. Despite these potential pitfalls, Apollo samples are dated using  $^{40}\text{Ar}/^{39}\text{Ar}$  “plateau” ages and interpreted in terms of impact ages (e.g., Chapman et al., 2007).

Given the previously mentioned limitations, virtually all of the  $^{40}\text{Ar}/^{39}\text{Ar}$  step-heating data from extra-terrestrial samples are disturbed (i.e., they contain age gradients). Indeed diffusive loss of  $^{40}\text{Ar}$  was recognized and modeled in the foundational works of  $^{40}\text{Ar}/^{39}\text{Ar}$  geochronology (Merrihue and Turner, 1966; Turner et al., 1966). Since that time however, the extra-terrestrial  $^{40}\text{Ar}/^{39}\text{Ar}$  community has, with the exception of Shuster et al. (2010), abandoned modeling the

$^{40}\text{Ar}$  disturbances in favor of assigning arbitrary plateau ages (Bogard et al., 2010; Kring and Cohen, 2002; Norman et al., 2006). The concept of a plateau age stems from  $^{40}\text{Ar}/^{39}\text{Ar}$  step-heating analyses of undisturbed terrestrial samples and its validity was not established for disturbed samples (Dalrymple and Lanphere, 1974). In contrast while the terrestrial  $^{40}\text{Ar}/^{39}\text{Ar}$  community was slow to embrace modeling disturbed age spectra it produced undoubtedly the greatest recent advance in  $^{40}\text{Ar}$  diffusion modeling, the multi-diffusion domain model (Lovera et al., 1989).

With this cautionary note about the interpretations of the major of  $^{40}\text{Ar}/^{39}\text{Ar}$  on extra-terrestrial samples, it is important to review the literature as it exists in order to see how it agrees and differs with the view of the Hadean Earth from the Hadean zircons. Arguably the most significant legacy of Apollo-era lunar exploration is the concept of the Late Heavy Bombardment (LHB), a hypothesized spike in impacts into the Earth-Moon system at  $\sim 3.9$  Ga (Tera et al., 1974). The original evidence for the LHB comes from Rb-Sr ages and disturbed U-Pb systematics in a handful of Apollo samples along with  $<10$  K-Ar ages. Since that original work, the remaining evidence has come from  $^{40}\text{Ar}/^{39}\text{Ar}$  analyses of Apollo samples (e.g., Chapman et al., 2007). That is to say, the Apollo  $^{40}\text{Ar}/^{39}\text{Ar}$  data are almost universally interpreted to support an impact spike (e.g., Kring and Cohen, 2002; Marchi et al., 2013). However, the lunar meteorite  $^{40}\text{Ar}/^{39}\text{Ar}$  ages do not show a preponderance of ages at  $\sim 3.9$  Ga but rather a broad hump between 3 and 3.5 Ga (Cohen et al., 2000) suggesting that the Apollo samples are not globally representative. Alternatively, the preponderance of 3.9 Ga ages in Apollo samples could represent a “stonewall” past which the lunar surface was saturated by impacts (Hartmann, 1975).

While the  $^{40}\text{Ar}/^{39}\text{Ar}$  data are interpreted to support the LHB, the mass delivered by this hypothesized event and in general by early impact events is difficult to constrain from geochronology data alone. In general the magnitude of impacts during the first ~500 Ma of Earth's history is constrained by the assumed mass added post-accretion and the size of the craters on the Moon. It is hypothesized that the planet added ~1% of its mass post core formation due to the abundance of highly siderophile elements (e.g., Pt) in the mantle being elevated above the level predicted from partition coefficients (e.g., Righter, 2003). Additional constraints come from the inferred impactor size based on the size of impact basins on the Moon. These estimates however have been revised recently to smaller sizes due to the increased heat flow and therefore more malleable target properties on the near side of the Moon (Miljkovic et al., 2013). So while there are some available constraints on the total mass added post core formation, it is not clear how they can be linked to any one impact or the timing of said impact events. Given the wide range of estimated magnitudes for the impact history of the early Earth, it is clear that its effects will vary widely depending on the timing and magnitude constraints. For example, depending on the intensity of impacts the planet could be entirely sterilized (Sleep et al., 1989) or create niches for extremophiles to develop (Abramov and Mojzsis, 2009). Indeed it has even been proposed that large impacts could cause volcanism (Elkins-Tanton and Hager, 2005) or in general destroy the Earth's crust (Marchi et al., 2014). It is therefore critically important to understand the flux and magnitude of impacts into the early Earth in order to have a clearer understanding of Earth's long-term evolution.

Additionally, recently proposed impact histories suggest moving the LHB back to 4.1 Ga from 3.9 Ga independently of the constraints provided by the Apollo  $^{40}\text{Ar}/^{39}\text{Ar}$  ages (Morbidelli et al., 2012). This curve also has considerable implications for impacts during the Hadean and

the consequences of this “new” impact history were explored by Marchi et al. (2014). These implications include that the bombardment during the early Earth history was frequent and violent enough to destroy the crust. As discussed in Section 1.1.2, this “worst of times” scenario is at odds with the constraints provided by Hadean zircons and the resolution to this dual history for the Earth will be explored in the remainder of this thesis.

### **1.3 High Accuracy Geochronology**

While the preceding sections focused on the environment and geophysical conditions of the Hadean Earth, in order to have this debate it is vital that the geochronology techniques used are accurate. Accuracy in geochronology can be separated into three categories: 1) Decay and other fundamental constants, 2) analytical, and 3) interpretation. While the rest of this thesis will largely revolve around the interpretation of  $^{40}\text{Ar}/^{39}\text{Ar}$  data and the distortions that arise from ignoring sample complexity, it is worth commenting for a moment on the other two aspects required for accurate geochronology.

Our knowledge of decay constants and branching ratios stems largely from 1970s era nuclear physics experiments (Boehnke and Harrison, 2014; Appendix A) with only a few measurements since that time (e.g., Kossert et al., 2013; Rotenberg et al., 2012). This is compounded by the fact that in the 1970s the geochronologic community defined a standard set of decay constants to facilitate age intercomparison (Steiger and Jäger, 1977). Indeed, the majority of recent community effort has been to improve inter-laboratory agreement and precision rather than first principle calibrations (e.g., Condon et al., 2015; Heizler et al., 2015; Renne et al., 2010; Schoene et al., 2006). As an example, the uncertainty of the  $^{40}\text{K}$  to  $^{40}\text{Ar}$  decay constant and branching

ratio from direct measurements is ~1% (Begemann et al., 2001) while internal precisions of isotope ratios are <0.1% (Heizler et al., 2015).

Besides the lack of constraints on decay constants, another concern is the presence of initial daughter product in the analyzed mineral. For example, U-Pb dating of zircon is much easier than that of apatite due in large part to the lower Pb incorporated into the former over the latter. However, U-series geochronology is problematic due to the fact that zircon incorporates considerable Th and the  $^{230}\text{Th}$  half-life is short enough for  $^{230}\text{Th}/^{232}\text{Th}$  to change considerably over magmatic timescales (Boehnke et al., 2016a; Schmitt, 2011). Therefore in order to correct for the initial  $^{230}\text{Th}$ , either an isochron analysis is performed or one melt composition is assumed to represent the magma from which every zircon crystallized (Schmitt, 2011). Stemming primarily from the recognition that a single melt composition cannot be used to correct zircon U-series data due to the short  $^{230}\text{Th}$  half life, a new method was proposed based on the assumption that the relative partitioning for U and Th was constant and the fact that most melts are within ~15% of secular equilibrium (Boehnke et al., 2016a; Appendix B). This method calculates a melt  $^{230}\text{Th}/^{232}\text{Th}$  based on the measured  $^{238}\text{U}/^{232}\text{Th}$  and then uses that value to correct the calculated age.

## 1.4 Overview

This thesis discusses zircon saturation systematics and the significant interpretational ambiguity in the  $^{40}\text{Ar}/^{39}\text{Ar}$  analyses of extra-terrestrial samples. When taken together, these findings support the view that the “best of times” scenario more accurately describes the bulk of the Hadean. Since the partial loss of  $^{40}\text{Ar}$  during natural re-heating events requires that the measured ages underestimate the timing of last complete resetting, the age of impact craters on

the Moon need to be revised. That is to say, the majority of the impact flux happened earlier than current models suggest and the “worst of times” scenario is likely applicable prior to 4.4 Ga.

## Chapter 2: Zircon Saturation Re-revisited

**Abstract.** Improvements in experimental, analytical and computation methodologies together with published studies yielding seemingly contradictory results prompted us to return to the determination of zircon stability in the range of felsic to intermediate melts expected in continental environments. We (re-)analyzed both the run products from the zircon crystallization study of Watson and Harrison (1983) and a new style of zircon dissolution experiments (up to 25 kbars) using a large radius ion microprobe to constrain a refined zircon solubility model. The new data yield broadly similar patterns as before when arrayed for temperature and confirm that the parameter  $M$   $[=(\text{Na}+\text{K}+2\text{Ca})/(\text{Al}:\text{Si})]$  is an appropriate compositional proxy for the chemical interactions through which zircon is dissolved. We used a Bayesian approach to optimize calculation of the coefficients in the zircon solution model, which is given by:

$$\ln D_{\text{Zr}} = (10108 \pm 32)/T(\text{K}) - (1.16 \pm 0.15) \cdot (M - 1) - (1.48 \pm 0.09)$$

where  $D_{\text{Zr}}$  is the distribution coefficient of Zr between zircon and melt and the errors are at one sigma. Sensitivity tests indicate that temperature and composition are the two dominant controls on zircon solubility in crustal melts with no observable effects due to pressure (up to 25 kbar) or variable water content. Comparison of the down-temperature extrapolation with natural examples confirms the validity of the model at ca. 700°C.

### Introduction

The recognition in the early 1980s that accessory minerals (e.g., zircon, monazite and apatite) are the principal hosts in the continents for geochemically important trace elements such as U, Th, and REE (Fourcade and Allègre, 1981; Gromet and Silver, 1983; Harrison et al., 1986)

inspired experimental studies into their stability in crustal melts (Watson and Harrison, 1983; Harrison and Watson, 1983, 1984; Rapp and Watson, 1985).

Because of its near ubiquitous presence in continental rocks and key role as a U-Pb chronometer, the solubility of zircon in a variety of melt compositions was the first to be extensively investigated (Watson, 1979; Dickinson and Hess, 1982; Watson and Harrison, 1983; Harrison and Watson, 1983). Watson and Harrison (1983) undertook experiments in which zircon was crystallized from seed  $ZrO_2$  under hydrothermal conditions from mixtures of five glasses ranging from felsic to mafic in composition. Electron microprobe analysis (EMPA) of glass portions of the run products showed that zircon solubility in crustal magmas was a simple function of temperature, Zr content and composition. Notably, the parameter  $M$   $[(Na+K+2Ca)/(Al+Si)]$  was shown to be a good compositional proxy for the mechanism of zircon solution (note that  $M$  is calculated by obtaining the molar amounts of each component, renormalizing, and then obtaining the ratio). Their summary model for zircon solubility was given by

$$\ln D_{Zr} = \frac{12900}{T(K)} - 0.858 \cdot (M - 1) - 3.80 \quad (1)$$

where  $\ln D_{Zr}$  is the distribution coefficient determined by ratioing the zirconium abundance  $[Zr]$  for zircon (i.e.,  $[Zr] = 500,000$  ppm) and melt (in ppm).

Harrison and Watson (1983) undertook zircon dissolution experiments that provided reversal confirmation of the crystallization studies, at least for the anhydrous case. It was found that zircon is relatively insoluble in anatectic melts. For example, a minimum melt at ca. 700°C was found to dissolve only ~40 ppm zircon, corresponding to about one-fifth of the average Zr concentration in the crust (e.g., Rudnick and Gao, 2003).

The results of these experiments have been widely used to predict the occurrence of zircon in crustal magmas and to estimate the peak temperature experienced by magmatic rocks (i.e., accessory mineral thermometry; Watson and Harrison, 1984a,b). However limitations in both the analytical and experimental approaches restricted the resolution of the model. From the experimental perspective, many crystallization run products were complex mixtures of micron-sized crystals, glass and bubbles. This made electron microprobe analysis (EPMA) problematic as it was difficult to avoid overlapping the electron beam onto adjacent crystals and secondary fluorescence effects could contribute signal from adjacent nm-scale zircons undetected in micrographs. This can be seen in Figure 2-1, a Zr ion image of one of the original run products showing abundant, tiny neoformed zircons (bright spots within the Zr-saturated glass). The above effects contributed to overall poor precisions for temperatures below  $\sim 900^{\circ}\text{C}$  (e.g., data at  $750^{\circ}\text{C}$  could have  $\pm 100\%$  uncertainty). Furthermore, subsequent published studies of zircon solubility in similar melt compositions yielded results that appeared somewhat at variance with that of Watson and Harrison (1983). Baker et al. (2002) found Zr dissolved at levels about one-third of that measured by Watson and Harrison (1983). They attributed this discrepancy to the higher  $f_{\text{O}_2}$  in their experiments which produced higher concentrations of  $\text{Fe}^{3+}$  which acted as a network former, thus reducing zircon solubility (and, effectively,  $M$ ). Ellison and Hess (1986) examined Zr solubility in anhydrous melts at  $1400^{\circ}\text{C}$  and 1 atm and found that the model of Watson and Harrison (1983) over predicted their results by about 40%. Keppler (1993) examined the effect of halogens on granitic melt structure under similar conditions as that of Watson and Harrison (1983) and found similar Zr solubilities to theirs in halogen-free melts. However, solubility rose quasi-geometrically when  $\geq 2\%$  F was added. More recently, Rubatto and Hermann (2007) measured Zr solubility in peraluminous melts at 20 kbar and reported Zr

concentrations ~40% lower than that of Watson and Harrison (1983) for the same temperature and composition. They attributed this difference to a previously undocumented pressure effect. Thus we have returned to this investigation 30 years later with a view to using an improved experimental design along with the superior sensitivity of a high resolution ion microprobe and improved computational methods to re-examine zircon solubility in crustal melts as a function of temperature, composition, and pressure.

## **Methods**

### *Experimental approach*

Most of the experiments reported by Watson and Harrison (1983) involved nucleation and growth of zircon from pre-synthesized ZrO<sub>2</sub>-bearing glasses, followed by measurement of Zr concentration in the quenched glass to determine the saturation level. This strategy was generally successful, but it also created analytical challenges because of the high nucleation density of zircon and its tendency to form small, needle-like crystals (Fig. 2-1). The 1983 study also included a few high-temperature reversal experiments in which large zircon slabs were partially dissolved in the melt. In this case, the Zr saturation level was estimated from the diffusion profile in the quenched glass near the dissolving zircon. The value of [Zr] at the zircon/glass interface – obtained by fitting the diffusion profile – was taken as the saturation concentration (see also Harrison and Watson, 1983). Although indirect, this approach offers the advantage of providing a clear field of quenched melt (free of small zircons) to analyze for Zr.

In the 1983 studies, the partial dissolution method yielded good information at 1200-1400°C but the prospects for obtaining data at temperatures approaching those relevant to natural systems were considered poor because Zr diffusion in silicic melts is slow (Harrison and Watson, 1983), and the resulting Zr profiles against a dissolving zircon slab would be too short for

accurate characterization with available instruments. In the present study, we adopted a conceptually similar dissolution approach (to avoid the problem of myriad small crystals), but instead of immersing a large slab of zircon in the melt of interest, we equilibrated small, interstitial melt pools (10-20  $\mu\text{m}$  dia.) with a surrounding matrix of crushed zircon.

### *Starting materials*

In keeping with the general strategy used by Watson and Harrison (1983), five starting compositions were prepared to yield a range of crustal melt compositions when heated under pressure in the presence of zircon. The nominal bulk compositions range from mafic tonalite to rhyolite (Table 2-1; note that these do not represent actual melt compositions because crystalline phases in addition to zircon and glass were present in most run products; see Table 2-2). These five compositions were prepared from reagent-grade oxides and natural minerals, including  $\text{CaSiO}_3$ ,  $\text{Mg}_2\text{SiO}_4$ ,  $\text{FeO}$ ,  $\text{TiO}_2$ ,  $\text{Al}_2\text{O}_3$ , microcline and albite (all purchased from Alfa Aesar). These components were pre-mixed to yield compositions deficient in  $\text{SiO}_2$  and  $\text{Al}_2\text{O}_3$  so the latter oxides could be “topped up” as silicic acid and  $\text{Al}(\text{OH})_3$  to set the amount of  $\text{H}_2\text{O}$  contained in the mixtures (silicic acid contains 12.3 wt%  $\text{H}_2\text{O}$  [quantified repeatedly by LOI]; gibbsite contains 34.6 wt%). Introduction of  $\text{H}_2\text{O}$  in this manner made it possible to accurately regulate the bulk  $\text{H}_2\text{O}$  content of the non-zircon portion of the experimental charges at  $5.9 \pm 0.2$  weight %. The oxide/mineral mixtures were ground in agate under alcohol and dried at room temperature before use.

Additionally, four relatively mafic compositions were prepared in order to evaluate zircon solubility in such systems at near-liquidus temperatures under dry conditions. These consisted of a natural N-MORB, a synthetic tonalite, a synthetic high-alumina basalt, and a natural basaltic andesite from Paricutin volcano. The natural materials were run as finely-ground rock powders;

the two synthetic mixes were fused and quenched to glasses prior to running the zircon saturation experiments in a piston-cylinder apparatus. Because these compositions strongly deviate from all of our other experiments, they are excluded from the zircon saturation calibration but discussed separately later.

A key aspect of this study involved calibration of matrix effects on sample sputtering during SIMS analysis for Zr (see *SIMS analytical details* section). Sputtering behavior is expected to depend not only upon major-element composition of the analyzed glasses, but also upon the presence and amount of dissolved H<sub>2</sub>O. We prepared three reference glasses and mixed them with USGS standard AGV-1 (236 ppm Zr) and Lake County obsidian (138 ppm Zr) in various proportions to create a broad composition range (Table 2-3). These materials were fused in a piston-cylinder apparatus both anhydrous (in graphite) and hydrous (in graphite encased in Ni) to obtain glasses suitable for electron- and ion-microprobe analysis.

### **Experimental procedures**

The zircon saturation experiments were conducted in a piston-cylinder apparatus using two container designs. The high-temperature series (ZSAT11; 1020°C) required gold capsules; all other experiments were conducted in silver cylinders incorporating a separate chamber (or “well”) for each of the five starting compositions described above (Table 2-1), plus a central buffer chamber to control the oxygen fugacity of the samples (see Fig. 2-2a). Prior to an experiment, each of the sample chambers of the silver cylinder was filled to  $\frac{1}{2}$  to  $\frac{2}{3}$  its full height with one of the five synthetic rock mixes. The remaining space at the top was filled with either crushed Mud Tank zircon or a mixture of crushed zircon and the synthetic rock powder present in the lower part of the chamber. The idea behind this strategy was that the melt fraction of the starting rock mix would wick into the crushed zircon at run conditions, leaving other silicate

phases mainly in the lower portion of the chamber. The intent was that melt penetrating the crushed zircon would attain saturation equilibrium with its host, and form intergranular pools among the zircon grains large enough to analyze for major elements by electron microprobe (EPMA) and for Zr by SIMS. In early experiments, the crushed zircon used in the starting material had been pre-sieved to ~44-72  $\mu\text{m}$  diameter, which resulted in generally small melt pools (<10  $\mu\text{m}$ ) with occasional pockets large enough to analyze. In later experiments (ZSAT9 and 10), the relatively uniform zircon fragments were replaced with broader size-spectrum material that had been passed through a 150- $\mu\text{m}$  sieve and also pre-mixed with 20-30% of the starting rock powder.

Prior to an experiment, the central buffer chamber (Fig. 2-2a) was filled with a mixture of FeO and silicic acid. Heating to run conditions and minor oxidation of this material produces a solid oxygen buffer assemblage of fayalite + magnetite + quartz (FMQ). The  $\text{H}_2\text{O}$  liberated from the silicic acid enables communication, via hydrogen diffusion, between the buffer and the five chambers in the Ag cylinder containing the hydrous zircon-saturation experiments. Previous experiments conducted in the RPI experimental lab suggest that the ‘ambient’  $f_{\text{O}_2}$  of the piston-cylinder assembly (Fig. 2-2c) at run conditions is not far displaced from the FMQ buffer. The post-experiment presence of all three phases of the buffer assemblage (and  $\text{H}_2\text{O}$ ) was confirmed in all cases by optical microscopy and testing with a magnet for the presence of  $\text{Fe}_3\text{O}_4$ . Other studies in the RPI lab using multi-chambered containers have confirmed that the external buffer regulates  $f_{\text{O}_2}$  in the experimental charges (e.g., Trail et al., 2012). Hydrogen diffuses relatively slowly in Ag relative to Pt and Pd, but the Ag “septa” between the buffer and the experimental charges were thin (200-300  $\mu\text{m}$ ; See Fig. 2-2a), and the temperatures of the experiments were close to the melting point of silver, where hydrogen diffusion is expected to be fast for this metal

(Chou, 1986). When the chambers of the silver container were loaded as desired, it was covered with a pressure-sealing Ag lid and positioned in a 19-mm NaCl-borosilicate glass piston-cylinder assembly (Fig. 2-2c) for treatment at elevated P-T conditions.

A different container system was needed for the highest-temperature experiments (ZSAT11) because 1020°C is above the melting point of Ag, even at 1 GPa. For ZSAT11, the samples were contained in Au tubes loaded with rock mix and zircon in a manner similar to that used for the lower-temperature experiments. Only three Au capsules could be run at one time (as opposed to five in the silver container system); the most silicic and the most mafic of the compositions listed in Table 2-1 were omitted from this series. The Au tubes were welded shut and inserted in pre-drilled holes in a graphite cylinder (Fig. 2-2b). The void space resulting from the somewhat irregular shape of the Au capsules was filled with unfired pyrophyllite powder in order to establish a finite  $P_{\text{H}_2\text{O}}$  outside the Au capsules and counteract any tendency for hydrogen loss from the charges at run conditions. This strategy appears to have been successful, because the  $\text{H}_2\text{O}$  contents of the quenched glasses show no evidence of  $\text{H}_2\text{O}$  loss as inferred from the significant difference between analyzed totals and 100 wt.%. Among the new experiments reported here, ZSAT11 was the only one not buffered at FMQ; it is also the only run incorporating a containment system similar to that used in the experiments of Watson and Harrison (1983).

The mafic-system experiments (ZSAT12 and 13) were run nominally dry in graphite capsules (no added  $\text{H}_2\text{O}$ ; powders held at 120°C prior to loading the experiments) at 1 GPa and 1175 and 1225°C, respectively.

Following treatment at elevated P-T conditions, the samples were quenched by shutting off the power to the furnace, which resulted in cooling to ~200°C in ~20 s. The generally cylindrical

samples were recovered from the piston-cylinder assembly, sectioned roughly along the cylinder axes, and polished (ultimately with colloidal silica) for EPMA and SIMS analysis.

#### *Electron microprobe analysis*

Major element contents of quenched glasses were determined with the RPI CAMECA SX100 electron microprobe. Glass pools free of inclusions were targeted with a 15 kV accelerating potential, a defocused beam of 30 to 40  $\mu\text{m}$ , and a current of 7 to 10 nA. Elements were standardized against synthetic glass standards and silicates. Sodium, Mg, and Si  $K_{\alpha}$  X-rays were collected through TAP crystals. Potassium, P, Ca, and Ti  $K_{\alpha}$  X-rays were collected through large PET crystals and Fe  $K_{\alpha}$  X-rays were measured through a large LIF crystal.

Major element contents and  $\text{ZrO}_2$  of ZSAT 12 and 13 were analyzed using the UCLA JEOL JXA-8200 SuperProbe. Glass pools away from other phases were analyzed with a 15 kV accelerating potential, a defocused beam of 8  $\mu\text{m}$  on ZSAT 13 and 2  $\mu\text{m}$  on ZSAT 12, and a current of 15 nA. The 8  $\mu\text{m}$  beam was sufficiently large to prevent Na loss, however some Na may have been lost using the 2  $\mu\text{m}$  beam size.

#### *SIMS analytical details*

A requirement of the dissolution-type experiment is that Zr released from the crushed Mud Tank zircon equilibrates with the melt (Fig. 2-3) occupying the inter-crystalline vein network. We chose to use the ion microprobe in scanning ion image analysis mode (e.g., Harrison and Schmitt, 2007) to take advantage of the 2D concentration distribution representations which directly permit assessment of the degree of equilibration within the glass vein networks. In addition to our new dissolution experiments, 22 of the crystallization experiments from the study of Watson and Harrison (1983) were also analyzed.

Epoxy mounts containing the run products were ultrasonically cleaned in a sequence of soapy water, deionized water, and methanol, and then Au coated. Isotope ratios were measured by focusing  $^{90}\text{Zr}^+$  and  $^{30}\text{Si}^+$  sequentially in the axial ETP electron multiplier through the use of peak switching. A mass resolving power (MRP) of  $\sim 4000$  was sufficient to separate the peaks of interest from molecular interferences without the use of energy filtering. For these analyses, we used a primary beam of  $\sim 50$  pA  $\text{O}^-$  in critical illumination with a  $\sim 3$   $\mu\text{m}$  diameter spot for the July 2007 and August 2011 analyses and an  $\sim 8$  pA  $\text{O}^-$  and  $\sim 4$   $\mu\text{m}$  spot for the February 2012 measurements rastered at 20 kHz over a  $30 \times 30$   $\mu\text{m}^2$  area. For the May 2012 session a primary beam of  $\sim 50$  pA  $\text{O}^-$  with a  $\sim 3$   $\mu\text{m}$  diameter spot was used. A dynamic transfer deflection synchronizes the primary beam raster with secondary ion beam deflection such that the secondary beam was constantly aligned with the center of the field aperture. Although ion yields vary greatly across the rastered field due to differential charging (which increases with distance from the edge of the analysis area), this effect can be compensated for by ratioing  $^{90}\text{Zr}^+$  to  $^{30}\text{Si}^+$ , which is homogeneously distributed throughout the glass. Integration times were  $\sim 25$  minutes over 100 cycles (1 cycle = 15 s).

All analytical sessions used LCO-1 hydrous glass as the primary standard to determine relative sensitivity factors for Zr/Si, but we also included SRM 610 (and 612) glasses as secondary standards. We rationalize that using LCO-1 as a primary standard mitigates variations in SIMS Zr/Si relative sensitivities (i.e., matrix effects) that are expected for different bulk compositions (e.g., experimental glasses vs. SRM 610). We did not employ energy filtering in an attempt to mitigate matrix effects due to the generally low count rates. In the course of our study, we determined that Zr/Si relative sensitivities increase with addition of water (all other components being equal). We subsequently (during the August 2011 session) evaluated matrix

effects across the range of experimental glass compositions (i.e., between felsic LCO-1 and mafic AGV-1 glasses). Two additional standards were adopted for the February 2012 session to assess the functional form of the correction which appears broadly linear. The overall magnitude of the felsic-to-mafic matrix effect (i.e., the change in  $^{90}\text{Zr}^+/\beta^{30}\text{Si}^+$  between felsic and mafic standards) depends on the specific run conditions (presputter time, presputter beam current, etc) and was ~10% and ~20% in the August 2011 and February 2012 sessions, respectively. The sign of this change also depends on specific run conditions and varied between positive and negative in the two sessions, the cause for this being a strong dependence of the relative sensitivity on secondary ion energy caused by localized charging of the analysis area. The May 2012 data was corrected using the same correction scheme as for the previous runs. The July 2007 data was corrected using the August 2011 correction scheme as they were collected under similar run conditions.

In contrast to the crystallization experiments (Fig. 2-1), note in Figure 3 that the analysis region of interest is free of neoformed zircon seeds. For quantitative imaging of the unknowns, we subdivided the image area into nine equal-size squares to provide an estimate of homogeneity in the standards and examined a region of interest (ROI) sufficiently removed from zircon to avoid beam overlap (Fig. 2-1).

#### *Error estimation*

There are two dominant sources of uncertainty: elemental abundance and/or ratio precision (assessed via counting statistics) and matrix effects. Overall errors were obtained by adding in quadrature the error calculated from counting statistics with the error from the slopes of the matrix effect calibration lines. Uncertainty due to actual sample heterogeneity is not considered because of the averaging nature of the ion imaging method. The  $2\sigma$  uncertainties in the ratio

varied between 2 and 24% while uncertainties in the calibrations added another 2 to 6% depending on the magnitude of the correction.

## Results

The complete data set was first plotted with respect to  $M$  and  $[Zr]$  (Fig. 2-4) to allow comparison with the Watson and Harrison (1983) data. The data at 1020° C and 925/950°C clearly array in a systematic fashion while the <900°C data show greater scatter. Our new results (Fig. 2-4) are remarkably similar to that presented in Fig. 1 of Watson and Harrison (1983). The biggest difference comes from the improved precision of the SIMS measurements as well as the confirmation that  $[Zr]_{\text{sat}}$  was reached since 1) element gradients were not seen in the 2D ion images, and 2) both the crystallization and dissolution experiments define the same relationship (Fig. 2-4).

A plot of  $\ln(D_{Zr})$  vs.  $10^4/T(K)$  as a function of  $M$  (Fig. 2-5) shows more clearly that even the lower temperature data (<900°C) contain valuable solubility information. The near parallel nature of these lines is evidence that the formulation of compositional dependence of Watson and Harrison (1983) appropriately describes the dataset. Part of scatter in the lines may reflect the effect of compositional interpolation (i.e., there is a range of  $\pm 0.1$  in  $M$  for each line).

### *EPMA vs. SIMS*

Results from quantitative ion imaging of the crystallization experiments were compared to the EPMA data of Watson and Harrison (1983) in Figure 2-6. A least squares regression with a slope of  $1.03 \pm 0.05$  and MSWD of 0.84 was calculated using the New York Regression (Mahon, 1996). Since the slope is indistinguishable from unity, we rule out any significant systematic difference between the EPMA and SIMS data sets.

### *Model calculation approach and fit*

Our view is that it is inadvisable to directly combine the present SIMS dataset with the EPMA data of Watson and Harrison (1983) to calculate a new model as they were obtained under very different analytical conditions. However, use of both is highly desirable as it prevents over-fitting a refined model by any one data set. The fact that the  $\ln(D_{Zr})$  vs.  $10^4/T(K)$  plot (Fig. 2-5) for constant  $M$  shows broadly parallel lines implies that the Watson and Harrison (1983) model is broadly consistent with our new results. Rather, our focus is to optimize model parameters about the original formulation while assessing the possibility of a pressure effect.

The original model of Watson and Harrison (1983) was obtained largely by visual curve fits to the  $[Zr]$  vs.  $M$  data. In our updated model, we utilized the Bayesian Linear Regression (BLR) method which allows for the calculation of a set of parameters based on the data from a prior probability distribution for the parameters (Gelman et al., 2003). First, a BLR was calculated for the Watson and Harrison (1983) data with an uninformative prior distribution (a uniform distribution from negative to positive infinity for each parameter). To produce the final model, a BLR was then calculated using the SIMS data and the output from the first BLR as the prior distribution. This has the effect of allowing the SIMS data to ‘update’ the model parameters.

In order to determine which parameters (i.e.,  $P$ ,  $T$ , and  $M$ ) are most important to the fit, several models were calculated, each considering a different subset of the parameters. Calculations were performed using MCMCpack (<http://mcmcpack.wustl.edu/>) and the R statistical software package (<http://www.r-project.org/>). Bayes Factors were calculated for each regression model in order to identify the best model (Kass and Raftery, 1995). To simplify the selection process, each Bayes Factor was converted into a probability – assuming that one of the models is correct. Model probabilities were calculated from Bayes Factors as their probabilities are normalized, unlike, say, using marginal log likelihoods (Gelman et al., 2003). Note that

Bayesian methods calculate the *evidence* for a hypothesis rather than just the probability that a hypothesis is consistent with the given data (such as a *T*-test). Furthermore, when evaluating models of differing complexity, the goodness of fit is potentially misleading as it biases towards selection of the most complex parameterization. When selecting among models, the principle of parsimony requires that complexity be penalized.

Given that *P* was explicitly included in the model calculation, we performed an omnibus fit on the entire dataset including the reanalyzed samples from Rubatto and Hermann (2007). Surprisingly, the probability of the *T+M* model is 0.997 with all other permutations yielding coefficients less than 0.002 (Table 2-4). Thus the best fit model (with 1  $\sigma$  errors) is given by

$$\ln D_{Zr} = \frac{10108 \pm 32}{T(K)} - (1.16 \pm 0.15) \cdot (M - 1) - (1.48 \pm 0.09) \quad (2)$$

Discussions of pressure, H<sub>2</sub>O, fO<sub>2</sub>, etc. effects follow, but note that the above model is specifically formulated to address peraluminous and metaluminous, rather than peralkaline (Watson, 1979) compositions.

## Discussion

### *New Parameters*

The model parameters in Eq. (2) are broadly similar to those of Watson and Harrison (1983) with differences arising from the improved analytical and computational methods. Comparison of the original and new models (with a nominal 5% error in *T*) for a constant *M* of 1.4 shows generally similar temperatures (Fig. 2-7A). Although the models diverge as *M* increases (for a constant [Zr]<sub>sat</sub>=150 ppm; Fig. 2-7B), differences are not significant at the level of uncertainty specified.

In order to estimate the uncertainty of calculated model temperatures, we used standard error propagation techniques to derive the following two formulas:

$$\sigma_{Zr} = \frac{\sigma_{Zr_{ppm}}}{Zr_{ppm}} \cdot D_{Zr} \quad (3)$$

$$\sigma_T = \left( \frac{\left( \frac{\sigma_{Zr}}{D_{Zr}} \right) + 1.3456 \cdot \sigma_M^2}{\ln(D_{Zr}) + 0.32 + 1.16 \cdot M} \right) \cdot T \quad (4)$$

where  $\sigma_{Zr}$  and  $\sigma_T$  are the one standard deviations of the Zr distribution coefficient and calculated temperature, respectively. The quantities  $Zr_{ppm}$ ,  $M$ ,  $\sigma_M$ , and  $\sigma_{Zr_{ppm}}$  are thus obtained from sample analysis,  $D_{Zr}$  is defined in equation 1 and  $T$  is calculated from equation 2.

#### *Compositional parameterization*

The original justification for  $M$  was to capture the likely zircon solubility dependence on the product of (Na+K+2Ca)/Al (i.e., the ratio of network modifiers to formers) and inverse silica activity (Watson and Harrison, 1983). That 1/Si appears to capture this latter control (rather than using  $1/a_{Si}$ ) was judged more valuable than the fact that  $M$  is not dimensionless (it has units  $\text{atom}^{-1}$ ) and thus requires compositional re-normalization. Specifically, our method for calculation of  $M$  requires transformation of the wt. % oxides listed in Table 2-3 to atomic proportions, re-normalization to total moles, and then insertion of the Na, K, Ca, Al, and Si molar fractions (over the total number of moles) into the  $M$  formulation.

We have examined several ways to modify  $M$  as to be dimensionless without success. For example, instead of Al · Si in the denominator, using Al+Si might capture the necessary compositional dependence while removing the dimensional character of  $M$ . However, we found that doing so increases the average difference between the calculated and known temperatures

for the calibration data by a factor of two. Another approach might be to explicitly use  $1/a_{\text{Si}}$ . We investigated this approach by calculating silica activities for the 930°C melt compositions using MELTS (Asimow and Ghiorso, 1998; Ghiorso and Sack, 1995) but found that the correlation coefficient between the saturation concentration and  $M$  decreased from 0.95 to 0.7.

A second inconvenience of  $M$  arising from its dimensional character is the need to renormalize molar abundances of all major element oxides. Calculating  $M$  using molar abundances of only the elements of which it is comprised, nearly identical temperatures (within 10°C) and similarly high correlation coefficients of 0.99 for the solubility model are obtained as for the original approach of calculating  $M$  in Watson and Harrison (1983). Thus, while the calculation of  $M$  is inconvenient (and because of the normalization indirectly dependent on other, typically minor components in evolved melts such as Fe and Mg), given the 30 year investment in this approach and significant literature available for comparison, we do not think this issue is significant enough to warrant a change in approach.

Baker et al. (2002) suggested that  $FM$  ( $=(\text{Na}+\text{K}+2(\text{Ca}+\text{Mg}+\text{Fe})) / (\text{Al} \cdot \text{Si})$ ); Ryerson and Watson, 1987) might be a better choice of compositional parameter than  $M$ . We repeated the procedure described earlier to assess whether  $M$  or  $FM$  best represents the compositional controls on zircon solubility for the compositional range. We found that replacing  $M$  with  $FM$  in our model results in a substantial deterioration of fit (i.e.,  $p = 0.19$  vs.  $p = 0.81$ ) and thus conclude that  $M$  is a far preferable compositional proxy.

#### *Effect of $f_{\text{O}_2}$ and halogens*

Baker et al (2002) measured the diffusion of Zr and zircon solubility in hydrous, metaluminous granitic melts with and without halogens (Cl or F) at 1,050-1,400°C and 10 kbar. Their results indicated an 800°C solubility about one third of that predicted by the Watson and

Harrison (1983) model which they attributed to differences in  $f_{O_2}$  affecting the structural role of iron in the melt. However, the Baker et al (2002) data plot (Fig. 2-8) is reasonably close to our new model fit strongly suggesting the earlier perceived differences were due to weak control of the model across much of the temperature range used by Baker et al (2002). Furthermore, this general agreement suggests little influence of oxygen fugacity on zircon solubility and a minimal role of iron and halogens at the levels used by Baker et al (2002).

### *Pressure effect*

Rubatto and Hermann (2007) measured  $[Zr]_{sat}$  in granitic ( $M \approx 1.1$ ) melts at 20 kbar and reported  $[Zr]$  ~40-70% lower than that predicted by Watson and Harrison (1983). Given this disparity, we investigated the possible role of pressure by both undertaking higher pressure dissolution experiments and re-analyzing the run products from the experiments of Rubatto and Hermann (2007), graciously provided by the authors. We undertook two hydrothermal runs at 25 kbar and 930° and 1000°C, with each run containing five capsules bearing melts of differing composition ( $1.3 \leq M \leq 1.5$ ). Measurement of these glasses (Fig. 2-9) yield estimates of  $[Zr]_{sat}$  that are not significantly different from the predictions of either the model of Watson and Harrison (1983) or this study.

As for the Rubatto and Hermann (2007) glasses, when we standardized using SRM 610 without the matrix corrections (discussed in the *SIMS analytical details* section) we found remarkable agreement with the concentrations they report. However, given that their glasses were reported to contain ~12% H<sub>2</sub>O, when we applied the hydrous and composition matrix corrections, Zr concentrations increased to levels consistent with the Watson and Harrison (1983) and this study. We cannot be sure what the full explanation is for this disparity but speculate that it could reflect a matrix mismatch between SRM 612 and the experimental glasses

under LA-ICPMS analysis. For example, evidence for this kind of matrix effect has been reported by Gaboardi and Humayun (2009).

#### *Implication for melt structure*

Previous work on silicate melt structures as a function of pressure suggested that  $\text{Al}^{3+}$  may shift from four-fold coordination to six-fold coordination at ~15 kbar (Kushiro, 1976). If correct, then it seems likely that the further melt depolymerization at higher pressure would result in an increase in zircon solubility. Allwardt et al (2005) showed that the coordination change depends on melt composition and that Ca has a large influence in lowering the required pressure from >30 kbar to <20 kbar. However, our experimental samples contained Ca and yet we find that zircon saturation is independent of pressure at or below 25 kbar. Although our experiments were not designed to be a sensitive test of this hypothesis, our results are consistent with little change in Al coordination at  $\leq 25$  kbar.

#### *Effect of water*

Given the significant influence of water on Zr diffusion coefficient below ~2%  $\text{H}_2\text{O}$  (Harrison and Watson, 1983), it seems likely that water content could have an effect on zircon solubility. In order to evaluate this possible effect, we compiled the anhydrous data of Harrison and Watson (1983), Ellison and Hess (1986) and Dickinson and Hess (1982) on a plot of  $\log(D_{\text{Zr}})$  versus inverse absolute temperature and compared it to predictions of our new model (Fig. 2-10). For  $M$  corresponding to the lunar granitoid composition of Dickinson and Hess (1982) (i.e., 1.79), the new model does a poorer job than the original of predicting Zr concentration, but the opposite is true for the fit to the Ellison and Hess (1986) and Harrison and Watson (1983) data. Thus the core issue in this apparent reversal of behavior is unlikely to be the presence or absence of water. It is far more likely that this disagreement reflects the lunar

compositions of Dickinson and Hess (1982) which lie outside the terrestrial compositional range used in the new calibration together with its high accuracy. The wide range of H<sub>2</sub>O concentrations used in the present study and that of Baker et al (2002) which are both well fit by our preferred model parameters suggests that water content does not strongly influence zircon solubility.

#### *Zircons from mafic melts?*

Zircon is not uncommon in mid-oceanic ridge (MOR) environments (Coogan and Hinton, 2006; Fu et al., 2008; Grimes et al., 2007; Lissenberg et al., 2009; Schmitt et al., 2011), which might be seen to suggest that it can crystallize from basaltic melts close to the liquidus. Although the model we present is not specifically calibrated for such compositional (i.e.,  $M > 2.5$ ) or temperature ( $> 1100^\circ\text{C}$ ) conditions, extrapolation suggests zircon could not crystallize from a MORB source above  $\sim 900^\circ\text{C}$  assuming any realistic Zr content. DeLong and Chatelain (1990) found systematic relationships for evolved MOR glasses on plots of  $M$  vs. [Zr] using the Watson and Harrison (1983) calibration. At high values of  $M$  (3.5 to 2.5), Zr concentrations rise from  $\sim 100$  to  $\sim 700$  ppm (at  $M=2.4$ ) due to fractionation of modal phases, whereupon [Zr] rapidly decreases with decreasing  $M$ . They interpreted this concentration reversal to indicate that zircon began crystallizing at  $\sim 840^\circ\text{C}$ . While  $M = 2.4$  is above the highest value of 2.1 used in both the Watson and Harrison experiments and the present study, this small extrapolation seems warranted as the DeLong and Chatelain (1990)  $840^\circ\text{C}$  estimate corresponds well to the solidus temperature of MORB gabbro under water-saturated conditions (Botcharnikov et al., 2008; Coogan et al., 2001). Furthermore, this prediction is consistent with a large database of Ti thermometry for MOR at  $800 \pm 100^\circ\text{C}$  (e.g., Fu et al., 2008; Grimes et al., 2009, 2008, 2007;

Hellebrand et al., 2007; Lissenberg et al., 2009; Schmitt et al., 2011; cf. Coogan and Hinton, 2006).

To directly test this proposed relationship, we undertook several experiments (Table 2-5) using basaltic compositions in order to establish the solubility of Zr in mafic magmas. Analysis of four different compositions at 1225°C and three at 1175°C yield ZrO<sub>2</sub> contents between 0.54 and 4.75 wt.% (Table 2-5). All run products contained neoformed zircons (in addition to plagioclase and pyroxene for ZSAT 12) and each temperature cohort yield a positive correlation between ZrO<sub>2</sub> and *M*. These results show conclusively that basaltic liquids require an unrealistically high abundance of >5000 ppm Zr to directly crystallize zircon, and thus zircons found in mafic environments must have crystallized from late stage, evolved melts.

Fu et al. (2005, 2008) appear to hold a further misapprehension regarding zircon crystallization from mafic magmas. They viewed the low Ti contents (8-10 ppm) in zircons from anorthosite and gabbroic rocks with liquidus temperatures of ~1000-1100°C as inconsistent with primary zircon crystallization. However, the low [Zr] of these magmas (ave. = 64 ppm, n = 69; Seifert et al., 2010) effectively precludes stabilizing igneous zircon, even during fractionation of Zr-poor modal phases (Harrison et al., 2007), until temperatures of ≤750°C are reached.

#### *Geologic controls*

Because of the relatively poorer resolution of the empirical model at lower temperatures, we compared our model with natural examples from volcanic systems where glass compositions and temperatures are known from other thermometers. There are abundant literature examples where the Watson and Harrison (1983) zircon thermometer has been successfully applied to volcanic rocks (e.g., Hancher and Watson, 2003), but vagaries exist in how input parameters for the model have been acquired and implemented (including the use of whole-rock vs. glass compositions, or

determination of Zr abundances being biased by method or laboratory). We thus focus on the example of the rhyolitic Bishop Tuff because 1) it has been intensely studied with a wealth of data for various magmatic thermometers being now available, and 2) we have compositional data acquired in-house under similar conditions as in this study, thus minimizing the potential for analytical bias. For our comparison, we use the UCLA CAMECA *ims1270* data from Schmitt and Simon (2004) to determine Zr abundances in melt inclusion glasses from Bishop Tuff. Here, we only consider data for the F6 unit of the early erupted Bishop Tuff (EBT) which has more homogeneous crystal populations and shows less evidence for strong pre-eruptive re-heating and compositional mixing compared to the late erupted Bishop Tuff (e.g., Wark et al., 2007; Thomas et al. 2010; Reid et al., 2011). Zr abundances were corrected for the hydrous vs. anhydrous matrix effect (i.e., Zr values increase by 20% relative to those in Table 2 of Schmitt and Simon, 2004). With the old calibration (Watson and Harrison, 1983), the average Zr-saturation temperature for the melt inclusions (n=10) is 745°C (minimum 729°C; maximum 758°C), whereas the new calibration yields an average of 704°C (minimum 682°C; maximum 730°C). This new value compares favorably with Fe-Ti-oxide results – a rapidly equilibrating thermometer closely tracking the eruption temperature – with most data for the EBT ranging between 700° and 720°C (Ghiorso and Evans, 2008).

#### *Implications for lower crustal heat production*

A longstanding view among many geochemists is that abundances of certain LILE and HFSE elements decrease with depth in the continental crust (e.g., Rudnick and Gao, 2003). This has generally been assumed to be due to intracrustal magmatic differentiation in which incompatible elements, including U, Th and K and thus heat generation, are partitioned into granitic melts which then buoyantly ascend to the upper crust (e.g., Taylor and McLennan, 1985; Kempton et

al., 1995). However, Harrison et al. (1986) noted that because U and Th are largely hosted in the continental crust in accessory phases which remain largely unmelted and unentrained during anatexis, removal of minimum melts from the lower crust would actually increase uranogenic and thorogenic heat generation there. Our refined model remains consistent with this conclusion for zircon-hosted U and Th, which is further bolstered by the observation of exceedingly low transport rates of U and Th in zircon (Cherniak and Watson, 2003) under crustal conditions, essentially precluding diffusive equilibration during melting. Furthermore, recent models of the composition of the continental crust (e.g., Hacker et al., 2011) emphasize that existing geochemical and geophysical constraints are consistent with considerably greater heat production in the lower crust than previously thought.

## **Conclusions**

We revisited the experimental calibration of zircon solubility in crustal melts using improved experimental, analytical and computational approaches. Our new SIMS data reveal no significant difference with that found in the study of Watson and Harrison (1983). Both data sets were used to calculate the parameters for a refined solubility model. The parameters that were found to control zircon saturation behavior are temperature and composition (as represented by  $M$ ). The new model is given by:  $\ln(D_{Zr}) = 10110/T(K) - 1.21 \cdot (M - 1) - 1.41$ . This refined model predicts broadly similar temperatures for most melt compositions and temperatures as that of Watson and Harrison (1983) but diverges at high zircon concentrations and  $M$ . There appears to be no pressure effect at  $\leq 25$  kbar and the compositional parameter  $M$  is shown to be a superior compositional proxy to a variety of other approaches investigated.

**Chapter 2 Tables and Figures**

<b>Oxide</b>	<b>LCO</b>	<b>B</b>	<b>C</b>	<b>TN</b>	<b>BTC</b>
SiO <sub>2</sub>	77.0	73.7	70.2	61.9	65.8
TiO <sub>2</sub>	0.1	0.3	0.5	0.8	0.8
Al <sub>2</sub> O <sub>3</sub>	13.1	13.5	13.9	16.9	18.6
FeO	0.7	1.8	2.9	5.8	4.8
MgO	0.1	1.1	2.2	3.0	1.6
CaO	0.5	1.7	3.1	5.7	2.8
Na <sub>2</sub> O	3.7	3.6	3.5	3.9	1.7
K <sub>2</sub> O	4.8	4.3	3.7	2.0	3.8
<b>Total</b>	100.0	100.0	100.0	100.0	99.9

**Table 2-1:** Anhydrous compositions of starting materials used in this study. These compositions were prepared by weighing CaSiO<sub>3</sub>, Mg<sub>2</sub>SiO<sub>4</sub>, FeO, TiO<sub>2</sub>, Al<sub>2</sub>O<sub>3</sub>, microcline, albite, silicic acid and Al(OH)<sub>3</sub> in appropriate portions to yield the rock-forming oxides shown plus 6 weight % H<sub>2</sub>O. See text for discussion.

Sample	Phases Present
ZSAT5A	quartz
ZSAT7A	none
ZSAT7B	pyroxene
ZSAT7C	pyroxene
ZSAT7D	amphibole, feldspar
ZSAT7E	garnet, corundum
ZSAT9A	quartz, feldspar, kyanite, garnet
ZSAT9B	quartz, pyroxene, garnet
ZSAT9C	quartz, garnet, pyroxene, rutile
ZSAT9D	amphibole, garnet
ZSAT9E	quartz, garnet, kyanite, rutile
ZSAT10A	quartz, garnet, kyanite
ZSAT10B	quartz, pyroxene, garnet
ZSAT10C	quartz, pyroxene, garnet
ZSAT10D	pyroxene, garnet
ZSAT10E	quartz, garnet, kyanite, rutile
ZSAT11B	none
ZSAT11C	none
ZSAT11D	none

**Table 2-2:** Summary of phases additional to zircon present in the experimental run products.

Sample	Duration	<i>T</i>	<i>P</i>	Analytical Total	SiO <sub>2</sub>	TiO <sub>2</sub>	Al <sub>2</sub> O <sub>3</sub>	FeO	MgO	CaO	Na <sub>2</sub> O	K <sub>2</sub> O	<i>M</i>	[Zr]	2σ
1	44	930	6	88.4	54.2	0.5	16.9	4.1	2.0	7.6	2.3	0.8	1.9	1442	117
2	44	930	6	88.9	56.2	0.6	16.8	3.1	1.6	5.9	3.3	1.4	1.79	1339	119
3	44	930	6	90.2	57.4	0.7	16.8	2.6	1.2	4.8	3.7	3.0	1.83	1405	121
4	44	930	6	88.9	58.8	0.6	17.1	3.6	1.4	2.6	1.5	3.3	1.01	367	47
5	19	1020	6	91.3	56.5	0.5	16.8	3.4	2.4	8.4	2.5	0.8	2.09	3178	332
6	19	1020	6	92.2	58.2	0.7	16.6	2.6	2.4	6.8	3.4	1.5	2.02	2801	285
7	19	1020	6	91.2	58.4	0.7	16.1	2.2	1.5	5.6	3.7	3.0	2.05	3452	342
8	19	1020	6	92.1	61.6	0.8	17.7	2.8	1.4	2.8	1.4	3.6	1.01	864	107
9	50	930	6	92	66.6	0.4	13.6	1.2	0.6	2.1	3.5	4.0	1.52	701	97
10	50	930	6	90.9	63.8	0.4	14.2	1.6	0.8	3.0	3.5	3.6	1.63	852	130
11	50	930	6	89.6	58.9	0.7	15.8	4.1	1.4	5.6	2.2	0.9	1.5	917	139
12	50	930	6	91.2	59.4	0.7	16.5	3.2	1.5	4.7	3.4	1.8	1.61	995	63
13	50	930	6	91.6	59.4	0.6	17.2	2.3	0.8	4.4	3.6	3.3	1.7	1183	98
14	50	930	6	95.1	64.2	0.6	17.8	3.7	1.6	1.8	1.6	3.8	0.88	300	75
15	284	800	1.7	91.2	68.1	0.1	13	1.1	0.1	1.2	3.4	4.2	1.36	155	14
16	284	800	1.7	91.7	68.1	0.2	13	1	0.1	1.2	3.6	4.5	1.44	223	59
20	284	800	1.7	92.3	69.5	0.2	13.2	1.4	0.7	1.5	1.6	4.2	1.05	226	65
21	240	800	1.2	92.5	66.6	0.2	13.7	1.4	b.d.	0.8	4.6	5.2	1.61	748	53
22	240	800	1.2	92	66.4	0.2	14.2	1.2	b.d.	1.4	3.8	4.8	1.47	452	29
24	240	800	1.2	92.4	68.5	0.4	13.3	1.9	0.8	1.6	1.7	4.2	1.1	178	24
25	240	750	2.1	91.2	68.9	0.1	12.4	0.9	b.d.	1.0	3.5	4.4	1.41	206	30
26	240	750	2.1	91.3	69	0.1	12.6	1.0	b.d.	1.0	3.0	4.6	1.32	265	50
ZSAT5A	72	850	10	92.4	71.9	0.1	12.2	0.7	0.1	0.2	3.6	3.5	1.15	277	15
ZSAT7A	48	925	10	92.6	71.7	0.1	12.1	0.8	0.1	0.2	4.1	3.5	1.24	666	35
ZSAT7B	48	925	10	93.6	70.4	0.2	12.4	1.3	0.7	1.3	4.1	3.3	1.46	742	40

ZSAT7C	48	925	10	93.9	68.3	0.4	13.2	1.9	0.9	2.0	4.2	3.0	1.55	849	56
ZSAT7D	48	925	10	93.4	64.1	0.4	15.0	3.0	0.9	3.3	4.3	2.3	1.63	1000	69
ZSAT7E	48	925	10	94.5	65.3	0.5	15.7	2.9	0.8	3.2	3.4	2.7	1.42	755	52
ZSAT9A	45	930	24*	94.2	68.3	0.8	15.2	0.8	0.1	0.3	4.9	4.6	1.34	968	92
ZSAT9B	45	930	24*	94.1	67.9	0.5	15.0	0.7	0.3	1.0	4.6	4.5	1.43	1084	82
ZSAT9C	45	930	24*	93.9	68.1	0.3	14.6	0.7	0.3	1.1	4.6	4.0	1.42	842	69
ZSAT9D	45	930	24*	92.9	66.7	0.3	15.6	0.7	0.3	2.0	5.0	2.4	1.39	749	61
ZSAT9E	45	930	24*	94.4	68.0	0.3	15.3	0.7	0.2	1.3	3.8	4.8	1.35	933	76
ZSAT10A	48	1000	25	95.2	70.4	0.1	13.9	0.9	0.2	0.3	5.0	4.3	1.42	1396	112
ZSAT10B	48	1000	25	95.5	69.3	0.2	14.6	0.3	0.9	1.0	4.9	4.3	1.49	1060	84
ZSAT10C	48	1000	25	95.4	69.1	0.4	14.7	0.9	0.4	1.4	4.7	3.7	1.45	1333	104
ZSAT10D	48	1000	25	93.5	65.9	0.5	15.8	1.1	0.4	2.5	5.1	2.1	1.49	1358	116
ZSAT10E	48	1000	25	94.4	68.1	0.4	14.8	0.9	0.2	1.7	3.7	4.5	1.42	2318	229
ZSAT11D	96	1020	10	89.2	57.0	0.8	16.0	2.4	2.6	5.1	3.7	1.6	1.81	2384	67
ZSAT11C	96	1020	10	93.1	66.7	0.5	13.4	1.1	1.9	2.8	4.0	2.7	1.64	1692	39
ZSAT11B	96	1020	10	95.4	71.0	0.2	13.6	0.4	1.0	1.7	4.3	3.2	1.45	996	38

\* pressure dropped from 25 to 23.5 kbar throughout the course of the run.

**Table 2-3:** Complete experimental results including run duration (hours),  $T$  ( $^{\circ}\text{C}$ ),  $P$  (kbar), major oxide composition of the melt (wt.%), and [Zr] (ppm).

Model	Probability
<i>T</i>	0.0029
<i>M</i>	0.0028
<i>P</i>	$2.1 \times 10^{-8}$
<i>T+P</i>	$7.0 \times 10^{-5}$
<i>P+M</i>	0.0079
<i>T+M</i>	0.908
<i>T+M+P</i>	0.078

**Table 2-4:** Probabilities for each of the calculated models. Assumed in calculating these probabilities is that one of the models is correct (i.e., probabilities sum to unity).

Sample	Duration	$T$	$P$	Analytical Total	SiO <sub>2</sub>	TiO <sub>2</sub>	Al <sub>2</sub> O <sub>3</sub>	FeO	MgO	CaO	Na <sub>2</sub> O	K <sub>2</sub> O	ZrO <sub>2</sub>	$M$
ZSAT12B	43.1	1175	10	98.6	62.0	0.1	15.6	7.1	2.4	4.9	3.1	2.7	0.5	1.84
ZSAT12D	43.1	1175	10	98.2	54.0	1.8	16.2	8.8	4.1	6.5	4.0	1.9	1.0	2.43
ZSAT13A	48	1225	10	98.9	47.1	1.5	15.3	8.9	8.1	10.1	2.8	0.2	4.8	3.35
ZSAT13B	48	1225	10	99.4	58.8	0.1	17.5	5.7	2.7	5.9	3.8	1.9	3.0	1.95
ZSAT13C	48	1225	10	99.4	52.4	1.0	18.4	5.2	4.2	9.6	3.6	0.5	4.5	2.61
ZSAT13D	48	1225	10	99.5	53.5	1.1	17.2	6.7	5.1	6.5	3.8	1.2	4.4	2.21

**Table 2-5:** Experimental results including run duration (hours),  $T$  (°C),  $P$  (kbar), major oxide composition of the melt (wt.%), and ZrO<sub>2</sub> (wt.%)

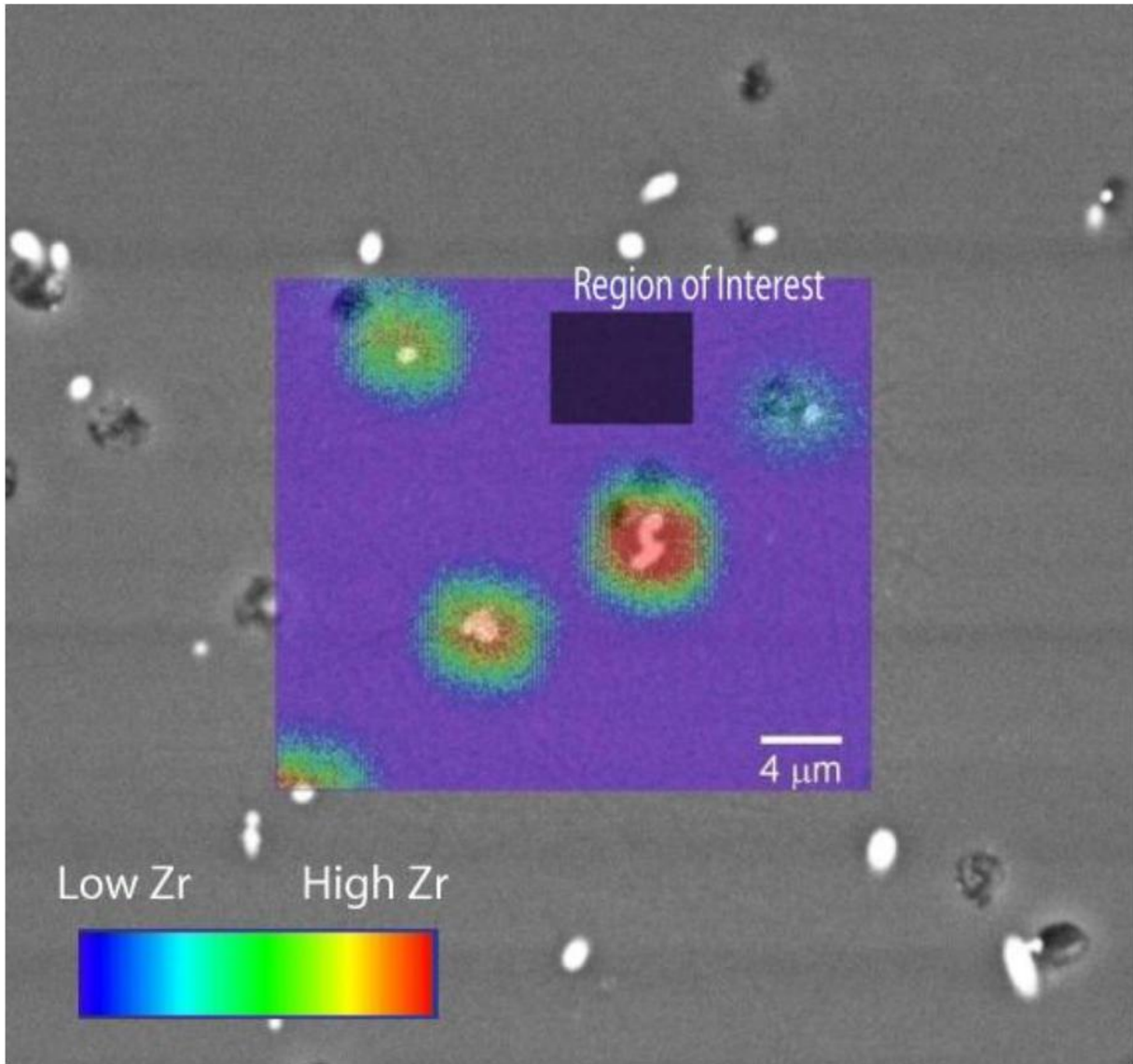


**Figure 2-1:** Scanning ion image of a run product from Watson and Harrison (1983) superimposed on the BSE image. The bright areas are neofomed zircons whereas the shaded region is the area from which the saturation concentration is calculated ( $[Zr] = 367$  ppm). The diffuse appearance of the ion-imaged zircon is not an effect of diffusion but rather due to the beam diameter ( $\sim 3 \mu\text{m}$ ).

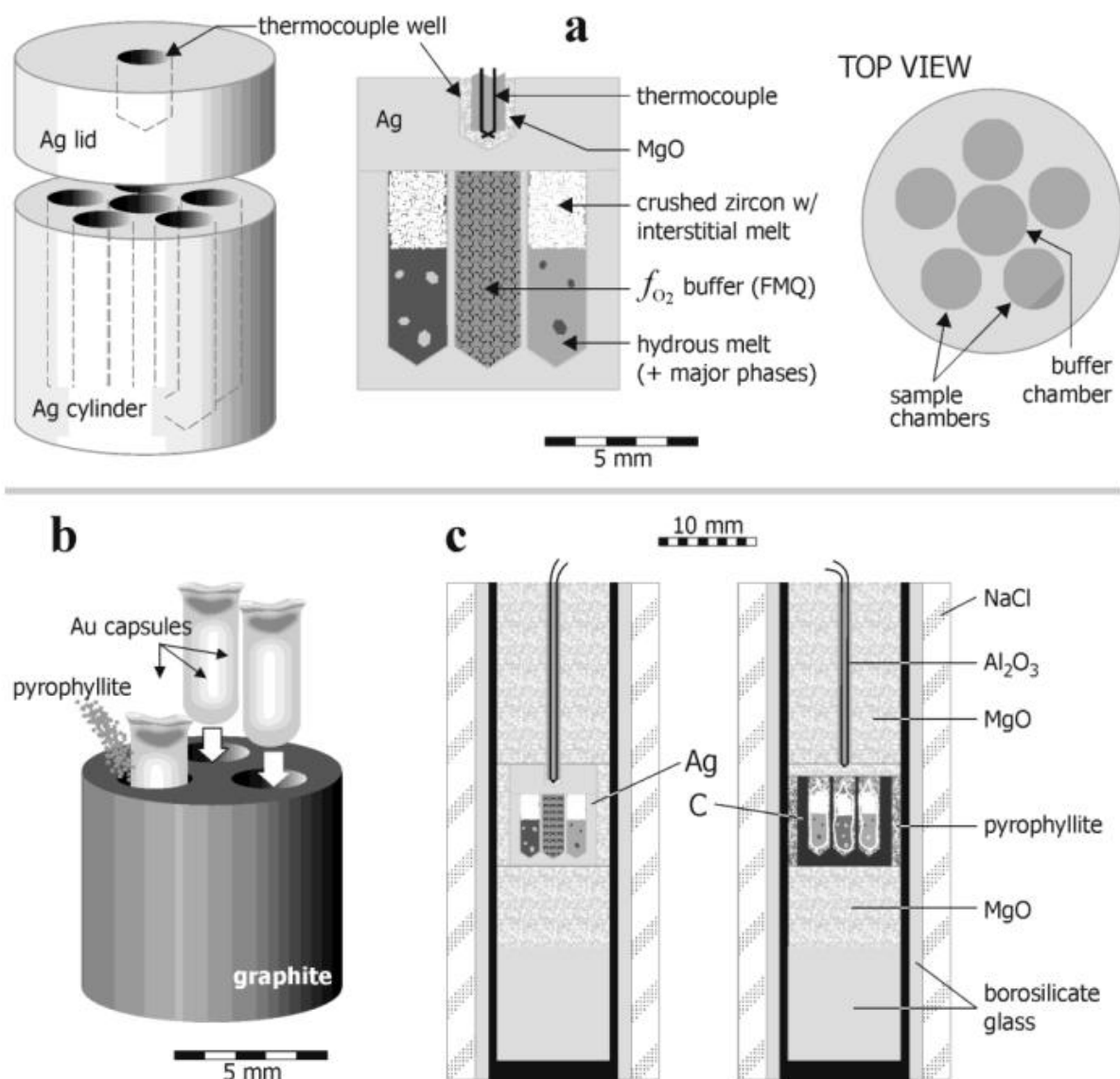


**Figure 2-2:** Schematic illustrations of the two container systems used for the zircon solubility experiments. (a) Three perspectives of the pressure-sealing Ag cylinder with 5 sample wells and a central chamber for the FMQ buffer; (b) graphite cylinder **drilled** to accept 3 pre-welded Au capsules (the void space is filled with pyrophyllite powder); (c) sections through the 19-mm piston-cylinder assembly used for each container system. Scale bars are on the figures; see text for further explanation.

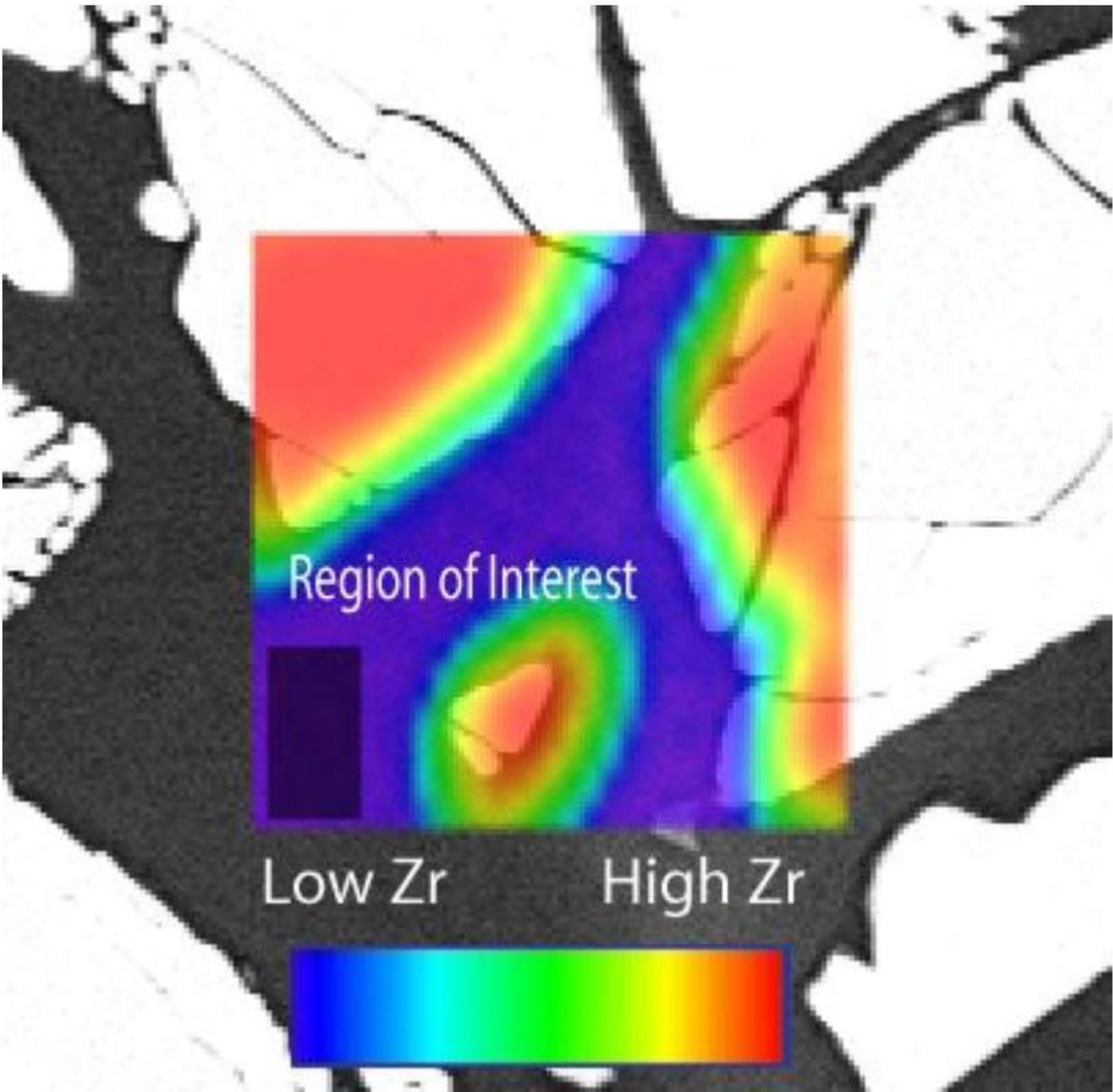


**Figure 2-3:** Scanning ion image of a run product from this study superimposed on the BSE image. The bright regions are the crushed Mud Tank zircon and the ROI for the saturation measurement is shaded ( $[Zr] = 1000$  ppm). Note the absence of neoformed zircon.

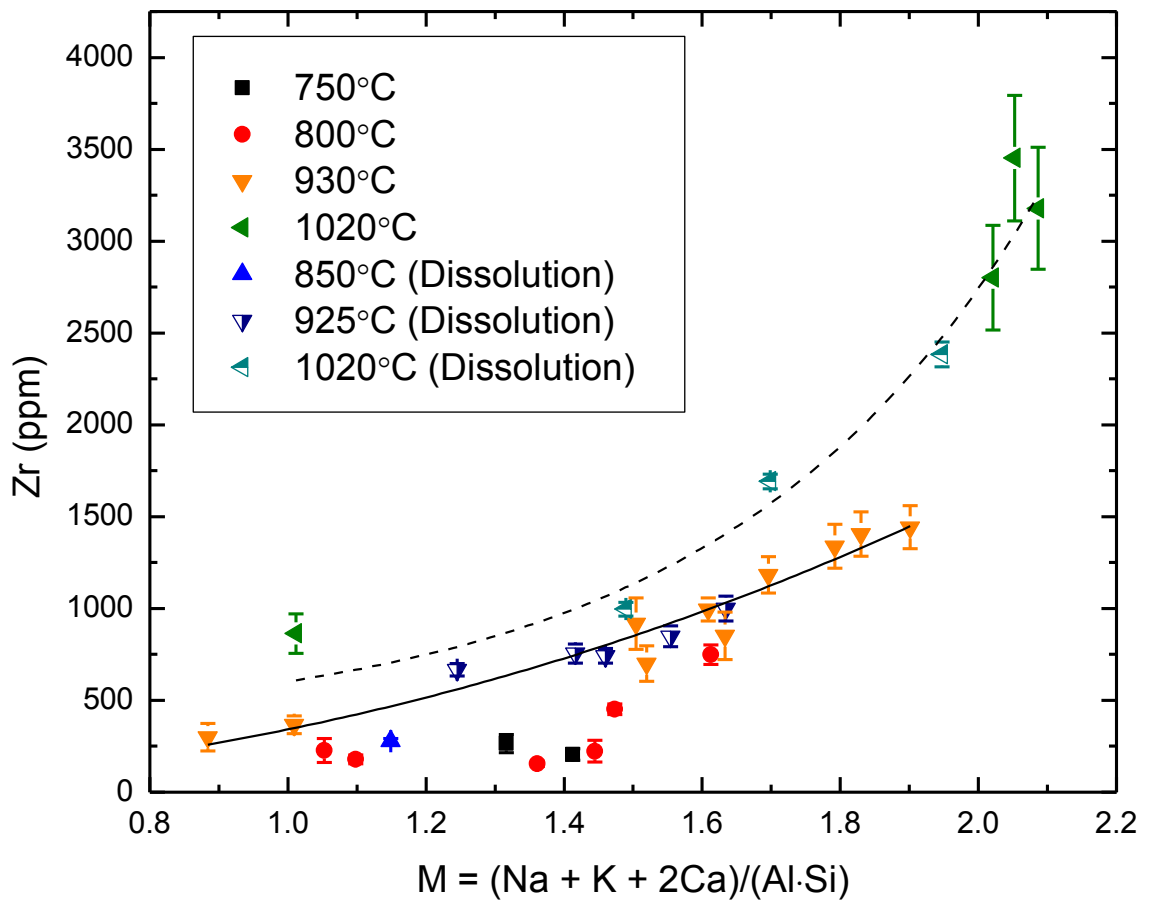


**Figure 2-4:** [Zr] measured on the SIMS plotted versus  $M$ . The two lines are fits to the data at 930°C and 1020°C (solid and dashed lines respectively). There is good resolution at high temperatures (>900°C) becoming less so at lower (<900°C) temperatures. The errors bars are at the level of  $2\sigma$ .

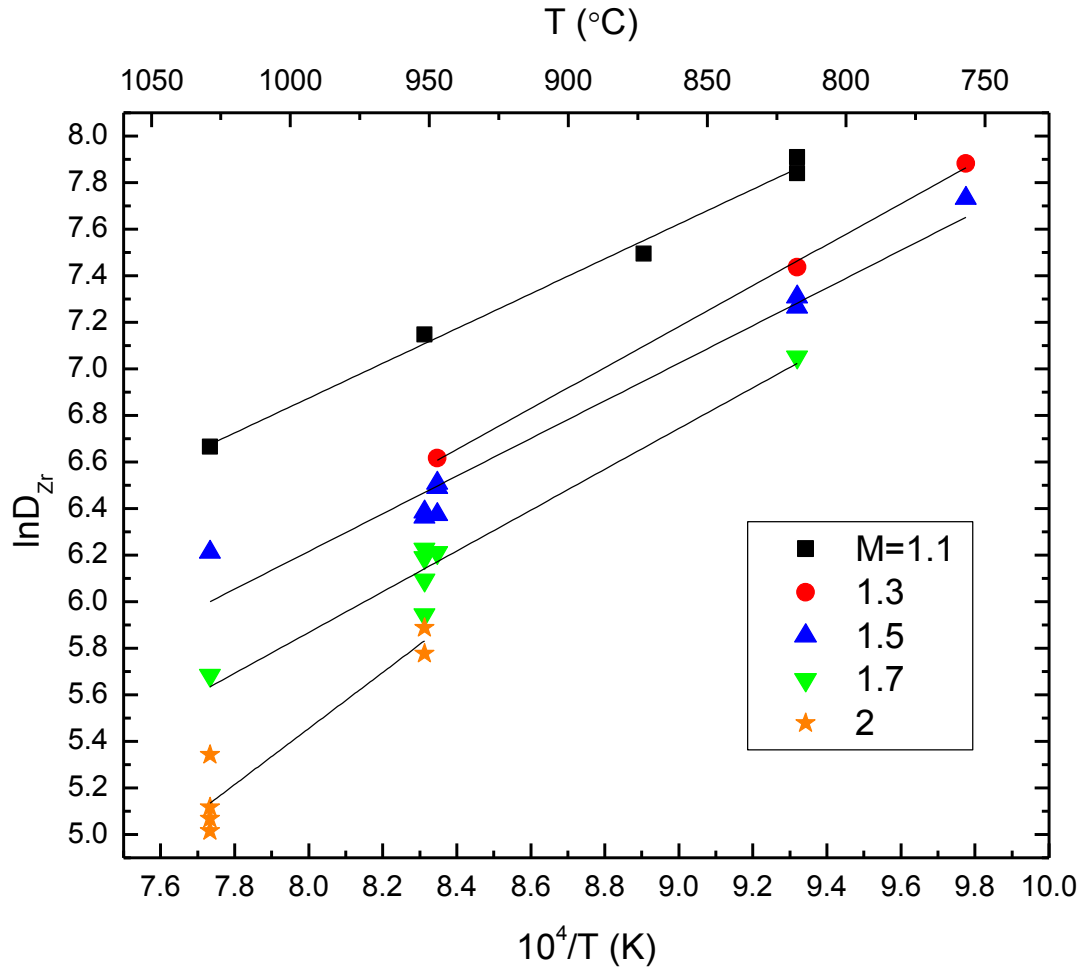


**Figure 2-5:** All SIMS data (this study) plotted on a graph of  $\ln(D_{Zr})$  versus inverse absolute temperature. The lines are linear fits (for a constant  $M$ ); their quasi-parallel nature suggests that the functional form of the model is generally valid.

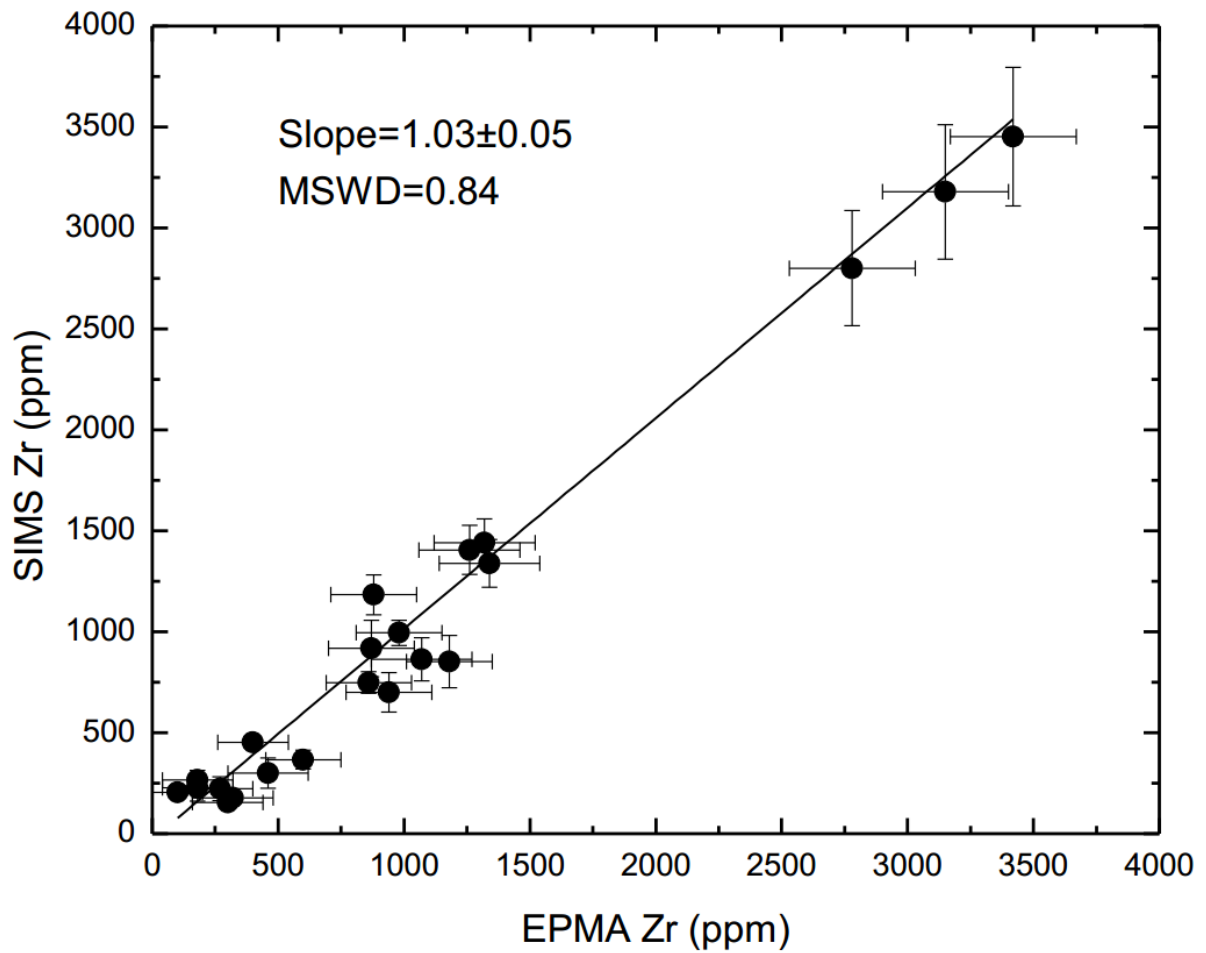


**Figure 2-6:** EPMA data (Watson and Harrison, 1983) plotted against SIMS data (this study). The best fit line has a slope indistinguishable from unity, ruling out any systematic biases between the two data sets. The error bars are at the level of  $2\sigma$ .

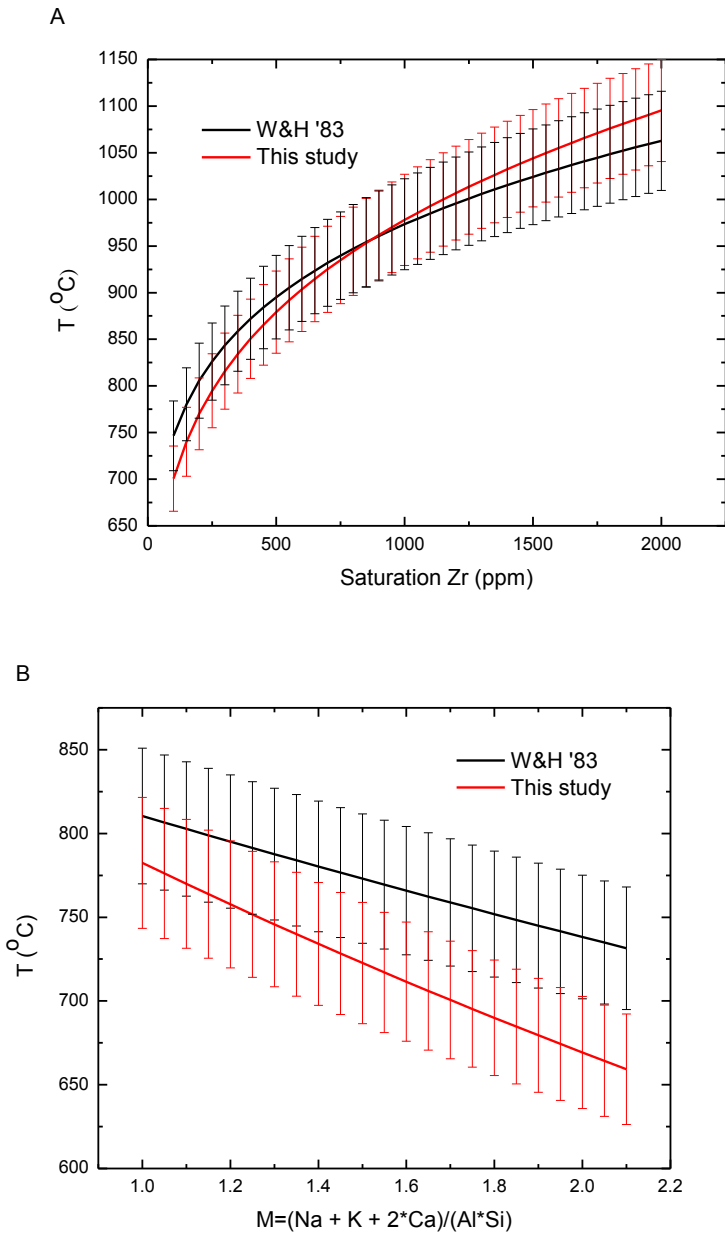


**Figure 2-7:** Plotted in A are both models for a constant  $M$  ( $=1.4$ ). Plotted in B are both models for a constant  $[\text{Zr}]_{\text{sat}}$  ( $=150\text{ppm}$ ). Error bars representing 5% uncertainty are shown for both lines.

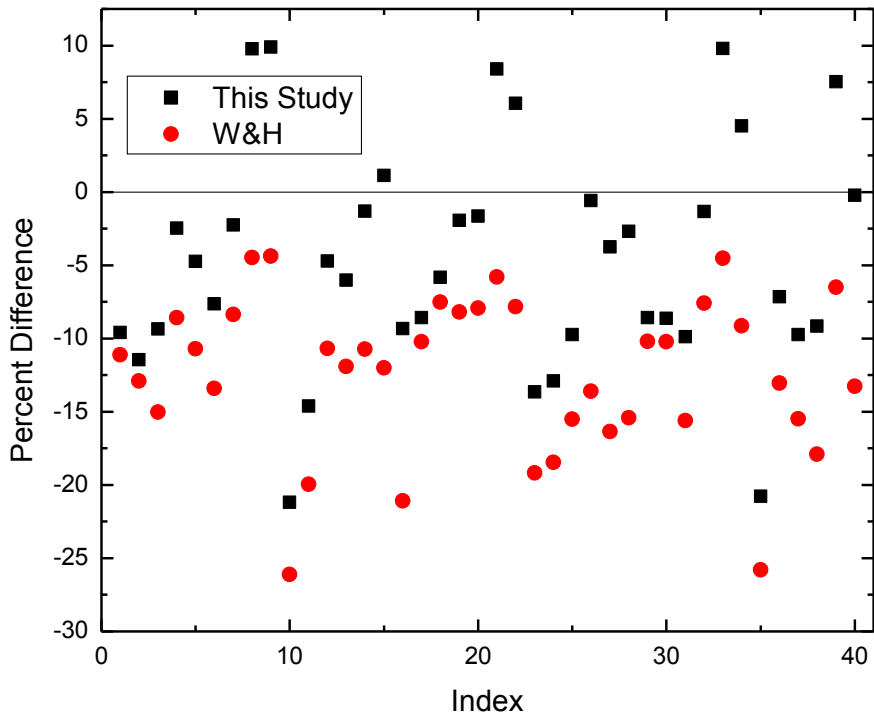


**Figure 2-8:** Results from Baker et al (2002) compared with model predictions for both the Watson and Harrison (1983) model and this study. The systematic offset in the prediction from the Watson and Harrison (1983) model is eliminated in this study due to a more accurate parameterization.

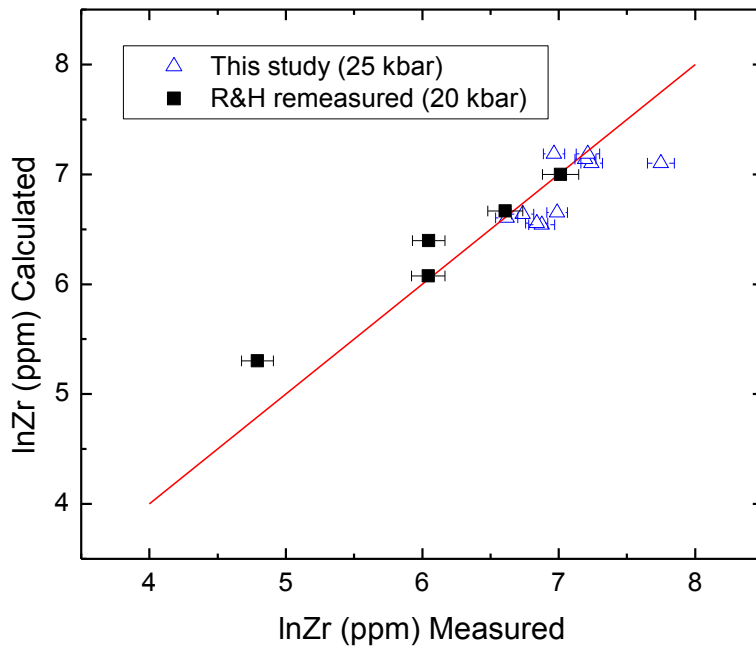


**Figure 2-9:** Dissolution experiments and samples from Rubatto and Hermann (2007) (measured May 2012) plotted with the calculated values. There is no observable pressure effect at 20-25 kbar.

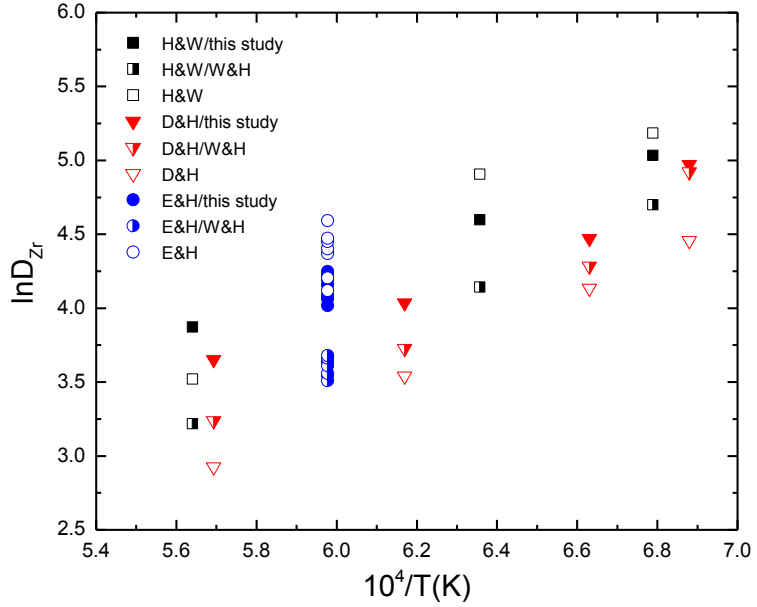


**Figure 2-10:** Results from Harrison and Watson (1983), Ellison and Hess (1986) and Dickinson and Hess (1982) are plotted with predictions for each data set calculated with the Watson and Harrison (1983) model as well as this study. For each study the data is presented in the unfilled symbol, the Watson and Harrison (1983) model in the half filled symbol, and this study in the filled symbol. The Harrison and Watson (1983) study is represented by black squares, the Ellison and Hess (1986) study in blue circles and the Dickinson and Hess (1982) study in red upside down triangles.

## Chapter 3: A Model for Meteoritic and Lunar $^{40}\text{Ar}/^{39}\text{Ar}$ Age Spectra: Resolving the Effects of Multi-activation Energies

### Abstract

Results of whole-rock  $^{40}\text{Ar}/^{39}\text{Ar}$  step-heating analyses of extra-terrestrial materials have been used to constrain the timing of impacts in the inner solar system, solidification of the lunar magma ocean, and development of planetary magnetic fields. Despite the importance of understanding these events, the samples we have in hand are non-ideal due to mixed provenance, isotopic disturbances from potentially multiple heating episodes, and laboratory artifacts such as nuclear recoil. Although models to quantitatively assess multi-domain, diffusive  $^{40}\text{Ar}^*$  loss have long been applied to terrestrial samples, their use on extra-terrestrial materials has been limited. Here we introduce a multi-activation energy, multi-diffusion domain model and apply it to  $^{40}\text{Ar}/^{39}\text{Ar}$  temperature-cycling, step-heating data for meteoritic and lunar samples. We show that age spectra of extra-terrestrial materials, the Jilin chondrite (K-4) and Apollo 16 lunar breccia (67514,43), yielding seemingly non-ideal behavior commonly interpreted as either laboratory artifacts or localized shock heating of pyroxene, are meaningful and can be understood in context of the presence of multi-diffusion domains containing multiple activation energies. Internally consistent results from both the meteoritic and lunar samples reveal high-temperature/short duration thermal episodes we interpret as due to moderate shock heating.

### 1. Introduction

The use of extraterrestrial materials in the pioneering development of the  $^{40}\text{Ar}/^{39}\text{Ar}$  age spectrum method (Merrihue, 1965; Merrihue and Turner, 1966) naturally followed from both the cosmochemical community's awareness of the benefits of coupling neutron irradiation

with incremental laboratory degassing (Jeffery and Reynolds, 1961) and the mineralogic stability of extraterrestrial samples during vacuum heating. Indeed, application of early interpretative models for  $^{40}\text{Ar}/^{39}\text{Ar}$  step-heating results (Turner et al., 1966) were confined to the extraterrestrial domain as the preferred minerals for use in terrestrial K-Ar dating were dominantly hydrous (biotite, muscovite, hornblende) which tended to yield complex age spectra during their breakdown in vacuo (e.g., Dalrymple and Lanphere, 1971; Lanphere and Dalrymple, 1971). Through the 1970s, geochronologists tended to prefer rule-based age spectrum interpretations (e.g., Dalrymple and Lanphere, 1974; Fitch et al., 1976) over the diffusion models favored by their extraterrestrial counterparts (e.g., Huneke, 1976; Wang et al., 1980). This began to reverse through the 1980s as analytical methods and laboratory heating apparatus improved sufficiently to permit routine recovery of both age and kinetic information from anhydrous terrestrial phases (e.g., Lovera et al., 1989). In time, quantitative models of Ar isotope behavior in silicates became essentially the exclusive domain of geochronologists (e.g., Lee, 1995; Lovera et al., 1991, 2002).

An important interpretive advance in interrogating  $^{40}\text{Ar}/^{39}\text{Ar}$  step-heating data over the past 30 years was the advent of the multi-diffusion domain (MDD) model (Lovera et al., 1989, 1991). This approach permits quantitative reconstruction of the thermal history experienced by a sample with a single site for parent potassium within a distribution of domain sizes – a likely property of most silicates (see McDougall and Harrison, 1999). There are two distinct sources of information available from an  $^{40}\text{Ar}/^{39}\text{Ar}$  step-heating experiment; the age spectrum and associated Arrhenius plot. The age spectrum is calculated from the flux of radiogenic Ar ( $^{40}\text{Ar}^*$ ) relative to reactor produced Ar ( $^{39}\text{Ar}$ ) that is released during discrete laboratory heating steps. The Arrhenius plot is derived by plotting diffusion coefficients

(calculated from inversion of the  $^{39}\text{Ar}$  release function assuming a single diffusion length scale) against the inverse absolute temperature of laboratory heating yielding estimates of the activation energy ( $E$ ) and frequency factor ( $D_0/r^2$ ), and the size ( $\rho$ ) and volume fraction ( $\phi$ ) of diffusion domains present. Sensible correlations between age and Arrhenius spectra show that Ar diffusion can occur by the same mechanisms in nature as in the laboratory (Lovera et al., 2002; Harrison and Lovera, 2014). The MDD model is broadly applicable to those phases that experienced diffusive loss of  $^{40}\text{Ar}$  in nature, but remain stable during laboratory vacuum heating (e.g., feldspars and pyroxenes).

Despite the wide range of grain size expected in lunar and meteoritic samples, MDD theory was not utilized in a cosmochemical context until recently (Shuster et al., 2010; Shuster and Cassata, 2015). With rare exception (e.g., Albarède, 1978), extraterrestrial materials are complex multi-mineralic aggregates and thus require consideration of simultaneous degassing of Ar isotopes originating from multiple potassium sites with differing activation energies. These potential complications are particularly salient given that whole-rock  $^{40}\text{Ar}/^{39}\text{Ar}$  step-heating analyses of these materials have been widely used to constrain the impact history of the inner solar system (Norman et al., 2006), when the lunar magma ocean crystallized (Dominik and Jessberger, 1978), and the timing of planetary magnetic fields (e.g., Shea et al., 2012).

Historically, explanations for the non-ideal age spectra of extra-terrestrial materials either invoke recoil redistribution and/or loss (e.g., Turner and Cadogan, 1974) or mixing of different age clasts (Dominik and Jessberger, 1978). Unfortunately, neither hypothesis has any falsifiability and therefore have not been rigorously tested. More recently, Cassata et al. (2010) performed MDD modeling on ALH84001, a Martian meteorite, and explored the

existence of a “kinetic crossover” (**Fig. 3-1**) between Ar diffusion in plagioclase and pyroxene to explain aspects of the age spectrum (apparently unaware that a model for  $^{40}\text{Ar}$  diffusion in samples containing multiple activation energies had previously been proposed by Harrison and McDougall (1981) and generalized by Harrison et al. (1991)) but dismissed the effect due to both the poor fit of their solution and the extreme temperatures required. Instead, they advocated for enhanced pyroxene degassing due to localized heating to explain their data. Based on a detailed investigation of  $^{40}\text{Ar}$  diffusion in pyroxene, which revealed possible “bursting” during partial melting, Cassata et al. (2011) proposed shock induced localized heating of pyroxene to explain a class of meteorite  $^{40}\text{Ar}/^{39}\text{Ar}$  age spectra, including results for the Jilin chondrite. As they did not attempt to obtain a quantitative fit to the age spectra, it remained unclear whether this mechanism is feasible and falsifiable.

We seek to address these issues by providing the first MDD modeling approach for multi-phase samples with differing activation energies that returns viable solutions in terms of model misfit and physical conditions. We apply this model to  $^{40}\text{Ar}/^{39}\text{Ar}$  step-heating results for two extraterrestrial samples – the Jilin chondrite (sample K-4) and Apollo 16 lunar breccia 67514,43. Using an optimization algorithm that calculates the best fits to both the Arrhenius plot and age spectrum, we show that simultaneous solutions for the temperature-time history of thermal episodes experienced by these chondrite and lunar samples can be achieved and potentially provide unique insights into shock histories.

## **2 Samples**

### *2.1 Jilin chondrite K-4*

The arrival of the Jilin chondrite in northwestern China in 1976 remains the largest meteorite fall ever recorded, with over two metric tonnes recovered. The Jilin petrography

has been extensively discussed (e.g., JIGKMS, 1977); in brief, this ordinary chondrite is comprised of olivine, orthopyroxene and troilite, with lesser amounts of other sulphide minerals, clinopyroxene, oligoclase, and orthoclase. Chondrules up to 2 mm in diameter comprise about 15% (by volume) of the meteorite and are supported in a finer grained matrix (Wang et al., 1980). Textures indicate that this H5 meteorite experienced early thermal metamorphism (approximately 700-800°C; Dodd, 1981) followed by moderate shock metamorphism (>950°C, Dodd, 1981; 12-27GPa, Xie et al., 2001), as evidenced by glassy veins, microcrystalline regions (JIGKMS, 1977), and moderate development of planar fractures (Xie et al., 2001).

Prior work showed that the Kirin chondrite experienced multiple thermal events that caused extensive diffusive loss of both  $^4\text{He}$  and  $^{40}\text{Ar}$  between ~2.6 to ~0.4 Ga (Wang et al., 1980; Harrison and Wang, 1981; Begemann et al., 1985; cf. Müller and Jessberger, 1985).  $^{40}\text{Ar}/^{39}\text{Ar}$  step-heating results for a number of Jilin fragments were interpreted to reflect Ar degassing from both feldspars and clinopyroxene (Wang et al., 1980; Harrison and Wang, 1981; Müller and Jessberger, 1985).

## *2.2 Apollo 16 lunar breccia 67514,43*

Sample 67514,43 was acquired from the vicinity of North Ray Crater in the lunar highlands by the Apollo 16 mission. We studied a thin section (67514,49) from its parent sample which shows a heavily brecciated but monomict, geochemically ferroan (Dowty et al., 1974) anorthosite. The dominant mineral, 88%, is plagioclase, accompanied by 10% pyroxene, 2% olivine, and <1% opaque oxides. EPMA analyses show the plagioclase is highly anorthitic ( $\text{An}_{96-99}$ ). The pyroxene, as modified by subsolidus exsolution, consists dominantly of roughly 10- $\mu\text{m}$  wide lamellae, with the low-Ca lamellae clustering near

En<sub>50</sub>Wo<sub>3</sub> and the high-Ca lamellae near En<sub>36</sub>Wo<sub>41</sub>. Olivine is uniformly Fo<sub>39-41</sub>. Although a few mineral and lithic fragments remain essentially unbrecciated up to 0.5 mm across, most of the rock's volume has been comminuted into a highly porous groundmass of fragments less than 0.1 mm across. In places, elongate clumps of high mafic-silicate abundance appear to represent sheared and broken derivatives of individual roughly 0.1 mm<sup>2</sup> mafic silicate grains, suggesting that even in the comminuted groundmass the scale of mixing during brecciation was generally only at a scale of order 1 mm. This texture as well as the uniformly "ferroan" mineral compositions together imply that 67514,49 is a monomict breccia. As a ferroanorthosite from Apollo 16, 67514,49 is indirectly linked to some of the most ancient Sm-Nd isochron ages obtained from the Moon (~4.3 Ga; Borg et al., 2014). We are aware of no previous <sup>40</sup>Ar/<sup>39</sup>Ar results for this sample.

### 3. Methods

We utilized a conventional double vacuum furnace attached to a MAP-215-50 rare gas mass spectrometer at the New Mexico Geochronology Research Laboratory. Blanks were determined by analyzing the same heating schedule without a sample in the furnace. We used an (<sup>40</sup>Ar/<sup>36</sup>Ar)<sub>o</sub> = 1 to correct for primordial Ar which generally had a <1% effect on age. Any inaccuracies in this correction are negligible given the scale of the disturbances we investigate. The sample was irradiated in the TRIGA reactor at the USGS Denver (DeBey et al., 2012) to a J factor of 0.014773(4). Correction factors for interfering nuclear reactions are: (<sup>39</sup>Ar/<sup>37</sup>Ar)<sub>Ca</sub> = 0.000690(2), (<sup>36</sup>Ar/<sup>37</sup>Ar)<sub>Ca</sub> = 0.0002724(1), (<sup>38</sup>Ar/<sup>39</sup>Ar)<sub>K</sub> = 0.01077(1), and (<sup>40</sup>Ar/<sup>39</sup>Ar)<sub>K</sub> = 0.00720(2). Neutron fluence was monitored with co-irradiated hornblende Hb3gr assuming an age of 1072 Ma (Jourdan et al., 2006). A full description of the methods can be found in Heizler et al. (1999).

### 3.1 Heating Schedule

Since virtually every previous  $^{40}\text{Ar}/^{39}\text{Ar}$  analysis of extra-terrestrial samples has used a monotonic laboratory heating schedule, some commentary regarding that used here is needed. In this study, we incorporated three cycled temperature routines into the heating schedule to gain maximum leverage in evaluating the presence of multiple activation energies while not unnecessarily lengthening analysis time. The three cycles begin at 600, 800 and, 1100°C when two 50°C step-downs occur in sequence (e.g., 600 to 550 and then 500°C). Further, we utilized isothermal duplicates at high temperatures to ensure complete degassing. As we will demonstrate, the use of this approach is essential to extracting meaningful thermal histories from samples containing multiple activation energies (see Harrison et al., 1991). The full heating schedules are given in Appendix C.

### 3.2 Diffusion Modeling

Fitting a domain size distribution with multiple activation energies is a complex optimization problem as more than 20 variables require adjustment (i.e.,  $E$ ,  $D_0/r^2$ ,  $\rho$ ,  $\phi$  for typically six to twenty domain sizes). Although an automated approach has been shown to reliably retrieve values of  $E$  and  $D_0/r^2$  for single- $E$  samples via linear regression of the early heating steps of an Arrhenius plot (Lovera, 1992), this approach is not feasible when two or more activation energies are present. Other workers have sought to hand fit such data through trial and error (e.g., Cassata et al., 2010) and while illustrative examples of fits are possible, the complexity of the problem precludes finding an optimal solution. We chose to use a global optimization algorithm to simultaneously invert both age and Arrhenius spectra. The Adaptive Particle Swarm (Zhan et al., 2009) utilizes a flock of particles to explore parameter space. A particle is an object that moves through the parameter space and remembers its own

best solution, as well as knowing the best solution any particle has found so far. The velocity of any one particle is calculated from the sum of the distances between the best solution for that particle and the overall best solution. This characteristic allows each particle to be influenced by its immediate and global environments. For a more in depth explanation we refer the reader to Kennedy and Eberhart (1995). Specifically, we utilize twenty particles initially randomly dispersed over a plausible parameter space with two thousand iterations of the algorithm.

In order to evaluate the fit of each candidate solution, we need a function to calculate the difference between the model fit and the laboratory data. We use a standard sum of squares measure (e.g., Gallagher, 2012) for both datasets. However this is complicated, as we have to fit both the age spectrum and Arrhenius plot. That is, the problem is one of multi-objective optimization (Deb, 2014). In theory, if the MDD model perfectly describes Ar diffusion in our sample, the best fit to the Arrhenius plot would be the best fit to the age spectrum. However in practice there is a continuous grain and sub-grain size distribution, while we can only model a discrete distribution due to computational limitations. Therefore, it is likely that our simplified model does not capture all of the detailed features in Ar release patterns from natural materials.

Given that we are optimizing two objective functions (i.e., the age and Arrhenius spectra), there is a continuum of best fit solutions to the joint objective function as improvements in one dimension lead to a worse result in the other. That is to say there exists a Pareto frontier (Deb, 2014) where a solution that better fits the Arrhenius plot will give a worse fit to the age spectrum and vice versa. This behavior arises because the objective function is a sum of two different fits to the dataset, therefore it is possible to have the same overall goodness of fit but

optimize one fit (e.g., age fit) at the expense of the other (i.e., the Arrhenius fit). This tradeoff introduces additional uncertainty in the parameters of interest (e.g., heating temperature). While a full calculation of the uncertainties in our solution is not feasible at present due to the computational complexity, we instead present both the top 10 and 200 solutions to examine the range of viable solutions.

Our diffusion model uses the standard equations describing diffusive loss in a spherical geometry due to a re-heating event (Turner, 1968). The only modification to these equations is that we consider a summed release over multiple discrete domain sizes with differing activation energies. Our modeling is performed assuming  $n = 20$  domain sizes for each  $E$  (and two activation energies in total) but virtually no change to the overall results occurs with more or less domain sizes down to  $n = 4$ . We did not model any data acquired at or above the temperature at which significant melting would occur (i.e.,  $>1100^{\circ}\text{C}$ ).

Given the vast dimension of parameter space, we used as much prior information as possible to limit the numerical range of the parameters. Activation energies for the low  $E$  phase were restricted between 20 and 60 kcal/mol, which encompasses the range of that determined for feldspars (e.g., Lovera et al., 1993; Cassata and Renne, 2013). For the high  $E$  phase, the range was constrained between 80 and 120 kcal/mol, again corresponding to that found for clinopyroxene (Cassata et al., 2011). The timing of both the reheating event and original formation are left as free parameters for the model but restricted to between present day and the 4.52 Ga gas retention age of the oldest known of H5 chondrites (Forest Vale; Turner et al., 1978).

## **4 Results**

### *4.1 Analytical Results*

Our analysis of Jilin sample K-4 revealed, as before, a disturbed  $^{40}\text{Ar}/^{39}\text{Ar}$  age spectrum (**Fig. 3-2A**) containing two distinct components; a high K/Ca and a low K/Ca phase. Following Wang et al. (1980), we interpret the high K/Ca phase as plagioclase and the low K/Ca phase as pyroxene. This interpretation is supported by our EPMA analyses of Jilin K-4, which yield an atomic K/Ca of  $0.4\pm 0.1$  for plagioclase (**Table C.1**) which is consistent with the K/Ca determined from the Ar isotope measurements (**Table C.2; Fig. 3-2A**).

We identify the portion of the age spectrum in which K/Ca drops from  $\sim 0.2$  to  $\sim 0.001$  as the transition to degassing dominated by clinopyroxene ( $\sim 72$  to  $100\%$   $^{39}\text{Ar}$  released). This finding is supported by the Arrhenius plot (**Figure 3-3A**) which shows that the low K/Ca phase is marked by a higher activation energy. The fact that the oldest age in this portion of degassing shows greater  $^{40}\text{Ar}$  loss (i.e., has younger ages) than the earlier degassed plagioclase portion is the key observation that plagioclase and clinopyroxene have swapped their relative Ar retentivities between the natural event and laboratory heating.

Our analysis of 67514,43 (**Fig 3-2B**) shows a qualitatively similar age spectrum and Arrhenius plot (**Fig. 3-3B**) to that of K-4. However, in contrast with our K-4 analysis, the K/Ca of 67514,43 shows possible evidence for 3 phases. The first phase (K/Ca  $\approx 0.003$ ) appears unretentive and is almost completely exhausted at  $\sim 20\%$   $^{39}\text{Ar}$  release, the second (K/Ca  $\sim 0.0015$ ) dominates between 20 and  $80\%$   $^{39}\text{Ar}$  release, and a third with K/Ca  $\approx 0.001$ . This behavior gives potential evidence for three distinct Ar bearing phases.

#### *4.2 Modeling Results*

Assuming for the moment that the vacuum degassing data can be directly applied to our samples, we found the top 200 solutions for the K-4 age spectrum are well fit by a reheating event at  $\sim 2.6$  Ga (**Fig 3-4A**) with a temperature between 2200 and 2900 K and durations of

300 to 1 $\mu$ sec (**Fig 3-5A**). Our top 10 solutions constrain the heating event to between 2400 and 2800 K with 9 out of 10 again indicating event durations between 50 and 1 $\mu$ sec. Further, the best fit activation energies of 40-50 and 100-120 kcal/mol for the low and high energy phase (**Fig 3-6A**) match well to measured values for Ar diffusion in sodic plagioclase and clinopyroxene (Cassata et al., 2011; Cassata and Renne, 2013), respectively. Finally, the goodness of fit (**Fig 3-7A**) for the Arrhenius spectrum versus that of the age spectrum shows the expected Pareto frontier (see section 2.2).

For 67514,43 the modeling well fits with a heating event at ~2.3 Ga (**Fig 3-4B**) with temperatures between 2200 and 2800 K and durations of 300 to 1  $\mu$ s (**Fig 3-5B**), respectively. The top 10 solutions are better constrained to between 2400 and 2800 K and 50 to 1  $\mu$ s. The activation energies are constrained to between 50-60 and 105-115 kcal/mol (**Fig 3-6B**) for the low and high activation energy phase respectively. Our modeling indicates that both samples experienced similar re-heating events.

## **5 Discussion**

### *5.1 Comparison with previous data*

As noted earlier, prior  $^{40}\text{Ar}/^{39}\text{Ar}$  step-heating results for the Kirin chondrite revealed evidence of multiple thermal events causing extensive diffusive loss of  $^{40}\text{Ar}$  (Wang et al., 1980; Harrison and Wang, 1981; cf. Müller and Jessberger, 1985). Due to their strongly contrasting retentivities, feldspars were essentially completely degassed during laboratory heating prior to onset of significant Ar loss from clinopyroxene (Lovera et al., 1997; Cassata et al., 2011) resulting in virtually complete thermal separation of the two Ar release patterns. Wang et al. (1980) noted paradoxically that the clinopyroxene portion of gas release yielded apparently younger ages than the peak of the plagioclase release despite requiring

considerably higher temperatures to degas in the laboratory. While our data replicates the broad findings of those studies, we have the advantage of the MDD model which allows us to explore this seemingly paradoxical behavior in detail. This behavior was also noted by Kennedy et al. (2013) in HED meteorites, where plagioclase separates showed older apparent ages than the pyroxene separate.

The apparent reversal of geologic and laboratory degassing behavior was recognized by Harrison and McDougall (1981) in feldspars containing highly retentive excess  $^{40}\text{Ar}$ . These authors argued that excess  $^{40}\text{Ar}$  diffused into low  $E$  anion vacancies during low temperature heating over millions of years. However, during high temperature laboratory heating, radiogenic and nucleogenic Ar originating in higher  $E$  cation sites were lost by diffusion at much greater rates than excess  $^{40}\text{Ar}$  which still reside in anion vacancies from which migration is sluggish due to the much lower  $E$ . Thus their samples showed an apparent rise to unrealistically old ages (up to 10 Ga) late in laboratory degassing as the excess  $^{40}\text{Ar}$  was finally released due to melting. This illustrates the non-intuitive effects of a kinetic crossover where, at low temperatures, one site (or phase) for Ar is less retentive than another but at high temperature (i.e., above the crossover), this behavior is reversed (**Fig. 3-1**). A kinetic crossover can also lead to apparent contradictions in an age spectrum where, for example, high temperature gas release (i.e., more retentive sites) yields younger apparent ages than that released at lower temperatures.

Numerical calculations carried out for two domains containing differing activation energies shows dramatically different age spectra depending on whether a thermal event occurred above or below the kinetic crossover (Fig. 1 in Harrison et al., 1991). This prediction was confirmed through analysis of aliquots of natural K-feldspar using different heating

schedules. By starting at high temperatures and cycling to lower temperatures (MH-10.cb), Harrison et al. (1991) (see their Fig. 9) were able to produce an essentially flat age spectrum for an originally stair-case type release pattern. As noted earlier, a specific kinetic crossover between plagioclase and pyroxene was examined to explain  $^{40}\text{Ar}/^{39}\text{Ar}$  analyses of Martian meteorites (Cassata et al., 2010) but ultimately rejected in favor of localized heating of the pyroxene. The above discussion underscores that caution must be taken in both the acquisition and interpretation of results from samples containing multi-activation energies as the laboratory heating schedule can alter the form of an age spectrum. Re-stated, the presence of multiple Ar activation energies dictates that an  $^{40}\text{Ar}/^{39}\text{Ar}$  age spectrum is *a function of both the natural and laboratory heating histories rather than an intrinsic property of the sample.*

## 5.2 Model fits and kinetic crossover

As shown in **Figure 3-8A**, our best solutions for K-4 produce excellent visual fits to the complex measured age spectrum. We emphasize that this is only possible by accepting fits with temperatures for the ca. 2.6 Ga thermal event over which Ar diffusion in clinopyroxene is faster than that of plagioclase. For example, all of our data was collected at a temperature of  $<1100^\circ\text{C}$  while the modeled conditions are  $>1900^\circ\text{C}$  suggesting the existence of a kinetic crossover between Ar diffusion in plagioclase and pyroxene. That is, in the natural heating event, clinopyroxene is less retentive of Ar than plagioclase due to the high temperatures of the event. This argument extends to our modeling of 67514,43 suggesting that it also experienced similar conditions. We propose that the laboratory data coupled with a MDD-type model can explain this seeming paradox of the Jilin age spectra without invoking localized pyroxene heating or recoil.

The use of temperature cycles provides the necessary leverage to uniquely fit activation energies for both phases (**Fig. 3-3**). Additionally as the cycles release Ar with different age than the steps immediately before and after it, we have altered the appearance of the age spectrum through changing our heating schedule. This further supports the conclusions of Harrison et al. (1991) who demonstrated that the K-feldspar age spectrum can be a function of the laboratory heating schedule provided multiple activation energies are present.

Despite the apparently good fits, in detail the model does not fit the laboratory data within the measured uncertainties. This is an expected result as our diffusion model almost surely underestimates the geometrical complexity of the actual sample (see section 2.2). Going forward with increased computing power, the ability to model more domain sizes should yield ever improving fits to the data. Our modeling also confirms that all apparent heating-step ages underestimate the true rock forming age of this sample (Boehnke et al., 2014). Model fits suggest that the cooling age of the Jilin chondrite is between 4.44 and 4.53 Ga, a range of ~130 Ma (**Fig 3-4**).

### *5.3 Shock heating*

Cassata et al. (2010) explored the existence of a kinetic crossover for plagioclase and pyroxene through a MDD model but rejected it in favor of a brief, high temperature shock heating event caused degassing of  $^{40}\text{Ar}$  from the pyroxene, obviating the need for a kinetic crossover, to interpret  $^{40}\text{Ar}/^{39}\text{Ar}$  data from Martian meteorites. Based on further work on Ar diffusion in pyroxene, they proposed localized shock heating of pyroxene as an explanation for the age spectrum of Jilin and other meteorites (Cassata et al., 2011). The observation of pyroxene melt veins in ALH84001 (e.g., Barber and Scott, 2006) was seen as support for their interpretation. However, Barber and Scott (2006) also report plagioclase glass indicating that

fusion was not limited to pyroxene. That said, we note that melt in both the samples we examined is a volumetrically minor feature and thus has little or no bearing on the  $^{40}\text{Ar}$  systematic.

Since the petrographic evidence is consistent with uniform heating of the entire sample, and thus broadly uniform temperature, the thermal history should be recoverable from an appropriate MDD model. Specifically, we propose that a multi-phase MDD model is fundamentally capable of retrieving shock temperatures from extraterrestrial samples (i.e., a single square-pulse thermal history can adequately and most simply explain the observed data).

Both the model of Cassata et al. (2010) and the present study require relatively rapid post-shock cooling in order to prevent complete diffusive loss of  $^{40}\text{Ar}$ . A partial explanation is simply the expected temperature drop of several 100s of  $^{\circ}\text{C}$  following passage of a shock wave. Furthermore, our best fit solutions are a square-pulse equivalent of the postulated thermal history implying that calculated peak temperatures are overestimates. Once temperatures have dropped several 100s of  $^{\circ}\text{C}$  below peak values, samples with activation energies for Ar of 40 to 90 kcal/mol cooling exponentially (as expected in the near surface of a parent body) cease to experience significant gas loss. A further consideration to the needed rapid cooling is discussed in detail in the next section.

Given the inherent uncertainties in parent body size and location of the sample within said body, especially after multiple impact events, the size of the resulting body is a major control on the cooling rate as heat diffusion in rock is generally slow. Our solutions require that most of the  $^{40}\text{Ar}^*$  loss happened during the high temperature heating event and not in the cooling from that event, suggesting a rapid cooling rate. The most plausible mechanism is that our

samples resided at the lunar surface or on the exterior of an asteroid, allowing for the fastest possible drop in temperature. While the event we are studying happened at ~2.6 Ga, cosmogenic nuclides have been interpreted to reflect a complex, multi-stage irradiation history for the Jilin chondrite (e.g., Begemann et al., 1985; Honda et al., 1982) potentially lending supporting the view that sample K-4 resided near the surface over the past ~2.6 Ga.

The MDD model has rather stringent constraints that may be violated in a shock scenario. The first constraint is that the domain size needs to be set prior to the diffusive loss of radiogenic  $^{40}\text{Ar}$  ( $^{40}\text{Ar}^*$ ) and maintained until the sample is analyzed in the laboratory. If indeed the MDD model can reconstruct heating due to shockwaves it would suggest that any significant damage is done at the onset of the shockwave rather than at the release. The second requirement is that the sample needs to remain solid throughout the entire process and therefore any post-shock temperatures must be below the zero pressure solidus or result in only minor (i.e., <1%) melting. Note that the confidence gained in assuring that the basic assumptions of the MDD have been met for slowly cooled samples by observing a high degree of correlation between age and Arrhenius spectra (Lovera et al., 2002) is not available for the case of re-heating or for samples containing multiple activation energies.

While disturbed age spectra reveal the loss of  $^{40}\text{Ar}^*$  prior to laboratory analysis, it doesn't necessarily reveal the loss mechanisms. Given that the  $^{40}\text{Ar}^*$  closest to a sub- or grain boundary is most readily lost from a sample, if a shockwave is capable of causing  $^{40}\text{Ar}$  migration, loss would preferentially occur from the exterior of each domain. Therefore, shock dislocation of  $^{40}\text{Ar}^*$  could mimic diffusive loss of  $^{40}\text{Ar}^*$  at high temperatures explaining the fact that the MDD model is capable of excellent visual fits. It remains to be tested whether or

not the conditions that are inferred from our inversion indeed reflect shock conditions or are simply a fortuitous feature of shock phenomena.

#### *5.4 Activation volume effects*

While it appears that the best fit model solutions require exceptionally high temperatures and short durations, our modeling to this point has not explicitly included a pressure dependence for the  $^{40}\text{Ar}^*$  diffusion. That pressure dependence is generally taken as the sum of the reference pressure activation energy (0 GPa for vacuum heating) and the product of pressure and activation volume ( $\Delta V$ ). If the activation volumes of plagioclase and pyroxene are equivalent, then our zero pressure temperature solutions will not change, although the durations become longer. Therefore, using identical  $\Delta V$  could take our modeled durations of microseconds and increase them to more plausible values for extra-terrestrial shock events (e.g., seconds).

Literature values for the  $\Delta V$  for dislocation creep and diffusion of trace elements do vary considerably between plagioclase and pyroxene, with the latter, for example, yielding both positive and negative values (Sneeringer et al., 1984; Cherniak and Dimanov, 2010). A further limitation is that most experimental estimates are determined under static pressures of 1 to 2 GPa, far outside our conditions of interest. Thus it is likely that both the durations and temperatures of our solutions are more apparent than real. We constructed an additional model to explore this phenomenon using a Markov Chain Monte Carlo approach (e.g., Boehnke et al., 2015; Gallagher, 2012) as implemented in the emcee python package (Foreman-Mackey et al., 2012). The model was run for a fixed pyroxene  $\Delta V$  of  $1 \text{ cm}^3/\text{mol}$  at 10 GPa and 1600 K (corresponding to conditions consistent with sample petrology; Stöffler et al., 1991; Xie et al., 2001) and directed to solve for the resulting corrected duration and

plagioclase  $\Delta V$  (represented as a multiple of the pyroxene activation volume). Our modeled solutions (**Fig. 3-9**) yield heating durations of 10-20 s at temperatures of  $\sim 1600$  K and a plagioclase  $\Delta V$  of 10-14  $\text{cm}^3/\text{mol}$ , the latter broadly consistent with literature values (Béjina et al., 2003; Cherniak and Dimanov, 2010) and  $\Delta V$  for Ar measured in silicates (Harrison et al., 1985, 2009). While this calculated shift in temperature and duration is model dependent, it is, as previously noted, consistent with both petrographic textures and the contrast between pyroxene and plagioclase  $\Delta V$  measurements (Béjina et al., 2003; Cherniak and Dimanov, 2010). That is to say, our modeling is purely exploratory and we only sought to demonstrate possible effects of pressure on Ar diffusion in a shock setting. Whether these specific values are borne out by subsequent experiments, there is little question that relating vacuum release Ar data to shock pressures requires that this effect be accounted for.

## 6 Conclusions

We have shown that highly non-ideal appearing  $^{40}\text{Ar}/^{39}\text{Ar}$  step-heating data for a sample of the Jilin chondrite (K-4) and an Apollo 16 lunar breccia (67514,43) can be well fit through use of a multi-activation energy and -diffusion domain model coupled to a novel optimization algorithm. This modeling reconciles the apparently younger ages from the clinopyroxene portion late in gas release with the apparently older plagioclase ages in the Jilin K-4 age spectrum. The best fit solutions are for a  $\sim 2.6$  Ga shock heating event which reaches ca. 2300 K for microseconds when applying diffusion coefficient obtained in vacuo. When modified using a reasonable contrast in activation volume between constituent minerals to account for the extremely high pressures experienced, the thermal conditions shift to 1600 K for up to tens of seconds. Modeling of an Apollo 16 sample (67514,43) returns similar thermal conditions suggesting that brief, high-temperature heating events are a common source for

highly irregular  $^{40}\text{Ar}/^{39}\text{Ar}$  age spectra of extra-terrestrial samples. While our data are consistent with shock heating, further work is needed, both experimentally and analytically, to test the hypothesis that  $^{40}\text{Ar}/^{39}\text{Ar}$  dating can uniquely recover the conditions of shock heating. In light of these modeling results, we caution against assigning age significance to apparent age spectra from shock heated samples due to the complicated nature of diffusion in multi-activation energy samples, especially at high, transient pressures.

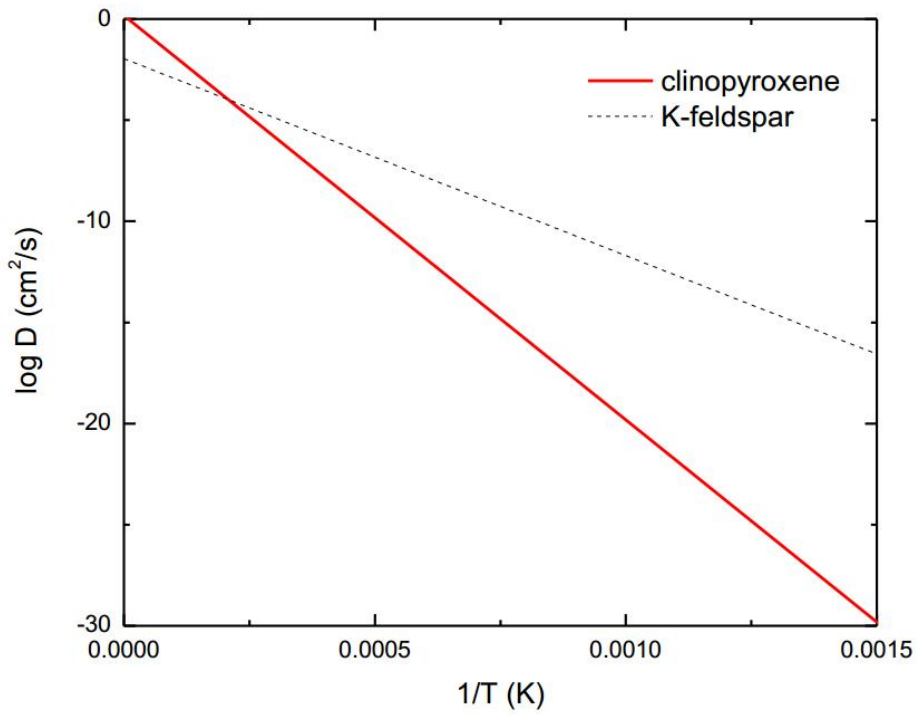


**Figure 3-1:** This figure shows an example Arrhenius relation for both feldspar (Foland, 1974) and clinopyroxene (Cassata et al., 2011). Note the reversal in relative diffusivity occurring at high temperatures, this is an example of a kinetic crossover.

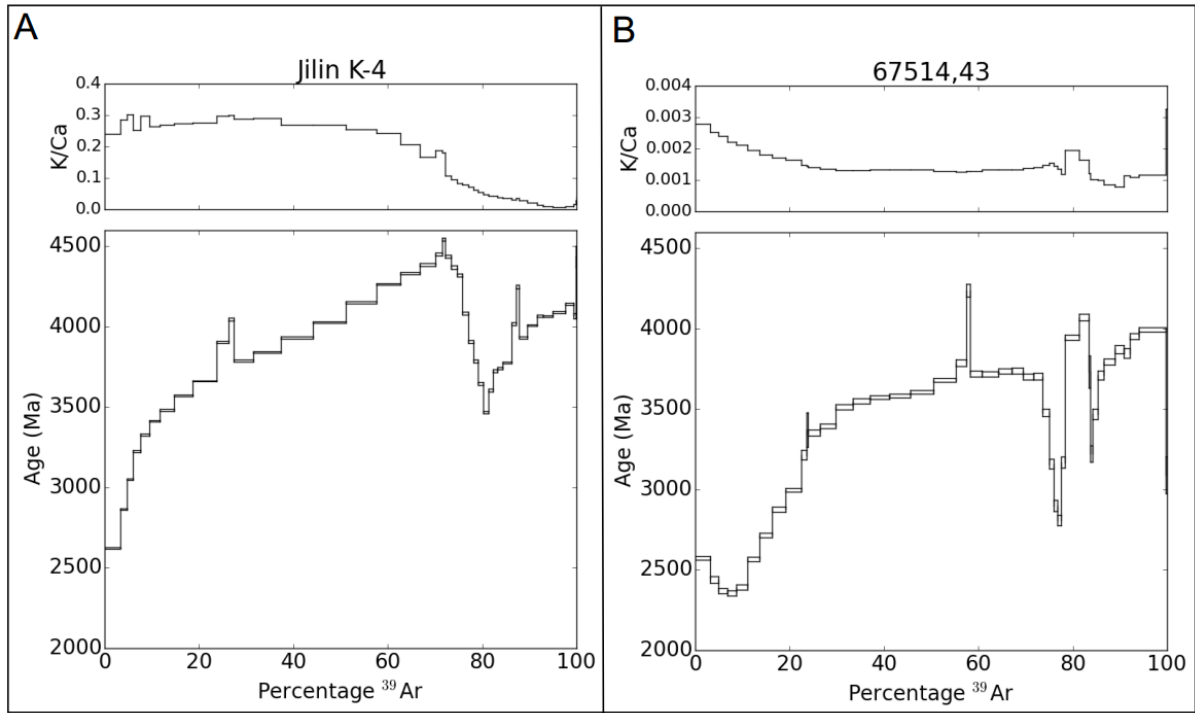


**Figure 3-2:** This figure shows the age spectra and K/Ca for both Jilin K-4 and 67514,43.

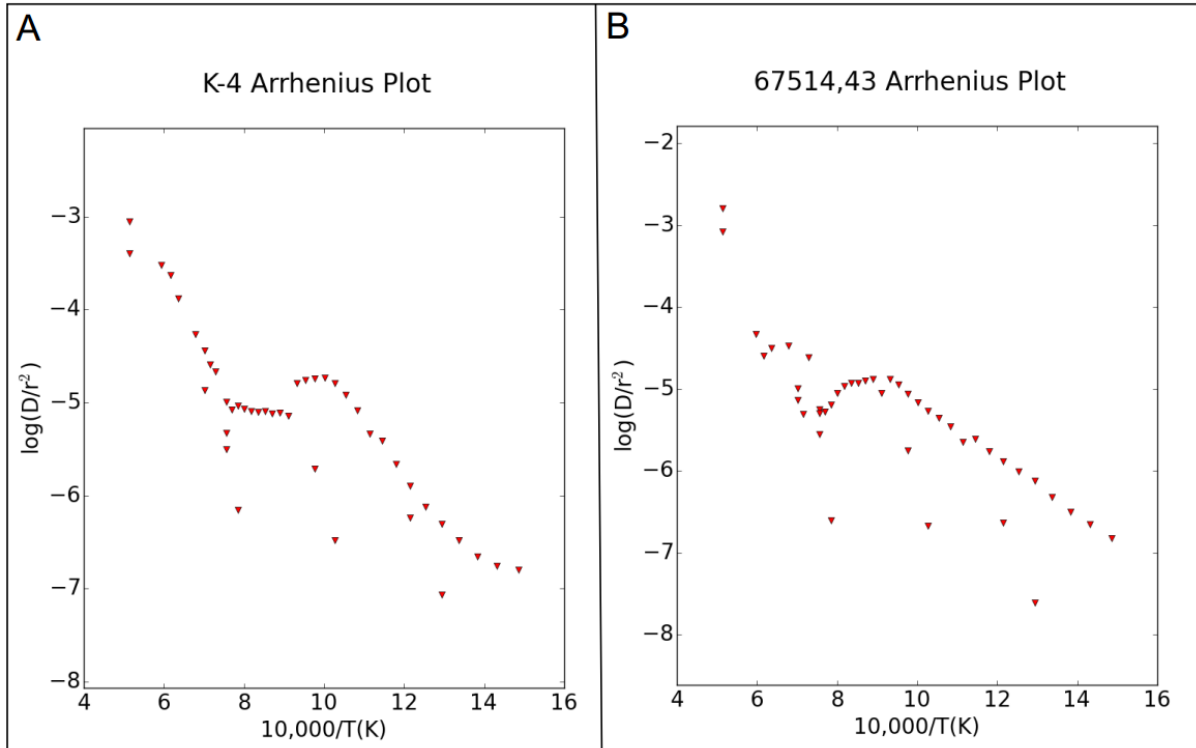


**Figure 3-3:** Arrhenius spectra for both Jilin K-4 and 67514,43. The temperature cycles provide far lower apparent diffusivities than the first heating step at that temperature. This provides further support for the existence of multiple diffusion domains and greatly constrains the activation energies. Uncertainties are much smaller than the symbols and therefore not shown.

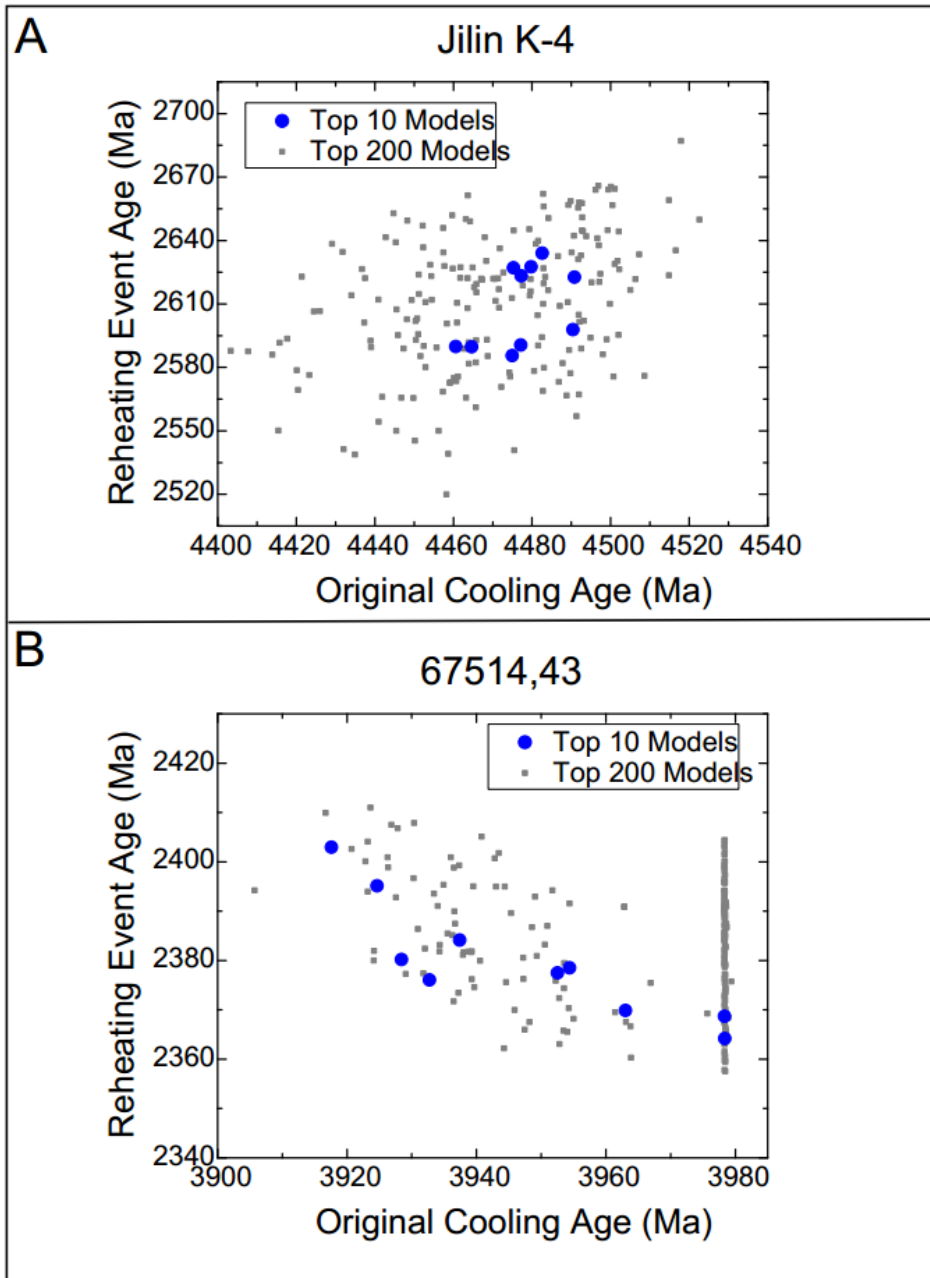


**Figure 3-4:** This figure shows the re-heating event age and the original age for the sample based on our model solutions for both K-4 (A) and 67514,43 (B). See Section 3.2 for justification of the cutoff values.

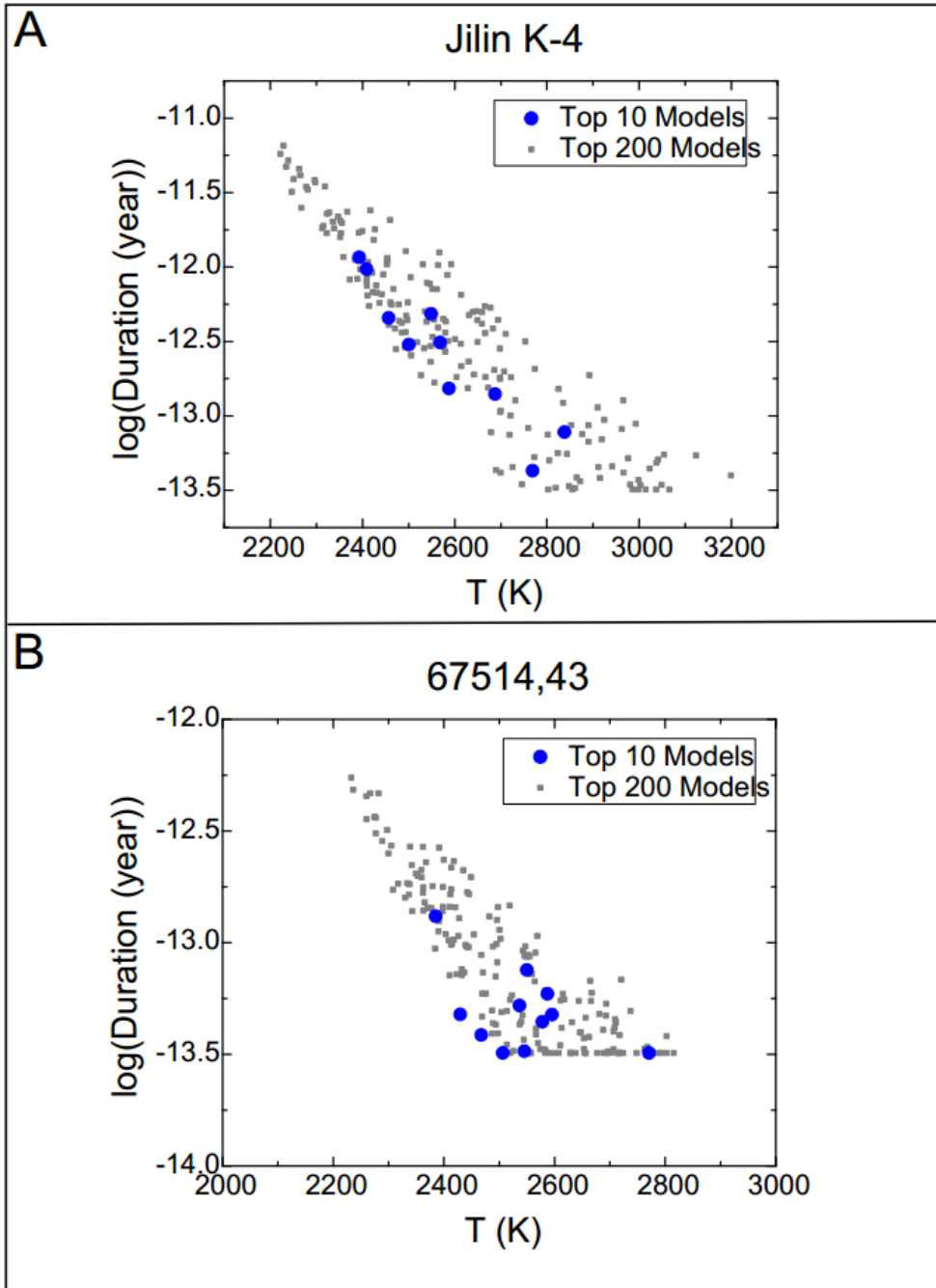


**Figure 3-5:** This figure shows the modeled duration and intensity of the heating event for both K-4 (A) and 67514,43 (B). See Section 3.2 for justification of the cutoff values.

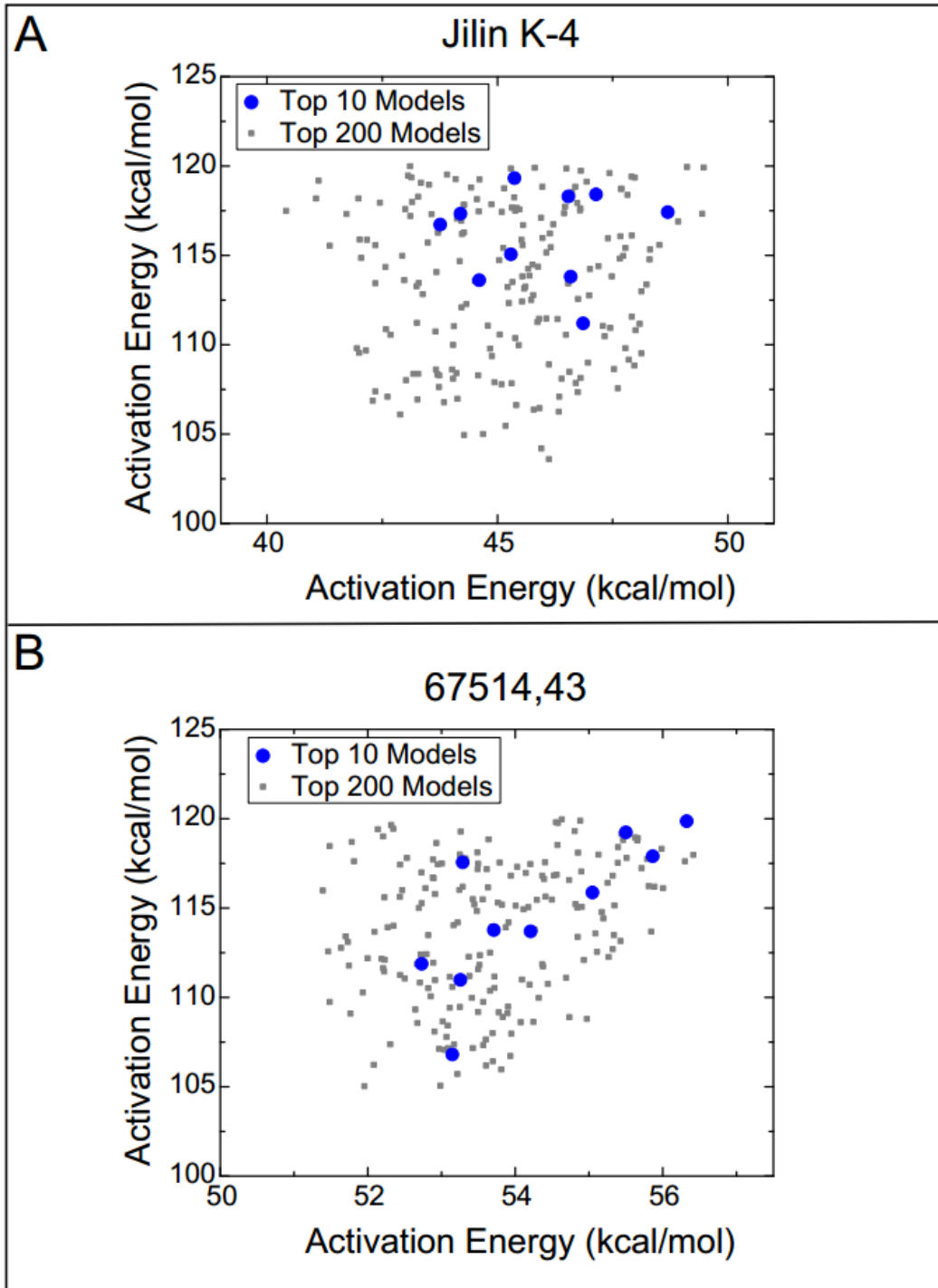


**Figure 3-6:** This figure shows the model activation energy for both phases for K-4 (A) and 67514,43 (B). Note that this broadly agrees with plagioclase and clinopyroxene activation energies. See Section 3.2 for justification of the cutoff values.

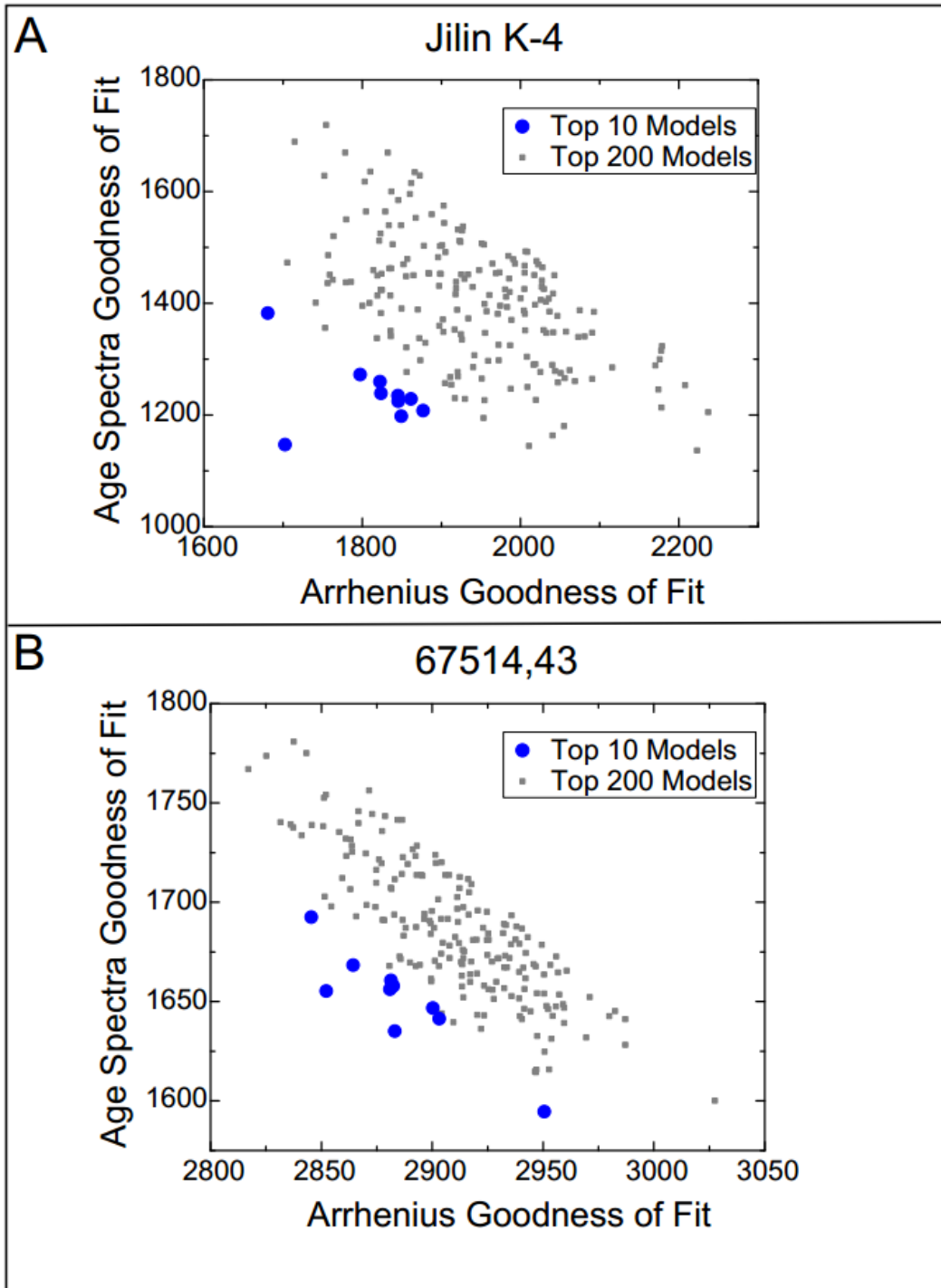


**Figure 3-7:** This shows the goodness of fit to the Arrhenius plot and age spectra for our model solutions. The negative correlation is a manifestation of a Pareto frontier.

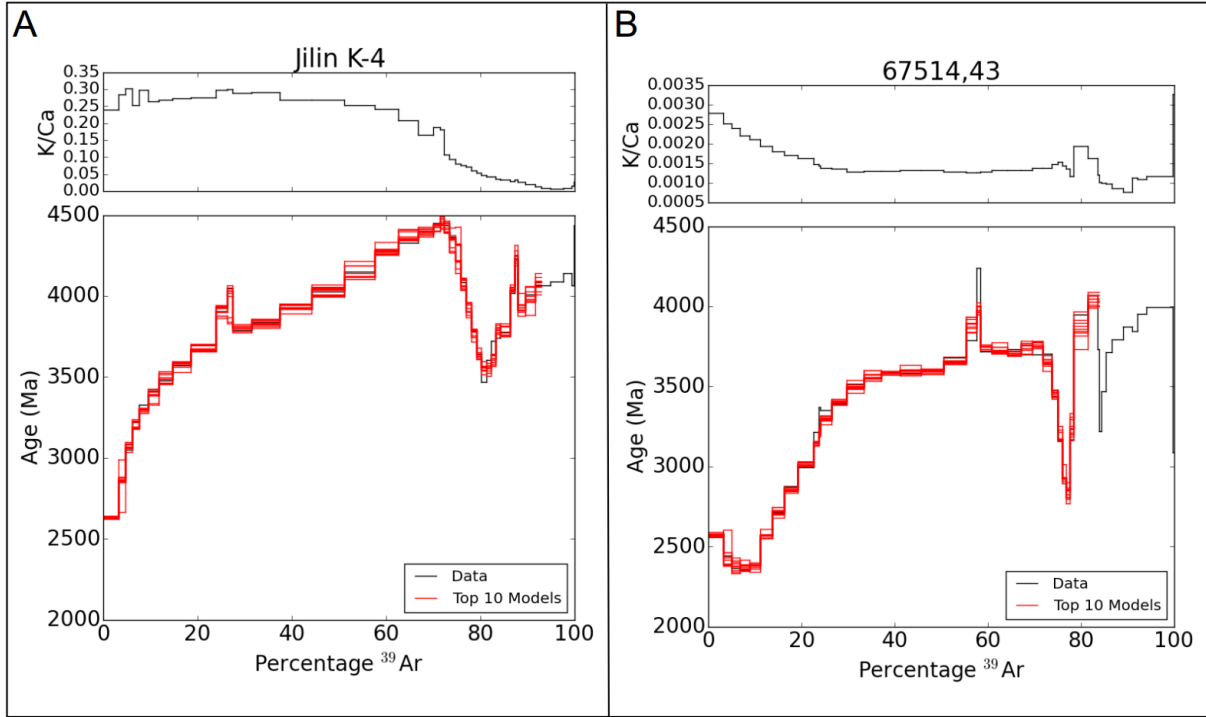


**Figure 3-8:** This shows the top 10 solutions fitted to the age spectrum for each K-4 and 67514,43.

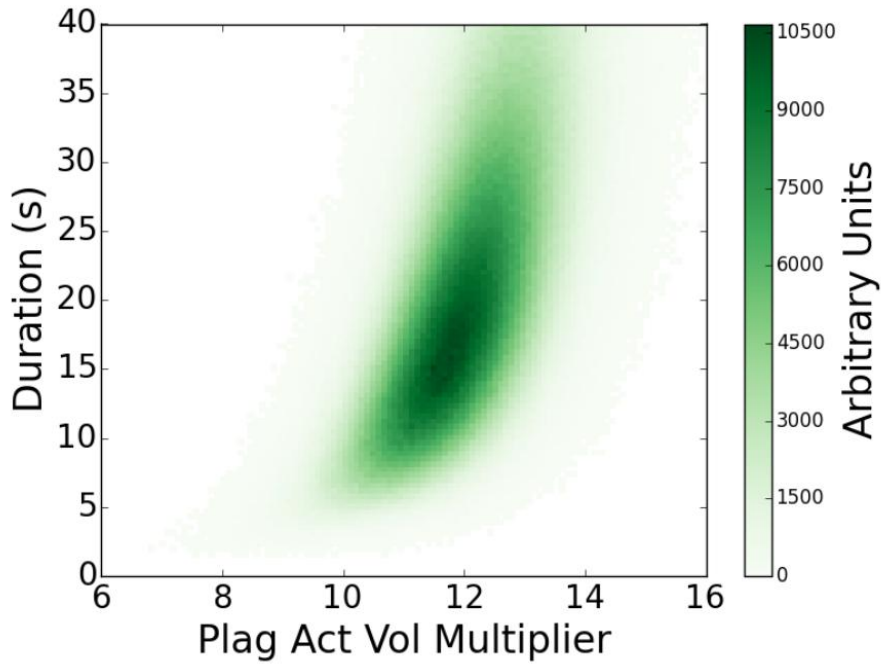


**Figure 3-9:** This shows the duration and plagioclase activation volume (represented as a multiplier of our assumed pyroxene activation volume of  $1 \text{ cm}^3/\text{mol}$ ) for the best fitting solution to the K-4 data at 10 GPa and 1600 K. Our solution here is only one of many which are possible depending on the assumed nature of the shock event and the activation volumes. The color bar represents an unnormalized probability density, that is darker green represents more likely solutions.

## Chapter 4: Illusory Late Heavy Bombardments

### Abstract

The Late Heavy Bombardment (LHB), a hypothesized impact spike at ~3.9 Ga, is one of the major scientific concepts to emerge from Apollo-era lunar exploration. A significant portion of the evidence for the existence of the LHB comes from histograms of  $^{40}\text{Ar}/^{39}\text{Ar}$  “plateau” ages (i.e., regions selected on the basis of apparent isochroneity). However, due to lunar volcanism and overprinting from subsequent impact events, virtually all Apollo-era samples show evidence for  $^{40}\text{Ar}/^{39}\text{Ar}$  age spectrum disturbances. This leaves open the possibility that partial  $^{40}\text{Ar}^*$  resetting could bias interpretation of bombardment histories due to “plateaus” yielding misleadingly young ages. We examine this possibility through a physical model of  $^{40}\text{Ar}^*$  diffusion in Apollo samples and test the uniqueness of the impact histories obtained by inverting “plateau” age histograms. Our results show that “plateau” histograms tend to yield age peaks, even in those cases where the input impact curve did not contain such a spike, in part due to the episodic nature of lunar crust formation. Restated, monotonically declining impact histories yield apparent age peaks that could be misinterpreted as LHB-type events. We further conclude that the assignment of apparent  $^{40}\text{Ar}/^{39}\text{Ar}$  “plateau” ages bear an undesirably high degree of subjectivity. When compounded by inappropriate interpretations of histograms constructed from “plateau” ages, interpretation of apparent, but illusory, impact spikes is likely.

### 1 Introduction

The Earth contributes relatively little to our knowledge of the early impactor flux to the inner solar system due to its constant resurfacing by the combined effects of erosion and cratonic growth. Although Moon’s longstanding stability and relatively short duration of

crust growth in principle transcends these terrestrial limitations, after nearly 50 years of lunar sample analysis our understanding of the Earth-Moon impact history remains limited (Chapman et al., 2007; Fassett and Minton, 2013; Hartmann, 1975). Reasons for this include the relatively small area of the lunar surface from which we have documented sample locations and the potentially cryptic nature of impact thermal signatures (Boehnke et al., 2014). Despite these limitations, there is broad consensus that impact rates were higher during and immediately after accretion of the terrestrial planets (Chambers, 2004) and possibly during a spike in impact rates (i.e., the Late Heavy Bombardment; LHB) at either ~3.9 (Chapman et al., 2007; Kring and Cohen, 2002; Tera et al., 1974) or ~4.1 Ga (Marchi et al., 2013; Morbidelli et al., 2012). The existence of an LHB (we use this term to describe any postulated spike in impact rate; e.g., 3.9 or 4.1 Ga), however, is not universally accepted. The apparent spike could instead reflect impact saturation of the surface, termed the “stonewall” effect (Hartmann, 1975).

Disagreement regarding the shape of impact curves and the existence of an LHB has profound implications for the geo- and biological development of our planet. The geologic effects implied by these impact histories range from planetary sterilization (Sleep et al., 1989), to a Hadean (>4 Ga) Earth covered by ca. 20 km of flood basalts (Marchi et al., 2014), to generation of hydrothermal systems providing enhanced environments for extremophiles (Abramov and Mojzsis, 2009). Whether or not impact rates during the Hadean could have sterilized Earth is of particular relevance as no microfossils older than ~3.5 Ga (Brasier et al., 2015) have been identified. However, a record of isotopically light carbon consistent with biologic activity extends back to 4.1 Ga (Bell et al., 2015; Mojzsis et al., 1996; Rosing, 1999) leaving open the possibility that life may have existed during the hypothesized bombardment

episodes. The existence of an LHB-type event has broader implications to other planets as well as its origin has been linked to dramatic changes in giant planet orbital dynamics (Gomes et al., 2005) and ejected debris from a large Mars impact (Minton et al., 2015).

$^{40}\text{Ar}/^{39}\text{Ar}$  data is not the only source of evidence that has been used to support the LHB hypothesis. Indeed, the original proposal of a ‘terminal lunar cataclysm’ (Tera et al., 1974) was based on the observation of widespread U-Pb fractionation at ca. 3.9 Ga together with nine Rb-Sr internal isochrons ranging from 3.85 to 4.0 Ga. In some ways it is surprising that global inferences were drawn from such a small sample population, more than half of which were derived from Apollo 14 collections. This further underscores the earlier noted issue that all Apollo-era samples are restricted to only ~4% of the lunar surface (Warren, 2003). Thus these data are equally consistent with a single, local event rather than a planetary-wide bombardment episode.

The bulk of the evidence now marshaled in support of the LHB comes from  $^{40}\text{Ar}/^{39}\text{Ar}$  step-heating analyses (Chapman et al., 2007; Kring and Cohen, 2002; Marchi et al., 2013). Specifically, compilations of  $^{40}\text{Ar}/^{39}\text{Ar}$  “plateau” ages are constructed under the assumption that a compilation of these ages can be related to impact intensity. However,  $^{40}\text{Ar}^*$  is not retentive in rocks at moderately elevated temperatures resulting in partial resetting of the isotopic system (Gardés and Montel, 2009; McDougall and Harrison, 1999; Watson and Cherniak, 2013). The pioneering studies that established  $^{40}\text{Ar}/^{39}\text{Ar}$  as a viable dating method explicitly addressed the importance of diffusive  $^{40}\text{Ar}^*$  loss in extra-terrestrial materials (Merrihue and Turner, 1966) and devised corrections for partial resetting effects (Turner, 1970; Turner et al., 1966). Over the intervening five decades, this approach was generally abandoned in favor of assigning age significance to seemingly flat portions of the age spectra,

termed “plateau ages”. In contrast with the flat release patterns from which this concept was first introduced (Dalrymple and Lanphere, 1974; Fleck et al., 1977), lunar and meteorite samples are rarely observed to have undisturbed age spectra. Since the vast majority of analyzed meteorite and lunar samples have been assigned “plateau” ages despite evidence of significant disturbance to the  $^{40}\text{Ar}/^{39}\text{Ar}$  system, a potentially significant bias can be introduced by the assignment of “plateau” ages.

An additional problem is that lunar crustal growth was episodic and limited to a relatively short duration (<500 Ma). As the majority (~85%) of the exposed surface of the Moon is thought to be a floatation crust formed during crystallization of a magma ocean (Warren, 1985), it must have formed relatively quickly after lunar accretion. The observed age spread for lunar samples (with the exclusion of Mare basalts and other impact derived samples) is ~400 Ma for the ferroan anorthosites, lunar zircons, and the Mg-gabbroic-suite (Borg et al., 2014; Carlson et al., 2014). The episodic nature of petrogenesis on the Moon suggests the possibility that apparent spikes in the compilation of  $^{40}\text{Ar}/^{39}\text{Ar}$  ages could reflect crust formation shifted towards younger ages due to partial  $^{40}\text{Ar}$  resetting with a monotonic impact flux.

To examine how well histograms of “plateau” ages represent the actual impact record and its support of an LHB-type event, we have re-evaluated the interpretation of  $^{40}\text{Ar}/^{39}\text{Ar}$  data for extra-terrestrial samples using a physical model describing  $^{40}\text{Ar}^*$  diffusive loss during post-formation heating events. This model, which accounts for partial resetting, permits us to assess whether or not  $^{40}\text{Ar}/^{39}\text{Ar}$  data can even in principle act as evidence for an impact spike or if the apparent spikes are simply artifacts due to episodic crust formation.

## **Method**

Our model simulates  $^{40}\text{Ar}^*$  distributions in synthetic samples produced in response to a proposed impact history. This simulation is then compared to a compilation of  $^{40}\text{Ar}/^{39}\text{Ar}$  data from Apollo samples (section 3). In all interpretations, even those involving an episodic flare-up, the background impact intensity is assumed to follow an exponential decline following accretion (Neukum et al., 2001; Zahnle et al., 2007). Thus we use an exponential decay with an added a linear component to allow a greater parameter range to be evaluated. The impact history is constrained to monotonically increase back in time from the present and is given by:

$$IC(t) = A + B \times t + C \times e^{Dt} \quad (1)$$

where A, B, C and, D are free parameters. In each time step (100 Ma), the sampled locations which experienced impact-related  $^{40}\text{Ar}^*$  degassing are randomly chosen without replacement from a set of 1,000 targets with equal probability of selection. When a randomly chosen sample is ‘impacted’ during a time step, we assign a fractional loss of  $^{40}\text{Ar}^*$  representing the thermal effect of that collision. Since we have no prior information regarding fractional loss of  $^{40}\text{Ar}^*$  in impact events, we use two models with differing assumptions. The first model assumes a uniform probability distribution between 0 and 1 fractional loss of  $^{40}\text{Ar}^*$  resulting from each impact (see Appendix D for justification).

To specifically test the assumptions inherent in Model 1, Model 2 assumes no a priori knowledge of the specific shape of the fractional  $^{40}\text{Ar}^*$  loss probability distribution. We assume instead that fractional loss follows a beta distribution (Pearson, 1916) and constrain the two shape parameters to produce normally distributed “plateau” ages at either 3.9 Ga or 4.1 Ga ( $\pm 0.2$  Ga;  $1\sigma$ ). The beta distribution was chosen because it is a flexible probability distribution which is constrained between 0 and 1. We characterize each target using a

spherical diffusion geometry for  $^{40}\text{Ar}^*$  and invert the fractional loss to the dimensionless parameter  $Dt/r^2$  (where  $D$  is diffusion coefficient,  $t$  is duration and  $r$  is the characteristic diffusion length scale) which in turn is used to calculate the age spectrum of the target from which a “plateau” age, that is the asymptotic portion of the late gas release (at 90%  $^{39}\text{Ar}$  release; see Appendix D), is assigned. Lastly, to compare the fractional loss seen in lunar samples to the synthetic targets, in Model 2 we define the width of the plateau to be the fractional  $^{39}\text{Ar}$  released from the age reaching 90% of the maximum age to complete degassing (see Appendix D). While utilizing only a single diffusion domain is an oversimplification – real samples are composed of multiple phases and a distribution of domain sizes (Boehnke et al., 2014) – this assumption is unlikely to significantly influence our results. Indeed, more sophisticated modeling of existing Apollo  $^{40}\text{Ar}/^{39}\text{Ar}$  data is currently not possible given the lack of accurate temperature control during the step-heating analyses and problematic heating schedules (Boehnke et al., 2014).

### **3 Model Constraints**

In samples that were partially reset during post-formational heating, the apparent age obtained during initial laboratory de-gassing is the best estimate for the timing of that loss (McDougall and Harrison, 1999; Turner et al., 1966). This is because early heating steps (typically  $\sim 400^\circ\text{C}$  for  $<30$  minutes) liberates  $^{40}\text{Ar}^*$  held near grain/subgrain boundaries. We thus tabulated “Last Heating Ages” (LHA; i.e., the age of the initial gas released) for 267 Apollo  $^{40}\text{Ar}/^{39}\text{Ar}$  analyses (see Appendix D for data and references). This age distribution is the primary constraint for all models and is similar, albeit more comprehensive, to the compilation of “initial” ages (Shuster et al., 2010). Our compilation (Fig. 4-1) shows an approximately linear increase in LHAs going back to 4 Ga followed by a sharp drop off at  $\sim 4$

Ga. This drop off is consistent with the loss of  $^{40}\text{Ar}$  generated prior to that time by subsequent thermal activity, akin to a stonewall effect (Hartmann, 1975). Before we discuss model results, we note that interpretation of this data in terms of  $>3$  Ga impacts is problematic due to intense endogenous magmatism (Warren and Taylor, 2014). Furthermore, rock comminution, mixing, and recoil effects can further obscure interpretation of  $^{40}\text{Ar}/^{39}\text{Ar}$  data. In spite of these effects, our LHA compilation would appear to suggest a monotonic decrease in impacts over at least the past  $\sim 3$  Ga.

Both models require knowledge of the basement crystallization age distribution and assume that lunar zircon  $^{207}\text{Pb}/^{206}\text{Pb}$  ages (Grange et al., 2011, 2009; Nemchin et al., 2008; Taylor et al., 2009) approximates this function (See Appendix D for compilation). While this could skew results to those compositions more likely to saturate zircon, compiled lunar Sm-Nd whole rock ages (Borg et al., 2014) lead to a similar age distribution.

#### **4 Results**

Apparent plateau ages returned by Model 1 (Fig. 4-2) reveal an age distribution characterized by an illusory bombardment spike at  $\sim 3.5$  Ga. This result shows that episodic, pre-4 Ga crust formation coupled with partial  $^{40}\text{Ar}$  loss due to the monotonically decreasing impact flux can bias age compilations toward the appearance of an impact spike. The Model 1 results agree well for  $>3$  Ga when compared to the distribution of lunar meteorite  $^{40}\text{Ar}/^{39}\text{Ar}$  “plateau” ages but our model over predicts young “plateau” ages (Fig. D.1). Results of Model 2 (Fig. D.2 and D.3) can reproduce both a canonical spike at 3.9 Ga and one at 4.1 Ga. We note that we do not specifically compare the shape of our spike to that of the literature data, as to our knowledge the specific shape of the “plateau” age distributions have never been used to constrain impact histories. That is to say, the literature interpretation is that a spike in

“plateau” ages at 3.9 Ga is evidence for the LHB but the specific distribution has not been cited in support. Since Model 2 is fixed to require an impact spike, we instead assess the plausibility of the underlying assumptions by examining the probability distribution of impact induced fractional  $^{40}\text{Ar}$  loss that is required to match the desired impact spike age. To compare the resulting distribution to that for Apollo samples, we need to calculate the fractional loss for each sample. Since there is virtually no published Apollo  $^{40}\text{Ar}/^{39}\text{Ar}$  data that has been fit by a diffusion model (c.f. 36) we compiled the fraction of gas included in the “plateau” for ~100 Apollo samples (Dalrymple and Ryder, 1996, 1993, Norman et al., 2010, 2006). Model 2 output agrees well with this compilation (Fig. 4-3) suggesting that the assumptions embodied in the model are reasonable despite the considerable complications in Apollo  $^{40}\text{Ar}/^{39}\text{Ar}$  data.

For both models, the simulated impact rates both exponentially and monotonically decrease with time (Fig. 4-4). Comparison of Model 1 with the cumulative frequency distribution for LHAs matches well. For Model 2, the fit to a 4.1 Ga impact spike is better than one at 3.9 Ga, although both are visually adequate solutions (Fig. D.5).

## **5 Discussion**

### **5.1 Implications for other extraterrestrial bodies**

Our modeling shows that, due to the nature of declining impact rates and the short duration of crust formation on extra-terrestrial bodies, apparent bombardment episodes can be a common artifact in  $^{40}\text{Ar}/^{39}\text{Ar}$  “plateau” age histograms. Indeed, age compilations of samples from H-chondrites and HED meteorites also show apparent spikes in impact activity between 3.5 and 4 Ga (Bogard, 2011; Marchi et al., 2013; Swindle et al., 2013). Model 1 in general produced curves that imply increased activity around 3 to 4 Ga and feature a paucity

of > 4 Ga ages. While our model is based on a lunar crustal age distribution which is too young to characterize meteorite parent bodies, the qualitative agreement between our results and meteorite data suggests that episodic petrogenesis coupled with a monotonically decreasing impact flux can explain meteorite  $^{40}\text{Ar}/^{39}\text{Ar}$  histograms.

A distinctive characteristic of meteorite  $^{40}\text{Ar}/^{39}\text{Ar}$  ages is the lack of “plateaux” between 4.1 and 4.4 Ga. This can be understood if those samples with bulk cooling ages of  $\geq 4.5$  Ga were shielded from impact thermal effects by their location away from the parent body surface, only becoming thermally affected during their last (typically <1 Ga) breakup event. Meteorite samples with  $^{40}\text{Ar}/^{39}\text{Ar}$  ages between 3.5 and 4 Ga are those that lay closer to parent body surfaces and thus experienced a protracted impact history. Thus the view that the lack of intermediate plateau ages in meteorites reflects an impact hiatus (Marchi et al., 2013) is non-unique and at least as well explained by relative position in parent bodies.

## **5.2 Mass Constraints**

Based on estimates of highly siderophile elements (HSE) concentrations in Earth’s mantle (Chou, 1978; Jones and Drake, 1986; Walker, 2009) and mantle noble gas systematics (Dauphas and Marty, 2002), it has been suggested that 0.5-1.5% of an Earth mass was accreted following core formation (the “Late Veneer”). While this estimate is not universally accepted (Righter, 2015; Righter et al., 2015), it is widely used to constraint impact models (Marchi et al., 2014) and mantle dynamic models (Maier et al., 2009). As we have shown, the act of inverting a distribution of  $^{40}\text{Ar}/^{39}\text{Ar}$  “plateau” ages into an impact curve, even to relatively late stages of planetary evolution (i.e., 3.9 to 4.1 Ga), is non-unique. Thus proposed bombardment histories for the period >4.1 to 4.5 Ga (Marchi et al., 2014; Morbidelli et al., 2012) are speculative. Indeed, these histories (Marchi et al., 2014; Morbidelli et al., 2012)

results in geochemical consequences that are incompatible with the terrestrial record. For example, virtually all workers agree that the Hadean (>4 Ga) zircon record requires a terrestrial hydrosphere (Harrison, 2009; Mojzsis et al., 2001; Rollinson, 2008; Shirey et al., 2008; Wilde et al., 2001); this is fundamentally incompatible with the models for the Hadean derived from impact histories (Marchi et al., 2014; Morbidelli et al., 2012) as these continually destroy the crust. Other geochemical inferences include the existence of an evolved, likely granitic continental crust (Amelin et al., 1999; Harrison et al., 2008), possibly formed by a subduction-like process (Harrison, 2009; Hopkins et al., 2008). Furthermore, the hypothesis that Hadean zircons formed in impact melts explicitly tested and rejected (Wielicki et al., 2012). Instead models from the impact history into the Earth-Moon system (Marchi et al., 2014), based on extrapolated impact curves based on  $^{40}\text{Ar}/^{39}\text{Ar}$  “plateau age” histograms propose that impacts delivering the Late Veneer caused Hadean Earth to be covered with ~20 km thick flood basalts.

In order to reconcile the Late Veneer with constraints inferred from Hadean zircons, we propose that the majority of all impacts happened at >4.4 Ga and that more recent cratering contributed only negligible mass and energy to the Earth-Moon system. Indeed, a recent re-evaluation of lunar basin forming impactors (Miljkovic et al., 2013) similarly agrees that estimates of delivered mass to the Moon based on observed crater sizes are substantially too large due to the use of incorrect target properties. Our modeling is insensitive to the magnitude of >4.4 Ga impacts and thus consistent with a higher, early impactor flux being responsible for the Late Veneer. Further evidence for a significant drop off in impact flux is that there are no lunar or terrestrial zircons (or samples of any kind) significantly older than 4.4 Ga (Borg et al., 2014; Holden et al., 2009) while the Hf isotopes in those zircons point to a

differentiation event at  $\geq 4.5$  Ga (Harrison, 2009; Taylor et al., 2009). While it may seem paradoxical that Late Veneer impacts, which could melt the crust and mantles of both the Earth and Moon, did not reset their Hf isotope systems, the large disparity in Lu and Hf concentrations between both the terrestrial crust/mantle (Palme and O'Neill, 2003; Rudnick and Gao, 2003) and FAN/KREEP (Floss et al., 1998; Warren and Wasson, 1979) works against leaving a record of such an event. That is, while impact mixing of crust and mantle is unlikely to significantly affect crustal Hf isotope evolution, it destroys or resets the chronology of rocks  $>4.4$  Ga. A scenario consistent with our re-analysis of the meaning of lunar  $^{40}\text{Ar}/^{39}\text{Ar}$  data, environmental constraints inferred from Hadean zircons (Harrison, 2009), the re-evaluation of lunar basin forming impactor size (Miljkovic et al., 2013), and the  $>4.5$  Ga age of core formation of (Yin et al., 2002) is that a Late Veneer was delivered to Earth between 4.5-4.4 Ga followed by relatively low impact rates.

## **6 Summary**

In order to examine the possibility of monotonically decreasing impact curves combined with episodic crust formation yielding the observed distribution of  $^{40}\text{Ar}/^{39}\text{Ar}$  “plateau” ages, we constructed three simulations. They are constrained to fit a compilation of Last Heating Ages (LHAs) of Apollo samples, which represent an estimate of the last time each sample experienced heating sufficient to cause measurable  $^{40}\text{Ar}$  loss. Model 2 is further constrained to create a spike in impacts at 3.9 Ga or 4.1 Ga. We show that  $^{40}\text{Ar}/^{39}\text{Ar}$  “plateau” age histograms will show apparent (but illusory) bombardment episodes under monotonically decreasing impact rates for bodies with early and episodic crust formation when coupled with the effects of partial resetting of the  $^{40}\text{Ar}/^{39}\text{Ar}$  system. Thus the most widely used evidence to support the LHB hypothesis yields unreliable impact histories.

Future work using improved chronological methods, such as in situ  $^{40}\text{Ar}/^{39}\text{Ar}$  dating (Mercer et al., 2015) as well as quantitative thermochronologic modeling (Shuster et al., 2010), can aid in establishing evidence for or against an LHB-type event. Until such evidence is gathered, we conclude that a monotonic decrease in impactor flux explains all existing  $^{40}\text{Ar}/^{39}\text{Ar}$  data from both lunar and meteoritic samples.

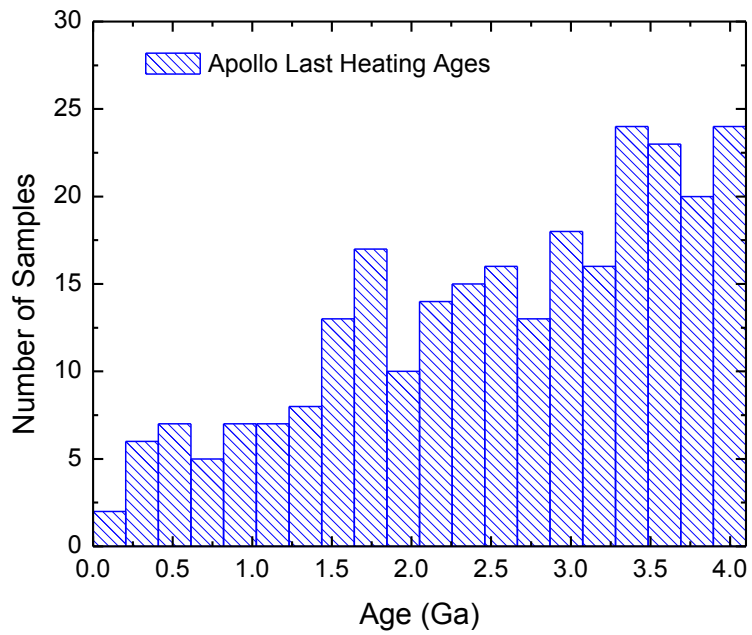


**Figure 4-1:** This is our compilation of 267 Last Heating Ages (LHA), which is the age of the gas released during the early heating steps.

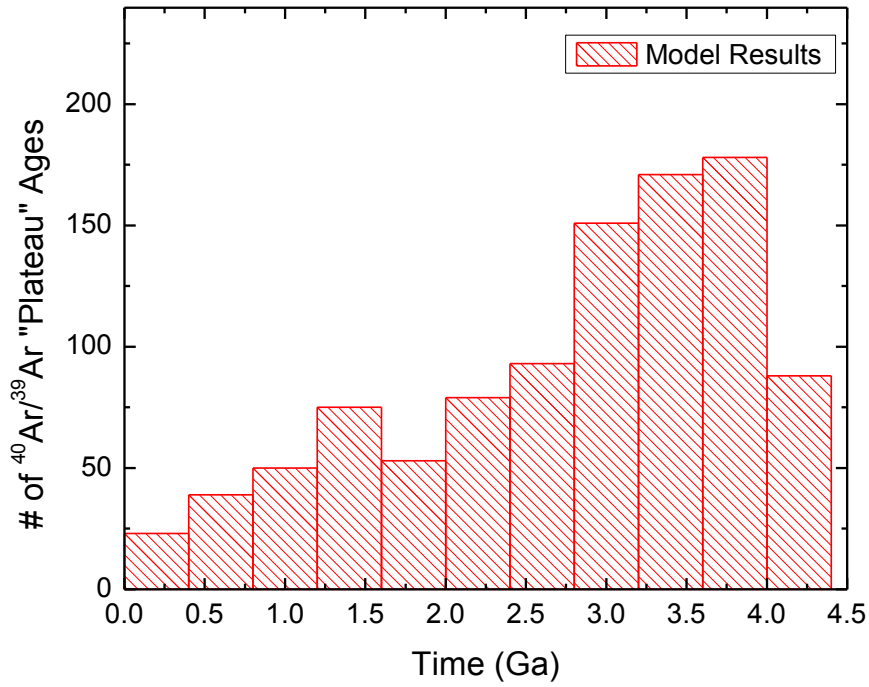


**Figure 4-2:** This is the distribution of “plateau” ages resulting from Model 1. While there are more broad features than observed in the Apollo data, there is a peak between 3.5 and 4 Ga showing that apparent bombardment spikes are common in “plateau” age histograms.

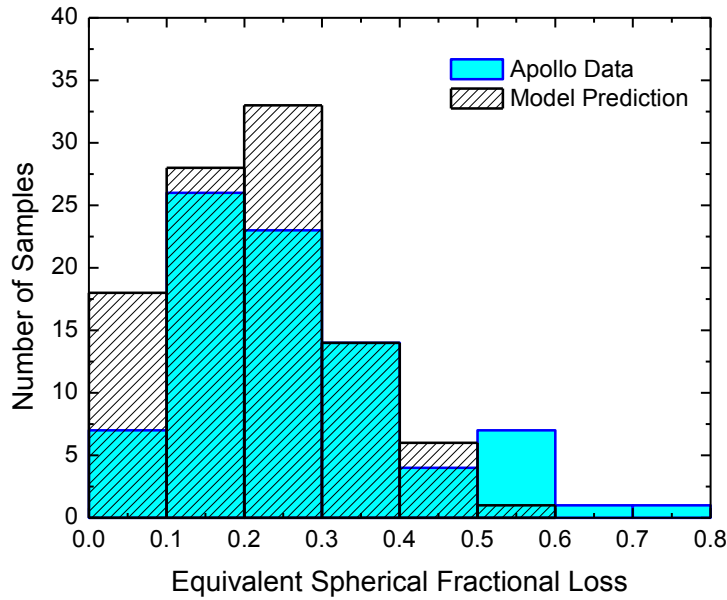


**Figure 4-3:** This is the actual spherical loss estimated to result in an impact event from the Apollo data compared with the distribution resulting from running Model 2 with a LHB at 3.9 Ga. The agreement between the two distributions shows that even selecting samples with little fractional loss (i.e., “good” plateaus) still introduce a significant bias to the inferred bombardment history.

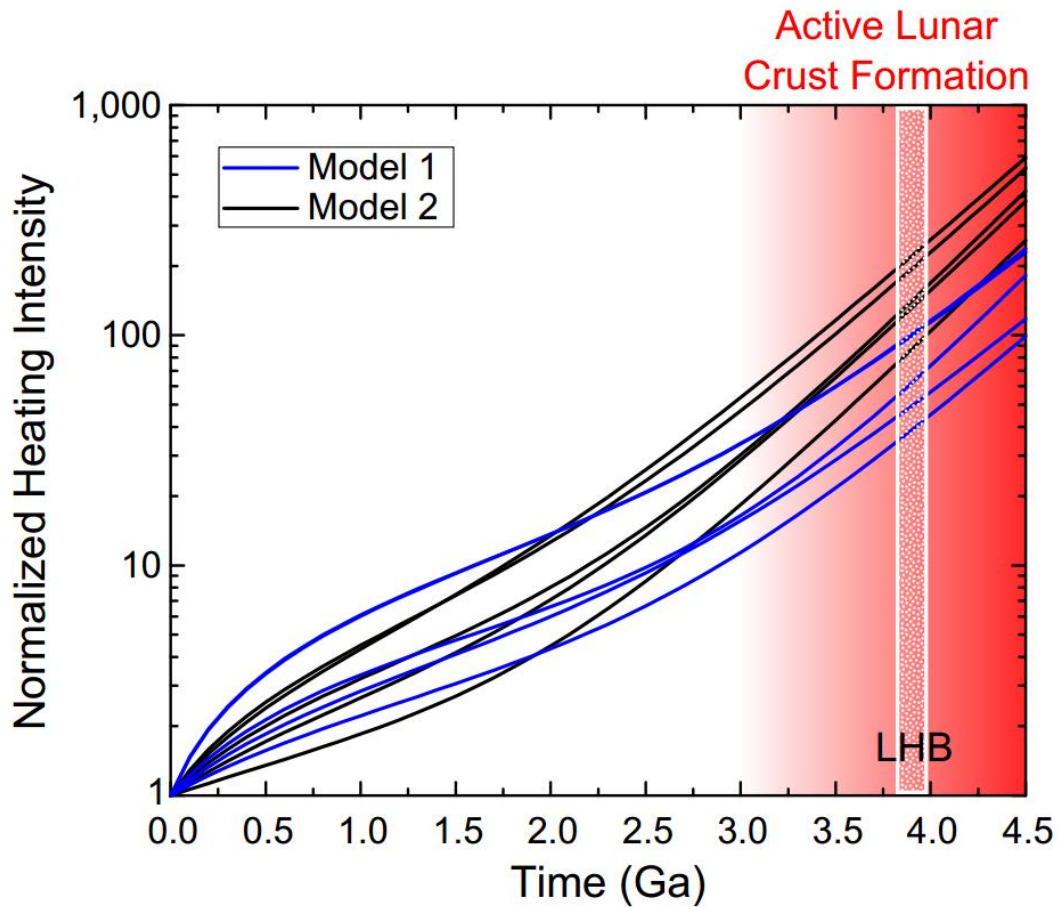


**Figure 4-4:** Here we show selected model runs for both Model 1 and Model 2 normalized to the present day impact rate. Both models suggest a drop in impacts of 2-5x over the last 2 Ga and neither has a spike at the timing of the LHB at ~3.9 Ga. We also show the timing of active crust formation and volcanism on the Moon in red and the LHB in white. During the interval shaded in red we do not believe  $^{40}\text{Ar}/^{39}\text{Ar}$  to be uniquely interpretable in terms of impacts due to the generally high thermal activity on the Moon.

## Chapter 5: Impact Mixing and Brecciation: The Silent Killer of Chronologic Information

### Abstract

Apollo samples have been used to study the age of the Moon and the early impact history of the Earth-Moon system. Unfortunately, the ferroan anorthosites, the oldest of those samples investigated, have experienced repeated impacts and virtually all are breccias. We examine the chronological complexity of ferroan anorthosites through  $^{40}\text{Ar}/^{39}\text{Ar}$  step-heating analyses of multiple rocks from several Apollo 16 soil samples. Our results show that despite being geochemically similar and in close proximity, a majority of our rocks in each soil sample cannot be related through a single thermal history. Based on this knowledge, we constructed a model to investigate the effects of mixing different aged minerals on internal isochrons. This model shows that statistically acceptable isochrons in which actual ages are  $>100$  Ma too young are possible. We then propose a possible explanation for the apparently young Sm-Nd ages of ferroan anorthosites and suggest chronologies based on whole-rock lunar samples be re-examined.

### 1. Introduction

The Apollo sample collection has provided key information in our understanding of lunar history and unique insights into planetary evolution (Warren, 1985; Wood et al., 1970) such as the Late Heavy Bombardment hypothesis (Tera et al., 1974). However, these generally multi-mineralic and fine grained materials commonly show effects of disturbances by thermal episodes and brecciation caused by impacts which complicate chronologic interpretations (Boehnke et al., 2014; Chapter 3). The vast majority of  $^{40}\text{Ar}/^{39}\text{Ar}$  step-heating analyses yield complex degassing patterns, including age gradients,

which are nonetheless generally interpreted in terms of plateau ages (Kring and Cohen, 2002; Norman et al., 2006; cf. Shuster et al., 2010) .

In an attempt to transcend these limitations, we have undertaken studies of diffusive Ar loss in Apollo and meteorite samples through an extension of the multi-diffusion domain model (Lovera et al., 1989) that includes consideration of multiple activation energies (Boehnke et al., 2014 Chapter 3). Previously, we proposed that shock heating and duration can be recovered from step-heating analyses that incorporate appropriate laboratory heating schedules (Boehnke et al., 2016b; Chapter 3). However, an important requirement for recovering accurate thermal histories is that the sample not be a mixture of rocks with different ages and thermal histories. To specifically test this requirement, we analyzed between two and five rocks each from a suite of Apollo 16 soil samples. The rocks within the soil sample are geochemically similar and therefore these analyses allow us to examine possible chronological discrepancies for rocks which may share an igneous crystallization history due to later impacts.

Apollo 16 samples are ideal for testing the potential effects of mixing and brecciation on lunar impact histories as they are thought to include the oldest crust of the Moon (Borg et al., 2014; Warren, 1985). The majority of samples returned by the Apollo 16 mission are ferroan anorthosites (FANs) which are thought to have crystallized as a floatation crust during the magma ocean epoch of lunar formation (Warren, 1985), that is they crystallized during the primary solidification of the Moon after its accretion. The FANs have the greatest potential for impact mixing simply due to their great antiquity.

While specific impact histories for the early Earth-Moon system are highly debated (e.g., Morbidelli et al., 2012; Zahnle et al., 2007), it is broadly accepted that impact rates

were higher immediately after planetary accretion (Chambers, 2004) as fragments were swept up by the emergent bodies. The lack of consensus regarding impact histories in part reflects the continuous resurfacing of Earth by plate tectonics and erosion which has removed >90% of impact craters (Johnson and Bowling, 2014) and the fact that the Apollo sample archive represents only ~4% of the lunar surface (Warren, 2003). Indeed the degree to which the Apollo rock suite is non-representative of the lunar surface is underscored by the fact that Apollo  $^{40}\text{Ar}/^{39}\text{Ar}$  “plateau” age compilations differ significantly from that derived from, the likely more globally representative, lunar meteorites (Figure 1 in Marchi et al., 2013).

In this paper we focus on complications arising from impact mixing and brecciation which limit the recovery of accurate crystallization ages from what ultimately are quasi-sedimentary rocks. Indeed, it is surprising that this issue has not been more emphasized as surely no one would attempt to date a terrestrial sedimentary rock to establish an igneous crystallization age; it is an undefined concept. However, over the last 40 years, whole rock analyses of Apollo breccias have been used to date lunar formation (Borg et al., 2011; Carlson et al., 2014; Carlson and Lugmair, 1988), the evolution of its early crust (Carlson and Lugmair, 1981; Papanastassiou and Wasserburg, 1972), and the provenance of the Descartes terrain (Norman et al., 2010). An enduring mystery is that several isochron ages obtained from these breccias yield statistical measures (e.g., MSWD) that are consistent with a single rock forming event (e.g., Borg et al., 2011). In order to examine whether or not constituents of breccias are consistent with a single chronologic history, we undertook  $^{40}\text{Ar}/^{39}\text{Ar}$  analyses on individual soil samples. Once we have shown that the majority of breccias are unlikely to meet the criteria of a single crystallization age, we propose that

mixing of two different aged samples can bias the age while still retaining an acceptable MSWD and demonstrate this through a simple numerical model.

## **2. Sample Description**

Our rocks (2-5 per sample) come from a suite of six Apollo 16 “coarse fine” (4-10 mm size fraction) samples obtained during the April 1972 mission. Specifically, we analyzed at least two ca. 3-5 mg aliquots each from samples 63504, 67484, 67714, 67514, 67704, and 67944. Geochemical analyses of these rocks span the range of composition of Apollo 16 impact melt rocks and breccias (Warren et al., 2013) with only a single exception, 67514. Rocks from 67514 plot on the low Sm-side on a plot of Sc vs Sm, which is used to show the compositional diversity in Apollo 16 impact melt breccias (Korotev, 1994), suggesting a common origin (Warren et al., 2013). Furthermore, Korotev (1994) argued that since Apollo 16 melt breccias and rocks can be divided into four compositional groups that they were likely created in  $\leq 4$  impact events. Therefore, this suite of samples allows us to examine both the notion that geochemically similar samples and those sharing a close proximity could be chronologically related.

## **3. Methods**

The analytical details for this work are described in Boehnke et al. (2016b) and reproduced here for reader convenience.

We utilized a conventional double vacuum furnace attached to a MAP-215-50 rare gas mass spectrometer at the New Mexico Geochronology Research Laboratory. Blanks were determined by analyzing the same heating schedule without a sample in the furnace. We used an  $(^{40}\text{Ar}/^{36}\text{Ar})_0 = 1$  to correct for primordial Ar which generally had a  $<1\%$  effect on age. Any inaccuracies in this correction are negligible given the scale of the disturbances we investigate.

The sample was irradiated in the TRIGA reactor at the USGS Denver (DeBey et al., 2012) to a J factor of 0.014773(4). Correction factors for interfering nuclear reactions are:  $(^{39}\text{Ar}/^{37}\text{Ar})_{\text{Ca}} = 0.000690(2)$ ,  $(^{36}\text{Ar}/^{37}\text{Ar})_{\text{Ca}} = 0.0002724(1)$ ,  $(^{38}\text{Ar}/^{39}\text{Ar})_{\text{K}} = 0.01077(1)$ , and  $(^{40}\text{Ar}/^{39}\text{Ar})_{\text{K}} = 0.00720(2)$ . Neutron fluence was monitored with co-irradiated hornblende Hb3gr assuming an age of 1072 Ma (Jourdan et al., 2006). A full description of the methods can be found in Heizler et al. (1999).

## 4. Results

### 4.1 Arrhenius Plots

Argon diffusivities as a function of laboratory heating temperature for each sample analyzed by the  $^{40}\text{Ar}/^{39}\text{Ar}$  step-heating method can be generated by translating the fractional loss of  $^{39}\text{Ar}$  through a solution of the diffusion equation (McDougall and Harrison, 1999). However, given the presence of multiple phases and diffusion domain sizes, plotting such data on an Arrhenius diagram generally yields complex patterns. Interpretation of these patterns requires use of quantitative modeling that incorporates information from the age spectrum (e.g., Lovera et al., 1989) together with insights from mineral chemistry.

There is no requirement that different portions of a thermally disturbed sample yield similar  $^{40}\text{Ar}/^{39}\text{Ar}$  age or Arrhenius spectra, only that they share a common thermal history. That is to say, different kinetic properties (e.g., grain sizes) would yield different age spectra even for the same thermal history (Lovera et al., 1989). Therefore, we first examine the diffusive properties of  $^{39}\text{Ar}$  in each analyzed rock to see whether or not they differ sufficiently to permit a shared thermal history for each soil sample to yield different age spectra. As shown in Figure 5-1A:5-3A, our analyses of multiple rocks from samples 63504, 67484, and 67714 return virtually identical Arrhenius plots. This means that each rock is similar enough that a shared thermal

history for the soil sample would result in essentially identical age spectra. However, the rocks of samples 67514, 67704, and 67944 (Figs. 4A-5A) yield Arrhenius plots that are distinctly different and thus could in principle support intra-sample age dispersions arising from a common thermal history.

If the distribution of  $^{40}\text{Ar}$  in all these samples is limited to thermally activated diffusion, then we would anticipate that our results would fall into the above two groupings. In fact, the data is far more complex requiring the action of additional low-temperature  $^{40}\text{Ar}$  loss mechanisms, potentially including comminution and mixing during brecciation. If such alteration occurs below the closure temperature for the domain sizes in each sample, a lack of correlation between Arrhenius and age spectra is expected (see Lovera et al., 2002).

## **4.2 Age Spectra**

The age spectra of rocks from our six soil samples show a variety of intra-sample age complexity. As shown in Figures 5-2B and 5-3B, while some samples (67484 and 67714) yield similar age spectra, others (63504, 67514, 67704, and 67944) show >1 Ga variations from one rock to another (Figs. 5-1B, 5-4B:5-6B). Therefore, independent of the complexity of the age spectra, it is not possible to assign a single age to at least four out of our six samples. We note that data from 67514,43 was previously presented in Boehnke et al. (2016b) and is included here for intercomparison. The full data is available in Table E.1.

## **5 Discussion**

### **5.1 A Thermal Signal?**

In principle, it is possible that observed intra-sample age differences in these samples arise from a shared thermal history. Indeed, this was demonstrated for multiple rocks of Apollo sample 63503, where one heating event at 3.3 Ga could explain the

observed spread in ages (Shuster et al., 2010). We therefore examined each of our samples for such a parsimonious solution.

Unfortunately, we were not able to similarly reconcile most of our data with a single re-heating event which generally obviates the need for subsequent detailed diffusion modeling (i.e., the data are pathologic in some respect that prevents recovering thermal history information). That being said, the sample that best illustrates this pathology is 67514 in which rock 22 yields the youngest ages and rock 24 the oldest, with rock 43 falling in between (Fig. 5-4B). If this distribution of age gradients arose due to a single event at  $\leq 900$  Ma (as required by 67514,22), then the Arrhenius plot (Fig. 5-4A) should show that 67514,22 has the smallest diffusion domains of the three rocks. However, 67514,43 has the *least* retentive domains for Ar while 67514,24 is the most retentive. In other words, a common thermal history for all rocks would yield younger apparent ages in 67514,43 than 67514,22. This reversal in apparent kinetic properties unambiguously shows that each analyzed rock in soil sample 67514 experienced a different thermal history. Sample 63504 provides further evidence of the chronologic complexity introduced by impact mixing and low-temperature comminution. Data for 63504 yields Arrhenius plots that are virtually identical (Fig. 5-1A). While the age spectra of 63504,12 and 63504,14 are similar, they differ by  $>1.5$  Ga from that of rock 63504,16 (Fig. 5-1B). This behavior is clearly inconsistent with a sample having experienced only a single thermal history given that similar Arrhenius plots would require similar age spectra.

By the reasoning outlined above, the same mismatch between age and Arrhenius spectra for sample 67484 (Fig. 5-2) also cannot be reconciled with a single thermal history. We now turn our attention to samples 67704 and 67944 whose age and Arrhenius spectra

are in principle reconcilable with a single thermal history. However, after extensive modeling attempts using the method of Boehnke et al. (2016b), we have failed to identify acceptable solutions that reconcile all of the parameters with a single thermal history. That said, the stochastic nature of global optimization algorithms does not guarantee that an acceptable solution doesn't exist, only that we did not find one. The last sample in our analysis, 67714 (Fig. 5-3), shows broad agreement among the shapes of the various age spectra (over the first ~30% of  $^{39}\text{Ar}$  release) which then diverge with a spread of ~500 Ma. This could suggest a shared thermal event affected soil sample 67714 with sufficiently high temperatures to induce partial  $^{40}\text{Ar}$  loss and thus a common thermal history. In this case, the computational complexity prevents finding an acceptable history because fitting 5 rocks with 10 domains per phase (e.g., plagioclase and pyroxene) and two phases each involves at least 200 free parameters.

## **5.2 Chronologic Significance of Breccias?**

One end-member model is that each mineral grain in a breccia could have a different crystallization age and thermal history. The other end-member is that the same igneous rock was being broken up and reassembled in which case the thermal histories and chronologies could be meaningful. Past analyses have shown that clasts can have  $^{40}\text{Ar}/^{39}\text{Ar}$  ages significantly older than the matrix of the breccia (Dominik and Jessberger, 1978) or that multiple discordant age spectra in Apollo regolith samples can be reconciled with a single heating event (Shuster et al., 2010). Since our data shows that rocks which share a close proximity and geochemical characteristics do not have to share a single thermal history, we suggest that impact mixing obscures the chronologic information of most lunar

breccias. Indeed, this is consistent with the findings that Apollo 17 impact melt breccias can record multiple impact events (Mercer et al., 2015).

### **5.3 Breccia: Isochron or Mixture?**

The chronologic complexity of the Apollo samples have been revealed by  $^{40}\text{Ar}/^{39}\text{Ar}$  step-heating analyses, which are capable of resolving micron scale  $^{40}\text{Ar}$  disturbances (e.g., Albarède, 1978). Indeed the chronologic complexity of lunar rocks from soil samples shows that lunar breccias are assembled from components which have different ages (this chapter). However, these complications may go unnoticed in bulk analyses (e.g., typically required by the Sm-Nd, Rb-Sr, or Lu-Hf methods) due to the large mass of material required for each mineral in the isochron (>50 mg; Carlson et al., 2014) and the fact that the sample is homogenized prior to analysis. Because discussion of the  $^{40}\text{Ar}/^{39}\text{Ar}$  data highlights the larger problem of dating lunar breccias, we now turn to implications for Sm-Nd and Rb-Sr analyses.

It has been known for nearly fifty years that apparent isochrons can be produced by mixing different sources (Bell and Powell, 1969). Thus the surprisingly young ages (ca. 4.35 Ga) for ferroan anorthosites (Borg et al., 2011) raise the possibility that they might represent something other than true isochron ages given that the analyzed samples are breccias. While the possibility that isochrons could be mixing lines has long been known, only those cases where the MSWD is incompatible with a single undisturbed crystallization age are likely to invoke this interpretation (e.g., Wendt, 1993). The enduring mystery of the Sm-Nd analyses of FANs is that the isochrons often appear statistically acceptable (Borg et al., 2011; Carlson and Lugmair, 1988; cf. Norman et al., 2003) which would rule out later disturbances.

Before we examine this in detail, it is worth noting that FANs are predominantly composed of plagioclase with minor mafic (e.g., pyroxene and olivine) phases (e.g., James et al., 1989; McGee, 1993). For this reason, isochron analyses of FANs are difficult and require large sample volumes (e.g., Carlson and Lugmair, 1988). Additionally, separation of pyroxene from olivine is challenging (Carlson and Lugmair, 1988) and therefore several studies analyze only the combined pyroxene + olivine (e.g., Borg et al., 2011). This however, compromises the robustness of the interpretation since the isochron now has only two components (plagioclase and pyroxene + olivine). For example, Borg et al. (2011) separated 60025 into plagioclase and pyroxene + olivine while also analyzing a whole rock (WR) aliquot which appear to yield an acceptable isochron age of  $4,367 \pm 11$  Ma. However, despite containing three separate components (WR, plagioclase, olivine + pyroxene), because the WR consists of only plagioclase, pyroxene, and olivine it is a binary mixture of the two analyzed end-members and in reality is only a two point isochron. That is to say, given the mineralogy of FANs, the WR analysis does not provide any fundamentally new chronological information beyond the two point tie line. We will return to the significance of this after discussing the potential effects of brecciation on a three point isochron.

While many such studies only utilize two point isochrons, numerous studies show statistically acceptable isochrons when separating FANs into plagioclase, pyroxene, and olivine (Borg et al., 1999; Carlson and Lugmair, 1988). Therefore, we now examine the possibility that two or more different aged samples mixed to create an incorrect isochron with a statistically acceptable MSWD. We utilized a Markov Chain Monte Carlo (e.g., Boehnke et al., 2015; Gelman et al., 2003; Sambridge et al., 2013) to simulate mixing of two rocks with similar mineralogy. Our model has two FAN-like model rocks in which one

crystallized at 4.52 Ga and the other between 3.5 and 4.4 Ga; mineralogy is assumed to be similar (e.g., each have plagioclase, pyroxene, and olivine). We use the data of Borg et al. (1999) for the Sm/Nd of each mineral (plagioclase, pyroxene, and olivine), and calculated the ingrowth of  $^{143}\text{Nd}$  using a half-life of 107 Ga (Boehnke and Harrison, 2014; Kossert et al., 2009). For our model we assume that two of the minerals are a 50:50 mixture from each model rock and used the Markov Chain Monte Carlo to ascertain the distribution of mixing proportions of the third mineral (it does not matter which of the mineral is used). The results are presented as the relative standard deviation in percent of the allowed mixing proportion from the 4.52 Ga component (see SOM). As shown in Figure 5-7, for the mixtures resulting in the oldest apparent ages (using a younger component with an age of 4.4 Ga) there is a 20% deviation allowed at one sigma, which is to say that the fraction of mineral three is  $0.5 \pm 0.1$ . Since the majority of FAN ages cluster around 4.4 Ga (Borg et al., 2014), the mixing does not have to perfectly homogenize the two component rocks, it simply has to be within the allowed variability (Fig. 5-7). This is particularly problematic for radiogenic systems where the half-life is long with respect to the age of the solar system.

We therefore propose that the Sm-Nd chronology of FANs could be disturbed by impact mixing and brecciation without affecting the MSWD of the resulting internal isochron. While our simulations focus on Sm/Nd, they are not specific to any one system and therefore affect U/Pb and Lu/Hf equally. Additionally, similar ages between these systems is not a meaningful indicator the sample is undisturbed as the diffusive properties of Nd and Pb, for example, are broadly similar (Cherniak, 2003, 1998, 1995). That is to say, a hypothetical heating event to 800°C could similarly reset both Sm-Nd and U-Pb on

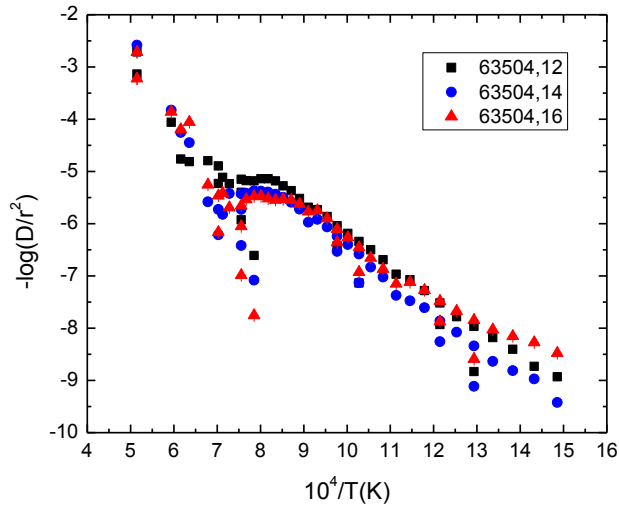
broadly similar timescales. Therefore, in our scenario, some FANs are reheated by impacts while others are not and they are subsequently mixed to varying degrees by low temperature brecciation. Indeed, such a scenario also explains the ~300 Ma range in “crystallization” ages of FANs (Carlson et al., 2014). We are not proposing that this explanation is universal, only that our  $^{40}\text{Ar}/^{39}\text{Ar}$  analyses suggest a complicated history for these breccias and therefore raise the possibility that seemingly well behaved isochrons are actually mixing lines.

## **6 Conclusion**

$^{40}\text{Ar}/^{39}\text{Ar}$  analyses of multiple rocks from six Apollo 16 soil samples show that impact mixing and low-temperature comminution must be involved in forming a significant fraction of Apollo breccias. We show that the kinetic behavior of  $^{39}\text{Ar}$  coupled with the age spectra is incompatible for rocks of at least three of our six samples sharing a similar thermal history. The other samples could be compatible with one thermal history, but we were unable to quantitatively model it due to the computational complexity of the problem.

$^{40}\text{Ar}/^{39}\text{Ar}$  step-heating analyses have high spatial resolution so they can reveal complexity that is averaged out by other bulk analytical techniques (e.g., Sm-Nd). With this in mind, we show that coupling the complexity revealed by our analyses with the bulk nature of Sm-Nd analyses could yield acceptable isochrons with erroneous ages. The complexities found in breccias are therefore significant enough to destroy the chronological significance of bulk analyses and dating FANs will require developing in-situ techniques that can see through these disturbances. Indeed, these results call for a complete re-examination of the chronology derived from whole-rock Apollo samples.

A:



B:

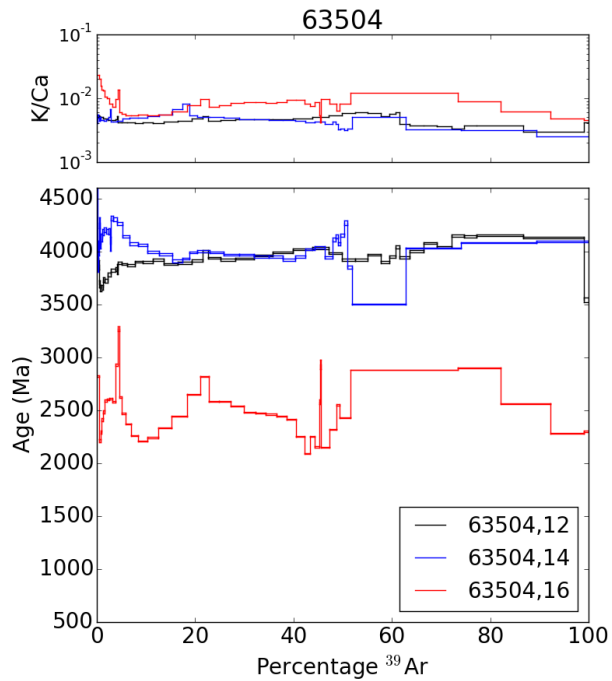
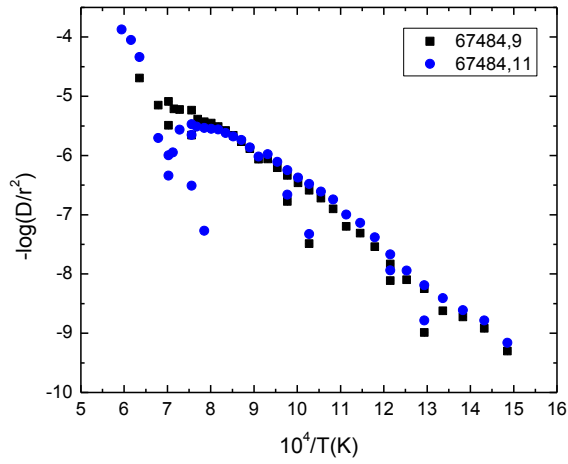


**Figure 5-1:** The Arrhenius plot and age spectra for rocks from the rake sample 63504.

Note the similar  $^{39}\text{Ar}$  diffusion kinetics with a >1 Ga age difference between the rocks rules out the possibility of a shared thermal history.

A:



B:

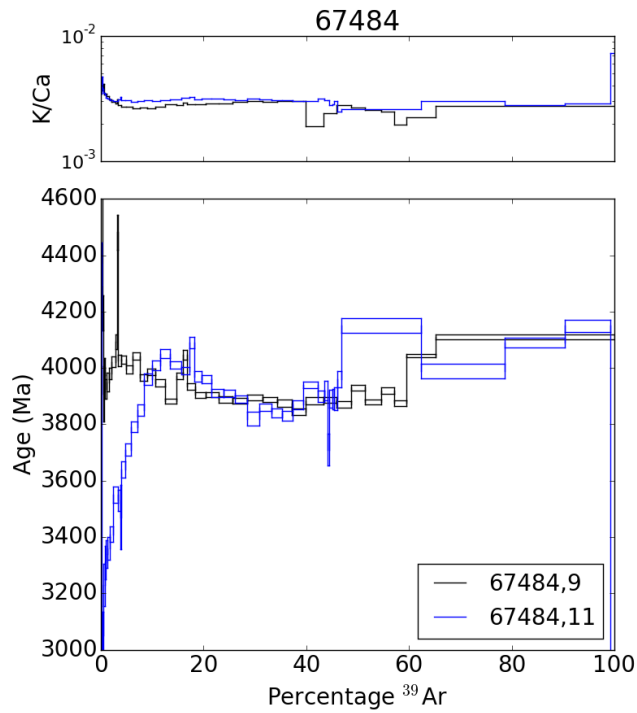
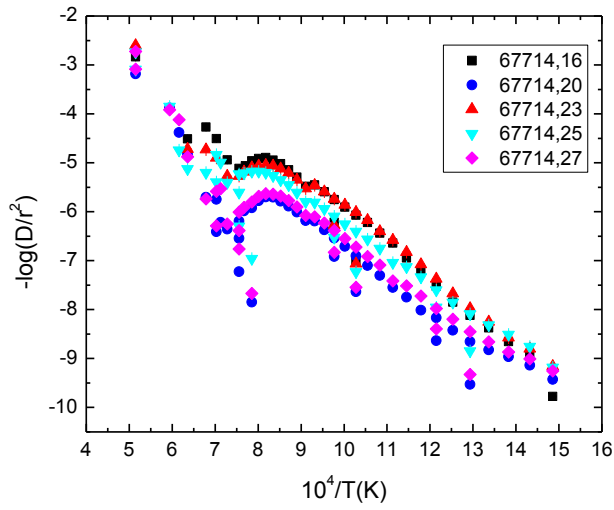


**Figure 5-2:** The Arrhenius plot and age spectra for rocks from the rake sample 67484.

Note the similar  $^{39}\text{Ar}$  diffusion kinetics with a >1 Ga age difference between the rocks rules out the possibility of a shared thermal history.

A:



B:

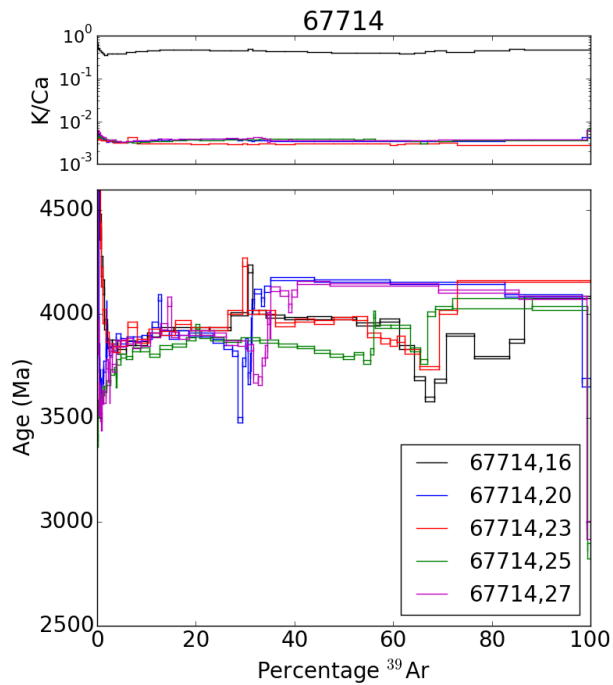
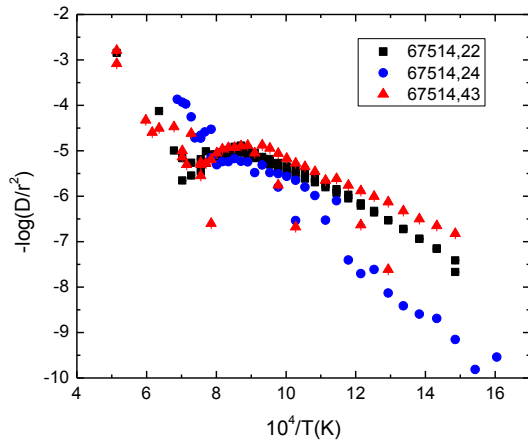


**Figure 5-3:** The Arrhenius plot and age spectra for rocks from the rake sample 67714.

Note the similar  $^{39}\text{Ar}$  diffusion kinetics with apparently similar ages for the first portion of the  $^{39}\text{Ar}$  release suggests the possibility of a shared thermal history.

A:



B:

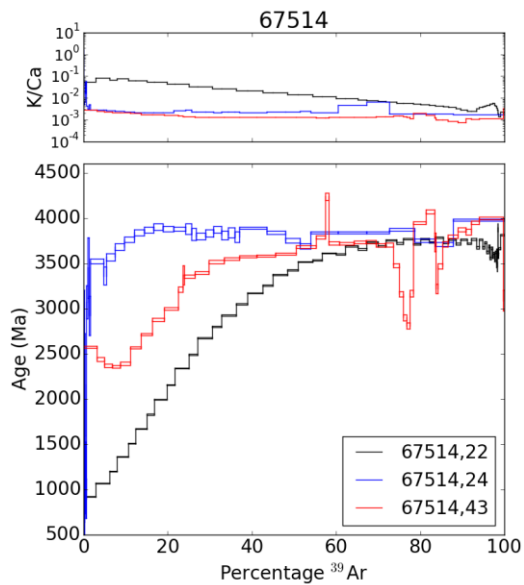
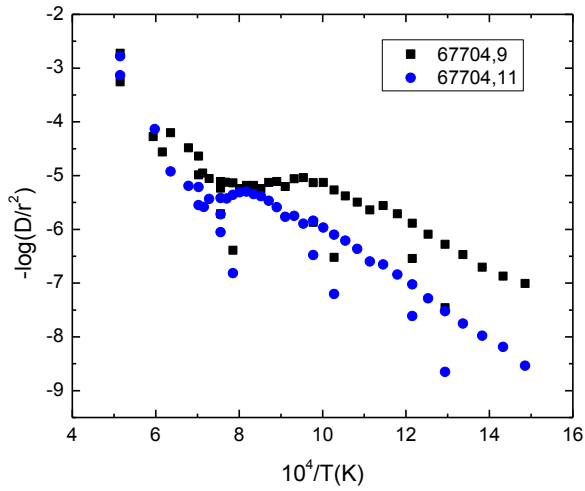


**Figure 5-4:** The Arrhenius plot and age spectra for rocks from the rake sample 67514.

Note the differing  $^{39}\text{Ar}$  diffusion kinetics and different age spectra are incompatible with a shared thermal history. This is because while rock 22 yields the youngest ages, it is not the least retentive sample.

A:



B:

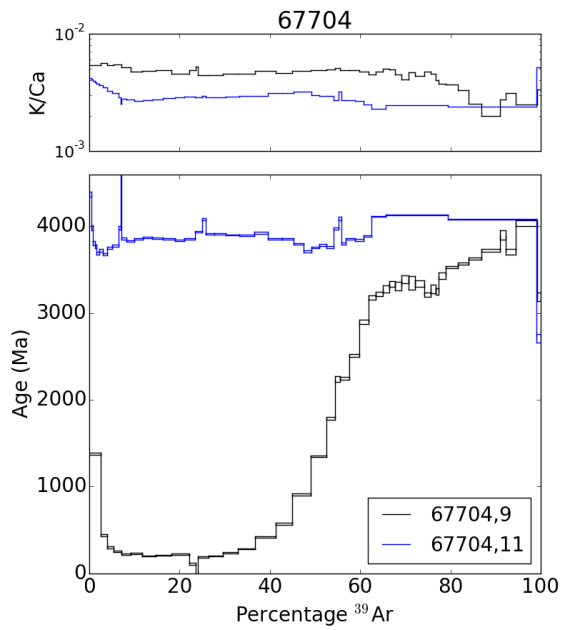
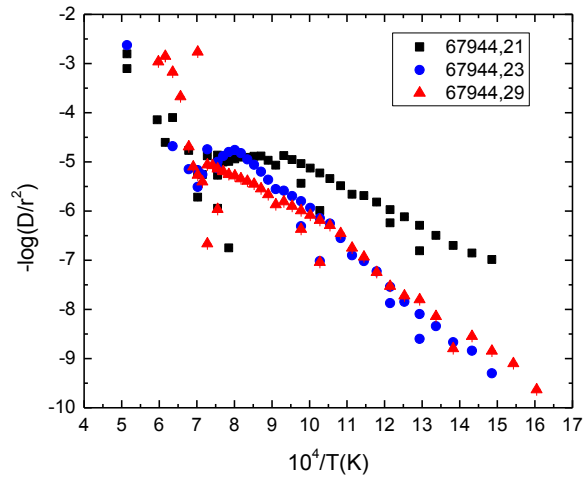


**Figure 5-5:** The Arrhenius plot and age spectra for rocks from the rake sample 67704.

Note the differing  $^{39}\text{Ar}$  diffusion kinetics and different age spectra are compatible with a shared thermal history. This is because the less retentive rock yields apparently younger ages.

A:



B:

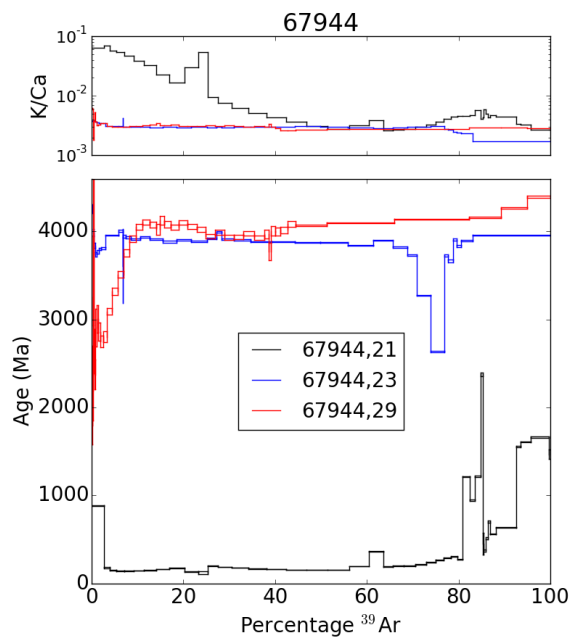


**Figure 5-6:** The Arrhenius plot and age spectra for rocks from the rake sample 67944.

Note the differing  $^{39}\text{Ar}$  diffusion kinetics and different age spectra are compatible with a shared thermal history. This is because the less retentive rock yields apparently younger ages.

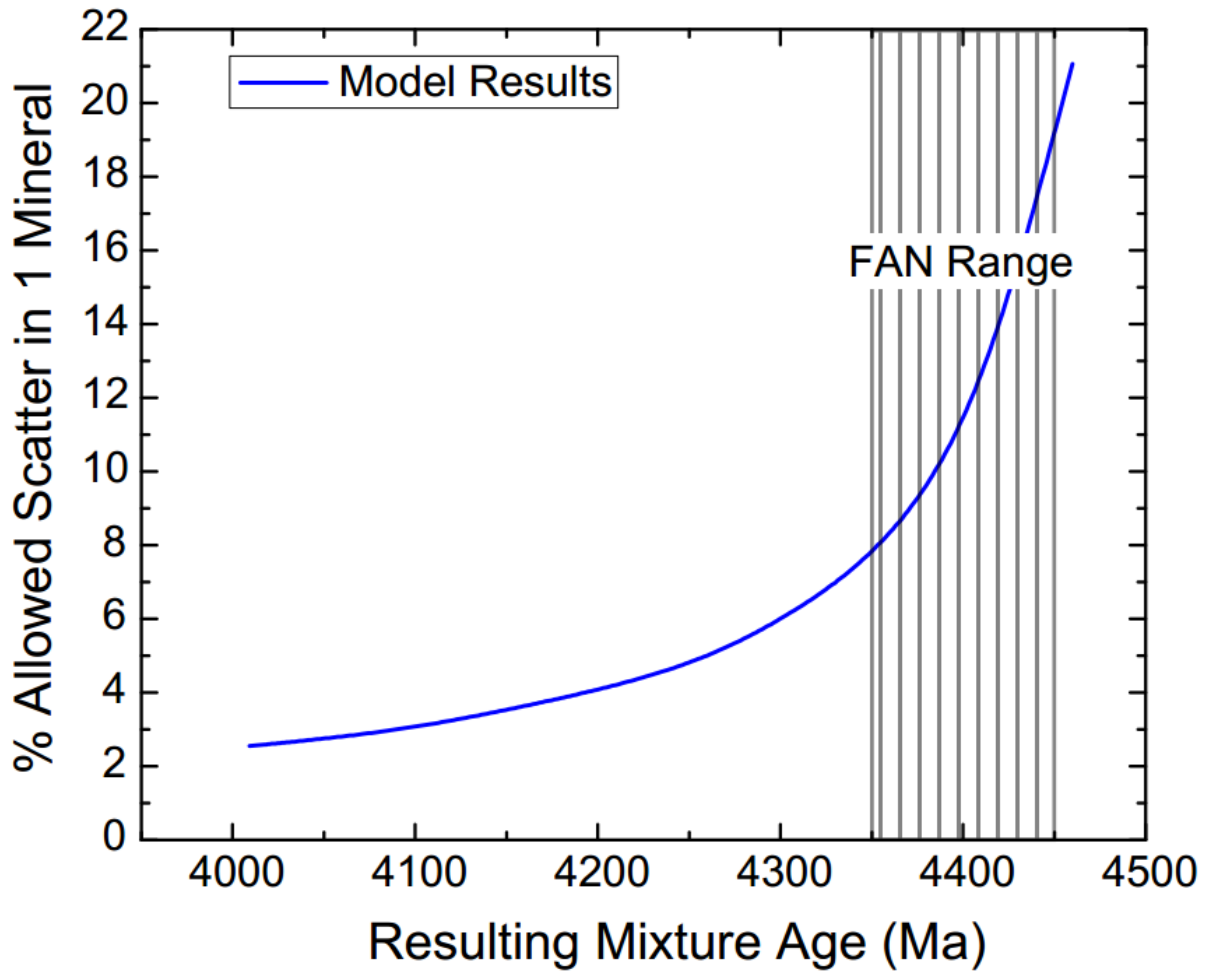


**Figure 5-7:** Our model results showing the allowed scatter in the mixing proportion of one mineral while still resulting in a statistically acceptable isochron. A detailed explanation can be found in the text.

## Chapter Six: Conclusions and Future Work

The overarching theme of this thesis is the test of two endmember hypotheses of early Earth – did it share much in common with the present or was it a prolonged, molten, hellscape. In effect, was it the best of times or the worst of times? The former scenario suggests that Hadean Earth saw liquid water, a granitic crust, an oxidizing atmosphere, and possibly a biosphere. The latter view suggests early Earth was covered by a continuously impacted mafic crust. Significantly, these end member visions arise, respectively, from analysis of terrestrial and extra-terrestrial samples. With a view toward establishing a single unifying framework for the >4 Ga Earth, I recalibrated the zircon solution model (Chapter 2), reconstructed  $^{40}\text{Ar}/^{39}\text{Ar}$  thermal histories from extraterrestrial samples containing multiple-activation energies leading to the proposal that shock heating conditions can be recovered (Chapter 3), examined systematic problems in interpretations of plateau ages from samples that yield disturbed  $^{40}\text{Ar}/^{39}\text{Ar}$  age spectra (Chapter 4), and examined the effects of brecciation on chronologic interpretations (Chapter 5). While these studies span a range of geochemical problems and techniques ranging from experimental petrology to rare gas thermochronology, they all address a single question in Earth history: what was the Hadean Earth like?

The simple fact that terrestrial Hadean zircons exist is evidence for >4 Ga felsic magmas. This is because experiments show that zircon stability (Watson and Harrison, 1983; Chapter 2) is dominantly a phenomenon of silicic magmas as highly unusual conditions are required to do so in their mafic counterparts. Compounding this fact of physical chemistry is the secular cooling of Earth which implies that Zr concentrations in mantle-derived melts early in Earth history were significantly lower than present (Keller et al., 2016). Thus zircon crystallizes much more readily

in modern magmas than throughout the Archean; to achieve comparable zircon productivity, a Hadean rock would have to have ~10 weight percent greater SiO<sub>2</sub> than a modern analog. From the standpoint of zircon productivity, a modern gabbro is a Hadean granodiorite (Keller et al., 2016).

The continuous reworking of Earth's surface makes it a poor recorder of its early history. The extraterrestrial record, however, has largely been in deep freeze for ~4.4 Ga and thus has seemingly greater potential in this role. However, many of these materials have problematic characteristics. For example, although lunar samples have been widely used to establish an inner solar system impact chronology, the complexity of chronologic interpretations for disturbed <sup>40</sup>Ar/<sup>39</sup>Ar age spectra have been underappreciated. The primary conclusions drawn from previous <sup>40</sup>Ar/<sup>39</sup>Ar analyses of Apollo rocks are that there was an increase in impacts at ca. 3.9 Ga (Chapman et al., 2007) above a generally high rate throughout the Hadean (Marchi et al., 2014). However, the samples examined in these studies are almost universally disturbed by later thermal events and therefore do not yield interpretable ages (McDougall and Harrison, 1999); this fact is usually ignored and “plateau ages” arbitrarily assigned (Kring and Cohen, 2002; Norman et al., 2006; c.f. Shuster et al., 2010).

In order to understand the systematic issues of assigning ages to disturbed samples, a study was undertaken to address the effects of diffusive <sup>40</sup>Ar loss in multi-phase samples (Chapter 3). As shown in Chapter 3, an extension of the multi-domain diffusion model (Lovera et al., 1989) that incorporates multiple activation energies can successfully fit step-heating data from the Jilin chondrite and Apollo 67514,43. This fit is surprising given the paradoxical character of the Jilin and 67514,43 age spectra wherein the seemingly more retentive pyroxene

yields younger ages than the less retentive plagioclase. This was reconciled in the model through exploiting the kinetic crossover (Harrison et al., 1991), a reversal in diffusivities at high temperatures, between plagioclase and pyroxene (Cassata et al., 2010). Without considering any effect of pressure on  $^{40}\text{Ar}$  diffusivity, temperatures of  $>2000\text{ K}$  for short durations permit fitting of the age spectra and provides evidence for  $^{40}\text{Ar}$  loss due to shock heating. While the experimental literature on activation volumes is highly variable, exploratory modeling was conducted which showed that temperatures of  $1600\text{ K}$  for 1-20 seconds at  $10\text{ GPa}$  can explain the  $^{40}\text{Ar}/^{39}\text{Ar}$  data and are consistent with petrography. Therefore we propose (Chapter 4) that the multi-domain diffusion model could be capable of recovering the duration and intensity of shock heating.

Having shown that in principle step-heating analyses of thermally disturbed samples are capable of providing meaningful chronologic information, the question arises whether impact histories derived from compiling arbitrarily assigned plateau ages simply misestimate the timing of bombardment episodes or are fundamentally incorrect (Chapter 4). In order to explore this issue, I compiled the ages from early heating steps for 267 Apollo  $^{40}\text{Ar}/^{39}\text{Ar}$  analyses, the timing of the last heating event (LHA). Using that data, a numerical model was constructed which treats each sample as a single diffusion domain (e.g., a sphere) and monotonically decreasing impact histories were generated, applied to the diffusion systematics of the samples, and evaluated in their fit to the LHA compilation. Once an appropriate impact history was found, the plateau ages were calculated for each sample and compiled. The results show that coupling the episodic nature of lunar crust formation with a monotonic impact history is prone to creating illusory bombardment episodes. That is to say, it is not possible to uniquely invert a compilation of plateau ages for disturbed samples into an impact history. Therefore, the majority of the

evidence now marshaled for the Late Heavy Bombardment can be reconciled with a monotonically decreasing impact flux.

Given the complexity of accurately interpreting samples that experienced diffusive  $^{40}\text{Ar}$  loss it is important to assess which samples meet the foundational requirement of the MDD model – that the rocks be undisturbed after the heating event. We undertook a study for Apollo 16 breccias to specifically ascertain the extent to which mixing and comminution affect the ability of step-heating  $^{40}\text{Ar}/^{39}\text{Ar}$  analyses to recover thermal histories. In order to examine these disturbances, we performed analyses of multiple aliquots from several Apollo 16 samples. Our results show that the majority of Apollo 16 samples cannot be reconciled with a single thermal history because aliquots with higher diffusivities often preserve older ages than aliquots with lower diffusivities. We interpret this to reflect the effect of low-temperature comminution during breccia formation/assembly (Chapter 5). That is, the sample was not heated sufficiently during breccia assembly to reset the  $^{40}\text{K}$ - $^{40}\text{Ar}$  system. Therefore, until high spatial resolution in-situ chronology for Apollo breccias is routinely applied, it seems unlikely that Apollo breccias can be used to infer the geologic history of the Moon. Additionally, modeling was performed to show that internal isochrons from these samples could yield erroneous ages which statistically acceptable MSWDs casting doubt on the calculation of Sm-Nd crystallization ages for ferroan anorthosites.

Based on these results, I suggest that choosing between a “best of times” or “worst of time” scenario is a false dichotomy. The biases in the interpretation of  $^{40}\text{Ar}/^{39}\text{Ar}$  data lead to age underestimation. The results of chapters 3-5 support the view that the majority of cratering activity took place earlier than 3.9 Ga and could potentially be pushed back to >4.4 Ga while the

evidence for the best of times scenario dates back to ~4.3 Ga. Therefore, the proposed path towards reconciliation is that the majority of preserved lunar impacts occurred at >4.4 Ga which was followed by a relatively benign period which permitted the geologic developments that led to the Hadean zircons. Indeed, such a scenario can be reconciled with almost all geologic constraints (see Chapter 4).

However, while this interpretation is consistent with essentially all of the available constraints it is not unique. That is to say, while the  $^{40}\text{Ar}/^{39}\text{Ar}$  data cannot be used to support a Late Heavy Bombardment, they do not preclude one. In order to fully address these questions new methodologies will need to be developed either based on high resolution in-situ dating (Mercer et al., 2015) or diffusion modeling of step-heating  $^{40}\text{Ar}/^{39}\text{Ar}$  data (Shuster et al., 2010). The more challenging issue is that the samples in hand are not ideal and represent only a small fraction of the lunar surface (Warren, 2003) and future missions to the Moon are required to improve this situation. Until such work comes to fruition, all of the available evidence can be reconciled with a simple history in which a high rate of impacts declined through 4.4 Ga and then played a minimal role in the development of the planet as inferred from Hadean zircons and the rock record.

## **Appendix A: A meta-analysis of geochronologically relevant half-lives: What's the best decay constant?**

### **Abstract**

Twenty-first century advances in both the analytical procedures and instrumentation used in geochronology promise age accuracy better than  $\pm 1\%$ , but realizing this potential requires knowledge of decay constants ( $\lambda$ ) that exceed this level. Given the paucity of improved recent measurements of  $\lambda$ , the community has experimented with hybrid methodologies utilizing data largely generated during the 1970s. In this paper, we perform a systematic review of laboratory decay constant determinations relevant to geochronology (i.e.,  $^{87}\text{Rb}$ ,  $^{147}\text{Sm}$ ,  $^{176}\text{Lu}$ ,  $^{230}\text{Th}$ ,  $^{232}\text{Th}$ ,  $^{235}\text{U}$  and  $^{238}\text{U}$ ) focusing on methodological consistency. For radioisotopes for which multiple studies are available, results are combined through a random effects model to yield the best available values and associated uncertainties. Unfortunately, despite its vital role in modern geochronology, only one experimental determination of  $^{238}\text{U}$  decay met our criteria for consideration, significantly limiting the ability to assess its reliability. Thus utilizing  $\lambda_{238}$  as an anchor for establishing other decay constants (e.g.,  $^{40}\text{K}$ ,  $^{176}\text{Lu}$ , spontaneous  $^{238}\text{U}$  fission) places an unverified result at the core of geochronology. For geochronology to attain its greatest potential, more and better laboratory determinations of decay constants are required, along with a community methodology that permits us to continuously take advantage of new data.

### **1. Introduction**

Although it would seem that utilization of the most accurate and precise decay constants ( $\lambda$ ) would be of fundamental importance to geochronologists, as a community they have tended to value on-going intercomparison over periodic review and revision (e.g., Renne et al., 1994, 1998, 2010, 2011; cf., Begemann et al., 2001). The existing convention for geochronological

decay constants ( $\lambda$ ), proposed by the Subcommittee of Geochronology and Stratigraphy and ratified at the International Geological Congress in 1976 (Steiger and Jäger, 1977), has remained unmodified for nearly four decades. However, concerns have been increasingly raised that these canonical values are inconsistent with more recent measurements (e.g., Begemann et al., 2001; Mattinson, 2000, 2010).

Because certain decay systems lend themselves to more precise measurement of  $\lambda$  than others, it has become commonplace to attempt to fix decay constants of poorly understood geochronological systems (e.g., spontaneous  $^{238}\text{U}$  fission,  $^{40}\text{K}$ ,  $^{176}\text{Lu}$ ) to that of  $^{238}\text{U}$  alpha decay (e.g., Hurford and Green, 1983; Kwon et al., 2002; Scherer et al., 2001) via concordant, coexisting minerals. In fact, establishing concordancy among coexisting phases has proven problematic in certain cases (e.g., Renne et al., 2010). More to the point, this approach puts a premium on ensuring that  $\lambda_{238}$  is precisely and accurately known when the value we use was generated more than 40 years ago using now obsolete analytical systems (Jaffey et al., 1971). Indeed, based on small discordances observed within apparently robust U-Pb zircon populations, Mattinson (2000) proposed that the more precisely determined  $\lambda_{238}$  be fixed at the value measured by Jaffey et al. (1971) and the corresponding  $\lambda_{235}$  be adjusted upward by  $\sim 0.1\%$  to bring those ages into concordance (also see Schoene et al., 2006 and Mattinson, 2010). In doing this, the uncertainty associated with  $\lambda_{235}$  was reduced to reflect only the analytical variance within those U-Pb ages. While this had the seemingly beneficial effect of improving the apparent accuracy of the U-Pb dating system (Schoene, 2014), it assumes a priori knowledge of the source of the discordance between  $^{207}\text{Pb}/^{235}\text{U}$  and  $^{206}\text{Pb}/^{238}\text{U}$  ages.

Concerns regarding the Steiger and Jäger (1977) convention are not limited to uranium isotopes. For example, the  $^{87}\text{Rb}$  decay constant was re-measured by Kossert (2003) who found it to be 1.4% lower than the conventionally accepted value. This value was subsequently confirmed by an accumulation experiment (i.e., growth of  $^{87}\text{Sr}^*$  in a purified  $^{87}\text{Rb}$  salt; Rotenberg et al., 2012). Furthermore, several now commonly utilized radiogenic systems that were not broadly used in 1977 (e.g.,  $^{147}\text{Nd}$ - $^{143}\text{Sm}$ ,  $^{176}\text{Lu}$ - $^{176}\text{Hf}$ ) were not considered in the Steiger and Jäger (1977) recommendations.

While the decay constant convention succeeded in providing a touchstone for inter-comparison, it did not provide a mechanism that could either motivate further study or accommodate improved measurements as they came available. In this paper, we propose a method for determining the best current value for decay constants by analyzing all published laboratory measurements collectively in a way that values studies of the highest quality. This general approach is referred to as meta-analysis and is commonly undertaken in the biomedical and social sciences where large numbers of investigations need to be evaluated (DerSimonian and Laird, 1986). Meta-analysis has also seen limited application in the physical sciences, perhaps the clearest example in nuclear physics where elementary particle properties are updated and maintained through a community collaboration (Particle Data Group, 2012) using similar techniques to traditional meta-analysis (Baker and Jackson, 2013). Given the critical nature of decay constants to geochronology, we re-examine the conventional values here and point to refined results that emerge from meta-analysis.

## **2. Method**

### **2.1 Study Selection Criteria**

The quality of scientific investigations varies from one study to the next with some results ultimately proving unreliable (e.g., Baker and Jackson, 2013). Thus simply obtaining weighted means of all collected data is inadvisable. Indeed, the first responsibility of meta-analysis is to identify poorly designed experiments or cases of under-reported results and exclude those studies lest they significantly bias the overall result (Baker and Jackson, 2013). Problematic cases of half life measurements in natural samples could arise if the initial isotope composition was not ascertained or if the study did not describe the methodology in sufficient detail to permit an appropriate vetting. Thus we propose the following criteria for inclusion in a meta-analysis of decay constants. A valid study must:

- 1) be peer reviewed and widely accessible;
- 2) describe the radioactive sample in detail, including weight and elemental and isotopic compositions;
- 3) describe the experimental apparatus in sufficient detail to assess potential analytical sources of error;
- 4) yield results with an appropriate signal/noise ratio;
- 5) not be superseded by, or included in, later results from the same laboratory; and
- 6) include measures of uncertainty derived from presented data.

While we acknowledge qualitative limitations of several of our criteria, our approach is surely preferable to having no threshold for inclusion whatsoever. Indeed, our proposal is offered as the basis of a community discussion that would lead to a consensus model rather than as canon. Note that we only provide a discussion of those published measurements that meet the

benchmark for inclusion. The specific bases for rejecting specific studies are provided in the online supplement.

## 2.2 Statistical Model

Since our goal is to combine the measurements of multiple studies, we first evaluate which model best fits the problem at hand. Weighted averages (or a fixed effect model) are commonly used in geochronology to calculate the best age based on repeated measurements, where weights reflect measurement uncertainties only. However, a weighted average is only strictly valid for the case of a single, homogenous population (i.e., MSWD  $\equiv$  1). A more appropriate statistical model would permit an estimate of the overall study heterogeneity to adjust the weight of each study. This approach is called a random effects model (Cochran, 1937), where weights are chosen based on both intra-study variance ( $\sigma$ ) and the disagreement among studies ( $\tau$ ). The weighting ( $W$ ) for each study used in this work is given by

$$W = \frac{1}{\sigma_i^2 + \tau^2} \quad (1)$$

where  $\sigma_i^2$  is the variance from each study and  $\tau^2$  is the same for all studies within one decay system. In order to calculate the parameter  $\tau^2$ , we use the approach of (Mandel and Paule, 1970) where the difference of each study from the weighted average is compared to the uncertainty of that study. When the spread of studies is less than or equal to that expected from the experimental variance, then  $\tau^2 = 0$  (thus returning a weighted mean). Note that when the dispersion is large,  $\tau^2 > 0$ . Our calculations were performed using the R statistical software (R Core Team, 2013) with the Meta package (Schwarzer, 2013).

## 2.3 Scaled Errors Versus Added Effect Model

The Particle Data Group calculates a weighted average and associated uncertainty based on the scaled variances of each study, where the scale factor reflects study heterogeneity (Particle Data Group, 2012). This model differs from the additive random effects model in that the relative weighting between studies is unchanged when uncertainties are scaled. Baker and Jackson (2013) compared the two models by changing the weighting ( $W'$ ) to:

$$W' = \frac{1}{\sigma_i^2 + \tau^2 + \sigma_i^{2\theta}} \quad (2)$$

where  $\theta$  is a free parameter that is determined by maximizing the log-likelihood function. This scaling reduces to an additive model when  $\theta = 0$  and a multiplicative model when  $\theta = 1$ . Baker and Jackson (2013) evaluated fifteen particle physics datasets and found that they were best fit by  $\theta \approx 0.22$ . This value is sufficiently close to 0 to conclude that the random effects model is superior to that of scaled uncertainties. We performed a similar test on the three decay constant datasets ( $^{87}\text{Rb}$ ,  $^{176}\text{Lu}$ , and  $^{235}\text{U}$ ) that contained sufficient measurements to permit the calculation (Fig. A.1) and come to a similar conclusion to Baker and Jackson (2013). Thus we chose to proceed using the traditional random effects model rather than pioneer a hybrid methodology that would have only marginal impact on the calculated decay constants and their associated uncertainties.

## 2.4 Interpreting Study Heterogeneity

As noted earlier, reporting a mean and standard deviation for combined data sets does not incorporate the fundamentally important knowledge of study disagreement beyond that expected from internal statistics (Higgins et al., 2009). As an intuitive aid to the calculations, we present a “forest” plot (Ioannidis et al., 2008) for each decay constant analysis that permits visual

inspection of study heterogeneity. Also included is a summary statistic,  $I^2$ , which is the percentage of the variance of the combined result from the disagreement between the studies that can be assigned to each study (Higgins and Thompson, 2002).

In biomedical meta-analysis, random effects models are interpreted as including the possibility of a difference in the effect under observation among the various studies (Higgins et al., 2009). Given that decay constants are, literally, physical constants, this interpretation is inappropriate for our case. Instead, we favor the view that individual study uncertainties have been underestimated leading to standard weighted averages with underestimated uncertainties (Rukhin, 2009; Zhang, 2006).

## **2.5 Statistical Model Limitations**

As this is, to our knowledge, the first use of a Random Effects Model in geochemistry, we discuss some potential limitations of the approach. The first is that our uncertainty calculation is only statistically optimal if the data is normally distributed (Rukhin et al., 2000). Given the low number of included studies overall ( $\leq 11$ ), this is generally not independently verifiable. However, DerSimonian and Kacker (2007) note that the Mandel and Paule (1970) approach is generally more robust than other mechanisms (e.g., weighted average). The second potential limitation is that the generally low number of experimental determination of decay constants does not permit tests for bias in the published studies. An example of such is the publication bias, where new results that differ substantially from established values be suppressed from publication. However, we feel this is unlikely to be a significant problem as half life studies always produce a result (i.e., there is no null effect), and, as evidenced by the highly variable reports of the  $^{176}\text{Lu}$  half life (Fig. A.2 C), workers in this field appear unfazed

about publishing disparate values. Finally, we wish to note here that a meta-analysis is only as good as the published literature and in several cases is clearly limited by the available studies.

## **2.6 Comparisons with Previous Compilations**

Although there have been numerous summaries of half lives and associated nuclear data (e.g., Nuclear Data Sheets), the methodologies utilized in their compilation are highly variable. In some cases a weighted average is used (e.g.,  $^{53}\text{V}$ ), and in others, a single best value (e.g.,  $^{53}\text{Mn}$ ) is reported (Junde, 2009). Unfortunately, it's generally unclear why such ad hoc selections are made. In other compilations, such as Holden (1989), uncertainties are increased arbitrarily to compensate for procedural errors or the effect of significant corrections with difficult to quantify effects. In the analysis that follows, we emphasize both consistency in statistical methodology as well our earlier described criteria for study inclusion.

## **3. Results**

### **3.1 Introduction**

The preferred decay constant emerging from our meta-analysis of each geochronological system is given in Table A.1. The included studies meet the criteria set forth in section 2.1 and in only one case ( $^{238}\text{U}$ ) was there an insufficient number of investigations to perform a meta-analysis. We now examine each system in detail, discuss the level of agreement among studies, and present the calculated value of  $\lambda$  and its variance. The uncertainties stated below correspond to standard uncertainties ( $k=1$ ).

### **3.2 $^{87}\text{Rb}$**

Given the large number of accumulation, decay counting, and natural age comparison studies published of the  $\beta^-$  decay of  $^{87}\text{Rb}$  to  $^{87}\text{Sr}$ , we begin with this geochronometric system (see

supplementary materials of Rotenberg et al., 2012). However, only three of the 32 studies (Kossert, 2003; Neumann and Huster, 1974; Rotenberg et al., 2012) meet the criteria of section 2.1 (see online supplement for excluded studies). These studies are split between decay counting (Kossert, 2003; Neumann and Huster, 1974) and accumulation (Rotenberg et al., 2012; note that Davis et al., 1977 was not used for reasons discussed in the SOM). Note that we utilize a random effects model to reanalyze the results of Rotenberg et al. (2012) as our analysis requires symmetric uncertainties; we calculate a half life of  $49.579 \pm 0.026$  Ga. The meta-analysis (Fig. A.2 A) shows that there is no excess variability between the studies (i.e.,  $I^2 = 0\%$ ). Given that the agreement between studies utilizing both decay counting and accumulation is very good, we conclude the half life of  $^{87}\text{Rb}$  is  $49.579 \pm 0.026$  Ga (i.e.,  $\lambda = 1.398 \times 10^{-11}/\text{yr}$ ).

### 3.3 $^{147}\text{Sm}$

Five of the sixteen studies of the  $\alpha$  decay of  $^{147}\text{Sm}$  to  $^{143}\text{Nd}$  (Donhoffer, 1964; Gupta and MacFarlane, 1970; Kossert et al., 2009; Su et al., 2010; Wright et al., 1961) meet section 2.1 criteria. While they all utilized some form of decay counting, three used a liquid scintillation detector (Donhoffer, 1964; Kossert et al., 2009; Wright et al., 1961), Gupta and MacFarlane (1970) used an ionization chamber, and Su et al. (2010) a silicon barrier detector. As shown in Figure A.2 B, there is excellent agreement between studies and, in this case, the random effects model collapses to a fixed effect model (i.e.,  $\tau^2 = 0$ ). Given the agreement between these five studies as well as the variety of methods used, we conclude that the half life of  $^{147}\text{Sm}$  is  $106.44 \pm 0.6$  Ga (i.e.,  $\lambda = 6.515 \times 10^{-12}/\text{yr}$ ).

### 3.4 $^{176}\text{Lu}$

Our meta-analysis of the  $\beta^-$  decay of  $^{176}\text{Lu}$  to  $^{176}\text{Hf}$  included nine published studies (Dalmaso et al., 1992; Gehrke et al., 1990; Grinyer et al., 2003; Komura et al., 1972; Kossert et al., 2013; Nir-El and Haquin, 2003; Norman, 1980; Prodi et al., 1969; Sguigna et al., 1982), all of which were by decay counting. This decay system is particularly challenging to measure experimentally because of the low and variable energy of the escaping electron. Several studies have attempted to circumvent this difficulty by measuring one or more of the emergent  $\gamma$  rays emitted during decay (e.g., Grinyer et al., 2003). These studies are further limited by self-absorption and attenuation effects, coincidence summing ambiguities, and the fact that not every decay emits a  $\gamma$  (and thus knowing the probability of a  $\gamma$  of a certain energy being produced is key; Ott et al., 2012). In light of these difficulties, it is unsurprising that there is significant scatter among these studies (Fig. A.2 C) that is above that expected from the stated uncertainties. Indeed, virtually all of the overall error ( $I^2 = 97\%$ ) derives from interstudy heterogeneity with a calculated half life for  $^{176}\text{Lu}$  of  $37.49 \pm 0.88$  Ga (i.e.,  $\lambda = 1.85 \times 10^{-11}/\text{yr}$ ).

### 3.5 $^{230}\text{Th}$

Two counting studies of the  $\alpha$  decay of  $^{230}\text{Th}$  to  $^{226}\text{Ra}$  (Attree et al., 1962; Meadows et al., 1980) meet our criteria for inclusion. While there is excellent agreement (Fig. A.2 D) between the two studies ( $I^2 = 0\%$ ), their limited number and similar methodologies leave open the possibility that future variance could be documented. We calculate a half life for  $^{230}\text{Th}$  of  $75,375 \pm 290$  years (i.e.,  $\lambda = 9.196 \times 10^{-5}/\text{yr}$ ).

### 3.6 $^{232}\text{Th}$

The  $\alpha$  decay of  $^{232}\text{Th}$  to  $^{228}\text{Ra}$  has been measured six times but only three of those studies (Farley, 1960; Macklin and Pomerance, 1956; Senftle et al., 1956) meet our criteria for inclusion

(see online supplement). Unfortunately, as with the other decay systems, one study (Farley, 1960) is significantly more precise than the rest limiting our ability to internally verify the result (Fig. A.2 E). The half life we calculate for  $^{232}\text{Th}$  is  $14.13 \pm 0.13$  Ga (i.e.,  $\lambda = 4.92 \cdot 10^{-11}/\text{yr}$ ).

### 3.7 $^{235}\text{U}$

For the  $\alpha$  decay of  $^{235}\text{U}$  to  $^{231}\text{Th}$ , four (Deruytter and Wegener-Penning, 1974; Fleming et al., 1952; Jaffey et al., 1971; White et al., 1965) studies are available for examination (section 2.1). While Jaffey et al. (1971) noted a “slight source of drift” in the  $\lambda_{235}$  measurements, the p-value of  $\sim 0.06$  that they ascertained is not significant at the currently accepted level of 0.05 (Fisher, 1925). Because  $^{231}\text{Th}$  has a half life of 26 hours, simple accumulation studies are not possible. However, the availability of highly enriched  $^{235}\text{U}$  and its short half life relative to  $^{238}\text{U}$  suggests the potential for decay counting experiments of superior precision and accuracy. Unfortunately, we detect study heterogeneity ( $I^2 \sim 45\%$ ) with the weighting dominated by Jaffey et al. (1971) result. Thus while we are able to calculate a half life of  $702.5 \pm 5.2$  Ma (i.e.,  $\lambda = 9.867 \cdot 10^{-12}/\text{yr}$ ), the need for more experiments to further verify and refine the  $^{235}\text{U}$  decay constant (Fig. A.2 F) is clear.

### 3.8 $^{238}\text{U}$

The  $\alpha$  decay of  $^{238}\text{U}$  to  $^{234}\text{Th}$  is pivotal to current geochronological practice. Schön et al. (2004) reviewed experimental determinations of  $\lambda_{238}$  but did not apply objective criteria for study inclusion when calculating recommended values. Unfortunately, only the study of Jaffey et al. (1971) meets the section 2.1 criteria. Three of the published works (Kovarik and Adams, 1938; Schiedt, 1935; Steyn and Strelow, 1960) do not address whether  $^{234}\text{U}/^{238}\text{U}$  was in equilibrium, while the Kienberger (1949) study did not provide adequate analytical details to assess the

reliability of their measurement. Although previous authors have expressed concern over the paucity of reliable U decay studies (Begemann et al., 2001; Mattinson, 2000; Schön et al., 2004), we suggest that this limitation is far more significant than previously expressed. In order to perform a meta-analysis or any verification of the accepted value, a priority for the geochronological community is support of new, high precision and accuracy measurements.

## **4. Discussion**

### **4.1 Revision of Accepted Values**

After eliminating studies for which insufficient details are provided (section 2.1) we have combined the results in a random effects model that weights studies both by their uncertainties as well as interstudy heterogeneity. The advantage of this approach is that when several studies agree (e.g.,  $^{147}\text{Sm}$ ) the combined result is more precise, and provides greater confidence, than any individual study. When there is substantial disagreement, (e.g.,  $^{176}\text{Lu}$ ), the overall uncertainty needs to be increased. Using this approach, we found preferred geochronological decay constants in most cases at variance with those used both by convention (i.e., Steiger and Jäger, 1977) and inter-decay-system comparison (e.g., Patchett and Tatsumoto, 1980). In two important cases there is either insufficient data ( $^{238}\text{U}$ ) or insufficient data on branched decay ( $^{40}\text{K}$ ) to meet the requirements of meta-analysis.

### **4.2 Uranium Decay Constants**

The decay of U to Pb has grown to be the most widely used decay system for geochronology (Schoene, 2014). Despite its popularity, decay constants for  $^{238}\text{U}$  and  $^{235}\text{U}$  have not been re-measured since Jaffey et al. (1971) although analytical capabilities have vastly improved over the intervening 43 years. The high intrinsic precision of ID-TIMS U-Pb zircon

dating (e.g., Schoene , 2014) has attracted users of other decay systems to calibrate their parent decay rate to that of  $^{238}\text{U}$  (e.g., Hurford and Green, 1983; Kwon et al., 2002; Mattinson, 2000). As noted above, we are only able to substantiate use of one  $^{238}\text{U}$  decay study for meta-analysis and four for  $^{235}\text{U}$ . It is at least arguable that until the  $^{238}\text{U}$  decay constant is re-measured through laboratory experiment, other geochronological systems should be calibrated to  $^{235}\text{U}$  rather than  $^{238}\text{U}$  (i.e., hold  $\lambda_{235}$  constant and adjust  $\lambda_{238}$  to achieve concordance of robust U-Pb zircon standards).

### **4.3 Geochronology Data Group**

Since decay constants are of foundational importance to geochronology, it is imperative that the values in use be the best available. This requires continuing assessment. That there has not been an update to the decay constant convention of 1976 underscores the lack of benefit that the geochronology community has gained from increasingly sophisticated experimental work. We propose the formation of an international group that regularly examines published experimental decay constant measurements, combines them through meta-analysis, and publishes the community consensus. Whether this arises directly from international cooperation among geochronologists or led by the International Council for Science organizations is a matter for discussion informed by past experience.

### **4.4 Age of Fish Canyon Tuff**

The Fish Canyon Tuff (FCT) is a voluminous ignimbrite sheet erupted over a relatively short period during the late Oligocene within the San Juan volcanic field, southern Colorado (Lipman et al., 1970). It appears to satisfy many of the criteria for an ideal dating standard material in that the rock is easily accessible and has a broad assemblage of unaltered and datable

modal and accessory minerals, including plagioclase, sanidine, biotite, hornblende, titanite, apatite and zircon. Steven et al. (1967) found that the phenocryst assemblage plotted on a  $27.9 \pm 0.7$  Ma K-Ar isochron (recalculated using the decay constants and isotopic abundances of Steiger and Jaeger, 1977). On this basis, Naeser et al. (1981) proposed apatite and zircon from the Fish Canyon Tuff as a fission track dating standard (cf. Galbraith 1986) and these and other phases, including sanidine, have been investigated for use as inter- and intra-laboratory standards using the  $^{40}\text{Ar}/^{39}\text{Ar}$ , (U-Th-Sm)/He and U-Pb methods (Bachmann et al., 2007, 2002, 2000; Baksi et al., 1996; Carpena and Mailhe, 1987; Cebula et al., 1986; Dazé et al., 2003; Dobson et al., 2008; Hurford and Hammerschmidt, 1985; Jourdan and Renne, 2007; Kohn et al., 2014; Kuiper et al., 2008; Lanphere and Baadsgaard, 2001, 1997; Lanphere and Dalrymple, 2000; Lanphere, 2004; Lipman et al., 1997, 1970; Oberli et al., 2002, 1990; Reiners and Farley, 1999; Reiners et al., 2002; Renne et al., 2011, 2010, 1998, 1994; Schmitz and Bowring, 2001; Schmitz et al., 2003; Schwarz et al., 2011; Spell and McDougall, 2003; Tagami et al., 2003).

Because of the difficulty of quantitatively extracting Ar from sanidine, even at temperatures well above melting, its age is usually determined by comparison with primary K-Ar standards (e.g., Jourdan and Renne, 2007). In recent years, numerous decay constants for  $^{40}\text{K}$  have been proposed which are mutually inconsistent outside of their respective quoted uncertainties (e.g., Kuiper et al., 2008; Renne et al., 2010). As an additional uncertainty, there remains an unexplained discrepancy between a 27.5 Ma Rb-Sr isochron (Lanphere and Baadsgaard, 2001) and the proposed U-Pb zircon age of 28.5 Ma (Schmitz and Bowring, 2001).

Clearly we cannot take full advantage of recent analytical developments permitting high-precision U-Pb (and  $^{40}\text{Ar}/^{39}\text{Ar}$ ) geochronology using obsolete decay constants. We recalculated

the Rb-Sr and U-Pb ages for the Fish Canyon Tuff of Lanphere and Baadsgaard (2001) and (Schmitz and Bowring (2001) using the  $\lambda$  values of Table A.1 and arrive at  $27.8 \pm 0.2$  Ma and  $28.5 \pm 0.1$  Ma, respectively. While this narrows the gap, the discrepancy is still larger than the assigned uncertainties. A further complication of using U-Pb zircon ages to date volcanic eruption of is that magmatic zircons can predate eruption by  $>500$  ka (Reid et al., 1997; see review in Schmitt, 2011). Indeed, while the U-Pb zircon analyses of Schmitz and Bowring (2001) yielded MSWD = 0.7, and were interpreted as a single age population, increasingly precise U-Pb measurements led to steadily increasing MSWDs. The data of Bachmann et al. (2007) yield an age spread with MSWD = 3 while the recent data of Wotzlaw et al. (2013) yield an MSWD = 64. This appears to underscore the conclusion of Reid et al. (1997) that zircons can form in magmas and quantitatively retain radiogenic Pb for many hundreds of thousands of years. One approach then would be to assume that the youngest  $^{207}\text{Pb}/^{235}\text{U}$  zircon age best approximates eruption and then apply our calculated decay constant. Although the data we note above (i.e., Bachmann et al., 2007; Schmitz and Bowring, 2001; Wotzlaw et al., 2013) are associated with very different measurement blank and analytical qualities, they present a range of minimums from 28.0 to 28.2 Ma which is consistent with the Rb-Sr isochron age (Lanphere and Baadsgaard, 2001) which, by its nature, is free of pre-eruption memory (cf., Halliday et al., 1989). Note that this range is younger than ages proposed for  $^{40}\text{Ar}/^{39}\text{Ar}$  sanidine using essentially ad hoc  $^{40}\text{K}$  decay constants (Kuiper et al., 2008; Renne et al., 2010) but agrees with the Fish Canyon sanidine age determined via  $^{40}\text{Ar}/^{39}\text{Ar}$  intercalibration using standards whose ages were determined by ab initio K-Ar dating (i.e., absolute measurements of both K and Ar)

coupled with the conventional  $^{40}\text{K}$  decay constant and branching ratio (Jourdan and Renne, 2007).

## 5. Conclusion

We compiled, systematically analyzed, and assigned uncertainties for decay constant (and thus half life) measurements of  $^{87}\text{Rb}$ ,  $^{147}\text{Sm}$ ,  $^{176}\text{Lu}$ ,  $^{230}\text{Th}$ ,  $^{232}\text{Th}$ ,  $^{235}\text{U}$ , and  $^{238}\text{U}$ . The range of agreement between different experimental values varies from excellent (i.e.,  $^{147}\text{Sm}$ ) to poor (i.e.,  $^{176}\text{Lu}$ ). In the case of  $^{238}\text{U}$ , only one study met the criteria for inclusion and thus caution should be taken using its half life as a basis for widespread comparison to other geochronometers. For the purposes of age comparison, it would appear that, given the larger number of studies and their good agreement, the  $^{235}\text{U}$  decay constant should instead form the basis of any scheme to adjust decay constants in light of results from natural samples. However, rather than leading to diminished uncertainties associated with  $\lambda_{235,238}$ , this proposal would increase the  $\lambda_{235}$  uncertainty by 50% above that reported by Jaffey et al. (1971).

Attempts to inter-calibrate geochronologic systems using coexisting phases from the Fish Canyon Tuff have proven problematic due to contrasting petrologic and kinetic controls. Our analysis suggests that an eruption age between 28.0 and 28.2 Ma is consistent with both current knowledge of decay constants and the contrasting behavior of the various mineral systems used (e.g., retention of daughter product at magmatic temperatures).

In this paper, we emphasize introduction of a methodology for systematically combining published decay constant data over advocating specific new decay constant values. Indeed, our analysis leads to the conclusion that numerous additional experimental decay constant

investigations are required before any new decay constant convention for a geochronologically significant nuclide be adopted.

Clearly, current knowledge of  $\lambda$  for many radiometric systems is the limiting parameter to achieving absolute age accuracies of better than ca. 1%. While much useful research can be undertaken knowing only relative age differences within a single decay system (e.g., Schoene et al., 2012), to truly achieve  $\pm 0.1\%$ , inter-decay system, absolute time accuracy requires significantly improved experimental determinations of  $\lambda$ . This cannot occur if we continue to anchor 21<sup>st</sup> century geochronology to often incomplete, 1970s-era nuclear physics reports. What our community appears to lack is the confidence to directly acquire fundamental new knowledge of decay constants with significantly improved precision and accuracy using the best contemporary facilities and to continuously refine knowledge of decay constants using objective measures of combination. The moment calls for a forging of new relationships across disciplinary boundaries to attain the next generation of geochronological accuracy that will drive future scientific breakthroughs.

Parent Isotope	Half Life	Standard Uncertainty	Units	Relative Standard Uncertainty (%)
$^{87}\text{Rb}$	49.579	0.026	Ga	0.05
$^{147}\text{Sm}$	106.44	0.6	Ga	0.56
$^{176}\text{Lu}$	37.49	0.88	Ga	2.35
$^{230}\text{Th}$	75,375	290	a	0.38
$^{232}\text{Th}$	14.13	0.13	Ga	0.92
$^{235}\text{U}$	702.5	5.2	Ma	0.74

**Table A.1:** Summary of half lives calculated in this study.

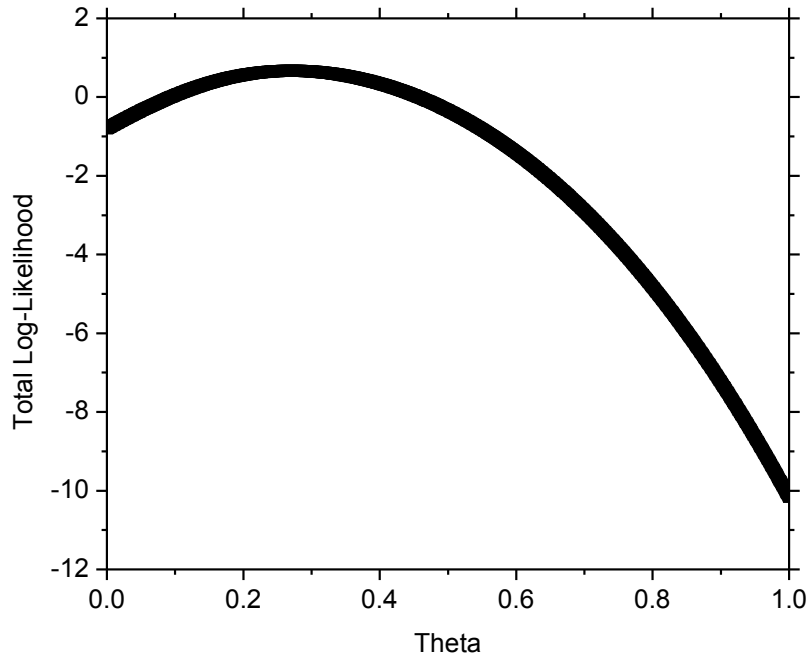
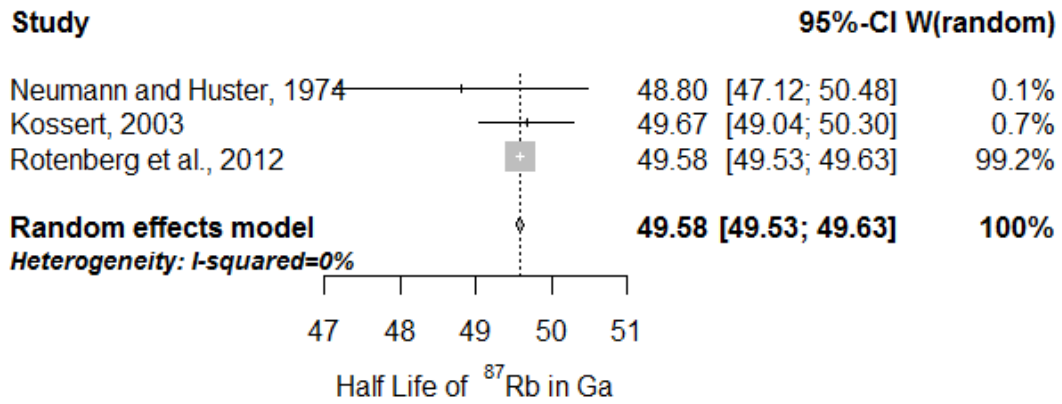
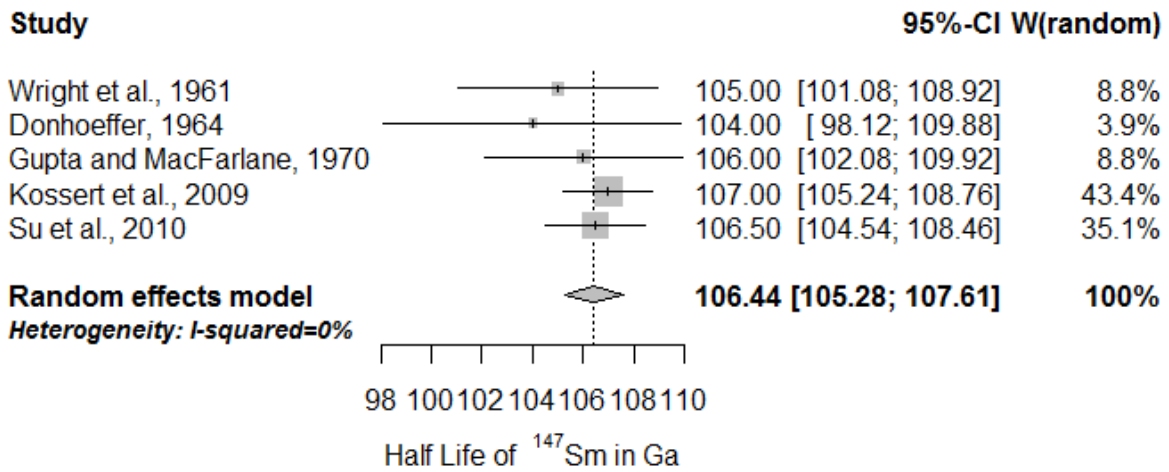


**Figure A.1:** Comparison of scaled errors ( $\theta = 1$ ) and a random effects model ( $\theta = 0$ ). Three decay systems were included in this analysis ( $^{87}\text{Rb}$ ,  $^{176}\text{Lu}$ , and  $^{235}\text{U}$ ). The maximum of the log-likelihood function is the model that best fits the data. We chose to use a random effects model given that it is a well established technique and close to the optimal fit for the data.

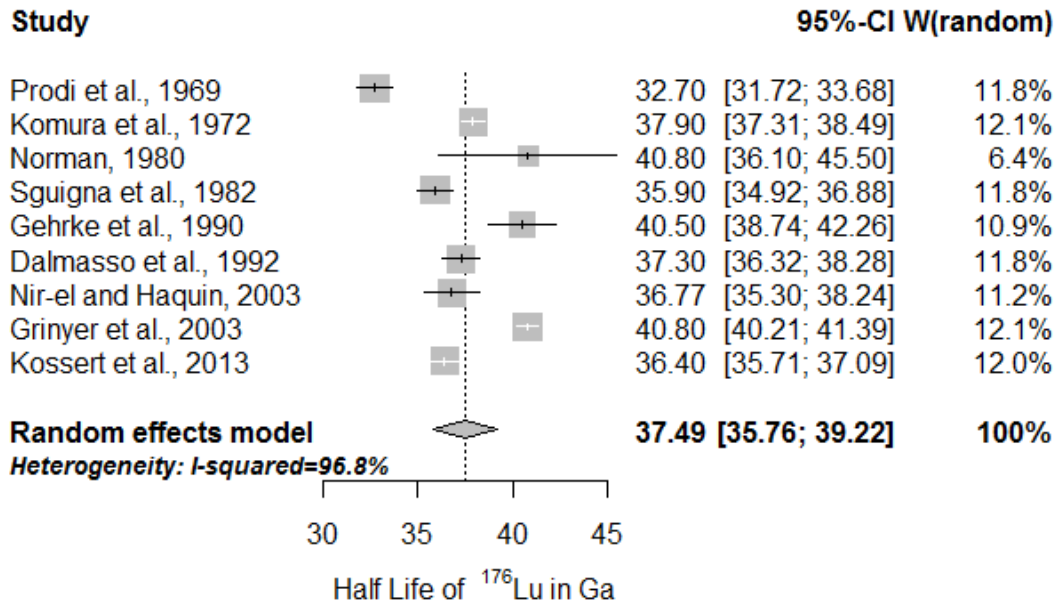
A)



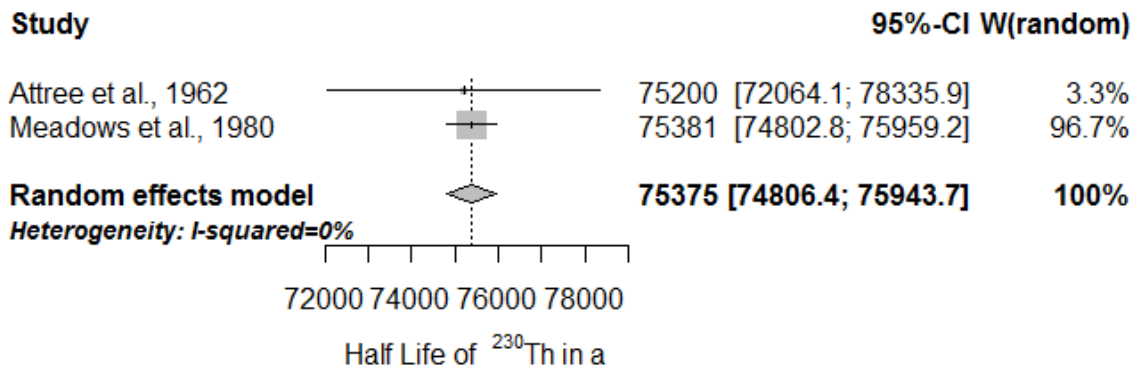
B)



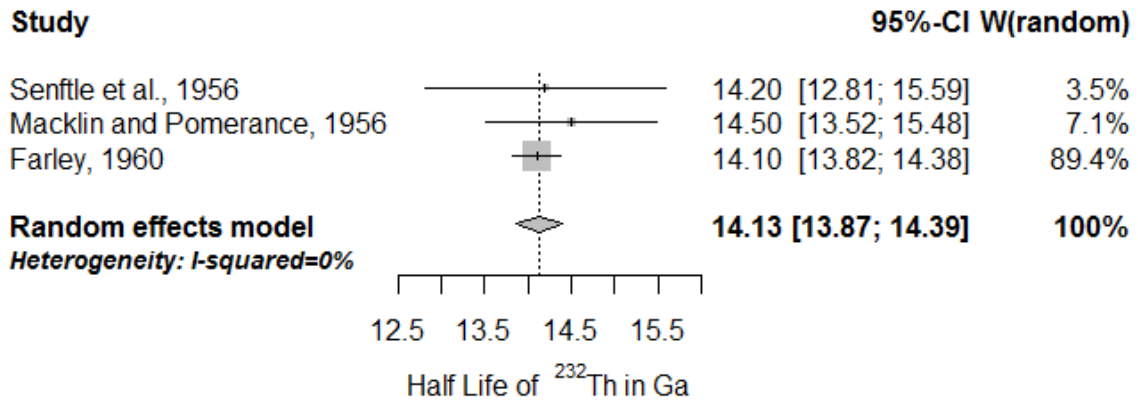
C)



D)



E)



F)

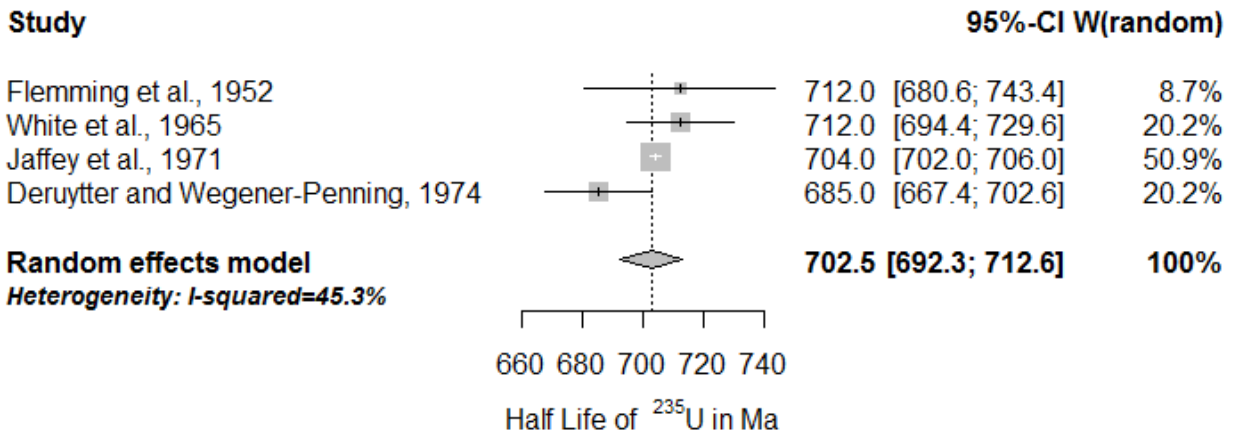


**Figure A.2:** Forest plots for our meta-analysis of the half life of  $^{87}\text{Rb}$ ,  $^{147}\text{Sm}$ ,  $^{176}\text{Lu}$ ,  $^{230}\text{Th}$ ,  $^{232}\text{Th}$  and,  $^{235}\text{U}$  (A-F). Note the range of agreement from excellent ( $^{147}\text{Sm}$ ) to poor ( $^{176}\text{Lu}$ ). The

numbers given in brackets are the 95% confidence interval for each study and the calculated value (in bold) and the numbers followed by the % sign are the weights for each study.

## **Appendix B: Zircon U/Th Model Ages in the Presence of Melt Heterogeneity**

### **Abstract**

In situ U-series zircon dating has yielded unique insights into magmatic processes and the complexity of zircon crystallization. However, the approach requires some knowledge of the state of isotopic disequilibrium of the melt from which zircon crystallizes. Current practices for correcting initial  $^{230}\text{Th}$  include use of an isochron array (defined by with several coexisting zircons) or two-point isochrons based on a tie between each zircon with a common glass (or whole rock) measurement. However, magmas are complex and measured U/Th in zircons from a single extrusive can vary by up to a factor of seven, casting doubt on the assumption that a single glass composition is representative of the magma from which each zircon crystallized. We propose a correction scheme using the measured zircon  $^{238}\text{U}/^{232}\text{Th}$ , a U/Th partition coefficient ratio between zircon and melt, and the observation that most magmas are within 15% ( $1\sigma$ ) of the equiline. Using this correction scheme, we show that uncertainties can be underestimated by up to a factor of three and that published dates are potentially biased towards older ages.

### **1 Introduction**

Detailed insights into magmatic processes require high-temperature and -spatial resolution chronometers with age resolutions of thousands to tens of thousands of years. Two systems that meet these criteria are U-Pb isotope dilution-thermal ionization (ID-TIMS; Barboni and Schoene, 2014) and in-situ U-series disequilibrium (Reid et al., 1997) zircon dating. While recent advances in precision

and accuracy of ID-TIMS U-Pb dating of very young zircons have been significant (e.g., Schoene, 2014), the time-intensive nature of the method limits its widespread application and/or the size of data sets. By contrast, in-situ U-series dating, either by secondary ion mass spectrometry (Reid et al., 1997) or laser ablation inductively coupled mass spectrometry (Bernal et al., 2014), requires minimal sample preparation permitting data output at a high rate. For zircons younger than the time over which secular equilibrium is achieved ( $\sim 400$  ka; Allegre and Condomines, 1976), in situ disequilibrium dating has provided unparalleled insights into magmatic timescales and the complexities of zircon crystallization. Indeed, the first application of this approach (Reid et al., 1997) showed that volcanic zircons typically crystallize well prior to eruption when the phase becomes saturated in the magma (Watson and Harrison, 1983; Boehnke et al., 2013), potentially over half a million years prior to the time of eruption (Wotzlaw et al., 2014). Other applications of this method include dating very young volcanism (Schmitt et al., 2013; Wright et al., 2015) and determining the provenance and nature of archeological materials and sites (Coffey et al., 2014; Schmitt et al., 2014).

Disequilibrium dating using  $^{230}\text{Th}$  exploits both the relatively short half-life ( $\sim 75.5$  ka; Cheng et al., 2013) and the strong fractionation of U from Th during zircon growth. Upon crystallization,  $^{230}\text{Th}$  ingrows from the decay of  $^{238}\text{U}$ , slowly erasing the initial  $^{230}\text{Th}$  deficit until secular equilibrium is attained. Since typically only one phase (i.e., zircon) is analyzed for in-situ U-Th dating methods, as opposed to the associated whole rock, one of the major challenges in calculating accurate ages from the measurements of  $^{230}\text{Th}$ ,  $^{232}\text{Th}$  and,  $^{238}\text{U}$  in zircon is determining the

initial  $^{230}\text{Th}/^{232}\text{Th}$  [ $(^{230}\text{Th}/^{232}\text{Th})_0$ ]. In the case of in situ zircon U-series disequilibrium dating, use of an isochron array is not possible in general due to the lack of other phases with differing U/Th for which it can be clearly established that they are crystallizing concurrently and have sufficiently high U and Th concentrations to permit in-situ analyses. This limitation also holds for U-Pb zircon dating, but the highly radiogenic nature of most signals permits non-radiogenic daughter subtractions using an assumed value (e.g., lab blank for TIMS or modern Pb for SIMS; Schoene, 2014; Ireland and Williams, 2003). This method is only viable if the half-lives of the daughter isotopes are much longer than the timescales of interest. In a similar way, U-series zircon disequilibrium dating uses two analogous methods for correcting  $(^{230}\text{Th}/^{232}\text{Th})_0$ . The first is use of an ‘isochron’ (as defined in Schmitt, 2011), a linear regression through multiple zircon data in which the slope is proportional to age. The key difference in disequilibrium dating to a traditional isochron is that zircon crystallization or another fractionating mechanism must be changing the melt U/Th significantly in order to create a spread in the zircon U/Th (U/Th always refers to  $^{238}\text{U}/^{232}\text{Th}$ ) results (Fig. B.1 A and B show an idealized case). In contrast, a traditional isochron uses multiple phases with different partition coefficients to create a spread in the parent/daughter. For the ‘isochron’ approach to yield a useful date, the zircons must crystallize relatively rapidly, thus the ‘isochron’ is limited in application to cases where zircons crystallized in discrete batches (e.g., Fig. 2a in Schmitt, 2011).

The second  $(^{230}\text{Th}/^{232}\text{Th})_0$  correction scheme is to measure a sample of glass (or whole rock) and assume that it was in equilibrium with each zircon (i.e., each

date is calculated from a two-point zircon-glass isochron; Reid et al., 1997). This approach has two key requirements: 1) that the magma is chemically homogeneous and 2) the magma is in equilibrium between the production and loss of  $^{230}\text{Th}$  (i.e., on the equiline). The second assumption has to be made because otherwise the melt value has to be age corrected for each zircon isochron, however this is not possible as the age for the correction is not known a priori. Therefore, using melts that are not in secular equilibrium biases age determinations. For further detail we refer the reader to Schmitt (2011).

However, melts by their very nature change composition throughout the magmatic process (e.g., Bachmann and Bergantz, 2004; Schmitt, 2011). Previous workers have argued that these changes are minor (Reid et al., 1997; Schmitt, 2011) due to the generally high U/Th of zircon in relation to the melt (i.e., that variations in  $(^{230}\text{Th}/^{232}\text{Th})_0$  lead only to minor corrections). The basis of this assumption is the claim that higher U/Th zircons have a correspondingly higher fraction of  $^{230}\text{Th}$  from radiogenic ingrowth compared to low U/Th zircons (Reid et al., 1997).

However, as zircon has an essentially fixed ratio of U and Th partition coefficients ( $K_{\text{zir/melt}}^{U/\text{Th}} \sim 6$ ; Schmitt, 2011), a high U/Th zircon must have crystallized from a high U/Th melt and vice versa. A high U/Th magma will also have a higher  $^{230}\text{Th}/^{232}\text{Th}$  than a low U/Th magma because  $^{230}\text{Th}/^{232}\text{Th}$  directly tracks U/Th, even on short (10's of thousands of years) timescales. This system stands in contrast to those involving longer half-lives such as Rb/Sr, where  $^{87}\text{Sr}/^{86}\text{Sr}$  does not change significantly over magmatic timescales. Therefore, variations in  $(\text{U}/\text{Th})_{\text{zir}}$  could

potentially bias age determinations (see Fig. B.1 C and D for illustration) that assume that a single melt composition accurately characterizes a global  $(^{230}\text{Th}/^{232}\text{Th})_0$  due to the rapid decay of  $^{230}\text{Th}$ . Indeed such evolution in  $(\text{U}/\text{Th})_{\text{melt}}$  has been demonstrated for the Long Valley rhyolite (Heumann et al., 2002).

In order to assess the significance of magma heterogeneity on age calculation, we compiled a database of zircon U/Th. Our compilation (references cited in Fig. B.2 caption) shows variations in  $(\text{U}/\text{Th})_{\text{zir}}$  between 1 and 7 (Fig. B.2). This range of U/Th shows that the melt from which zircons crystallized was chemically heterogeneous and changing on timescales comparable to that of zircon crystallization. We explore this source of uncertainty through an alternate correction scheme where the melt is constrained to be in the proximal vicinity of the equiline through an actualistic model. We confirm the broad observations derived from U-series zircon disequilibrium dating (e.g., pre-eruptive zircon growth) but show that specific age and uncertainty determinations for zircons in geochemically complex magma chambers can be significantly misestimated.

## **2 Method**

Zircon data from the Belfond Dome, Lesser Antilles (Schmitt et al., 2010), nicely illustrate the complexities introduced by a spread in  $(\text{U}/\text{Th})_{\text{zir}}$ . Specifically, we use zircon data for samples SL-25 and SL-51 that are not in secular equilibrium (Schmitt et al., 2010). These zircons show both a large spread in U/Th and apparent age, providing a clear demonstration of our new correction scheme for zircon U/Th model ages. We also use the results for depth-profile analyses performed on zircons SL-25-35 and SL-25-38 (Schmitt et al., 2010).

## 2.1 Partition Coefficients of U and Th

Meaningful modeling of data with heterogeneous  $(U/Th)_{\text{magma}}$  requires accurate knowledge of U and Th zircon/melt partition coefficients. Selection of this parameter requires care as Luo and Ayers (2009) convincingly demonstrated the limitations of present experimental methods in determination of zircon/melt partition coefficients due to kinetic effects during crystallization (e.g., Watson, 1996). We believe that the most accurate  $D_U/D_{Th}$  is that estimated from natural samples. We used zircon and glass data from the Salton Buttes rhyolites, California (Wright et al., 2015) due to their young eruption ages and limited spread in U/Th (suggesting limited magma evolution). We supplement the data by Wright et al. (2015) by also considering the partition coefficients presented by Stelten et al. (2015). Using an unweighted average of six datasets ( $MSWD \approx 0.63$ ;  $n = 6$ ), we calculate  $K_{zircon/melt}^{U/Th} = 7 \pm 0.40$  ( $1\sigma$ ) by dividing the  $(U/Th)_{zircon}$  by  $(U/Th)_{glass}$  which is similar to the value of  $\sim 6$  suggested by Schmitt (2011). Any inaccuracies in  $K_{zircon/melt}^{U/Th}$  will present a systematic uncertainty and do not affect the calculated spread in  $(U/Th)_{\text{magma}}$  or the relative difference in ages as we use the same partition coefficients for all our calculations.

## 2.2 Variations in $(^{230}\text{Th}/^{232}\text{Th})_{\text{magma}}$

If every magmatic system evolved strictly along the equiline, then we could simply calculate each age by assuming the melt from which the zircon crystallized was in isotopic equilibrium. As we have noted from examination of numerous datasets, this appears not to be true in most cases. Thus for our model, we need to

estimate the typical variation of the melt with respect to the equiline during zircon crystallization. We compiled a database of whole rock and glass ( $^{230}\text{Th}/^{232}\text{Th}$ ) and ( $^{238}\text{U}/^{232}\text{Th}$ ) measurements to examine the natural spread in these parameters. We did not age correct our values and it is therefore possible that some values would plot further from the equiline than shown. However, as most of the rocks in our compilation are sufficiently young we do not perceive this as a significant bias. The data shows that melts can be off the equiline by up to 50% (Fig. B.3) but we calculate a standard deviation for their variance from the equiline of 15%. Glass analyses plot in a more restricted range because whole rock analyses likely include accessory phases that can significantly fractionate U from Th. For our purposes, whole rock analyses are more representative of the melt but we include glass analyses in our calculation for completeness. Assuming that this is globally representative, we use this value as an input parameter in our modeling.

### 2.3 Model

For each zircon, we calculate a  $(\text{U}/\text{Th})_{\text{magma}}$  based on knowledge of  $K_{\text{zir}/\text{melt}}^{\text{U}/\text{Th}}$  (see 2.1). From the  $(\text{U}/\text{Th})_{\text{magma}}$  we calculate a  $(^{230}\text{Th}/^{232}\text{Th})_{\text{magma}}$  using the assumption that the melt is within 15% (at  $1\sigma$ ) of the equiline (i.e.,  $^{230}\text{Th}/^{238}\text{U}_{\text{magma}} = 1 \pm 0.15$ ) and then calculate a two-point isochron date. This procedure is repeated for each zircon.

Propagating uncertainties through our new model is accomplished by a parametric bootstrap resampling method (Efron, 1979). That is, we perform each calculation 1000 times and sample the corresponding data from their uncertainties

(e.g., for the  $(^{230}\text{Th}/^{232}\text{Th})_{\text{magma}}$  we use a normal distribution with a mean on the equiline and a relative standard deviation of 15%).

Our model is implemented in Python version 3.4.2 and uses numpy (Van Der Walt et al., 2011) for the array structure and mathematical functions.

### **3 Results**

Given the broad spread of U/Th recorded by SL-25 and SL-51 zircons, there is a correspondingly broad range of calculated  $(\text{U}/\text{Th})_{\text{magma}}$  (Fig. B.4). These variations appear random for the individual zircons (open symbols, Fig. B.4) but smooth for the depth profile analyses (closed symbols, Fig. B.4).

Our modeling shows that the additional uncertainty due to the lack of knowledge regarding the U/Th of the melt typically increases the errors from 5-10% to 30% for young zircons. Further, young dates are generally biased to older ages (Fig. B.5) while older dates could be biased young. At this time, due to the high uncertainty on the melt composition, these biases are not significant at the  $2\sigma$  level. However, despite the large uncertainties, the age changes could be geologically significant. For example, the Belfond dome data (Schmitt et al., 2010) imply a gap in zircon crystallization between  $\sim 20$  ka and the eruption at  $\sim 14$  ka. Using our correction, the evidence for episodic crystallization is reduced as the  $\sim 20$  ka dates shift down to  $\sim 14$  ka, albeit with much larger uncertainties.

### **4 Discussion**

#### **4.1 Time variation or heterogeneity?**

Since it is clear that zircon crystallization is capable of rapidly altering melt U/Th, it is possible that the variance in this parameter in other systems is due to

time variation rather than heterogeneity. Indeed, Charlier and Zellmer (2000) observe temporal variations in magma U/Th in zircons from the Taupo Volcanic Zone, New Zealand. However, since the Belfond Dome lava has multiple coexisting  $(U/Th)_{\text{magma}}$  (Fig. B.3), changes in  $(U/Th)_{\text{magma}}$  would need to occur often and at rates higher than the age resolution of U-series disequilibrium dating. This finding implies that  $(U/Th)_{\text{magma}}$  is not controlled by a single dominant process (e.g., accessory phase crystallization), but appears to vary often and due to other processes. We further note that the variations in  $(U/Th)_{\text{magma}}$  among individual zircons is larger than that from the two depth-profiling analyses. This is the expected results as the depth-profiling results show that melt U/Th changes slowly, if at all, and is different between zircons. This suggests that the melt is compositionally heterogeneous and that zircons record only their local environment.

Both of these interpretations are consistent with the findings of Bourdon et al. (1994) that major and accessory phases can significantly fractionate U/Th. For example, sphene and amphibole record lower U/Th than coexisting feldspar and glass, respectively (Bourdon et al., 1994). Therefore, magmatic evolution or reheating a cold mush (Cooper and Kent, 2014) could result in both time varying and heterogeneous  $(U/Th)_{\text{magma}}$ .

#### **4.2 Changing $D_U/D_{Th}$ ?**

Given the complexities of experimentally determining zircon partition coefficients and the general lack of agreement among various studies (see review in Hanchar and van Westrenen, 2007), it is worth considering if the variations we

emphasize could be solely due to differences in partition behavior. We find this an unlikely explanation because factors such as temperature and pressure are likely to change both partition coefficients in similar ways (i.e., their ratio is unaffected; Luo and Ayers, 2009). Indeed, at constant pressure and entropy, changes in individual partition coefficients are linear in  $1/T$  such that their dependence would systematically cancel and thus not affect  $K_{zir/melt}^{U/Th}$ . Additionally U and Th are broadly similar in their geochemical behavior and melt compatibility, fractional crystallization for example does not significantly change U/Th.

One factor that could significantly influence  $D_U$  but leave  $D_{Th}$  unaffected is a change in the oxidation state from  $U^{4+}$  to  $U^{6+}$  (Burnham and Berry, 2012). While such an effect has been reported in the literature (Bacon et al., 2007), this is likely to be a minor effect for at least two reasons. First,  $U^{6+}$  is more compatible in aqueous fluids than melts and is likely to be removed from the melt (Langmuir, 1978) if fluid is present, and second,  $U^{6+}$  does not become the dominant valence state until highly oxidized conditions rarely reached in crustal magmas (Halse, 2014). Furthermore, differing  $D_U/D_{Th}$  among zircons still requires heterogeneity or temporal change in the magma chamber which casts the same doubts on the use of a single glass composition for model age calculations.

Another consideration is that U and Th compatibility strongly depends on the melt chemistry and is known to vary significantly with Al/Na (Xing et al., 2013). While the majority of the change happens equally to both  $D_U$  and  $D_{Th}$  therefore leaving  $D_U/D_{Th}$  relatively unchanged there could be effects if there were large

changes in melt composition. At present there is not enough information to assess the significance of this effect within a single magma system. It is unlikely to be significant in most situations as both the data from Wright et al. (2015) and Stelten et al. (2015) yielded similar  $D_U/D_{Th}$ .

### **4.3 Viability and comparison of model zircon U-Th disequilibrium ages**

In general, analyses of glass and whole rock samples do not lie on the equiline (Fig. B.3). Thus  $(^{230}Th/^{232}Th)_{magma}$ , even if homogeneous, must evolve over time. Our modeling shows that for magma chambers in which zircons record a spread U/Th, current approaches to calculating model ages using a single glass or whole rock composition may significantly underestimate age uncertainty and can potentially misestimate age (Fig. B.5). With our correction scheme, the biggest contributor to the uncertainty comes from our lack of knowledge of melt composition. Future refinement of this value through the analysis of more glass in each sample or focusing attention to zircons with adhering glass or melt inclusions could significantly improve the uncertainties. Although we should note that one has to establish that the adhering glass represents the melt from which the zircon crystallized. Indeed using melt inclusions to correct each zircon age is the ideal case.

Without these refinements, our findings complicate intercomparison of age distributions between samples. For example, Schmitt et al. (2010) compared zircon U/Th age distributions between different samples of the same geologic unit and argued that they record the same history. This comparison was performed through comparing the probability density functions (PDF) through a Kolmogorov-Smirnov

test (K-S test) derived from the ages and analytical uncertainties (Schmitt et al., 2010). As our modeling shows that larger uncertainties are warranted, due to the incorporation of the uncertainty in the melt composition, any peaks in the PDF will broaden and reduce the resolving power (i.e., specificity) of the K-S test. In other words, our modeling leads to an increase in the false positive rate (i.e., the rate at which one erroneously concludes two samples share a zircon crystallization history and by extension a magmatic history).

We emphasize that our findings do not cast doubt on the validity of U-series zircon disequilibrium dating as the observation of pre-eruptive zircon growth has been independently validated by U-Pb zircon dating (e.g., Barboni and Schoene, 2014; Wotzlaw et al., 2014). Indeed we are not questioning the basis of U-series disequilibrium dating, only the specific age and uncertainty determinations for zircons in geochemically complex magma chambers.

#### **4.4 Origin of Magma Heterogeneity**

Our results support previous conclusions that magma chambers are heterogeneous at the scale of a volcanic hand sample (Bachmann and Bergantz, 2004). In principle, in addition to accessory phase crystallization, two processes arise to explain a continuum of  $(U/Th)_{\text{zircon}}$  – magma mixing (Burgisser and Bergantz, 2011; Turner and Campbell, 1986) and re-melting of a cold mush (Bachmann and Bergantz, 2004). Indeed it is widely recognized that volcanic eruptions can be triggered by injections of fresh magma (e.g., Murphy et al., 1998; Pallister et al., 1992) which results in a compositional gradient across the magma chamber. These fresh injections would also raise the temperature, possibly

removing the magma from the zircon stability field (Watson and Harrison, 1983; Boehnke et al., 2013) causing zircons to dissolve and reform as the system cools. These zircons would then record the heterogeneities present in the system as it cools.

#### **4.5 Implications for Other Phases**

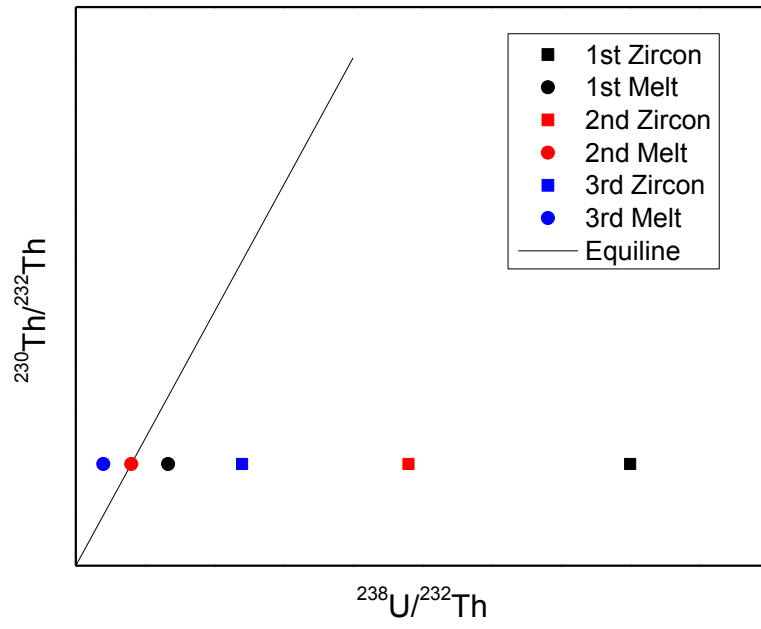
U/Th disequilibrium dating is viable in any phase that fractionates U from Th but is most useful in minerals which are closed to diffusive loss of U and Th at magmatic temperatures (Cherniak and Watson, 2003). U/Th measurements have been undertaken on co-existing feldspars, apatite, and sphene (Bourdon et al., 1994), chevkinite (Vazquez et al., 2014) and allanite (Vazquez and Reid, 2004). Our model is not specific to zircon and could be applied to understanding these different phases by using appropriate  $D_U/D_{Th}$ . However, if the phase does not strongly fractionate U/Th then the correction becomes more important to the final age calculation. It is also more complicated if one were to use a phase that prefers Th over U (e.g., monazite) as the  $(^{230}Th/^{232}Th)_0$  is more important when one is measuring the decay towards the equiline rather than the ingrowth of  $^{230}Th$ . This is mostly due to the fact that melts have  $^{230}Th/^{232}Th < \sim 3$  and therefore a regression will be very sensitive to the  $(^{230}Th/^{232}Th)_0$ . Caution is advised with minerals that do not strongly prefer U over Th, if one does not have direct measurements of the melt composition or is unable to use an isochron.

#### **5 Conclusion**

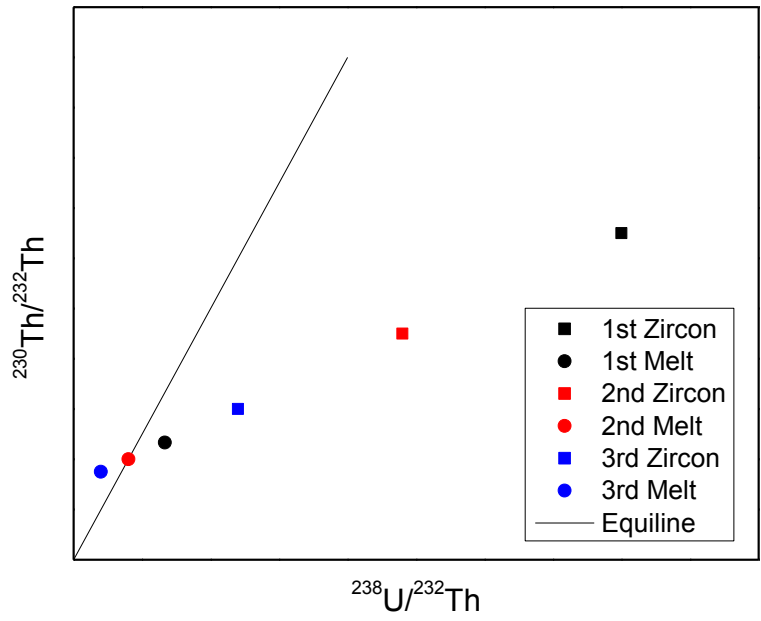
We show that assuming a single melt composition when calculating disequilibrium zircon ages in magmas with a spread in  $(U/Th)_{zircon}$  can result in

significant underestimates of age uncertainties and may yield erroneous dates. We propose a correction scheme based on knowledge that magmas are typically within 15% ( $1\sigma$ ) of the equiline when most zircons crystallize. This approach shows that published ages may have uncertainties that are underestimated by up to a factor of three. Due to the uncertainties in the melt composition, the specificity of tests comparing age distributions is reduced and thus caution is suggested when making such comparisons. Going forward, significant community effort is urged to further constrain  $(U/Th)_{\text{magma}}$  variations and improvements in the precision of zircon U-series disequilibrium dating will better allow the validity of the proposed correction scheme to be evaluated.

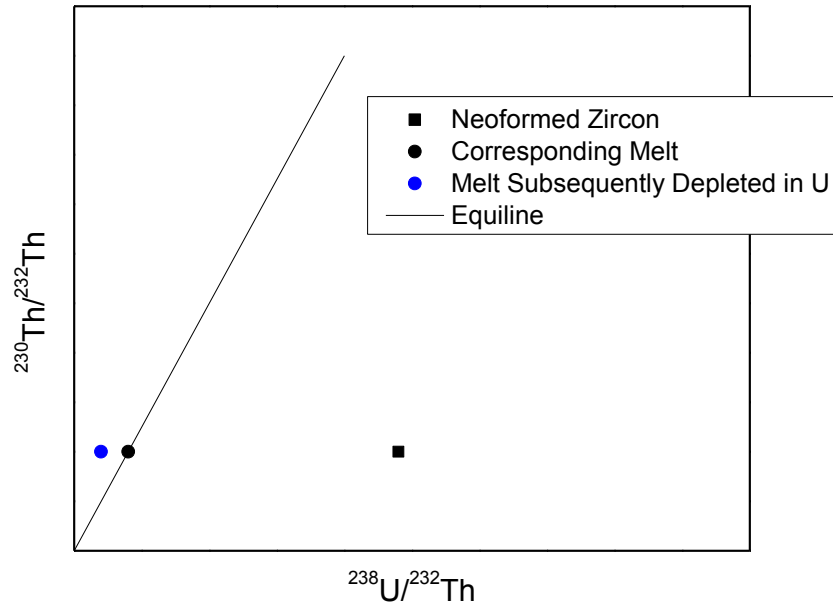
A



B



C



D

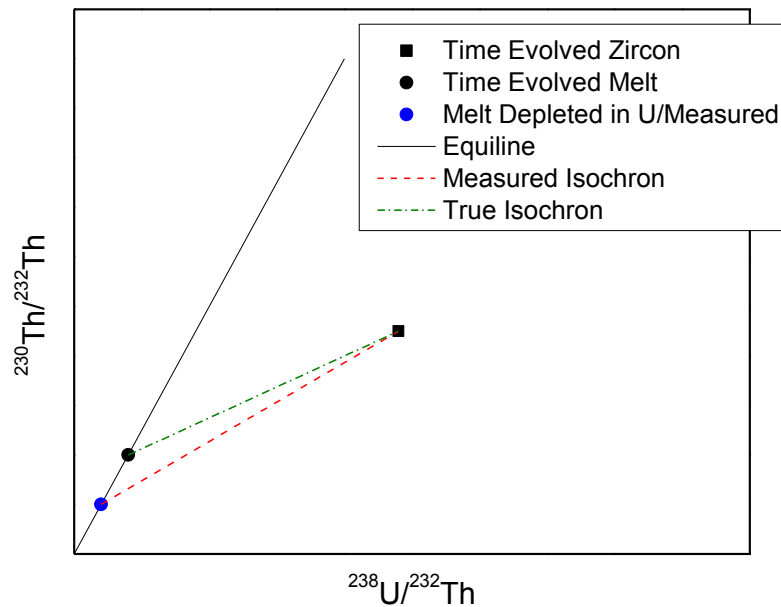


**Figure B.1:** This figure shows a cartoon of what happens when zircons crystallize at the same time and change the melt U/Th significantly. In panel A, the zircons crystallize and progressively deplete the melt in U relative to Th. Panel B shows what happens after a period of time passes and that due to the changing melt U/Th the zircons can be used to construct an isochron. Panel C shows a different example where a zircon crystallizes from a melt (black circle) and the melt composition subsequently changes (blue circle). Panel D shows what happens to the situation shown in C after some time elapses, the measured melt value (blue circle) is not representative of the melt from which the zircon crystallized and so the age inferred from an isochron is incorrect.



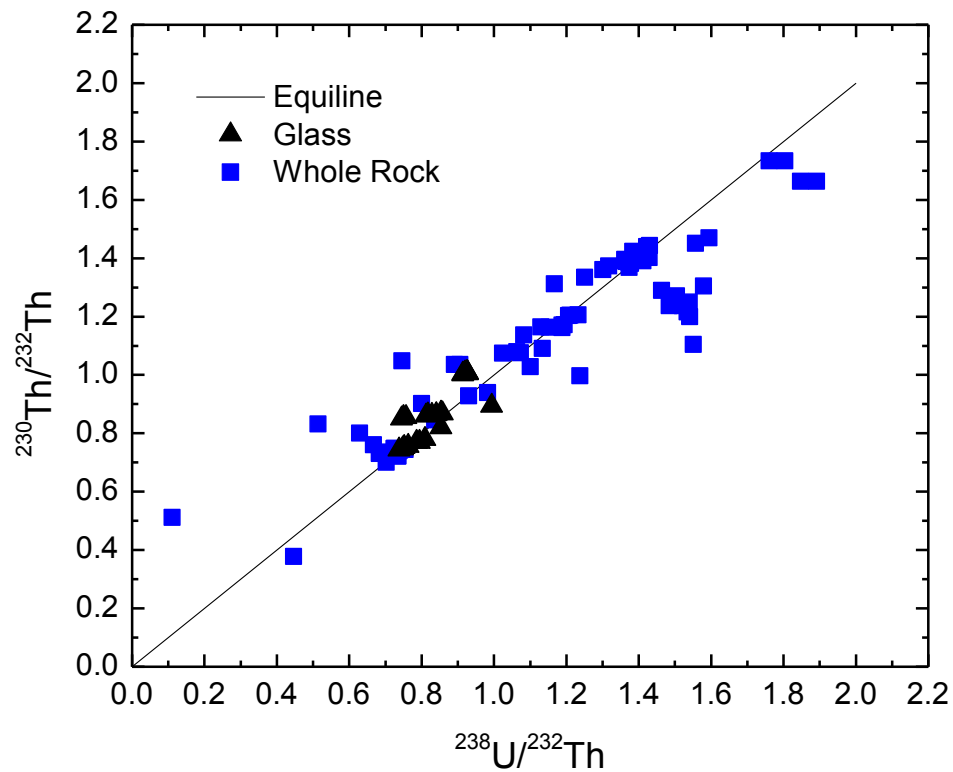
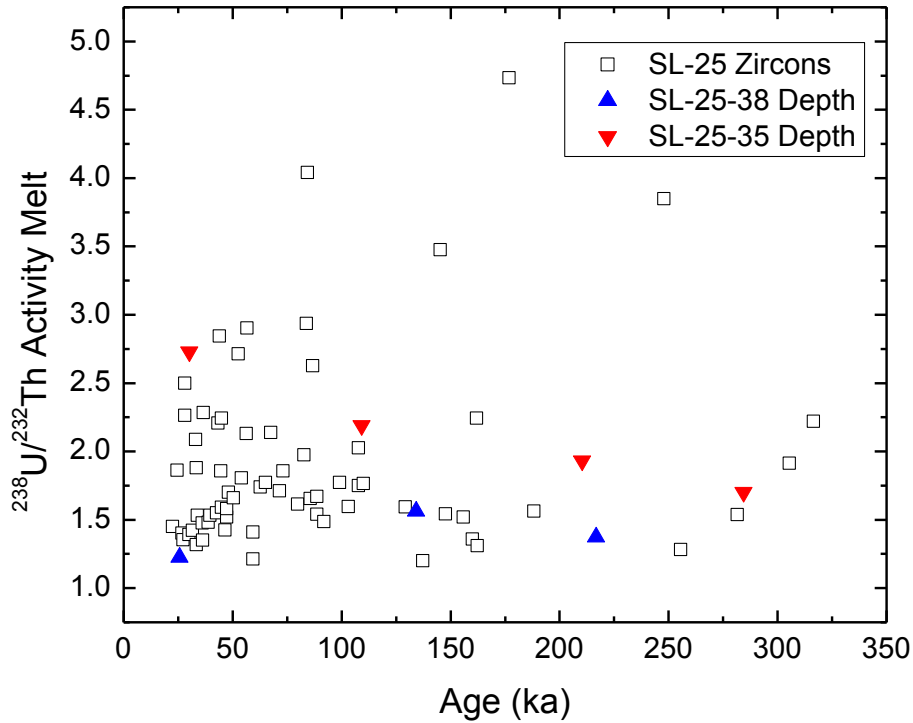
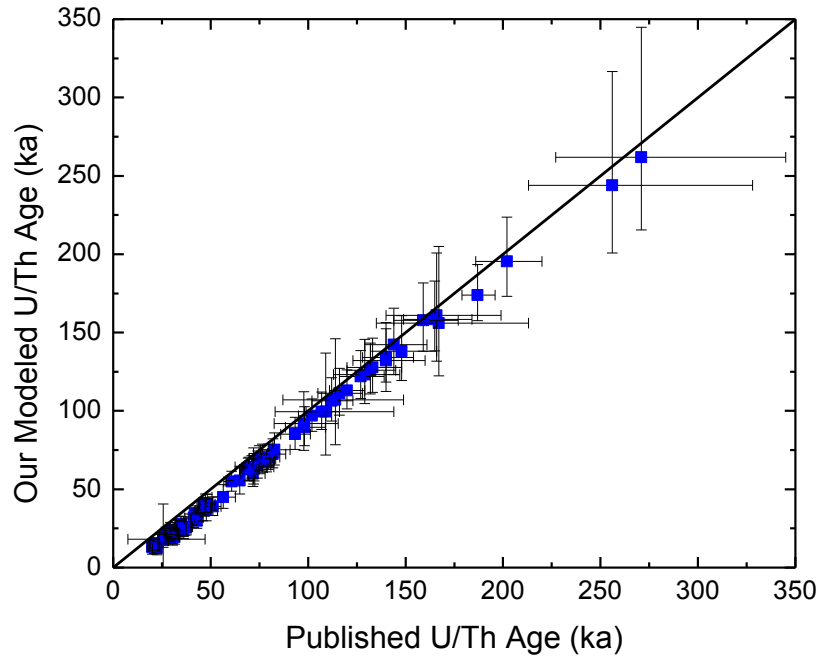


**Figure B.3:** This is a compilation of various whole rock and glass data (Bourdon et al., 1994; Charlier and Wilson, 2010; Charlier et al., 2003; Reagan et al., 2003; Reid et al., 1997; Turner et al., 1996; Vazquez and Lidzbarski, 2012; Wright et al., 2015; Zou et al., 2010) showing that magmas are generally not on the equiline, suggesting rapid changes in  $(\text{U}/\text{Th})_{\text{Magma}}$ .



A)



B)

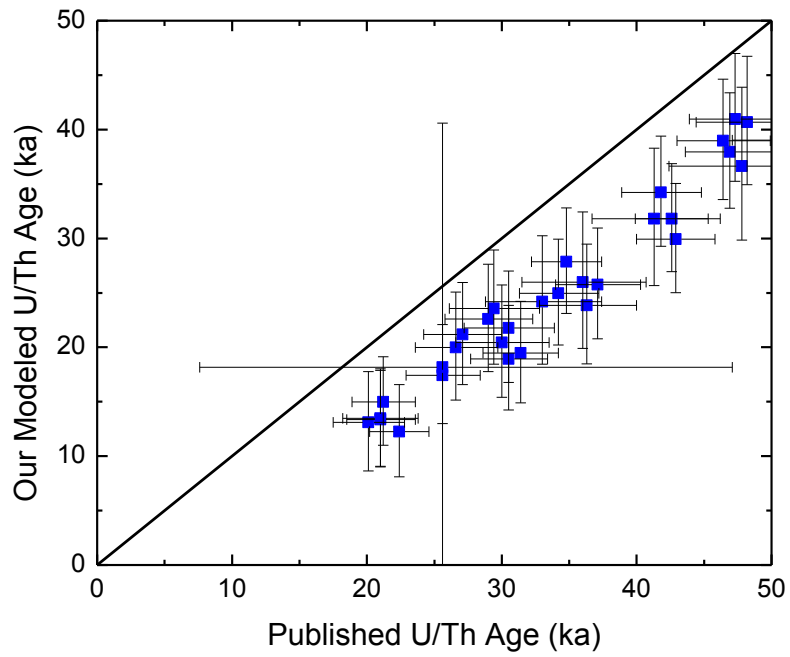


**Figure B.5:** This figure shows an age comparison between our model results and the published model ages as a function of the published ages for each zircon. Zircons are from the Belfond Dome samples SL-25 and SL-51 (Schmitt et al., 2010). A one to one line is shown as a guide for the eye. B contains a zoomed in portion between 0 and 50 ka. All uncertainties shown are at  $1\sigma$ .

### Appendix C

Element											
TiO2	0.04	0.072	0.066	0.323	0.074	0.076	0.036	0.027	0.032	0.007	0.066
SiO2	65.164	65.092	65.245	61.2	64.388	63.573	64.823	64.478	64.715	65.417	64.653
Na2O	10.218	9.869	10.285	9.275	10.241	9.961	10.079	9.992	10.183	10.782	10.21
FeO	0.367	0.385	0.342	0.813	0.533	0.713	0.612	0.605	0.623	0.671	0.796
K2O	0.662	0.888	0.68	0.478	0.595	0.833	0.947	0.806	0.647	0.507	0.78
Cr2O3	-	0.011	0.066	0.157	-	0.009	-	0.003	0.03	0.016	0.017
Al2O3	21.48	21.147	21.569	22.313	21.454	21.481	21.494	21.144	21.093	21.327	21.421
MgO	0.002	0.155	0.006	0.028	0.247	0.035	0.002	0.408	0.306	0.01	0.393
MnO	-	-	-	0.016	0.017	0.004	0.003	0.013	0.024	-	-
CaO	2.051	2.366	2.042	3.677	2.428	2.287	2.31	2.218	2.651	2.003	2.318
-----											
Total	99.984	99.985	100.301	98.28	99.977	98.972	100.306	99.694	100.304	100.74	100.654
Cation											
Ti	0.004	0.0071	0.0065	0.033	0.0074	0.0077	0.0036	0.0028	0.0032	0.0007	0.0065
Si	8.6309	8.635	8.6183	8.3221	8.5586	8.5456	8.592	8.5929	8.5843	8.6231	8.5525
Na	2.6243	2.5386	2.6344	2.4456	2.6396	2.5964	2.5904	2.5821	2.619	2.7559	2.6189
Fe	0.0407	0.0427	0.0378	0.0924	0.0593	0.0802	0.0678	0.0674	0.0691	0.0739	0.088
K	0.1119	0.1502	0.1146	0.0829	0.101	0.1429	0.1602	0.1371	0.1095	0.0853	0.1316
Cr	-	0.0012	0.0069	0.0169	-	0.001	-	0.0003	0.0031	0.0017	0.0018
Al	3.3534	3.3066	3.3583	3.5764	3.3612	3.4035	3.358	3.3214	3.2979	3.3137	3.3399
Mg	0.0003	0.0307	0.0012	0.0056	0.0489	0.007	0.0004	0.081	0.0605	0.002	0.0774
Mn	-	-	-	0.0018	0.0019	0.0004	0.0003	0.0014	0.0027	-	-
Ca	0.2911	0.3363	0.2891	0.5358	0.3459	0.3294	0.3281	0.3167	0.3768	0.283	0.3286
-----											
Total	15.0567	15.0484	15.0672	15.1125	15.1238	15.1142	15.1008	15.1032	15.1261	15.1393	15.1453
K/Ca	0.384403985	0.446625	0.396403	0.154722	0.291992	0.433819	0.488266	0.432902	0.290605	0.301413	0.400487

Element								
TiO <sub>2</sub>	0.016	0.036	0.081	0.074	0.022	0.022	0.022	0.008
SiO <sub>2</sub>	60.537	63.957	62.955	63.912	65.175	64.756	64.804	64.775
Na <sub>2</sub> O	8.515	10.21	9.998	10.095	10.479	10.332	10.529	10.425
FeO	0.504	0.436	0.385	0.649	0.364	0.477	0.653	0.736
K <sub>2</sub> O	0.703	0.898	0.779	0.788	0.811	0.825	0.573	0.911
Cr <sub>2</sub> O <sub>3</sub>	0.022	-	0.013	-	-	0.037	0.046	-
Al <sub>2</sub> O <sub>3</sub>	23.054	21.252	20.987	21.293	21.401	21.728	21.391	21.684
MgO	0.306	0.059	0.013	0.05	0.016	0.008	-	0.021
MnO	0.033	-	0.032	0.012	0.009	0.011	0.018	0.014
CaO	4.247	2.016	2.29	2.221	2.067	2.193	2.351	2.419
-----								
Total	97.937	98.864	97.533	99.094	100.344	100.389	100.387	100.993
Cation								
Ti	0.0016	0.0036	0.0083	0.0075	0.0022	0.0022	0.0022	0.0008
Si	8.253	8.5931	8.5767	8.575	8.6206	8.5714	8.5847	8.5493
Na	2.2508	2.66	2.6412	2.6261	2.6875	2.6517	2.7045	2.668
Fe	0.0575	0.049	0.0439	0.0729	0.0403	0.0528	0.0723	0.0813
K	0.1222	0.154	0.1354	0.1349	0.1369	0.1394	0.0969	0.1533
Cr	0.0024	-	0.0014	-	-	0.0039	0.0049	-
Al	3.7046	3.3657	3.37	3.3673	3.3365	3.3899	3.34	3.3734
Mg	0.0621	0.0118	0.0027	0.01	0.0031	0.0015	-	0.0041
Mn	0.0038	-	0.0037	0.0014	0.001	0.0012	0.002	0.0016
Ca	0.6204	0.2903	0.3343	0.3193	0.293	0.311	0.3337	0.342
-----								
Total	15.0785	15.1275	15.1176	15.1144	15.1212	15.125	15.1412	15.1739
K/Ca	0.19697	0.530486	0.405025	0.422487	0.467235	0.448232	0.290381	0.448246

**Table C.1:** This table shows the results from EPMA analyses of plagioclase from Jilin.

ID	Temp. (°C)	<sup>40</sup> Ar/ <sup>39</sup> Ar	<sup>37</sup> Ar/ <sup>39</sup> Ar	<sup>36</sup> Ar/ <sup>39</sup> Ar (x 10 <sup>-3</sup> )	<sup>39</sup> Ar <sub>K</sub> (x 10 <sup>-15</sup> mol)	K/Ca	<sup>40</sup> Ar* (%)	<sup>39</sup> Ar (%)	Age (Ma)	±1σ (Ma)	Time (min)
<b>67514.43</b> , lunar basalt, 13.08 mg, J=0.014663±0.04%, D=1.01±0.001, NM-261E, Lab#=62030-01											
A	400	183.5	183.3	1030.8	0.229	0.003	100.0	3.2	2574.1	12.0	10
B	425	163.6	203.1	981.6	0.130	0.003	100.0	5.0	2438.4	19.1	10
C	450	153.8	213.1	1036.3	0.126	0.002	100.0	6.8	2367.1	17.1	10
D	475	150.4	230.0	1079.5	0.142	0.002	100.0	8.8	2355.6	15.9	10
E	500	153.0	241.1	1169.6	0.171	0.002	100.0	11.1	2390.7	15.2	10
F	525	171.2	262.1	1319.0	0.177	0.002	100.0	13.6	2566.5	14.0	10
G	550	186.9	282.5	1453.1	0.191	0.002	100.0	16.3	2713.7	14.0	10
H	575	206.4	298.3	1610.2	0.207	0.002	100.0	19.2	2875.4	16.0	10
I	600	221.2	313.5	1739.0	0.239	0.002	100.0	22.5	2995.8	13.3	10
J	550	248.4	346.1	1923.4	0.081	0.001	100.0	23.6	3213.2	29.9	40
K	500	273.1	355.0	2120.3	0.024	0.001	100.0	24.0	3370.1	105.9	120
L	625	267.5	365.9	2142.3	0.174	0.001	100.0	26.4	3353.8	18.4	10
M	650	272.4	375.5	2164.1	0.237	0.001	100.0	29.7	3395.2	14.8	10
N	675	289.3	392.7	2315.8	0.260	0.001	100.0	33.3	3513.9	16.2	10
O	700	296.1	392.4	2339.1	0.266	0.001	100.0	37.0	3549.5	14.2	10
P	725	301.8	387.6	2333.6	0.292	0.001	100.0	41.1	3572.5	12.7	10
Q	750	304.3	386.0	2357.6	0.318	0.001	100.0	45.6	3583.1	11.8	10
R	775	309.3	383.4	2355.5	0.351	0.001	100.0	50.5	3605.1	12.1	10
S	800	320.4	396.1	2400.6	0.344	0.001	100.0	55.3	3679.4	12.9	10
T	750	340.2	403.2	2498.6	0.161	0.001	100.0	57.5	3786.1	20.2	40
U	700	449.9	401.5	2920.6	0.055	0.001	100.0	58.3	4237.4	40.5	120
V	825	328.6	395.9	2425.4	0.183	0.001	100.0	60.8	3719.5	16.7	10
W	850	331.7	385.1	2406.0	0.242	0.001	100.0	64.2	3718.1	15.3	10
X	875	334.9	385.4	2365.2	0.208	0.001	100.0	67.1	3733.8	16.5	10
Y	900	336.1	384.2	2386.2	0.174	0.001	100.0	69.5	3737.7	18.6	10
Z	925	333.0	369.6	2402.6	0.158	0.001	100.0	71.7	3701.3	17.7	10

AA	950	333.9	367.4	2473.9	0.134	0.001	100.0	73.6	3702.4	22.5	10
AB	975	295.1	346.0	2507.1	0.102	0.001	100.0	75.0	3477.3	23.1	10
AC	1000	242.4	333.2	2717.2	0.070	0.002	100.0	76.0	3158.6	29.7	10
AD	1025	199.9	351.4	3036.4	0.055	0.001	100.0	76.8	2897.9	34.3	10
AE	1050	183.9	375.4	3301.1	0.056	0.001	100.0	77.6	2808.8	33.6	10
AF	1050	221.8	434.3	3590.4	0.060	0.001	100.0	78.4	3167.9	35.8	22
AG	1100	426.8	261.7	2189.1	0.211	0.002	100.0	81.3	3946.5	15.7	10
AH	1050	440.2	313.5	2372.3	0.152	0.002	100.0	83.5	4069.6	20.7	40
AI	1000	322.3	423.5	3013.3	0.021	0.001	100.0	83.8	3731.2	101.1	120
AJ	1125	214.6	500.8	3955.6	0.034	0.001	100.0	84.2	3220.6	51.9	10
AK	1150	251.2	504.3	3738.0	0.070	0.001	100.0	85.2	3467.9	31.4	10
AL	1150	289.3	516.8	3574.7	0.096	0.001	100.0	86.6	3710.9	27.6	22
AM	1200	279.5	593.4	4036.4	0.174	0.001	100.0	89.0	3792.6	18.5	10
AN	1300	269.5	663.5	4205.4	0.134	0.001	100.0	90.8	3871.0	24.6	10
AO	1350	337.7	449.2	2794.6	0.092	0.001	100.0	92.1	3846.0	30.0	10
AP	1400	354.7	465.2	2947.3	0.137	0.001	100.0	94.0	3951.5	19.1	10
AQ	1670	374.8	437.0	2760.6	0.404	0.001	100.0	99.7	3995.0	13.4	6
AR	1670	267.9	156.5	1471.9	0.022	0.003	100.0	100.0	3088.4	112.5	6

ID	Temp. (°C)	<sup>40</sup> Ar/ <sup>39</sup> Ar	<sup>37</sup> Ar/ <sup>39</sup> Ar	<sup>36</sup> Ar/ <sup>39</sup> Ar (x 10 <sup>-3</sup> )	<sup>39</sup> Ar <sub>K</sub> (x 10 <sup>-15</sup> mol)	K/Ca	<sup>40</sup> Ar* (%)	<sup>39</sup> Ar (%)	Age (Ma)	±1σ (Ma)	Time (min)
----	---------------	------------------------------------	------------------------------------	---	--	------	--------------------------	-------------------------	-------------	-------------	---------------

**K-4 <120<60**, nonmag, 21.05 mg, J=0.014773±0.03%, D=1.01±0.001, NM-261H, Lab#=62045-03

A	400	215.6	2.123	131.3	2.95	0.24	100.0	3.3	2622.2	5.0	10
B	425	255.6	1.789	30.04	1.315	0.29	100.0	4.7	2863.8	5.8	10
C	450	290.1	1.691	20.03	1.223	0.30	100.0	6.1	3049.4	6.4	10
D	475	326.3	2.020	14.96	1.417	0.25	100.0	7.7	3226.1	6.9	10
E	500	348.6	1.714	12.88	1.683	0.30	100.0	9.5	3326.7	6.4	10
F	525	368.5	1.928	10.68	2.03	0.26	100.0	11.8	3412.4	5.7	10

G	550	384.8	1.902	9.455	2.65	0.27	100.0	14.7	3479.6	4.9	10
H	575	408.1	1.872	7.914	3.53	0.27	100.0	18.6	3571.5	4.4	10
I	600	432.1	1.850	8.280	4.69	0.28	100.0	23.8	3661.6	3.8	10
J	550	502.8	1.714	8.439	2.27	0.30	100.0	26.3	3903.7	5.6	40
K	500	549.0	1.703	12.94	0.927	0.30	100.0	27.4	4046.3	8.5	120
L	625	467.5	1.768	7.635	3.72	0.29	100.0	31.5	3786.7	5.0	10
M	650	482.9	1.756	8.086	5.32	0.29	100.0	37.4	3838.6	5.0	10
N	675	511.2	1.892	8.278	6.09	0.27	100.0	44.1	3930.5	5.6	10
O	700	542.2	1.892	9.448	6.36	0.27	100.0	51.2	4026.2	6.4	10
P	725	584.8	2.013	11.11	5.73	0.25	100.0	57.5	4149.9	7.0	10
Q	750	626.4	2.111	12.99	4.56	0.24	100.0	62.6	4263.0	6.4	10
R	775	651.9	2.459	16.59	3.75	0.21	100.0	66.8	4329.5	7.6	10
S	800	673.6	3.072	21.48	2.97	0.17	100.0	70.0	4384.7	8.7	10
T	750	701.1	2.706	26.88	1.302	0.19	100.0	71.5	4451.0	9.6	40
U	700	740.2	2.821	61.86	0.645	0.18	100.0	72.2	4541.8	9.8	120
V	825	693.6	4.782	36.59	1.113	0.11	100.0	73.4	4435.4	8.1	10
W	850	665.5	5.443	46.47	1.135	0.094	100.0	74.7	4367.4	11.6	10
X	875	646.7	6.232	56.11	1.048	0.082	100.0	75.9	4320.6	10.2	10
Y	900	559.5	6.592	60.94	1.052	0.077	100.0	77.0	4082.6	10.7	10
Z	925	501.6	7.109	71.61	0.985	0.072	100.0	78.1	3905.7	10.5	10
AA	950	464.5	8.475	92.28	0.952	0.060	100.0	79.2	3783.9	10.7	10
AB	975	425.0	9.422	123.1	0.951	0.054	100.0	80.2	3643.6	8.9	10
AC	1000	379.4	10.86	116.1	0.962	0.047	100.0	81.3	3467.3	7.5	10
AD	1025	413.4	11.89	117.4	0.839	0.043	100.0	82.2	3602.9	8.9	10
AE	1050	446.5	11.84	97.52	0.959	0.043	100.0	83.3	3724.4	8.1	10
AF	1050	450.3	13.80	123.1	0.905	0.037	100.0	84.3	3740.1	7.6	22
AG	1100	459.8	14.88	69.76	1.75	0.034	100.0	86.2	3774.7	6.0	10
AH	1050	534.0	16.83	101.9	0.897	0.030	100.0	87.2	4018.2	8.4	40
AI	1000	614.8	14.54	141.0	0.560	0.035	100.0	87.8	4246.6	10.1	120

AJ	1125	505.6	18.77	86.91	1.534	0.027	100.0	89.5	3931.6	7.2	10
AK	1150	527.0	25.80	100.7	1.81	0.020	100.0	91.6	4007.0	5.9	10
AL	1150	542.0	36.98	163.3	1.229	0.014	100.0	92.9	4065.7	8.7	22
AM	1200	533.3	58.52	243.2	1.76	0.009	100.0	94.9	4064.2	5.7	10
AN	1300	535.3	73.92	1000.2	2.52	0.007	100.0	97.7	4088.5	7.0	10
AO	1350	560.9	52.10	1995.4	1.582	0.010	100.0	99.4	4139.3	7.3	10
AP	1409	543.5	33.44	4198.0	0.437	0.015	100.0	99.9	4065.9	17.6	10
AQ	1670	686.9	18.99	4060.7	0.067	0.027	100.0	100.0	4435.7	64.0	6
AR	1670	627.7	13.21	2249.2	0.021	0.039	100.0	100.0	4279.4	133.1	6

---

**Notes:**

Isotopic ratios corrected for blank, radioactive decay, and mass discrimination, not corrected for interfering reactions.

Errors quoted for individual analyses include analytical error only, without interfering reaction or J uncertainties.

Weight percent K<sub>2</sub>O calculated from <sup>39</sup>Ar signal, sample weight, and instrument sensitivity.

D= 1 AMU in favor of light isotopes

Isotopic abundances after Steiger and Jäger (1977).

Ages calculated relative to HBgr3 (PP20) hornblende interlaboratory standard at 1072 Ma

Decay Constant (LambdaK (total)) = 5.463e-10/a

Correction factors:

$$(^{39}\text{Ar}/^{37}\text{Ar})_{\text{Ca}} = 0.000653 \pm 3.6\text{e-}07$$

$$(^{36}\text{Ar}/^{37}\text{Ar})_{\text{Ca}} = 0.0002633 \pm 3.4\text{e-}7$$

$$(^{38}\text{Ar}/^{39}\text{Ar})_{\text{K}} = 0.01077$$

$$(^{40}\text{Ar}/^{39}\text{Ar})_{\text{K}} = 0.007529 \pm 2.37\text{e-}04$$


---

**Table C.2:** Complete <sup>40</sup>Ar/<sup>39</sup>Ar data for Apollo sample 67514,43 and K-4 from the Jilin chondrite

## Appendix D

### Detailed Model Description:

We chose to generate trial solutions utilizing a Markov Chain Monte Carlo (MCMC) approach as it is more efficient than the standard Monte Carlo method, although similar results would result from both. For each iteration of the simulation we performed the following steps:

- 1) Choose values for the constants A, B, C, and D (and in Model 2, the shape parameters for the beta distribution).
- 2) Generate a distribution of target ages using the lunar zircon  $^{207}\text{Pb}$ - $^{206}\text{Pb}$  age distribution
- 3) For each time step, randomly select impact targets and assign a fractional loss, either from a uniform distribution (Model 1) or from the specified beta distribution (Model 2)
- 4) Based on the fractional loss in each impact, the “plateau” age for each target was calculate based on it's  $^{40}\text{Ar}/^{39}\text{Ar}$  spectrum at 90%  $^{39}\text{Ar}$  loss (i.e., a laboratory heating was simulated and the age selected at which the spectrum asymptotically approaches uniform values; the “plateau”).
- 5) The goodness of fit for each simulated solution is then evaluated relative to the distribution of LHAs (Model 1 and 2) and the distribution of “plateau” ages (Model 2).

Normalized example age spectra are shown in Fig. D.4. Once each simulation was run, we have thousands of potential parameters with fits of varying quality to the data; we selected the best set of parameters (A, B, C, and D as well as beta distribution shape parameters; model 2 only) for this work. That is to say out of all of the potential solutions, we selected the one that best fit the available constraints. We made this choice because we are only interested in whether or not our model can reproduce the observed data, rather than what the uncertainties on each parameter are. To visually assess whether or not the best model parameters reproduce the LHA distribution we have plotted the cumulative frequency distribution for our models and the data (see Figure D.5). Note that each model run fits well visually with a 4.1 Ga for LHB and provides a better fit than a 3.9 Ga LHB in Model 2.

### Age at 90% $^{39}\text{Ar}$ Release:

We chose to utilize the age at 90% of the  $^{39}\text{Ar}$  release for two reasons A) it is usually on the flat part of the age spectrum and B) it is computationally required to define a cut off value. In Model 1, changing the value to say 95% or 85% provides no change to the result. In Model 2, where a beta distribution is fit to the fractional  $^{40}\text{Ar}$  loss, changing the  $^{39}\text{Ar}$  value to another one would simply shift the distribution of fractional  $^{40}\text{Ar}$  loss. That is, choosing a higher value of  $^{39}\text{Ar}$  loss would shift the distribution to higher fractional  $^{40}\text{Ar}$  loss and vice versa. Therefore, the specific choice in value does not strongly influence our results.

### Model 2 “Gas in Plateau”:

To assess the fractional loss, we assume that each sample can be described by a spherical diffusion geometry. To convert from fraction of gas in the “plateau” in the literature data to fractional loss, we calculate the loss required match the modeled “plateau” width to that of each sample (Fig. D.6). Because Apollo samples have complex age spectra due to numerous potential causes including diffusive loss, rock comminution, and recoil effects our analysis is necessarily imprecise. Therefore, the agreement between our Model 2 results and the information gleaned from analyses of Apollo samples suggests but does not prove that our model is reasonable. We note that our model presents a best case scenario as these other factors further obscure the true impact chronology.

### **Justifying a Uniform Distribution for Fractional Loss**

Model 1 assumes a uniform distribution for fractional loss within a volume heated by an impact (e.g., the same proportion experience 10% as 80% loss). Although the primary justification is that a uniform distribution in 1D represents maximum entropy when a parameter can vary continuously in a certain range (Jaynes, 1968), it closely resembles a diffusive approximation. We simulated the distribution of fractional loss occurring from a hemispherical melt. Using a hemispherical melt (radius = 100 m) and the standard analytical solution (Carslaw and Jaeger, 1959), we calculated the temperature-time history along a trajectory away from the hemisphere. Our choice of radius is purely illustrative and our calculation is independent of impactor size. Once the thermal structure is calculated, we used typical diffusion parameters for Apollo samples (36) to calculate the probability distribution of each fractional loss. That is to say, we find the fraction of material that experienced 1% loss, 2% loss, up to 99% (see Fig. D.7). The distribution we find is well described by a uniform probability distribution of fractional loss outside of the melt region. While our model does not account for impact ejecta, the thermal effects of the shockwave, or the fact that real impact melt sheets are not truly hemispherical, it represents a reasonable first approximation. Indeed accounting for these factors is likely a minor effect relative to the degree of our understanding the retentiveness of  $^{40}\text{Ar}$  in the average lunar sample.

### **LHA Data Compilation**

Each LHA represents one Apollo sample, for samples with multiple analyses we chose the most recent. Papers that did not include sufficient information to determine a LHA were not used in our analysis. We followed a similar methodology as Shuster et al. (2010) in compiling our LHAs and our compilation is similar to theirs (see their Figure 4). The references for the data are as follows: Alexander and Davis (1974), Alexander and Kahl (1974), Bernatowicz et al. (1978), Cadogan and Turner (1976), Dominik and Jessberger (1978), Husain and Schaeffer (1973), Husain et al. (1972), Jessberger et al. (1976), Jessberger et al. (1977), Jessberger et al. (1978), Kirsten and Horn (1974), Leich et al. (1975), Maurer et al. (1978), Marvin et al. (1987), Norman et al. (2006), Schaeffer and Schaeffer (1977), Schaeffer et al. (1976), Staudacher et al.

(1978), Stettler et al. (1974), Turner and Cadogan (1975), Turner et al. (1971), Turner et al. (1973), and York et al. (1972).

LHA  
(Ga)

0.18	1.8	2.83	3.59
0.2	1.8	2.84	3.59
0.26	1.804	2.851	3.59
0.262	1.84	2.86	3.6
0.303	1.9	2.874	3.6
0.36	1.93	2.88	3.61
0.395	1.931	2.89	3.63
0.4	1.969	2.892	3.63
0.411	2	2.9	3.642
0.478	2	2.9	3.65
0.5	2	2.9	3.65
0.5	2	2.9	3.65
0.53	2.01	3	3.65
0.54	2.02	3	3.65
0.6	2.05	3.02	3.66
0.678	2.06	3.035	3.665
0.7	2.1	3.05	3.68
0.75	2.1	3.05	3.7
0.8	2.1	3.05	3.7
0.8	2.1	3.07	3.7
0.863	2.1	3.07	3.7
0.9	2.1	3.073	3.7
0.9	2.152	3.1	3.7
0.95	2.18	3.1	3.708
1	2.2	3.1	3.744
1	2.2	3.1	3.75
1.01	2.22	3.127	3.77
1.05	2.25	3.127	3.8
1.1	2.313	3.15	3.8
1.143	2.329	3.15	3.8
1.161	2.33	3.15	3.81
1.19	2.35	3.17	3.82
1.2	2.368	3.17	3.84
1.229	2.37	3.177	3.844
1.231	2.385	3.2	3.85
1.289	2.4	3.2	3.85
1.299	2.4	3.211	3.855
1.304	2.4	3.212	3.9
1.32	2.4	3.291	3.9
1.342	2.4	3.3	3.9

1.355	2.4	3.3	3.9
1.384	2.41	3.3	3.9
1.467	2.435	3.3	3.9
1.479	2.465	3.331	3.9
1.49	2.482	3.34	3.9
1.505	2.5	3.35	3.913
1.525	2.5	3.35	3.923
1.53	2.5	3.35	3.93
1.58	2.51	3.355	3.94
1.582	2.52	3.357	3.96
1.59	2.52	3.37	3.974
1.6	2.521	3.38	4
1.61	2.53	3.4	4
1.62	2.55	3.4	4
1.628	2.554	3.4	4
1.65	2.627	3.42	4
1.67	2.64	3.45	4
1.68	2.65	3.45	4
1.68	2.66	3.45	4
1.695	2.7	3.47	4
1.7	2.7	3.478	4.07
1.702	2.713	3.48	4.1
1.74	2.724	3.486	4.11
1.77	2.77	3.49	
1.8	2.8	3.53	
1.8	2.8	3.55	
1.8	2.8	3.56	
1.8	2.81	3.58	

**Table D.1:** Compilation of Apollo  $^{40}\text{Ar}/^{39}\text{Ar}$  ages from the early heating steps (the Last Heating Ages). See Chapter 4 for a more detailed explanation. References are provided in the text for this Appendix.

Zircon Pb/Pb Ages in Ga

4.106	4.2	4.23	4.295	4.331	4.341	4.349
4.11	4.201	4.232	4.295	4.331	4.341	4.351
4.11	4.201	4.233	4.296	4.332	4.341	4.352
4.117	4.202	4.233	4.297	4.332	4.341	4.353
4.119	4.204	4.237	4.298	4.332	4.341	4.353
4.123	4.205	4.239	4.298	4.333	4.341	4.353
4.129	4.205	4.24	4.298	4.333	4.341	4.353
4.142	4.205	4.241	4.305	4.334	4.341	4.355
4.146	4.205	4.241	4.305	4.334	4.341	4.355
4.15	4.206	4.243	4.306	4.334	4.341	4.355
4.153	4.206	4.243	4.308	4.335	4.342	4.355
4.153	4.207	4.245	4.311	4.335	4.342	4.356
4.158	4.207	4.246	4.311	4.335	4.342	4.356
4.161	4.207	4.248	4.312	4.335	4.342	4.358
4.162	4.207	4.252	4.313	4.336	4.343	4.358
4.163	4.209	4.252	4.316	4.336	4.344	4.361
4.172	4.209	4.257	4.316	4.336	4.344	4.362
4.175	4.209	4.263	4.316	4.337	4.344	4.366
4.177	4.211	4.264	4.32	4.337	4.344	4.367
4.178	4.211	4.265	4.321	4.338	4.344	4.368
4.178	4.213	4.267	4.324	4.338	4.345	4.368
4.179	4.213	4.267	4.324	4.338	4.345	4.368
4.179	4.214	4.274	4.325	4.338	4.345	4.369
4.179	4.215	4.275	4.326	4.338	4.345	4.373
4.179	4.215	4.275	4.326	4.338	4.346	4.379
4.183	4.216	4.276	4.327	4.338	4.346	4.387
4.184	4.216	4.28	4.327	4.339	4.346	4.395
4.185	4.218	4.282	4.328	4.339	4.347	4.397
4.186	4.219	4.283	4.328	4.339	4.347	4.404
4.188	4.224	4.284	4.328	4.339	4.347	4.409
4.189	4.225	4.284	4.328	4.339	4.348	4.416
4.192	4.226	4.286	4.329	4.339	4.348	
4.192	4.226	4.287	4.33	4.34	4.348	
4.196	4.227	4.287	4.331	4.34	4.349	
4.197	4.228	4.29	4.331	4.34	4.349	

**Table D.2:** A compilation of literature  $^{207}\text{Pb}/^{206}\text{Pb}$  zircon ages which are assumed to represent the age distribution of the lunar crust. References are provided in the text of Chapter 4.

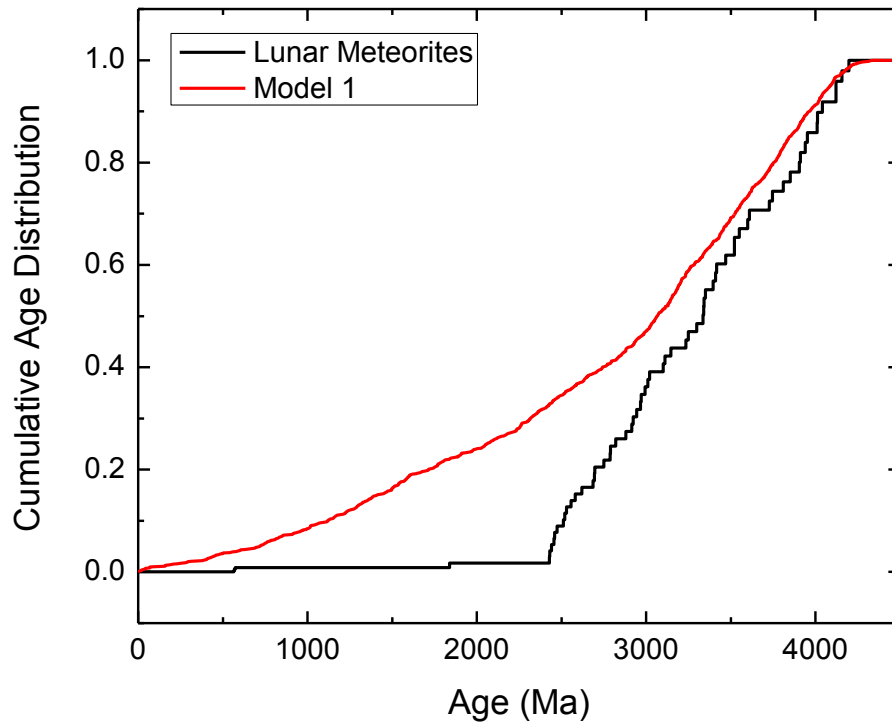


**Figure D.1:** Model 1 results compared to the distribution of  $^{40}\text{Ar}/^{39}\text{Ar}$  “plateau” ages from lunar meteorites. The Meteorite data is our compilation of the references listed in Marchi et al. (2013).

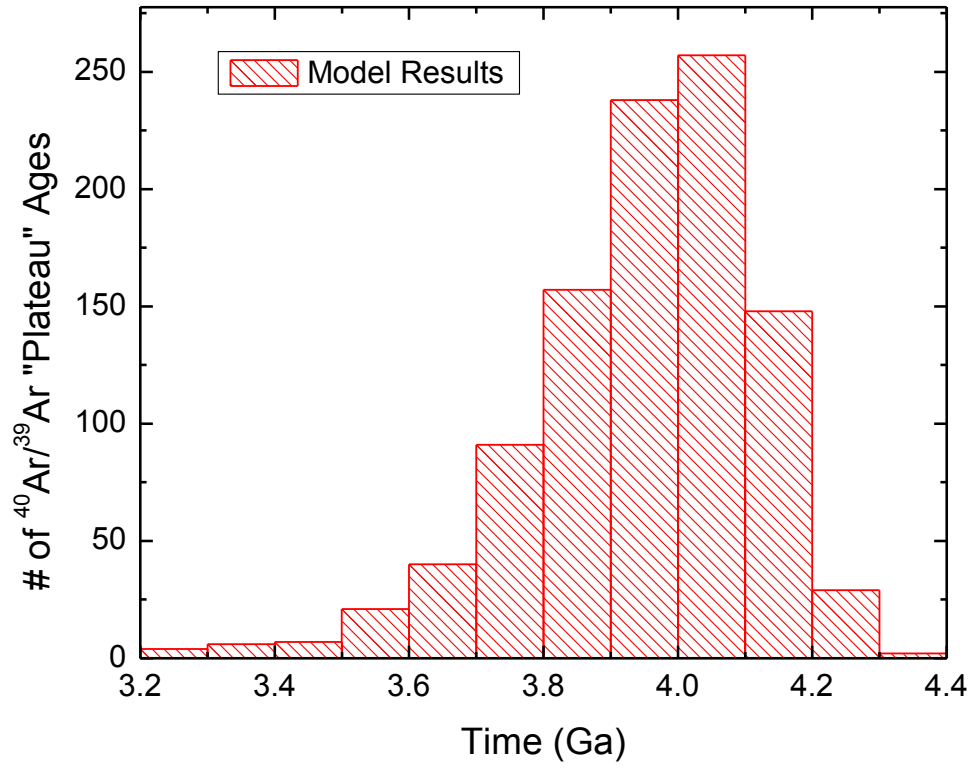


**Figure D.2:** Model 2 results for a 3.9 Ga impact spike.

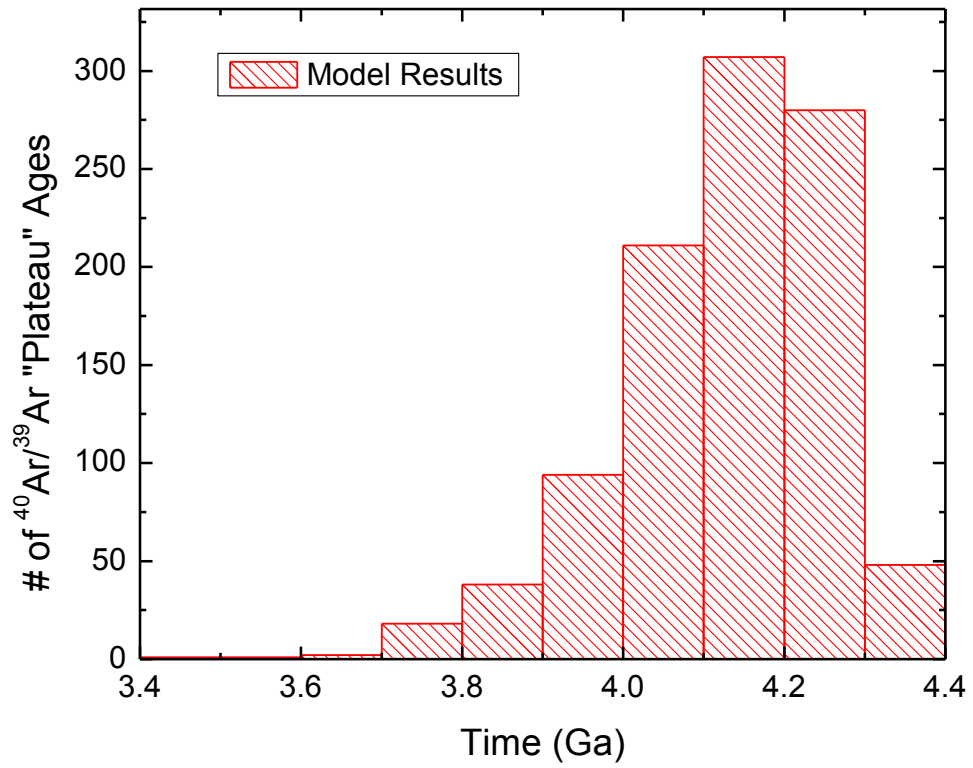


**Figure D.3:** Model 2 results for a 4.1 Ga impact spike.

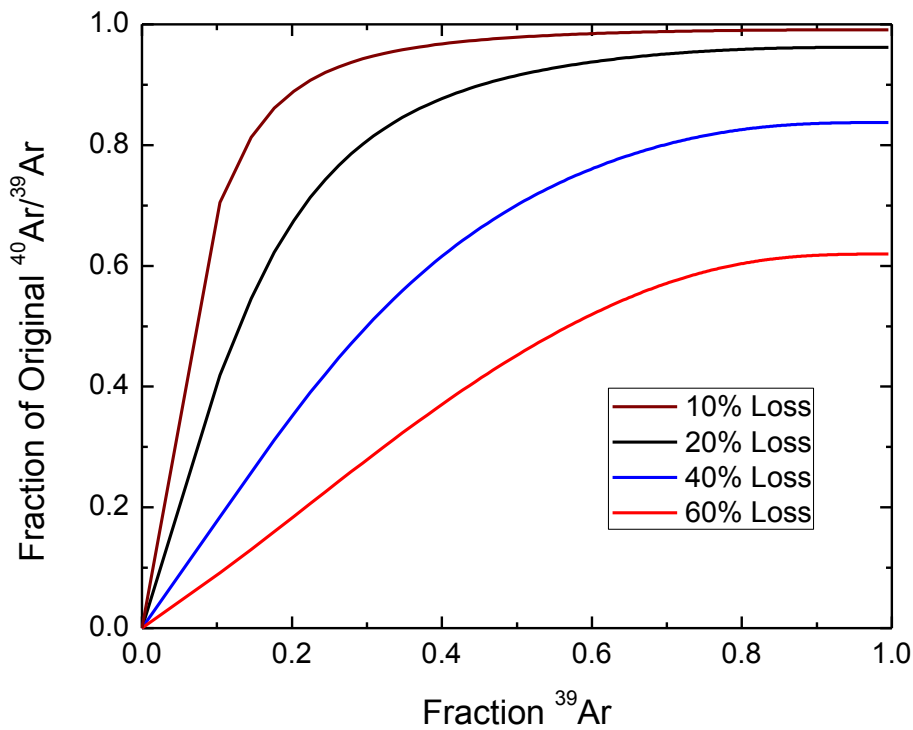


**Figure D.4:** Age spectra showing the effects of diffusive loss at  $^{40}\text{Ar}/^{39}\text{Ar} = 0$  of a sample that originally formed at  $^{40}\text{Ar}/^{39}\text{Ar} = 1$ . We show here examples with 10, 20, 40, and 60% loss to show how the age spectra changes. The specific form of the age spectra is dependent on the geometry chosen, but the general behavior is the same (that is diffusive loss in all geometries leads to “plateau” ages that are too young). Additionally the shape does not change considerably from one event to multiple events and therefore this is a general example of one or multiple loss events.

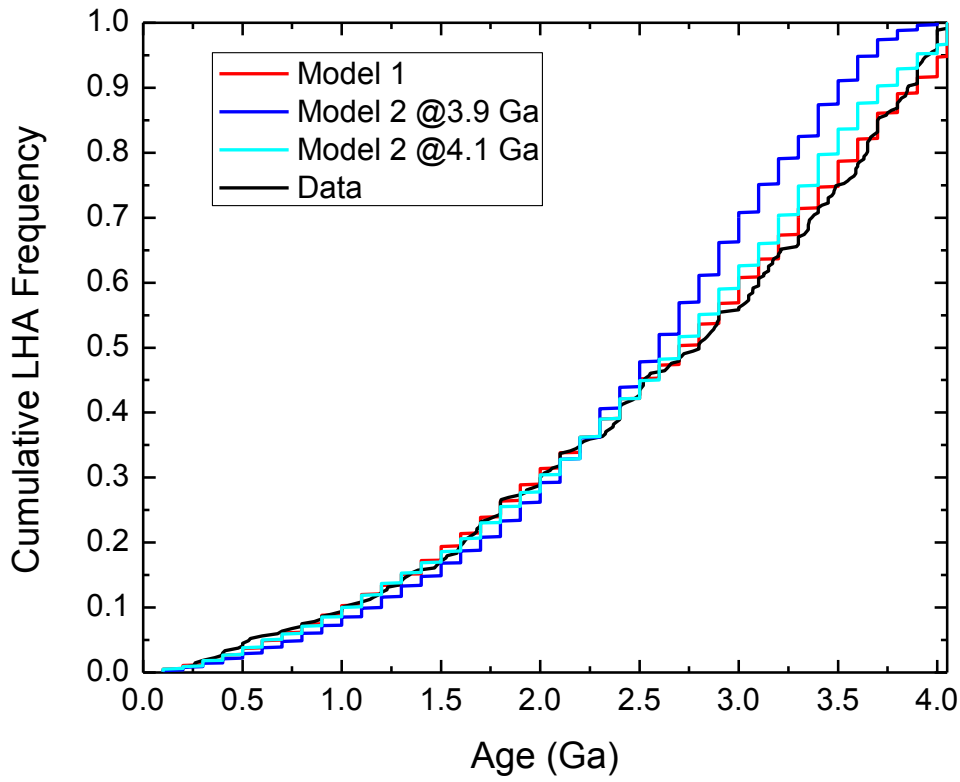


**Figure D.5:** A comparison of the cumulative LHA distribution between the models and data. Note the good visual agreement between the data and model 1. For model 2, although both model runs fit the data well, the simulation constrained to a bombardment at 4.1 Ga provides a better fit than the one at 3.9 Ga.

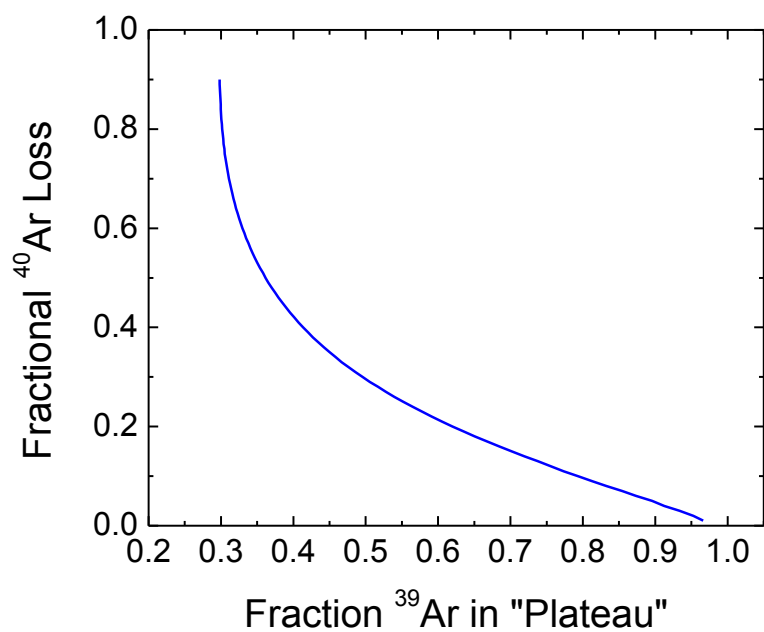


**Figure D.6:** The relationship between plateau “width” and fractional <sup>40</sup>Ar loss for a single diffusion domain with spherical geometry. This is used to assess the plausibility of Model 2.

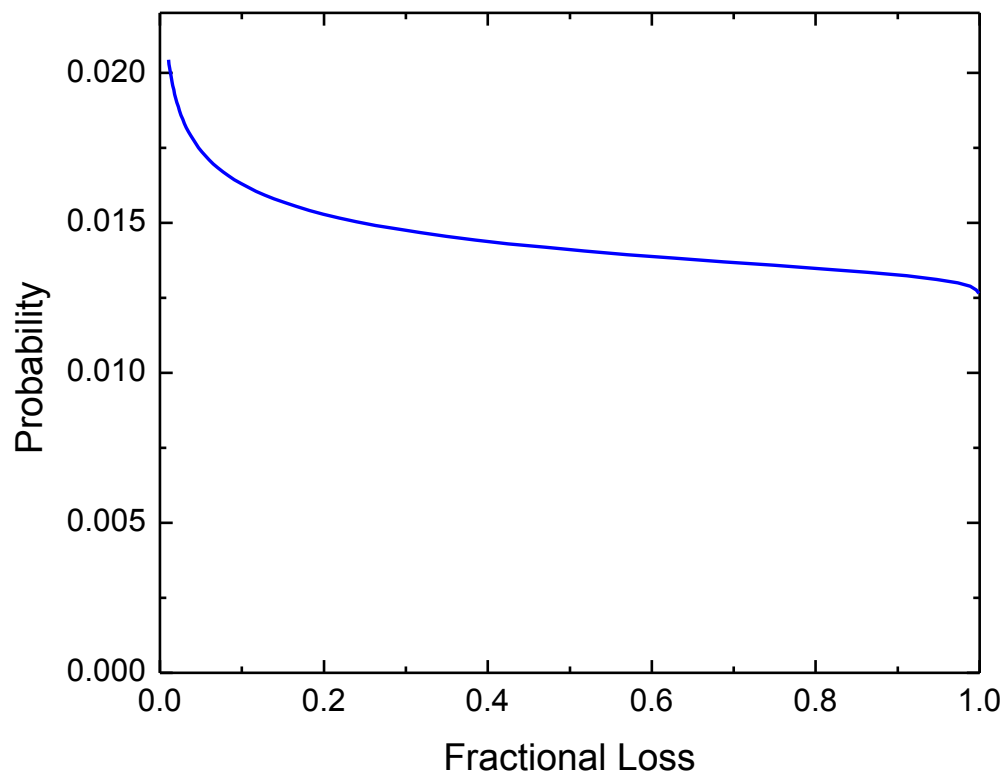


**Figure D.7:** The probability distribution for fractional  $^{40}\text{Ar}$  loss as calculated for a hemispherical impact. We approximate this as a uniform distribution for model 1.

## Appendix E

ID	Temp (C)	<sup>39</sup> Ar <sub>K</sub> (mol)	Age (Ma)	±1σ (Ma)	Time (min)	<sup>39</sup> Ar (fraction)	K/Ca	log(D/(r*r))
67484,9								
1	400	3.08E-17	5827.6	59.2	11	0.19	4.38E-03	-9.30
2	425	2.62E-17	5350.4	58.8	11	0.36	3.80E-03	-8.92
3	450	2.57E-17	4195.7	61.7	11	0.52	3.67E-03	-8.72
4	475	1.16E-17	3909.2	98.3	5	0.59	4.15E-03	-8.62
5	500	4.58E-17	4004.7	30.0	11	0.88	3.41E-03	-8.25
6	525	4.64E-17	3925.8	35.4	11	1.17	3.44E-03	-8.10
7	550	6.39E-17	3949.8	33.8	11	1.57	3.31E-03	-7.83
8	575	9.18E-17	3979.7	19.6	11	2.15	3.12E-03	-7.54
9	600	1.15E-16	4021.6	19.1	11	2.87	3.00E-03	-7.31
10	550	5.55E-17	4093.7	26.4	41	3.22	2.88E-03	-8.11
11	500	2.02E-17	4481.5	62.3	121	3.35	3.11E-03	-8.99
12	625	1.01E-16	4027.1	20.3	11	3.98	2.81E-03	-7.20
13	650	1.62E-16	4029.3	14.4	11	5.00	2.71E-03	-6.90
14	675	1.95E-16	3993.7	14.6	11	6.23	2.71E-03	-6.72
15	700	2.14E-16	4041.4	12.7	11	7.57	2.64E-03	-6.59
16	725	2.34E-16	3966.4	11.9	11	9.04	2.68E-03	-6.46
17	750	2.60E-16	3985.3	12.2	11	10.68	2.66E-03	-6.33
18	775	2.92E-16	3946.9	11.7	11	12.51	2.72E-03	-6.21
19	800	3.44E-16	3882.3	9.6	11	14.68	2.83E-03	-6.06
20	750	2.15E-16	3971.7	11.2	41	16.03	2.79E-03	-6.78
21	700	1.14E-16	4045.4	17.4	121	16.74	2.92E-03	-7.49
22	825	2.55E-16	3935.2	11.7	11	18.34	2.82E-03	-6.06
23	850	3.40E-16	3903.8	11.0	11	20.48	2.86E-03	-5.89
24	875	3.89E-16	3904.3	8.5	11	22.93	2.88E-03	-5.77
25	900	4.36E-16	3887.2	11.3	11	25.66	2.90E-03	-5.66
26	925	4.57E-16	3882.4	10.0	11	28.54	2.97E-03	-5.58
27	950	4.67E-16	3894.9	9.2	11	31.47	3.00E-03	-5.51
28	975	4.70E-16	3887.7	9.0	11	34.43	2.98E-03	-5.45
29	1000	4.42E-16	3874.3	13.4	11	37.20	3.04E-03	-5.43
30	1025	4.38E-16	3844.6	10.9	11	39.96	3.02E-03	-5.39
31	1050	5.50E-16	3883.2	11.9	11	43.41	1.91E-03	-5.24
32	1050	3.91E-16	3887.1	10.0	23	45.87	2.42E-03	-5.66
33	1100	4.61E-16	3870.6	10.4	11	48.77	2.80E-03	-5.22
34	1125	4.28E-16	3930.5	10.4	11	51.46	2.70E-03	-5.21
35	1150	5.13E-16	3878.2	8.4	11	54.68	2.55E-03	-5.09
36	1150	3.87E-16	3918.3	11.5	23	57.11	2.48E-03	-5.49

37	1200	3.71E-16	3875.5	9.7	11	59.44	1.96E-03	-5.15
38	1300	9.14E-16	4043.1	6.2	11	65.18	2.25E-03	-4.69
39	1670	5.54E-15	4109.9	9.0	7	100.00	2.75E-03	-2.60
67484,11								
1	400	2.79E-17	4370.0	75.1	10	0.22	3.47E-03	-9.16
2	425	2.35E-17	2930.0	85.7	10	0.40	4.71E-03	-8.78
3	450	2.21E-17	3050.0	83.3	10	0.57	3.77E-03	-8.61
4	475	2.56E-17	3230.0	75.6	10	0.77	3.49E-03	-8.41
5	500	3.17E-17	3310.0	59.5	10	1.02	3.43E-03	-8.19
6	525	4.23E-17	3340.0	49.6	10	1.35	3.19E-03	-7.94
7	550	5.90E-17	3360.0	40.4	10	1.81	3.17E-03	-7.67
8	575	8.45E-17	3410.0	26.8	10	2.47	3.07E-03	-7.38
9	600	1.09E-16	3550.0	28.5	10	3.32	3.04E-03	-7.14
10	550	5.60E-17	3530.0	36.7	40	3.75	3.10E-03	-7.94
11	500	2.19E-17	3470.0	114.0	120	3.92	3.25E-03	-8.79
12	625	9.97E-17	3640.0	28.3	10	4.70	3.08E-03	-7.00
13	650	1.45E-16	3710.0	21.9	10	5.83	3.06E-03	-6.74
14	675	1.60E-16	3790.0	18.5	10	7.08	2.99E-03	-6.61
15	700	1.77E-16	3850.0	19.9	10	8.45	3.03E-03	-6.48
16	725	1.88E-16	3960.0	20.1	10	9.91	3.05E-03	-6.37
17	750	2.12E-16	4010.0	16.9	10	11.60	3.02E-03	-6.25
18	775	2.48E-16	4050.0	16.4	10	13.50	3.05E-03	-6.11
19	800	2.82E-16	4010.0	13.2	10	15.70	3.13E-03	-5.98
20	750	2.03E-16	3990.0	13.3	40	17.30	3.22E-03	-6.66
21	700	1.21E-16	4090.0	20.3	120	18.20	3.28E-03	-7.33
22	825	1.89E-16	3970.0	18.5	10	19.70	3.13E-03	-6.02
23	850	2.45E-16	3960.0	15.0	10	21.60	3.15E-03	-5.86
24	875	2.91E-16	3910.0	14.8	10	23.90	3.15E-03	-5.74
25	900	2.94E-16	3910.0	12.7	10	26.20	3.09E-03	-5.68
26	925	3.03E-16	3890.0	12.7	10	28.50	3.06E-03	-5.62
27	950	3.11E-16	3820.0	25.0	10	30.90	3.17E-03	-5.56
28	975	2.87E-16	3860.0	13.4	10	33.20	3.11E-03	-5.55
29	1000	2.71E-16	3840.0	15.4	10	35.30	3.08E-03	-5.54
30	1030	2.63E-16	3830.0	16.4	10	37.30	3.05E-03	-5.51
31	1050	2.67E-16	3870.0	15.4	10	39.40	3.00E-03	-5.47
32	1050	3.53E-16	3940.0	12.2	22	42.20	3.01E-03	-5.65
33	1100	1.81E-16	3900.0	19.7	10	43.60	3.16E-03	-5.57
34	1050	7.93E-17	3920.0	33.9	40	44.20	3.05E-03	-6.51
35	1000	4.06E-17	3710.0	55.8	120	44.50	3.07E-03	-7.27
36	1130	7.01E-17	3890.0	32.4	10	45.10	2.79E-03	-5.95
37	1150	6.15E-17	3890.0	35.7	10	45.50	2.84E-03	-6.00

38	1150	6.04E-17	3890.0	39.8	22	46.00	3.04E-03	-6.34
39	1200	1.15E-16	3960.0	28.6	10	46.90	2.47E-03	-5.71
40	1300	1.98E-15	4150.0	25.3	10	62.30	2.62E-03	-4.34
41	1350	2.10E-15	3990.0	26.2	10	78.60	3.03E-03	-4.05
42	1410	1.51E-15	4090.0	16.6	10	90.40	2.82E-03	-3.87
43	1670	1.13E-15	4150.0	21.4	6	99.20	2.88E-03	-3.15
44	1670	1.00E-16	2620.0	60.9	6	100.00	7.27E-03	-2.73

63504,12

1	400	9.85E-17	3910.0	29.2	10	0.28	4.97E-03	-8.93
2	425	6.01E-17	3870.0	42.5	10	0.46	5.34E-03	-8.73
3	450	8.20E-17	3690.0	33.6	10	0.69	5.21E-03	-8.40
4	475	9.43E-17	3650.0	30.7	10	0.96	5.07E-03	-8.18
5	500	1.13E-16	3660.0	23.0	10	1.29	5.13E-03	-7.97
6	525	1.32E-16	3730.0	22.8	10	1.67	4.80E-03	-7.78
7	550	1.85E-16	3720.0	17.9	10	2.20	4.85E-03	-7.52
8	575	2.40E-16	3780.0	16.3	10	2.89	4.58E-03	-7.28
9	600	2.96E-16	3820.0	14.4	10	3.74	4.47E-03	-7.07
10	550	1.38E-16	3830.0	19.7	40	4.14	4.62E-03	-7.93
11	500	4.84E-17	3830.0	49.5	120	4.28	5.20E-03	-8.83
12	625	2.65E-16	3890.0	12.2	10	5.04	4.14E-03	-6.97
13	650	4.14E-16	3880.0	10.1	10	6.23	4.16E-03	-6.69
14	675	5.15E-16	3870.0	10.6	10	7.71	4.13E-03	-6.50
15	700	5.94E-16	3900.0	9.1	10	9.42	4.09E-03	-6.34
16	725	6.86E-16	3900.0	10.4	10	11.40	4.12E-03	-6.19
17	750	7.79E-16	3920.0	8.3	10	13.60	4.07E-03	-6.04
18	775	9.56E-16	3880.0	8.0	10	16.40	4.31E-03	-5.87
19	800	1.06E-15	3890.0	8.1	10	19.40	4.41E-03	-5.73
20	750	7.36E-16	3910.0	10.5	40	21.60	4.77E-03	-6.42
21	700	3.90E-16	4000.0	11.1	120	22.70	5.23E-03	-7.14
22	825	8.32E-16	3940.0	7.7	10	25.10	4.38E-03	-5.69
23	850	1.07E-15	3920.0	7.8	10	28.20	4.53E-03	-5.52
24	875	1.29E-15	3930.0	7.5	10	31.90	4.65E-03	-5.37
25	900	1.36E-15	3960.0	7.2	10	35.80	4.66E-03	-5.28
26	925	1.43E-15	3990.0	8.6	10	39.90	4.70E-03	-5.18
27	950	1.35E-15	4020.0	9.0	10	43.80	4.82E-03	-5.14
28	975	1.19E-15	4030.0	8.1	10	47.20	5.00E-03	-5.14
29	1000	9.61E-16	3980.0	7.9	10	49.90	5.34E-03	-5.18
30	1030	8.84E-16	3920.0	9.8	10	52.50	5.86E-03	-5.18
31	1050	8.62E-16	3920.0	8.6	10	55.00	6.01E-03	-5.15
32	1050	9.72E-16	3970.0	7.5	22	57.80	5.82E-03	-5.40
33	1100	5.95E-16	3900.0	10.0	10	59.50	5.28E-03	-5.24

34	1050	4.58E-16	3950.0	10.9	40	60.80	5.68E-03	-5.93
35	1000	2.76E-16	4040.0	14.1	120	61.60	6.01E-03	-6.61
36	1130	6.86E-16	3940.0	9.1	10	63.60	3.90E-03	-5.11
37	1150	1.03E-15	4000.0	9.3	10	66.50	3.73E-03	-4.90
38	1150	9.43E-16	4080.0	8.0	22	69.20	3.69E-03	-5.23
39	1200	1.04E-15	4040.0	7.6	10	72.20	3.57E-03	-4.80
40	1300	8.85E-16	4150.0	11.9	10	74.70	3.33E-03	-4.81
41	1350	8.88E-16	4140.0	10.4	10	77.30	3.67E-03	-4.76
42	1410	3.25E-15	4150.0	5.7	10	86.70	3.77E-03	-4.06
43	1670	4.29E-15	4130.0	8.0	6	99.00	2.99E-03	-3.14
44	1670	3.47E-16	3540.0	23.9	6	100.00	4.13E-03	-2.71

63504,14

1	400	5.47E-17	4730.0	54.9	10	0.16	4.03E-03	-9.42
2	425	5.22E-17	3860.0	56.2	10	0.32	5.56E-03	-8.97
3	450	4.64E-17	4030.0	67.4	10	0.45	4.97E-03	-8.82
4	475	5.08E-17	4270.0	53.1	10	0.60	4.41E-03	-8.64
5	500	7.47E-17	4070.0	41.0	10	0.82	5.02E-03	-8.34
6	525	1.00E-16	4130.0	35.8	10	1.12	4.58E-03	-8.08
7	550	1.22E-16	4180.0	28.8	10	1.48	4.58E-03	-7.86
8	575	1.64E-16	4200.0	23.0	10	1.96	4.41E-03	-7.61
9	600	1.73E-16	4190.0	21.2	10	2.47	4.65E-03	-7.48
10	550	9.67E-17	4190.0	27.8	40	2.75	5.13E-03	-8.26
11	500	3.75E-17	4070.0	67.1	120	2.87	6.73E-03	-9.11
12	625	1.56E-16	4310.0	21.6	10	3.32	4.27E-03	-7.37
13	650	2.86E-16	4300.0	17.0	10	4.17	4.25E-03	-7.02
14	675	3.53E-16	4260.0	15.1	10	5.21	4.44E-03	-6.83
15	700	4.92E-16	4140.0	13.5	10	6.66	4.73E-03	-6.58
16	725	5.82E-16	4070.0	13.1	10	8.37	4.96E-03	-6.40
17	750	6.61E-16	4060.0	13.4	10	10.30	4.94E-03	-6.24
18	775	7.98E-16	3990.0	11.0	10	12.70	5.27E-03	-6.06
19	800	8.94E-16	3970.0	11.0	10	15.30	5.48E-03	-5.92
20	750	7.26E-16	3910.0	13.1	40	17.40	6.68E-03	-6.53
21	700	4.85E-16	3930.0	8.5	120	18.90	8.11E-03	-7.13
22	825	5.30E-16	3990.0	10.3	10	20.40	5.33E-03	-5.97
23	850	8.41E-16	4000.0	9.9	10	22.90	5.13E-03	-5.72
24	875	9.83E-16	3990.0	8.9	10	25.80	5.12E-03	-5.59
25	900	1.06E-15	3970.0	8.0	10	28.90	4.96E-03	-5.50
26	925	1.05E-15	3970.0	8.3	10	32.00	4.72E-03	-5.44
27	950	1.02E-15	3950.0	10.2	10	35.00	4.60E-03	-5.39
28	975	9.47E-16	3950.0	9.2	10	37.80	4.49E-03	-5.38
29	1000	8.59E-16	3920.0	11.9	10	40.40	4.52E-03	-5.37

30	1030	7.06E-16	3950.0	11.5	10	42.40	4.37E-03	-5.42
31	1050	6.45E-16	4020.0	9.7	10	44.30	4.17E-03	-5.43
32	1050	6.60E-16	4040.0	10.6	22	46.30	4.27E-03	-5.73
33	1100	5.67E-16	3940.0	11.9	10	48.00	3.96E-03	-5.42
34	1050	2.20E-16	4110.0	17.2	40	48.60	4.22E-03	-6.42
35	1000	1.41E-16	4140.0	21.3	120	49.00	3.88E-03	-7.08
36	1130	2.10E-16	4070.0	16.7	10	49.60	3.26E-03	-5.82
37	1150	2.54E-16	4150.0	16.2	10	50.40	3.35E-03	-5.73
38	1150	1.78E-16	4270.0	21.2	22	50.90	3.15E-03	-6.22
39	1200	3.40E-16	3850.0	13.4	10	51.90	3.30E-03	-5.58
40	1300	3.71E-15	3500.0	4.4	10	62.90	5.04E-03	-4.45
41	1350	3.81E-15	4030.0	5.4	10	74.10	3.27E-03	-4.26
42	1410	5.20E-15	4080.0	5.8	10	89.40	3.11E-03	-3.83
43	1670	3.59E-15	4090.0	6.3	6	100.00	2.51E-03	-2.58

63504,16

1	400	2.55E-16	2820.0	10.2	10	0.48	2.30E-02	-8.48
2	425	1.57E-16	2210.0	13.7	10	0.77	2.00E-02	-8.27
3	450	1.41E-16	2290.0	15.8	10	1.04	1.54E-02	-8.16
4	475	1.46E-16	2410.0	13.9	10	1.31	1.37E-02	-8.03
5	500	1.76E-16	2480.0	14.3	10	1.64	1.31E-02	-7.85
6	525	2.09E-16	2590.0	10.7	10	2.03	1.06E-02	-7.67
7	550	2.62E-16	2600.0	10.0	10	2.52	9.89E-03	-7.48
8	575	3.39E-16	2610.0	7.9	10	3.15	8.07E-03	-7.27
9	600	3.87E-16	2580.0	8.0	10	3.87	7.28E-03	-7.12
10	550	2.33E-16	2930.0	10.3	40	4.31	9.56E-03	-7.87
11	500	1.23E-16	3270.0	21.9	120	4.54	1.35E-02	-8.59
12	625	2.62E-16	2620.0	8.0	10	5.03	5.98E-03	-7.15
13	650	4.36E-16	2470.0	6.7	10	5.84	5.66E-03	-6.87
14	675	6.02E-16	2370.0	5.5	10	6.97	5.34E-03	-6.66
15	700	7.88E-16	2260.0	5.5	10	8.44	5.35E-03	-6.45
16	725	9.87E-16	2210.0	4.0	10	10.30	5.48E-03	-6.26
17	750	1.16E-15	2240.0	3.8	10	12.50	5.40E-03	-6.10
18	775	1.48E-15	2330.0	4.4	10	15.20	5.56E-03	-5.90
19	800	1.70E-15	2440.0	3.9	10	18.40	6.16E-03	-5.75
20	750	1.37E-15	2650.0	3.2	40	21.00	7.68E-03	-6.36
21	700	9.82E-16	2820.0	4.2	120	22.80	9.70E-03	-6.93
22	825	1.06E-15	2580.0	4.6	10	24.80	7.20E-03	-5.77
23	850	1.33E-15	2580.0	4.3	10	27.30	7.69E-03	-5.62
24	875	1.40E-15	2540.0	3.4	10	29.90	8.37E-03	-5.55
25	900	1.30E-15	2480.0	3.4	10	32.30	8.60E-03	-5.53
26	925	1.14E-15	2470.0	3.7	10	34.40	8.58E-03	-5.55

27	950	1.11E-15	2460.0	4.2	10	36.50	8.45E-03	-5.52
28	975	1.14E-15	2440.0	3.9	10	38.70	8.75E-03	-5.47
29	1000	1.04E-15	2410.0	4.0	10	40.60	9.40E-03	-5.48
30	1030	8.48E-16	2250.0	4.4	10	42.20	9.38E-03	-5.54
31	1050	6.15E-16	2090.0	5.2	10	43.30	8.18E-03	-5.66
32	1050	5.25E-16	2250.0	5.8	22	44.30	7.48E-03	-6.05
33	1100	5.24E-16	2150.0	5.8	10	45.30	8.66E-03	-5.69
34	1050	1.04E-16	2580.0	21.2	40	45.50	5.29E-03	-6.99
35	1000	5.30E-17	2930.0	44.3	120	45.60	4.15E-03	-7.76
36	1130	9.35E-16	2150.0	3.4	10	47.30	9.54E-03	-5.42
37	1150	7.89E-16	2320.0	3.8	10	48.80	8.26E-03	-5.46
38	1150	3.33E-16	2550.0	7.3	22	49.40	6.40E-03	-6.16
39	1200	1.17E-15	2430.0	3.7	10	51.60	8.17E-03	-5.25
40	1300	1.17E-14	2880.0	2.3	10	73.50	1.20E-02	-4.05
41	1350	4.59E-15	2900.0	3.0	10	82.10	8.91E-03	-4.19
42	1410	5.38E-15	2560.0	2.6	10	92.20	6.17E-03	-3.86
43	1670	3.69E-15	2280.0	2.8	6.02	99.10	4.84E-03	-3.22
44	1670	4.97E-16	2300.0	9.3	6	100.00	4.56E-03	-2.72

67514,22

1	400	7.15E-16	920.1	2.9	14	2.90	5.63E-02	-7.67
2	400	8.35E-16	1068.5	3.2	29	6.20	8.61E-02	-7.41
3	425	4.63E-16	1201.3	5.1	14	8.00	6.80E-02	-7.15
4	425	7.02E-16	1358.0	3.8	29	10.60	7.65E-02	-7.16
5	450	4.48E-16	1507.2	5.9	14	12.30	6.16E-02	-6.94
6	450	7.68E-16	1669.8	4.7	29	15.00	6.29E-02	-6.94
7	475	5.02E-16	1830.0	6.2	14	16.80	5.30E-02	-6.73
8	475	8.97E-16	1995.2	5.2	29	19.80	5.54E-02	-6.72
9	500	5.78E-16	2155.6	6.8	14	21.70	4.30E-02	-6.53
10	500	1.02E-15	2337.0	4.8	29	25.00	4.47E-02	-6.53
11	525	6.91E-16	2487.0	6.9	14	27.10	3.42E-02	-6.32
12	525	1.15E-15	2672.5	5.7	29	30.60	3.42E-02	-6.36
13	550	7.79E-16	2796.5	6.9	14	32.80	2.66E-02	-6.16
14	550	1.26E-15	2923.9	5.1	29	36.30	2.79E-02	-6.21
15	575	9.38E-16	3051.1	7.3	14	38.90	2.14E-02	-5.97
16	575	1.43E-15	3171.0	5.2	29	42.50	2.15E-02	-6.05
17	600	9.77E-16	3254.1	7.8	14	45.00	1.72E-02	-5.85
18	600	1.50E-15	3372.5	5.7	29	48.50	1.72E-02	-5.93
19	625	1.02E-15	3422.9	9.0	14	50.90	1.41E-02	-5.73
20	625	1.60E-15	3515.5	6.8	29	54.40	1.39E-02	-5.80
21	650	1.08E-15	3530.9	8.0	14	56.70	1.15E-02	-5.61
22	650	1.66E-15	3610.1	6.1	29	60.00	1.14E-02	-5.70

23	675	1.11E-15	3597.0	7.1	14	62.20	9.71E-03	-5.51
24	675	1.64E-15	3686.8	5.7	29	65.20	9.42E-03	-5.61
25	700	1.10E-15	3657.0	9.8	14	67.20	8.10E-03	-5.43
26	700	1.61E-15	3730.7	6.9	29	70.00	7.86E-03	-5.54
27	725	1.09E-15	3687.4	8.1	14	71.80	6.95E-03	-5.35
28	725	1.60E-15	3752.5	6.9	29	74.40	6.65E-03	-5.45
29	750	1.08E-15	3722.7	9.2	14	76.00	5.95E-03	-5.27
30	750	1.61E-15	3769.3	5.9	29	78.40	5.77E-03	-5.37
31	775	1.08E-15	3708.3	7.9	14	80.00	5.31E-03	-5.18
32	775	1.53E-15	3771.7	7.3	29	82.10	5.06E-03	-5.30
33	800	9.83E-16	3730.2	7.7	14	83.50	4.62E-03	-5.14
34	800	1.47E-15	3780.5	7.5	29	85.40	4.36E-03	-5.23
35	825	9.81E-16	3726.7	11.1	14	86.70	4.02E-03	-5.05
36	825	1.39E-15	3764.5	7.9	29	88.40	3.72E-03	-5.16
37	850	9.26E-16	3714.1	9.9	14	89.50	3.29E-03	-4.97
38	850	1.32E-15	3763.9	7.1	29	91.10	2.87E-03	-5.08
39	875	8.64E-16	3715.7	8.3	14	92.10	2.51E-03	-4.89
40	875	1.12E-15	3764.1	8.8	29	93.30	2.57E-03	-5.04
41	900	6.16E-16	3671.2	13.2	14	94.00	3.29E-03	-4.92
42	900	7.46E-16	3762.5	8.5	29	94.80	3.72E-03	-5.10
43	925	4.18E-16	3675.5	13.7	14	95.30	4.07E-03	-4.98
44	925	5.48E-16	3729.8	10.2	29	95.80	4.22E-03	-5.14
45	950	3.05E-16	3624.8	15.0	14	96.20	4.70E-03	-5.03
46	950	3.86E-16	3689.4	12.9	29	96.60	4.73E-03	-5.21
47	975	2.28E-16	3556.8	15.3	14	96.80	5.30E-03	-5.08
48	975	2.85E-16	3663.2	14.0	29	97.10	5.24E-03	-5.26
49	1000	1.92E-16	3571.2	19.1	14	97.30	5.87E-03	-5.08
50	1025	4.16E-16	3609.9	11.9	29	97.70	5.69E-03	-5.01
51	1025	9.99E-17	3548.7	26.6	14	97.80	4.77E-03	-5.27
52	1050	2.32E-16	3625.0	14.8	29	98.10	4.42E-03	-5.19
53	1050	5.64E-17	3493.8	43.6	14	98.10	3.75E-03	-5.45
54	1100	1.71E-16	3635.9	20.5	29	98.30	3.59E-03	-5.26
55	1100	4.04E-17	3458.6	52.0	14	98.30	3.43E-03	-5.55
56	1150	9.38E-17	3607.5	29.4	14	98.40	2.81E-03	-5.16
57	1150	5.98E-17	3893.6	41.0	29	98.50	2.29E-03	-5.65
58	1200	8.12E-17	3585.4	31.7	9	98.60	1.85E-03	-4.99
59	1300	4.78E-16	3660.6	10.9	9	99.00	1.44E-03	-4.13
60	1670	9.81E-16	3813.8	8.0	9	100.00	2.35E-03	-2.85
67514,24								
1	350	7.00E-18	-15.6	61.5	3.75	0.09	1.57E+00	-9.54
2	375	1.68E-18	1130.0	2070.0	3.75	0.11	5.12E-03	-9.81

3	400	5.27E-18	635.0	414.0	3.75	0.17	6.51E-03	-9.16
4	425	9.32E-18	2160.0	567.0	3.75	0.29	6.71E-03	-8.69
5	450	7.91E-18	1470.0	526.0	3.75	0.38	5.44E-02	-8.60
6	475	9.22E-18	1130.0	399.0	3.75	0.50	1.68E-02	-8.41
7	500	1.34E-17	895.0	217.0	3.75	0.66	5.92E-02	-8.13
8	525	2.99E-17	3070.0	182.0	3.75	1.03	4.32E-03	-7.62
9	550	1.81E-17	3450.0	336.0	3.75	1.25	3.06E-03	-7.70
10	575	2.87E-17	2920.0	215.0	3.75	1.60	4.85E-03	-7.40
11	600	2.55E-16	3520.0	25.6	3.75	4.74	2.83E-03	-6.10
12	625	5.88E-17	3360.0	98.7	3.75	5.46	2.96E-03	-6.53
13	650	1.59E-16	3570.0	40.1	3.75	7.41	2.67E-03	-5.99
14	675	1.82E-16	3680.0	33.9	3.75	9.65	2.46E-03	-5.80
15	700	1.97E-16	3760.0	30.9	3.75	12.10	2.33E-03	-5.65
16	725	1.94E-16	3840.0	31.9	3.75	14.40	2.20E-03	-5.56
17	750	1.85E-16	3870.0	32.2	3.75	16.70	2.17E-03	-5.50
18	775	1.67E-16	3900.0	35.3	3.75	18.80	2.15E-03	-5.48
19	800	2.13E-16	3880.0	26.7	3.75	21.40	2.17E-03	-5.31
20	750	2.35E-16	3880.0	23.0	14.8	24.30	2.65E-03	-5.80
21	700	1.04E-16	3880.0	56.5	39.8	25.60	2.86E-03	-6.54
22	825	1.04E-16	3820.0	63.2	3.75	26.80	2.26E-03	-5.48
23	850	1.66E-16	3800.0	38.0	3.75	28.90	2.29E-03	-5.25
24	875	1.56E-16	3830.0	42.0	3.75	30.80	2.28E-03	-5.23
25	900	1.65E-16	3870.0	37.5	3.75	32.80	2.23E-03	-5.17
26	925	1.30E-16	3810.0	50.7	3.75	34.40	2.29E-03	-5.24
27	950	1.22E-16	3840.0	53.0	3.75	35.90	2.29E-03	-5.24
28	975	9.93E-17	3790.0	61.5	3.75	37.10	2.33E-03	-5.31
29	1000	5.18E-16	3890.0	12.7	3.75	43.50	2.22E-03	-4.53
30	1030	3.71E-16	3840.0	18.1	3.75	48.00	2.28E-03	-4.58
31	1050	2.72E-16	3750.0	23.6	3.75	51.40	2.38E-03	-4.66
32	1080	2.13E-16	3690.0	28.6	3.75	54.00	2.43E-03	-4.72
33	1100	5.27E-16	3840.0	12.1	3.75	60.50	2.17E-03	-4.25
34	1050	5.54E-16	3840.0	10.1	14.8	67.30	4.76E-03	-4.72
35	1000	4.40E-16	3840.0	12.8	39.8	72.70	6.71E-03	-5.15
36	1130	4.89E-16	3870.0	13.4	3.75	78.70	1.85E-03	-3.97
37	1150	4.05E-16	3750.0	16.1	3.75	83.60	1.84E-03	-3.93
38	1180	3.50E-16	3710.0	19.0	3.75	87.90	1.94E-03	-3.87
39	1650	9.81E-16	3980.0	9.8	0.75	100.00	1.81E-03	-1.67

67514,43

1	400	2.29E-16	2574.1	12.0	10	3.19	2.78E-03	-6.82
2	425	1.30E-16	2438.4	19.1	10	5.00	2.51E-03	-6.65
3	450	1.26E-16	2367.1	17.1	10	6.77	2.39E-03	-6.50

4	475	1.42E-16	2355.6	15.9	10	8.75	2.22E-03	-6.32
5	500	1.71E-16	2390.7	15.2	10	11.14	2.12E-03	-6.13
6	525	1.77E-16	2566.5	14.0	10	13.61	1.95E-03	-6.00
7	550	1.91E-16	2713.7	14.0	10	16.28	1.81E-03	-5.88
8	575	2.07E-16	2875.4	16.0	10	19.16	1.71E-03	-5.76
9	600	2.39E-16	2995.8	13.3	10	22.50	1.63E-03	-5.61
10	550	8.13E-17	3213.2	29.9	40	23.64	1.47E-03	-6.63
11	500	2.44E-17	3370.1	105.9	120	23.98	1.44E-03	-7.62
12	625	1.74E-16	3353.8	18.4	10	26.40	1.39E-03	-5.65
13	650	2.37E-16	3395.2	14.8	10	29.70	1.36E-03	-5.46
14	675	2.60E-16	3513.9	16.2	10	33.33	1.30E-03	-5.35
15	700	2.66E-16	3549.5	14.2	10	37.04	1.30E-03	-5.27
16	725	2.92E-16	3572.5	12.7	10	41.11	1.32E-03	-5.17
17	750	3.18E-16	3583.1	11.8	10	45.56	1.32E-03	-5.06
18	775	3.51E-16	3605.1	12.1	10	50.45	1.33E-03	-4.94
19	800	3.44E-16	3679.4	12.9	10	55.25	1.29E-03	-4.88
20	750	1.61E-16	3786.1	20.2	40	57.50	1.27E-03	-5.75
21	700	5.50E-17	4237.4	40.5	120	58.27	1.27E-03	-6.68
22	825	1.83E-16	3719.5	16.7	10	60.82	1.29E-03	-5.05
23	850	2.42E-16	3718.1	15.3	10	64.20	1.32E-03	-4.88
24	875	2.08E-16	3733.8	16.5	10	67.10	1.32E-03	-4.90
25	900	1.74E-16	3737.7	18.6	10	69.53	1.33E-03	-4.93
26	925	1.58E-16	3701.3	17.7	10	71.73	1.38E-03	-4.93
27	950	1.34E-16	3702.4	22.5	10	73.60	1.39E-03	-4.96
28	975	1.02E-16	3477.3	23.1	10	75.03	1.47E-03	-5.05
29	1000	7.00E-17	3158.6	29.7	10	76.00	1.53E-03	-5.19
30	1025	5.51E-17	2897.9	34.3	10	76.77	1.45E-03	-5.28
31	1050	5.59E-17	2808.8	33.6	10	77.55	1.36E-03	-5.26
32	1050	5.99E-17	3167.9	35.8	22	78.39	1.17E-03	-5.55
33	1100	2.11E-16	3946.5	15.7	10	81.34	1.95E-03	-4.62
34	1050	1.52E-16	4069.6	20.7	40	83.47	1.63E-03	-5.30
35	1000	2.11E-17	3731.2	101.1	120	83.76	1.20E-03	-6.60
36	1125	3.39E-17	3220.6	51.9	10	84.24	1.02E-03	-5.31
37	1150	7.04E-17	3467.9	31.4	10	85.22	1.01E-03	-5.00
38	1150	9.61E-17	3710.9	27.6	22	86.56	9.87E-04	-5.14
39	1200	1.74E-16	3792.6	18.5	10	88.98	8.60E-04	-4.47
40	1300	1.34E-16	3871.0	24.6	10	90.85	7.69E-04	-4.50
41	1350	9.16E-17	3845.9	30.0	10	92.13	1.14E-03	-4.59
42	1400	1.37E-16	3951.5	19.1	10	94.04	1.10E-03	-4.33
43	1670	4.04E-16	3995.0	13.4	6	99.69	1.17E-03	-3.08
44	1670	2.24E-17	3088.4	112.5	6	100.00	3.26E-03	-2.79

67704,9

1	400	2.96E-16	1380.0	14.1	10	2.58	5.36E-03	-7.01
2	425	1.58E-16	442.0	11.9	10	3.96	5.61E-03	-6.87
3	450	1.61E-16	297.0	13.1	10	5.36	5.40E-03	-6.70
4	475	2.03E-16	254.0	10.4	10	7.13	5.50E-03	-6.47
5	500	2.38E-16	217.0	8.6	10	9.20	5.19E-03	-6.28
6	525	2.82E-16	226.0	7.6	10	11.70	4.78E-03	-6.09
7	550	3.48E-16	199.0	5.6	10	14.70	4.83E-03	-5.89
8	575	4.03E-16	209.0	6.0	10	18.20	4.87E-03	-5.71
9	600	4.53E-16	220.0	4.4	10	22.20	4.54E-03	-5.56
10	550	1.61E-16	110.0	11.2	40	23.60	4.92E-03	-6.54
			-					
11	500	5.57E-17	1770.0	546.0	120	24.00	5.25E-03	-7.46
12	625	2.84E-16	190.0	7.3	10	26.50	4.46E-03	-5.64
13	650	3.50E-16	198.0	5.8	10	29.60	4.44E-03	-5.49
14	675	3.93E-16	236.0	5.3	10	33.00	4.59E-03	-5.38
15	700	4.35E-16	284.0	5.0	10	36.80	4.59E-03	-5.27
16	725	5.12E-16	417.0	8.8	10	41.30	4.84E-03	-5.13
17	750	4.33E-16	573.0	11.0	10	45.00	4.65E-03	-5.13
18	775	4.66E-16	905.0	12.3	10	49.10	4.84E-03	-5.04
19	800	3.91E-16	1350.0	10.8	10	52.50	4.87E-03	-5.06
20	750	2.19E-16	1790.0	16.9	40	54.40	4.99E-03	-5.87
21	700	1.39E-16	2240.0	29.6	120	55.60	5.12E-03	-6.52
22	825	2.28E-16	2250.0	18.0	10	57.60	4.87E-03	-5.20
23	850	2.61E-16	2510.0	17.9	10	59.90	4.92E-03	-5.11
24	875	2.32E-16	2900.0	21.4	10	61.90	4.74E-03	-5.13
25	900	1.68E-16	3180.0	26.2	10	63.40	4.52E-03	-5.24
26	925	1.82E-16	3220.0	24.5	10	65.00	4.75E-03	-5.18
27	950	1.72E-16	3280.0	39.8	10	66.50	5.03E-03	-5.18
28	975	1.42E-16	3340.0	33.2	10	67.70	4.93E-03	-5.24
29	1000	1.72E-16	3310.0	49.4	10	69.20	4.49E-03	-5.14
30	1030	1.67E-16	3390.0	46.0	10	70.70	4.09E-03	-5.12
31	1050	1.62E-16	3350.0	79.2	10	72.10	4.71E-03	-5.11
32	1050	2.49E-16	3340.0	37.3	22	74.20	4.40E-03	-5.23
33	1100	1.58E-16	3210.0	24.6	10	75.60	4.78E-03	-5.05
34	1050	1.31E-16	3280.0	47.4	40	76.80	4.59E-03	-5.71
35	1000	7.87E-17	3250.0	36.4	120	77.40	4.05E-03	-6.39
36	1130	1.70E-16	3430.0	37.0	10	78.90	3.74E-03	-4.95
37	1150	3.15E-16	3530.0	15.7	10	81.70	3.69E-03	-4.64
38	1150	2.68E-16	3570.0	14.0	22	84.00	3.31E-03	-4.99
39	1200	3.31E-16	3630.0	13.2	10	86.90	2.52E-03	-4.48
40	1300	4.66E-16	3720.0	16.5	10	91.00	1.99E-03	-4.20

41	1350	1.55E-16	3900.0	54.6	10	92.30	2.76E-03	-4.56
42	1410	2.37E-16	3710.0	33.2	10	94.40	3.12E-03	-4.28
43	1670	5.54E-16	4040.0	32.6	6	99.20	2.50E-03	-3.26
44	1670	9.06E-17	3190.0	49.4	6	100.00	3.36E-03	-2.73

67704,11

1	400	1.19E-16	4370.7	25.8	11	0.46	4.18E-03	-8.54
2	425	9.86E-17	3983.9	28.3	11	0.84	4.07E-03	-8.19
3	450	9.96E-17	3804.5	26.2	11	1.22	3.99E-03	-7.98
4	475	1.19E-16	3770.8	21.7	11	1.67	3.87E-03	-7.75
5	500	1.49E-16	3692.0	18.4	11	2.24	3.77E-03	-7.52
6	525	1.92E-16	3720.9	17.3	11	2.98	3.62E-03	-7.28
7	550	2.61E-16	3679.1	13.2	11	3.98	3.49E-03	-7.02
8	575	3.01E-16	3754.9	11.2	11	5.13	3.28E-03	-6.84
9	600	3.59E-16	3774.8	11.1	11	6.51	3.13E-03	-6.65
10	550	1.26E-16	3981.8	22.5	41	6.99	2.86E-03	-7.61
11	500	3.24E-17	4872.6	76.4	121	7.12	2.53E-03	-8.65
12	625	3.03E-16	3856.5	11.8	11	8.28	2.81E-03	-6.60
13	650	4.35E-16	3832.4	8.5	11	9.95	2.75E-03	-6.36
14	675	5.07E-16	3852.7	8.6	11	11.89	2.69E-03	-6.21
15	700	5.45E-16	3871.3	9.5	11	13.98	2.72E-03	-6.10
16	725	6.17E-16	3865.8	7.4	11	16.35	2.77E-03	-5.97
17	750	6.93E-16	3854.4	8.7	11	19.01	2.84E-03	-5.84
18	775	5.25E-16	3839.2	9.1	11	21.02	2.89E-03	-5.90
19	800	6.45E-16	3855.0	8.5	11	23.50	2.93E-03	-5.75
20	750	4.03E-16	3937.3	10.0	41	25.04	2.88E-03	-6.48
21	700	2.11E-16	4082.0	14.0	121	25.85	2.96E-03	-7.21
22	825	4.95E-16	3913.2	9.3	11	27.75	2.87E-03	-5.77
23	850	6.69E-16	3911.0	8.0	11	30.31	2.87E-03	-5.59
24	875	7.79E-16	3900.9	7.9	11	33.30	2.93E-03	-5.47
25	900	8.37E-16	3898.3	9.4	11	36.52	2.96E-03	-5.38
26	925	8.07E-16	3925.7	9.2	11	39.61	2.94E-03	-5.34
27	950	7.98E-16	3854.2	7.9	11	42.67	3.12E-03	-5.30
28	975	6.97E-16	3855.8	10.5	11	45.34	3.14E-03	-5.31
29	1000	5.72E-16	3798.4	8.1	11	47.54	3.23E-03	-5.36
30	1025	4.55E-16	3711.6	10.9	11	49.29	3.20E-03	-5.43
31	1050	4.36E-16	3754.5	9.4	11	50.96	2.98E-03	-5.42
32	1050	4.32E-16	3786.6	9.6	23	52.62	2.95E-03	-5.72
33	1100	3.77E-16	3761.6	9.8	11	54.06	2.96E-03	-5.43
34	1050	3.23E-16	3973.1	11.9	41	55.30	2.70E-03	-6.05
35	1000	1.59E-16	4089.6	18.0	121	55.91	3.24E-03	-6.81
36	1125	2.40E-16	3800.0	12.6	11	56.83	2.71E-03	-5.58

37	1150	5.31E-16	3854.1	7.5	11	58.87	2.70E-03	-5.21
38	1150	4.78E-16	3842.0	9.6	23	60.70	2.67E-03	-5.55
39	1200	4.87E-16	3891.2	9.3	11	62.57	2.50E-03	-5.19
40	1300	8.27E-16	4115.4	7.6	11	65.75	2.29E-03	-4.92
41	1400	3.56E-15	4131.2	4.1	11	79.39	2.47E-03	-4.13
42	1670	5.12E-15	4080.1	5.3	7	99.03	2.40E-03	-3.13
43	1670	2.54E-16	2709.9	48.2	7	100.00	5.19E-03	-2.78

67714,16

1	400	1.53E-17	5350.0	134.0	11	0.11	0.66395	-9.78
2	425	2.71E-17	4490.0	73.9	11	0.31	0.48712	-8.95
3	450	2.73E-17	4600.0	72.5	11	0.51	0.50994	-8.66
4	475	3.40E-17	4420.0	60.5	11	0.76	0.44428	-8.37
5	500	4.24E-17	4230.0	49.3	11	1.07	0.40733	-8.12
6	525	5.63E-17	4130.0	36.6	11	1.49	0.38364	-7.85
7	550	8.42E-17	3950.0	24.5	11	2.11	0.3557	-7.52
8	575	1.29E-16	3860.0	17.8	11	3.05	0.38033	-7.18
9	600	1.57E-16	3860.0	14.7	11	4.21	0.38206	-6.94
10	625	2.23E-16	3820.0	10.8	11	5.85	0.37766	-6.64
11	650	2.61E-16	3860.0	11.8	11	7.77	0.41501	-6.44
12	675	3.21E-16	3860.0	8.7	11	10.10	0.42924	-6.22
13	700	3.47E-16	3900.0	9.0	11	12.70	0.44953	-6.07
14	725	4.00E-16	3930.0	7.4	11	15.60	0.46278	-5.91
15	750	4.54E-16	3930.0	7.4	11	19.00	0.46297	-5.75
16	775	5.23E-16	3930.0	7.7	11	22.80	0.4633	-5.59
17	800	5.78E-16	3930.0	7.8	11	27.10	0.45293	-5.45
18	750	4.62E-16	4000.0	7.4	61	30.50	0.45496	-6.22
19	700	1.38E-16	4220.0	18.4	121	31.50	0.48645	-7.00
20	825	3.76E-16	4010.0	8.5	11	34.20	0.45598	-5.48
21	850	5.12E-16	3990.0	6.6	11	38.00	0.43131	-5.29
22	875	6.10E-16	3980.0	7.0	11	42.50	0.42685	-5.15
23	900	6.86E-16	3980.0	7.6	11	47.50	0.41222	-5.02
24	925	6.77E-16	3980.0	7.0	11	52.50	0.40107	-4.95
25	950	6.47E-16	3950.0	7.4	11	57.30	0.39987	-4.89
26	975	5.29E-16	3970.0	8.3	11	61.20	0.39933	-4.91
27	1000	4.16E-16	3840.0	8.9	11	64.20	0.37652	-4.96
28	1030	3.01E-16	3690.0	10.3	11	66.40	0.39729	-5.06
29	1050	2.46E-16	3590.0	12.3	11	68.30	0.42707	-5.11
30	1100	3.37E-16	3680.0	9.2	11	70.70	0.44648	-4.94
31	1150	7.69E-16	3900.0	6.7	11	76.40	0.42079	-4.51
32	1200	9.64E-16	3790.0	5.5	11	83.50	0.45477	-4.27
33	1300	4.19E-16	3870.0	9.7	11	86.60	0.49018	-4.51

34	1670	1.83E-15	4080.0	5.9	11	100.00	0.45986	-2.84
67714,20								
1	400	3.80E-17	4890.0	52.6	10	0.16	4.98E-03	-9.43
2	425	2.71E-17	4590.0	62.3	10	0.27	5.37E-03	-9.14
3	450	2.66E-17	3920.0	68.8	10	0.39	4.56E-03	-8.97
4	475	2.74E-17	3790.0	68.6	10	0.50	4.66E-03	-8.82
5	500	3.17E-17	3680.0	54.9	10	0.64	4.64E-03	-8.65
6	525	4.22E-17	3650.0	42.7	10	0.81	4.30E-03	-8.42
7	550	5.86E-17	3650.0	30.8	10	1.06	4.15E-03	-8.17
8	575	6.57E-17	3700.0	32.9	10	1.34	3.88E-03	-8.01
9	600	9.36E-17	3750.0	26.5	10	1.73	3.73E-03	-7.75
10	550	4.10E-17	3840.0	44.3	40	1.91	3.70E-03	-8.63
11	500	1.47E-17	3920.0	146.0	120	1.97	3.49E-03	-9.53
12	625	1.03E-16	3860.0	24.3	10	2.40	3.37E-03	-7.55
13	650	1.47E-16	3820.0	18.6	10	3.02	3.40E-03	-7.30
14	675	1.85E-16	3840.0	17.5	10	3.80	3.30E-03	-7.10
15	700	2.31E-16	3890.0	16.2	10	4.77	3.32E-03	-6.90
16	725	2.84E-16	3870.0	13.1	10	5.97	3.26E-03	-6.71
17	750	3.33E-16	3880.0	11.6	10	7.37	3.24E-03	-6.54
18	775	3.96E-16	3880.0	11.8	10	9.04	3.38E-03	-6.37
19	800	4.78E-16	3890.0	10.4	10	11.10	3.50E-03	-6.19
20	750	3.05E-16	3950.0	14.0	40	12.30	3.64E-03	-6.92
21	700	1.61E-16	4080.0	16.2	120	13.00	3.83E-03	-7.63
22	825	3.45E-16	3910.0	12.2	10	14.50	3.61E-03	-6.18
23	850	4.53E-16	3890.0	8.7	10	16.40	3.71E-03	-6.01
24	875	5.20E-16	3910.0	11.0	10	18.60	3.77E-03	-5.89
25	900	5.67E-16	3900.0	9.5	10	21.00	3.74E-03	-5.79
26	925	5.96E-16	3900.0	9.3	10	23.50	3.83E-03	-5.70
27	950	5.31E-16	3870.0	9.4	10	25.70	3.83E-03	-5.70
28	975	4.02E-16	3840.0	10.5	10	27.40	3.88E-03	-5.78
29	1000	2.70E-16	3810.0	13.3	10	28.50	3.86E-03	-5.92
30	1030	2.22E-16	3490.0	14.5	10	29.50	3.53E-03	-5.99
31	1050	1.34E-16	3770.0	20.9	10	30.10	3.91E-03	-6.19
32	1050	1.27E-16	3860.0	24.2	22	30.60	3.76E-03	-6.55
33	1100	8.78E-17	3690.0	29.7	10	31.00	3.54E-03	-6.35
34	1050	4.68E-17	3770.0	43.5	40	31.20	3.54E-03	-7.22
35	1000	3.32E-17	3920.0	63.3	120	31.30	3.65E-03	-7.85
36	1130	1.17E-16	4050.0	23.5	10	31.80	3.47E-03	-6.22
37	1150	3.30E-16	4110.0	11.8	10	33.20	3.54E-03	-5.75
38	1150	1.52E-16	4060.0	20.8	22	33.80	3.55E-03	-6.41
39	1200	3.35E-16	4120.0	14.5	10	35.20	3.55E-03	-5.70

40	1300	2.07E-15	4170.0	6.1	10	44.00	3.38E-03	-4.83
41	1350	3.67E-15	4160.0	6.4	10	59.40	3.45E-03	-4.38
42	1410	5.48E-15	4150.0	5.7	10	82.60	3.45E-03	-3.88
43	1670	3.74E-15	4090.0	5.3	6	98.30	3.69E-03	-3.18
44	1670	3.97E-16	3670.0	20.5	6	100.00	4.17E-03	-2.68

67714,23

1	400	2.71E-17	6030.0	79.0	10	0.22	3.74E-03	-9.16
2	425	2.18E-17	5430.0	96.3	10	0.40	3.82E-03	-8.80
3	450	2.32E-17	4800.0	89.0	10	0.58	3.88E-03	-8.57
4	475	3.32E-17	4380.0	61.8	10	0.85	3.78E-03	-8.25
5	500	4.36E-17	4180.0	46.0	10	1.20	3.65E-03	-7.97
6	525	6.19E-17	3990.0	33.0	10	1.70	3.60E-03	-7.67
7	550	8.69E-17	3890.0	25.3	10	2.41	3.51E-03	-7.37
8	575	1.21E-16	3840.0	18.6	10	3.39	3.44E-03	-7.07
9	600	1.54E-16	3830.0	15.0	10	4.64	3.12E-03	-6.82
10	625	1.97E-16	3860.0	13.4	10	6.23	3.12E-03	-6.58
11	650	2.23E-16	3950.0	12.5	10	8.03	4.20E-03	-6.40
12	675	2.89E-16	3870.0	10.5	10	10.40	3.04E-03	-6.17
13	700	3.25E-16	3920.0	10.4	10	13.00	3.02E-03	-6.01
14	725	3.61E-16	3910.0	9.4	10	15.90	2.99E-03	-5.86
15	750	3.83E-16	3960.0	10.1	10	19.00	3.00E-03	-5.74
16	775	4.40E-16	3930.0	7.8	10	22.60	2.97E-03	-5.59
17	800	4.83E-16	3930.0	8.2	10	26.50	2.99E-03	-5.46
18	750	3.75E-16	4010.0	8.7	60	29.50	2.92E-03	-6.27
19	700	1.12E-16	4250.0	20.6	120	30.40	3.01E-03	-7.06
20	825	2.99E-16	4010.0	10.3	10	32.80	2.90E-03	-5.52
21	850	4.00E-16	4010.0	8.9	10	36.10	2.99E-03	-5.35
22	875	4.80E-16	3950.0	10.0	10	40.00	2.94E-03	-5.21
23	900	5.00E-16	3970.0	6.2	10	44.00	2.99E-03	-5.12
24	925	4.96E-16	3960.0	8.5	10	48.00	3.03E-03	-5.06
25	950	4.49E-16	3980.0	7.1	10	51.70	3.00E-03	-5.05
26	975	3.85E-16	3980.0	9.3	10	54.80	3.07E-03	-5.06
27	1000	3.22E-16	3900.0	10.7	10	57.40	3.03E-03	-5.09
28	1030	2.42E-16	3870.0	13.3	10	59.30	2.98E-03	-5.18
29	1050	1.86E-16	3860.0	14.5	10	60.80	2.82E-03	-5.27
30	1100	1.77E-16	3880.0	14.8	10	62.30	2.92E-03	-5.27
31	1150	3.82E-16	3820.0	9.9	10	65.40	3.01E-03	-4.90
32	1200	4.91E-16	3740.0	8.1	10	69.30	3.05E-03	-4.73
33	1300	4.34E-16	4010.0	8.9	10	72.90	3.14E-03	-4.72
34	1670	3.36E-15	4160.0	4.0	6.83	100.00	2.76E-03	-2.60

67714,25

1	400	9.44E-17	3390.0	29.3	10	0.21	5.13E-03	-9.18
2	425	8.64E-17	3560.0	27.3	10	0.41	4.43E-03	-8.76
3	450	9.22E-17	3530.0	25.5	10	0.61	4.32E-03	-8.51
4	475	1.01E-16	3580.0	24.8	10	0.84	4.38E-03	-8.32
5	500	1.26E-16	3590.0	21.1	10	1.13	4.20E-03	-8.09
6	525	1.63E-16	3630.0	21.6	10	1.49	4.11E-03	-7.85
7	550	2.18E-16	3640.0	14.2	10	1.98	3.93E-03	-7.60
8	575	2.98E-16	3670.0	11.0	10	2.65	3.79E-03	-7.34
9	600	3.63E-16	3720.0	14.0	10	3.47	3.65E-03	-7.13
10	550	1.79E-16	3730.0	16.1	40	3.87	3.51E-03	-7.96
11	500	6.43E-17	3690.0	42.6	120	4.02	3.39E-03	-8.85
12	625	3.08E-16	3770.0	13.0	10	4.71	3.39E-03	-7.04
13	650	4.92E-16	3800.0	9.8	10	5.81	3.30E-03	-6.75
14	675	6.11E-16	3790.0	8.9	10	7.19	3.32E-03	-6.56
15	700	7.08E-16	3830.0	8.6	10	8.78	3.21E-03	-6.40
16	725	8.12E-16	3830.0	8.5	10	10.60	3.25E-03	-6.25
17	750	9.50E-16	3800.0	8.0	10	12.70	3.39E-03	-6.10
18	775	1.11E-15	3840.0	8.5	10	15.20	3.48E-03	-5.94
19	800	1.24E-15	3850.0	8.4	10	18.00	3.58E-03	-5.81
20	750	8.18E-16	3880.0	7.6	40	19.90	3.70E-03	-6.53
21	700	4.42E-16	3940.0	11.8	120	20.80	3.78E-03	-7.23
22	825	9.25E-16	3890.0	7.1	10	22.90	3.55E-03	-5.79
23	850	1.25E-15	3880.0	6.8	10	25.70	3.66E-03	-5.61
24	875	1.52E-15	3870.0	6.9	10	29.10	3.73E-03	-5.46
25	900	1.65E-15	3880.0	6.3	10	32.90	3.77E-03	-5.35
26	925	1.71E-15	3870.0	7.1	10	36.70	3.83E-03	-5.27
27	950	1.70E-15	3850.0	9.0	10	40.50	3.89E-03	-5.20
28	975	1.56E-15	3840.0	6.8	10	44.00	3.92E-03	-5.18
29	1000	1.39E-15	3820.0	8.0	10	47.20	3.97E-03	-5.18
30	1030	1.16E-15	3800.0	7.2	10	49.80	3.89E-03	-5.21
31	1050	1.02E-15	3790.0	8.3	10	52.10	3.85E-03	-5.23
32	1050	8.72E-16	3810.0	7.0	22	54.00	3.73E-03	-5.61
33	1100	5.94E-16	3770.0	9.6	10	55.40	3.87E-03	-5.41
34	1050	2.95E-16	3820.0	15.0	40	56.00	3.88E-03	-6.30
35	1000	1.88E-16	4000.0	17.0	120	56.40	3.91E-03	-6.96
36	1130	1.36E-15	3940.0	7.6	10	59.50	3.59E-03	-5.00
37	1150	1.74E-15	3940.0	7.7	10	63.40	3.56E-03	-4.83
38	1150	9.40E-16	3830.0	8.8	22	65.50	3.49E-03	-5.40
39	1200	6.22E-16	3770.0	11.7	10	66.90	3.10E-03	-5.20
40	1300	7.02E-16	4000.0	9.9	10	68.50	3.57E-03	-5.13
41	1350	1.54E-15	4030.0	7.2	10	72.00	3.49E-03	-4.74
42	1410	7.21E-15	4050.0	24.6	10	88.20	3.58E-03	-3.85

43	1670	4.98E-15	4030.0	9.9	6	99.30	3.58E-03	-3.09
44	1670	2.94E-16	2860.0	38.8	6	100.00	6.87E-03	-2.74
67714,27								
1	400	3.68E-17	5520.0	63.6	10	0.20	5.43E-03	-9.26
2	425	2.44E-17	3890.0	83.6	10	0.33	6.17E-03	-9.01
3	450	2.28E-17	3590.0	78.6	10	0.45	5.11E-03	-8.87
4	475	2.73E-17	3590.0	68.1	10	0.59	5.42E-03	-8.66
5	500	3.35E-17	3540.0	53.4	10	0.77	4.78E-03	-8.45
6	525	4.60E-17	3480.0	41.6	10	1.01	4.69E-03	-8.20
7	550	5.81E-17	3600.0	33.3	10	1.32	4.41E-03	-7.98
8	575	7.94E-17	3600.0	29.7	10	1.74	4.25E-03	-7.72
9	600	9.72E-17	3760.0	23.2	10	2.26	3.78E-03	-7.52
10	550	4.33E-17	3720.0	46.5	40	2.49	3.63E-03	-8.39
11	500	1.43E-17	3720.0	148.0	120	2.56	3.60E-03	-9.33
12	625	8.73E-17	3820.0	26.0	10	3.02	3.57E-03	-7.42
13	650	1.50E-16	3740.0	19.1	10	3.82	3.71E-03	-7.09
14	675	1.77E-16	3860.0	16.8	10	4.75	3.40E-03	-6.92
15	700	2.21E-16	3860.0	17.5	10	5.93	3.37E-03	-6.72
16	725	2.62E-16	3870.0	14.0	10	7.31	3.40E-03	-6.55
17	750	3.06E-16	3850.0	15.0	10	8.94	3.53E-03	-6.39
18	775	3.55E-16	3860.0	14.0	10	10.80	3.66E-03	-6.23
19	800	3.90E-16	3900.0	11.3	10	12.90	3.74E-03	-6.10
20	750	2.54E-16	3940.0	13.6	40	14.20	3.83E-03	-6.83
21	700	1.35E-16	4060.0	21.5	120	15.00	3.97E-03	-7.54
22	825	3.03E-16	3900.0	12.3	10	16.60	3.79E-03	-6.07
23	850	3.98E-16	3890.0	10.5	10	18.70	3.86E-03	-5.90
24	875	4.63E-16	3910.0	11.3	10	21.10	3.87E-03	-5.77
25	900	4.93E-16	3910.0	10.0	10	23.70	3.98E-03	-5.68
26	925	4.71E-16	3900.0	9.8	10	26.20	3.94E-03	-5.64
27	950	4.32E-16	3860.0	10.9	10	28.50	4.00E-03	-5.63
28	975	3.46E-16	3860.0	13.0	10	30.40	3.99E-03	-5.69
29	1000	2.47E-16	3840.0	14.6	10	31.70	4.09E-03	-5.80
30	1030	1.83E-16	3690.0	19.7	10	32.60	4.23E-03	-5.91
31	1050	1.41E-16	3680.0	20.8	10	33.40	4.19E-03	-6.01
32	1050	1.27E-16	3770.0	19.8	22	34.10	4.01E-03	-6.38
33	1100	7.69E-17	3820.0	31.3	10	34.50	3.87E-03	-6.25
34	1050	9.30E-17	3980.0	27.9	40	35.00	3.28E-03	-6.76
35	1000	3.39E-17	3950.0	67.1	120	35.10	3.83E-03	-7.67
36	1130	3.73E-16	4120.0	11.0	10	37.10	3.61E-03	-5.53
37	1150	3.09E-16	4100.0	13.0	10	38.80	3.60E-03	-5.58
38	1150	1.28E-16	4030.0	20.9	22	39.40	3.68E-03	-6.29

39	1200	2.00E-16	4100.0	16.0	10	40.50	3.54E-03	-5.74
40	1300	1.25E-15	4150.0	7.1	10	47.10	3.62E-03	-4.88
41	1350	4.17E-15	4140.0	5.4	10	69.20	3.62E-03	-4.12
42	1410	3.05E-15	4110.0	6.8	10	85.40	3.69E-03	-3.92
43	1670	2.61E-15	4080.0	6.6	6	99.20	3.67E-03	-3.09
44	1670	1.49E-16	2960.0	44.2	6	100.00	6.31E-03	-2.73

67944,21

1	400	8.39E-16	885.0	3.1	10	2.64	6.46E-02	-6.99
2	425	4.44E-16	179.0	4.4	10	4.04	6.94E-02	-6.85
3	450	4.41E-16	151.5	4.5	10	5.43	5.64E-02	-6.70
4	475	5.30E-16	140.4	3.7	10	7.10	5.46E-02	-6.49
5	500	6.47E-16	142.0	3.1	10	9.14	4.71E-02	-6.29
6	525	7.39E-16	146.0	2.7	10	11.46	3.88E-02	-6.12
7	550	8.21E-16	151.0	2.4	10	14.05	3.21E-02	-5.97
8	575	9.39E-16	161.1	2.1	10	17.01	2.28E-02	-5.82
9	600	1.03E-15	173.8	2.0	10	20.25	1.66E-02	-5.69
10	550	9.55E-16	134.2	1.9	40	23.26	2.98E-02	-6.24
11	500	6.72E-16	120.3	15.8	120	25.38	5.42E-02	-6.81
12	625	7.08E-16	197.7	2.8	10	27.61	9.60E-03	-5.66
13	650	9.38E-16	186.0	2.2	10	30.56	7.59E-03	-5.49
14	675	1.14E-15	177.7	1.8	10	34.15	6.24E-03	-5.34
15	700	1.26E-15	167.4	1.6	10	38.13	5.19E-03	-5.23
16	725	1.35E-15	160.4	1.6	10	42.37	4.35E-03	-5.13
17	750	1.42E-15	154.3	1.4	10	46.86	3.65E-03	-5.04
18	775	1.46E-15	152.1	1.4	10	51.46	3.08E-03	-4.95
19	800	1.49E-15	152.7	1.4	10	56.14	2.75E-03	-4.87
20	750	1.38E-15	195.8	0.7	40	60.49	3.23E-03	-5.44
21	700	1.02E-15	363.2	1.3	120	63.69	3.90E-03	-5.99
22	825	6.43E-16	189.0	3.1	10	65.72	2.66E-03	-5.07
23	850	7.44E-16	196.7	2.7	10	68.06	2.67E-03	-4.97
24	875	8.21E-16	198.7	2.4	10	70.64	2.78E-03	-4.88
25	900	7.36E-16	213.6	2.7	10	72.96	2.98E-03	-4.89
26	925	6.40E-16	242.0	3.0	10	74.98	3.24E-03	-4.91
27	950	5.88E-16	267.4	3.3	10	76.83	3.66E-03	-4.91
28	975	5.00E-16	287.6	3.9	10	78.41	4.06E-03	-4.94
29	1000	4.15E-16	303.1	4.7	10	79.71	4.41E-03	-4.99
30	1025	3.74E-16	275.4	5.5	10	80.89	4.62E-03	-5.01
31	1050	4.80E-16	1215.9	5.2	10	82.40	4.55E-03	-4.86
32	1050	3.80E-16	945.5	7.1	22	83.60	4.76E-03	-5.27
33	1100	3.99E-16	1217.0	6.0	10	84.86	5.71E-03	-4.88
34	1050	1.48E-16	2377.1	18.7	40	85.32	4.15E-03	-5.95

35	1000	5.82E-17	451.5	121.7	120	85.51	4.35E-03	-6.75
36	1125	1.48E-16	375.6	12.9	10	85.97	5.86E-03	-5.26
37	1150	1.58E-16	511.6	11.6	10	86.47	4.99E-03	-5.21
38	1150	1.06E-16	703.7	13.4	22	86.81	4.33E-03	-5.72
39	1200	4.03E-16	561.3	5.0	10	88.07	4.78E-03	-4.77
40	1300	1.42E-15	636.0	1.9	10	92.53	4.48E-03	-4.10
41	1350	3.25E-16	1554.3	6.9	10	93.56	3.38E-03	-4.60
42	1409	7.07E-16	1606.2	5.1	10	95.78	3.32E-03	-4.15
43	1670	1.26E-15	1662.6	4.7	6	99.74	2.71E-03	-3.11
44	1670	8.24E-17	1466.4	53.0	6	100.00	2.68E-03	-2.81

67944,23

1	400	3.12E-17	4249.6	36.3	11	0.19	3.74E-03	-9.30
2	425	3.03E-17	4265.3	39.6	11	0.38	3.82E-03	-8.84
3	450	2.77E-17	3986.6	40.3	11	0.56	3.88E-03	-8.67
4	475	4.04E-17	3843.0	27.5	11	0.81	3.78E-03	-8.34
5	500	5.03E-17	3738.8	26.9	11	1.12	3.65E-03	-8.09
6	525	6.48E-17	3765.5	20.4	11	1.53	3.60E-03	-7.85
7	550	9.44E-17	3800.5	14.9	11	2.11	3.51E-03	-7.54
8	575	1.39E-16	3813.9	12.4	11	2.98	3.44E-03	-7.23
9	600	4.72E-16	3957.7	7.1	41	5.92	3.12E-03	-7.02
10	550	1.34E-16	4007.5	12.6	121	6.75	3.12E-03	-7.87
11	500	2.14E-18	3610.1	421.4	11	6.76	4.20E-03	-8.60
12	625	1.02E-16	3946.7	14.5	11	7.40	3.04E-03	-6.90
13	650	1.99E-16	3933.3	9.6	11	8.64	3.02E-03	-6.55
14	675	3.22E-16	3913.5	9.8	11	10.65	2.99E-03	-6.26
15	700	3.35E-16	3937.1	7.6	11	12.74	3.00E-03	-6.15
16	725	4.43E-16	3914.0	7.5	11	15.50	2.97E-03	-5.93
17	750	4.90E-16	3884.8	9.6	11	18.56	2.99E-03	-5.80
18	775	5.09E-16	3904.6	8.0	11	21.73	2.92E-03	-5.70
19	800	5.47E-16	3885.0	7.9	11	25.14	3.01E-03	-5.58
20	750	3.35E-16	3921.2	9.7	41	27.22	2.90E-03	-6.31
21	700	1.78E-16	3997.0	10.0	121	28.33	2.99E-03	-7.02
22	825	4.32E-16	3911.9	6.3	11	31.03	2.94E-03	-5.56
23	850	5.86E-16	3905.7	9.3	11	34.68	2.99E-03	-5.36
24	875	7.22E-16	3883.4	6.4	11	39.18	3.03E-03	-5.20
25	900	8.29E-16	3885.5	5.7	11	44.34	3.00E-03	-5.06
26	925	8.79E-16	3878.3	5.7	11	49.82	3.07E-03	-4.95
27	950	9.62E-16	3875.9	6.1	11	55.82	3.03E-03	-4.82
28	975	9.03E-16	3842.9	6.9	11	61.45	2.98E-03	-4.76
29	1000	6.91E-16	3899.7	6.8	11	65.75	2.82E-03	-4.80
30	1025	4.95E-16	3820.8	8.5	11	68.83	2.92E-03	-4.88

31	1050	3.41E-16	3730.2	9.7	11	70.96	3.01E-03	-5.00
32	1050	4.74E-16	3276.2	5.9	23	73.91	3.05E-03	-5.13
33	1100	4.84E-16	2635.1	7.0	11	76.93	3.14E-03	-4.74
34	1125	1.35E-16	3728.8	12.7	11	77.77	2.76E-03	-5.26
35	1150	1.60E-16	3665.2	13.2	11	78.76	2.71E-03	-5.17
36	1150	1.45E-16	3908.4	13.1	23	79.67	2.49E-03	-5.51
37	1200	1.51E-16	3833.0	12.0	11	80.61	2.40E-03	-5.15
38	1300	3.99E-16	3895.2	9.0	11	83.09	2.38E-03	-4.68
39	1670	2.71E-15	3960.8	4.3	7	100.00	1.72E-03	-2.63

67944,29

1	350	9.46E-18	3255.6	701.0	3.75	0.08	6.28E-03	-9.63
2	375	1.04E-17	2044.7	462.8	3.75	0.16	6.28E-03	-9.10
3	400	1.08E-17	2247.7	453.2	3.75	0.25	6.28E-03	-8.84
4	425	1.43E-17	2188.5	340.1	3.75	0.37	5.96E-03	-8.55
5	450	6.36E-18	3962.9	1027.5	3.75	0.42	1.83E-03	-8.79
6	475	2.21E-17	2638.4	248.6	3.75	0.60	3.79E-03	-8.14
7	500	3.35E-17	2374.3	167.1	3.75	0.88	5.27E-03	-7.80
8	525	2.96E-17	2910.8	214.1	3.75	1.12	3.66E-03	-7.72
9	550	3.63E-17	3006.5	158.5	3.75	1.42	3.18E-03	-7.53
10	575	5.35E-17	2860.8	102.1	3.75	1.86	3.30E-03	-7.25
11	600	8.23E-17	2751.0	67.2	3.75	2.53	3.48E-03	-6.93
12	625	9.38E-17	2804.4	58.8	3.75	3.30	3.50E-03	-6.75
13	650	1.39E-16	3091.7	38.4	3.75	4.44	3.11E-03	-6.45
14	675	1.52E-16	3318.3	39.1	3.75	5.69	3.01E-03	-6.29
15	700	1.54E-16	3513.1	36.6	3.75	6.96	3.04E-03	-6.19
16	725	1.60E-16	3756.5	37.9	3.75	8.27	2.98E-03	-6.08
17	750	1.66E-16	3916.7	35.8	3.75	9.64	3.12E-03	-5.99
18	775	1.76E-16	4053.1	32.7	3.75	11.08	3.07E-03	-5.90
19	800	1.87E-16	4107.3	29.5	3.75	12.62	3.16E-03	-5.81
20	750	1.78E-16	4079.6	31.0	14.75	14.08	3.25E-03	-6.37
21	700	9.30E-17	4025.2	60.3	39.75	14.84	3.47E-03	-7.04
22	825	1.21E-16	4127.1	52.9	3.75	15.84	3.16E-03	-5.87
23	850	1.78E-16	4083.2	37.3	3.75	17.29	3.22E-03	-5.67
24	875	2.11E-16	4051.5	30.3	3.75	19.03	3.24E-03	-5.54
25	900	2.33E-16	4102.9	27.1	3.75	20.94	3.09E-03	-5.45
26	925	2.40E-16	4055.7	26.9	3.75	22.91	3.12E-03	-5.39
27	950	2.42E-16	4024.2	26.5	3.75	24.90	3.11E-03	-5.34
28	975	2.49E-16	3946.5	25.5	3.75	26.95	3.22E-03	-5.28
29	1000	2.42E-16	3990.3	27.0	3.75	28.93	3.08E-03	-5.25
30	1025	2.53E-16	3934.6	26.7	3.75	31.01	3.17E-03	-5.19
31	1050	2.62E-16	3937.8	23.4	3.75	33.16	3.13E-03	-5.14

32	1075	2.78E-16	3980.5	25.0	3.75	35.44	3.02E-03	-5.07
33	1100	2.63E-16	3932.3	24.7	3.75	37.60	3.13E-03	-5.06
34	1050	1.21E-16	3969.1	50.1	14.75	38.60	3.03E-03	-5.97
35	1100	6.33E-17	3774.4	97.8	39.75	39.12	3.36E-03	-6.66
36	1125	1.06E-16	4007.7	56.2	3.75	39.98	3.01E-03	-5.40
37	1150	1.39E-16	3998.4	46.0	3.75	41.13	2.83E-03	-5.27
38	1175	1.94E-16	4017.2	35.4	3.75	42.72	2.62E-03	-5.10
39	1200	2.18E-16	4085.9	30.3	1.75	44.51	2.64E-03	-4.69
40	1250	8.32E-16	4070.0	8.3	0.75	51.34	2.73E-03	-3.67
41	1300	1.78E-15	4099.4	3.9	0.75	65.99	2.74E-03	-3.17
42	1350	1.99E-15	4141.4	3.7	0.75	82.37	2.80E-03	-2.85
43	1400	8.32E-16	4160.0	8.5	0.75	89.20	2.93E-03	-2.96
44	1150	7.02E-16	4266.3	9.9	0.75	94.96	2.96E-03	-2.77
45	1650	6.14E-16	4397.6	12.4	0.75	100.00	2.88E-03	-1.72

---

**Notes:**

Isotopic ratios corrected for blank, radioactive decay, and mass discrimination, not corrected for interfering reactions.  
 Errors quoted for individual analyses include analytical error only, without interfering reaction or J uncertainties.

Plateau error is weighted error of Taylor (1982).

Decay constants and isotopic abundances after Steiger and Jäger (1977).

# symbol preceding sample ID denotes analyses excluded from plateau age calculations.

Weight percent K<sub>2</sub>O calculated from <sup>39</sup>Ar signal, sample weight, and instrument sensitivity.

Ages calculated relative to FC-2 Fish Canyon Tuff sanidine interlaboratory standard at 27.84 Ma

Decay Constant (LambdaK (total)) = 5.463e-10/a

Correction factors:

$$(^{39}\text{Ar}/^{37}\text{Ar})_{\text{Ca}} = 0.00069 \pm 2\text{e-}06$$

$$(^{36}\text{Ar}/^{37}\text{Ar})_{\text{Ca}} = 0.0002724 \pm 0$$

$$(^{38}\text{Ar}/^{39}\text{Ar})_{\text{K}} = 0.01077$$

$$(^{40}\text{Ar}/^{39}\text{Ar})_{\text{K}} = 0.0072 \pm 2\text{e-}05$$


---

**Table E.1:** <sup>40</sup>Ar/<sup>39</sup>Ar results for the Apollo 16 samples discussed in Chapter 5

## References

- Abe, Y., 1993. Physical state of the very early Earth. *Lithos* 30, 223–235.
- Abramov, O., Mojzsis, S.J., 2009. Microbial habitability of the Hadean Earth during the late heavy bombardment. *Nature* 459, 419–422.
- Albarède, F., 1978. The recovery of spatial isotope distributions from stepwise degassing data. *Earth Planet. Sci. Lett.* 39, 387–397.
- Alexander E.C. and Davis P.K. 1974.  $^{40}\text{Ar}$ - $^{39}\text{Ar}$  ages and trace element contents of Apollo 14 breccias. *Geochim. Cosmochim. Acta* 38, 911–928.
- Alexander E.C. and Kahl S.B. 1974.  $^{40}\text{Ar}$ - $^{39}\text{Ar}$  studies of lunar breccias. *Proc. Lunar Planet. Sci. Conf.* 5<sup>th</sup>, 1353–1373.
- Amelin, Y., Lee, D.C., Halliday, A.N., Pidgeon, R.T., 1999. Nature of the Earth's earliest crust from hafnium isotopes in single detrital zircons. *Nature* 399, 252–255.
- Asimow, P.D., Ghiorso, M.S., 1998. Algorithmic modifications extending MELTS to calculate subsolidus phase relations. *Am. Mineral.* 83, 1127–1132.
- Baker, D.R., Conte, A., Freda, C., Ottolini, L., 2002. The effect of halogens on Zr diffusion and zircon dissolution in hydrous metaluminous granitic melts. *Contrib. to Mineral. Petrol.* 142, 666–678.
- Barber, D.J., Scott, E.R.D., 2006. Shock and thermal history of Martian meteorite Allan Hills 84001 from transmission electron microscopy. *Meteorit. Planet. Sci.* 41, 643–662.
- Begemann, F., Li, Z., Schmitt-Strecker, S., Weber, H.W., Xu, Z., 1985. Noble gases and the history of Jilin meteorite. *Earth Planet. Sci. Lett.* 72, 247–262.
- Begemann, F., Ludwig, K.R., Lugmair, G.W., Min, K., Nyquist, L.E., Patchett, P.J., Renne, P.R., Shih, C.Y., Villa, I.M., Walker, R.J., 2001. Call for an improved set of decay constants for geochronological use. *Geochim. Cosmochim. Acta* 65, 111–121.
- Béjina, F., Jaoul, O., Liebermann, R.C., 2003. Diffusion in minerals at high pressure: a review. *Phys. Earth Planet. Inter.* 139, 3–20.
- Bell, E.A., Boehnke, P., Harrison, T.M., 2016. Recovering the primary geochemistry of Jack Hills zircons through quantitative estimates of chemical alteration. *Geochim. Cosmochim. Acta* 191, 187–202.
- Bell, E.A., Boehnke, P., Harrison, T.M., Mao, W.L.L., 2015a. Potentially biogenic carbon preserved in a 4.1 billion-year-old zircon. *Proc. Natl. Acad. Sci.* 112, 14518–14521.
- Bell, E.A., Boehnke, P., Hopkins-Wielicki, M.D., Harrison, T.M., 2015b. Distinguishing primary and secondary inclusion assemblages in Jack Hills zircons. *Lithos* 234–235, 15–26.

- Bell, E.A., Harrison, T.M., Kohl, I.E., Young, E.D., 2014. Eoarchean crustal evolution of the Jack Hills zircon source and loss of Hadean crust. *Geochim. Cosmochim. Acta* 146, 27–42.
- Bell, K., Powell, J.L., 1969. Strontium Isotopic Studies of Alkalic Rocks: The Potassium-rich Lavas of the Birunga and Toro—Ankole Regions, East and Central Equatorial Africa. *J. Petrol.* 10, 536–572.
- Bernatowicz T.J., Hohenberg C.M., Hudson B., Kennedy, B.M. and Podosek F.A. (1978). Argon ages for lunar breccias 14064 and 15405. *Proc. Lunar Planet. Sci. Conf.* 9<sup>th</sup>, 905–919.
- Boehnke, P., Barboni, M., Bell, E.A., 2016a. Zircon U/Th Model Ages in the Presence of Melt Heterogeneity. *Quat. Geochronol.* 34, 69–74.
- Boehnke, P., Caffee, M.W.W., Harrison, T.M.M., 2015. Xenon Isotopes in the MORB Source Are Not Distinctive of Early Global Degassing. *Geophys. Res. Lett.* 42, 4367–4374.
- Boehnke, P., Harrison, T.M., 2014. A meta-analysis of geochronologically relevant half-lives: what's the best decay constant? *Int. Geol. Rev.* 56, 905–914.
- Boehnke, P., Harrison, T.M., Heizler, M.T., Warren, P.H., 2016b. A Model for Meteoritic and Lunar  $^{40}\text{Ar}/^{39}\text{Ar}$  Age Spectra: Resolving the Effects of Multi-activation Energies. *Earth Planet. Sci. Lett.* 453, 267–275.
- Boehnke, P., Heizler, M.T., Harrison, T.M., Lovera, O.M., Warren, P.H., 2014. Avoiding Interpretative Pitfalls in Analysis of  $^{40}\text{Ar}/^{39}\text{Ar}$  Step-heating Data from Thermally Disturbed Meteoritic and Lunar Samples, in: *Proceedings of the 45th Lunar and Planetary Science Conference*.
- Boehnke, P., Watson, E.B.B., Trail, D., Harrison, T.M.M., Schmitt, A.K.K., 2013. Zircon Saturation Re-Revisited. *Chem. Geol.* 351, 324–334.
- Bogard, D.D., 2011. K–Ar ages of meteorites: Clues to parent-body thermal histories. *Chemie der Erde - Geochemistry* 71, 207–226.
- Bogard, D.D., Dixon, E.T., Garrison, D.H., 2010. Ar–Ar ages and thermal histories of enstatite meteorites. *Meteorit. Planet. Sci.* 45, 723–742.
- Borg, L., Norman, M., Nyquist, L., Bogard, D., Snyder, G., Taylor, L., Lindstrom, M., 1999. Isotopic studies of ferroan anorthosite 62236: A young lunar crustal rock from a light rare-earth-element-depleted source. *Geochim. Cosmochim. Acta* 63, 2679–2691.
- Borg, L.E., Connelly, J.N., Boyet, M., Carlson, R.W., 2011. Chronological evidence that the Moon is either young or did not have a global magma ocean. *Nature* 477, 70–2.
- Borg, L.E., Gaffney, A.M., Shearer, C.K., 2014. A review of lunar chronology revealing a preponderance of 4.34–4.37 Ga ages. *Meteorit. Planet. Sci.* 732, 715–732.

- Botcharnikov, R.E., Almeev, R.R., Koepke, J., Holtz, F., 2008. Phase Relations and Liquid Lines of Descent in Hydrous Ferrobasalt--Implications for the Skaergaard Intrusion and Columbia River Flood Basalts. *J. Petrol.* 49, 1687–1727.
- Bowring, S.A., Williams, I.S., 1999. Priscoan (4.00-4.03 Ga) orthogneisses from northwestern Canada. *Contrib. to Mineral. Petrol.* 134, 3–16.
- Brasier, M.D., Antcliffe, J., Saunders, M., Wacey, D., 2015. Changing the picture of Earth's earliest fossils (3.5-1.9 Ga) with new approaches and new discoveries. *Proc. Natl. Acad. Sci.* 112, 4859-4864.
- Cadogan P.H. and Turner G. (1976). The chronology of the Apollo 17 Station 6 boulder. *Proc. Lunar Planet. Sci. Conf.* 7<sup>th</sup>, 2267–2285.
- Carley, T.L., Miller, C.F., Wooden, J.L., Padilla, A.J., Schmitt, A.K., Economos, R.C., Bindeman, I.N., Jordan, B.T., 2014. Iceland is not a magmatic analog for the Hadean: Evidence from the zircon record. *Earth Planet. Sci. Lett.* 405, 85–97.
- Carlson, R.W., Borg, L.E., Gaffney, A.M., Boyet, M., 2014. Rb-Sr, Sm-Nd and Lu-Hf isotope systematics of the lunar Mg-suite: the age of the lunar crust and its relation to the time of Moon formation. *Philos. Trans. R. Soc. A Math. Phys. Eng. Sci.* 372, 20130246.
- Carlson, R.W., Lugmair, G.W., 1981. Time and duration of lunar highlands crust formation. *Earth Planet. Sci. Lett.* 52, 227–238.
- Carlson, R.W., Lugmair, G.W., 1988. The age of ferroan anorthosite 60025: oldest crust on a young Moon? *Earth Planet. Sci. Lett.* 90, 119–130.
- Carmichael, I.S.E., 1991. The redox states of basic and silicic magmas: a reflection of their source regions? *Contrib. to Mineral. Petrol.* 106, 129–141.
- Cassata, W.S., Renne, P.R., 2013. Systematic variations of argon diffusion in feldspars and implications for thermochronometry. *Geochim. Cosmochim. Acta* 112, 251–287.
- Cassata, W.S., Renne, P.R., Shuster, D.L., 2011. Argon diffusion in pyroxenes: Implications for thermochronometry and mantle degassing. *Earth Planet. Sci. Lett.* 304, 407–416.
- Cassata, W.S., Shuster, D.L., Renne, P.R., Weiss, B.P., 2010. Evidence for shock heating and constraints on Martian surface temperatures revealed by  $^{40}\text{Ar}/^{39}\text{Ar}$  thermochronometry of Martian meteorites. *Geochim. Cosmochim. Acta* 74, 6900–6920.
- Chambers, J.E., 2004. Planetary accretion in the inner Solar System. *Earth Planet. Sci. Lett.* 223, 241–252.
- Chapman, C.R., Cohen, B.A., Grinspoon, D.H., 2007. What are the real constraints on the existence and magnitude of the late heavy bombardment? *Icarus* 189, 233–245.
- Cherniak, D.J., 1995. Diffusion of lead in plagioclase and K-feldspar: an investigation using Rutherford Backscattering and Resonant Nuclear Reaction Analysis. *Contrib. to Mineral. Petrol.* 120, 358–371.

- Cherniak, D.J., 1998. Pb diffusion in clinopyroxene. *Chem. Geol.* 150, 105–117.
- Cherniak, D.J., 2003. REE diffusion in feldspar. *Chem. Geol.* 193, 25–41.
- Cherniak, D.J., Dimanov, A., 2010. Diffusion in Pyroxene, Mica and Amphibole. *Rev. Mineral. Geochemistry* 72, 641–690.
- Cherniak, D.J., Watson, E.B., 2003. Diffusion in Zircon. *Rev. Mineral. Geochemistry* 53, 113–143.
- Chou, C.L., 1978. Fractionation of siderophile elements in the earth's upper mantle, in: *Proceedings of the 9th Lunar and Planetary Science Conference*, 219–230.
- Chou, I.M., 1986. Permeability of precious metals to hydrogen at 2 kb total pressure and elevated temperatures. *Am. J. Sci.* 286, 638–658.
- Cohen, B.A., Swindle, T.D., Kring, D.A., 2000. Support for the Lunar Cataclysm Hypothesis from Lunar Meteorite Impact Melt Ages. *Science* 290, 1754–1756.
- Condon, D.J., Schoene, B., McLean, N.M., Bowring, S.A., Parrish, R.R., 2015. Metrology and traceability of U–Pb isotope dilution geochronology (EARTHTIME Tracer Calibration Part I). *Geochim. Cosmochim. Acta* 164, 464–480.
- Coogan, L.A., Hinton, R.W., 2006. Do the trace element compositions of detrital zircons require Hadean continental crust? *Geology* 34, 633–636.
- Coogan, L.A., Wilson, R.N., Gillis, K.M., MacLeod, C.J., 2001. Near-solidus evolution of oceanic gabbros: Insights from amphibole geochemistry. *Geochim. Cosmochim. Acta* 65, 4339–4357.
- Dalrymple, G.B., Lanphere, M.A., 1971.  $^{40}\text{Ar}/^{39}\text{Ar}$  Technique of K-Ar Dating: A Comparison with the Conventional Technique. *Earth Planet. Sci. Lett.* 12, 300–308.
- Dalrymple, G.B., Lanphere, M.A., 1974.  $^{40}\text{Ar}/^{39}\text{Ar}$  age spectra of some undisturbed terrestrial samples. *Geochim. Cosmochim. Acta* 38, 715–738.
- Dalrymple, G.B., Ryder, G., 1993. Age Spectra of Apollo 15 Impact Melt Rocks by Laser Heating and Their Bearing on the History of Lunar Basin Formation. *J. Geophys. Res.* 98, 13,085–13,095.
- Dalrymple, G.B., Ryder, G., 1996. Argon-40/argon-39 age spectra of Apollo 17 highlands breccia samples by laser step heating and the age of the Serenitatis basin. *J. Geophys. Res.* 101, 26,069–26,084.
- Dauphas, N., Marty, B., 2002. Inference on the nature and the mass of Earth's late veneer from noble metals and gases. *J. Geophys. Res.* 107, 1–7.
- Deb, K., 2014. Multi-objective Optimization, in: *Search Methodologies*. pp. 403–449.
- DeBey, T.M., Roy, B.R., Brady, S.R., 2012. The U.S. Geological Survey's TRIGA reactor.

- DeLong, S.E., Chatelain, C., 1990. Trace-element constraints on accessory-phase saturation in evolved MORB magma. *Earth Planet. Sci. Lett.* 101, 206–215.
- Dickinson, J.E., Hess, P.C., 1982. Zircon saturation in lunar basalts and granites. *Earth Planet. Sci. Lett.* 57, 336–344.
- Dobrzhinetskaya, L., Wirth, R., Green, H., 2014. Diamonds in Earth's oldest zircons from Jack Hills conglomerate, Australia, are contamination. *Earth Planet. Sci. Lett.* 387, 212–218.
- Dominik, B., Jessberger, E.K., 1978. Early Lunar Differentiation: 4.42-AE-Old Plagioclase Clasts in Apollo 16 Breccia 67435. *Earth Planet. Sci. Lett.* 38, 407–415.
- Dowty, E., Prinz, M., Keil, K., 1974. Ferroan anorthosite: A widespread and distinctive lunar rock type. *Earth Planet. Sci. Lett.* 24, 15–25.
- Elkins-Tanton, L.T., Hager, B.H., 2005. Giant meteoroid impacts can cause volcanism. *Earth Planet. Sci. Lett.* 239, 219–232.
- Ellis, D.J., Thompson, A.B., 1986. Subsolidus and partial melting reactions in the quartz-excess  $\text{CaO} + \text{MgO} + \text{Al}_2\text{O}_3 + \text{SiO}_2 + \text{H}_2\text{O}$  system under water excess and water-deficient conditions to 10 kbar: some implications for the origin of peraluminous melts from mafic rocks. *J. Petrol.* 27, 91–121.
- Ellison, A.J., Hess, P.C., 1986. Solution behavior of +4 cations in high silica melts: petrologic and geochemical implications. *Contrib. to Mineral. Petrol.* 94, 343–351.
- Fassett, C.I., Minton, D.A., 2013. Impact bombardment of the terrestrial planets and the early history of the Solar System. *Nat. Geosci.* 6, 520–524.
- Fitch, F.J., Hooker, P.J., Miller, J.A., 1976.  $^{40}\text{Ar}/^{39}\text{Ar}$  dating of the KBS Tuff in Koobi Fora Formation, East Rudolf, Kenya. *Nature* 263, 740–744.
- Fleck, R.J., Sutter, J.F., Elliot, D.H., 1977. Interpretation of discordant  $^{40}\text{Ar}/^{39}\text{Ar}$  age-spectra of mesozoic tholeiites from antarctica. *Geochim. Cosmochim. Acta* 41, 15–32.
- Floss, C., James, O.B., McGee, J.J., Crozaz, G., 1998. Lunar ferroan anorthosite petrogenesis: clues from trace element distributions in FAN subgroups. *Geochim. Cosmochim. Acta* 62, 1255–1283.
- Foland, K.A., 1974.  $\text{Ar}^{40}$  diffusion in homogeneous orthoclase and an interpretation of Ar diffusion in K-feldspars. *Geochim. Cosmochim. Acta* 38, 151–166.
- Foreman-Mackey, D., Hogg, D.W., Lang, D., Goodman, J., 2012. emcee: The MCMC Hammer. *Publ. Astron. Soc. Pacific* 125, 306–312.
- Fourcade, S., Allegre, C.J., 1981. Trace elements behavior in granite genesis: A case study the calc-alkaline plutonic association from the Querigut Complex (Pyrenees, France). *Contrib. to Mineral. Petrol.* 76, 177–195.

- Froude, D.O., Ireland, T.R., Kinny, P.D., Williams, I.S., Compston, W., 1983. Ion microprobe identification of 4,100-4,200 Myr-old terrestrial zircons. *Nature* 304, 616–618.
- Fu, B., Cavosie, A.J., Clechenko, C.C., Fournelle, J., Kita, N.T., Lackey, J.S., Page, F., Wilde, S.A., Valley, J.W., 2005. Ti-in-zircon thermometer: preliminary results, in: *EOS Transactions*, V41F, 1538.
- Fu, B., Page, F.Z., Cavosie, A.J., Fournelle, J., Kita, N.T., Lackey, J.S., Wilde, S.A., Valley, J.W., 2008. Ti-in-zircon thermometry: applications and limitations. *Contrib. to Mineral. Petrol.* 156, 197–215.
- Gaboardi, M., Humayun, M., 2009. Elemental fractionation during LA-ICP-MS analysis of silicate glasses: implications for matrix-independent standardization. *J. Anal. At. Spectrom.* 24, 1188–1197.
- Gallagher, K., 2012. Transdimensional inverse thermal history modeling for quantitative thermochronology. *J. Geophys. Res.* 117, B02408.
- Gardés, E., Montel, J.M., 2009. Opening and resetting temperatures in heating geochronological systems. *Contrib. to Mineral. Petrol.* 158, 185–195.
- Gelman, A., Carlin, J.B., Stern, H.S., Rubin, D.B., 2003. *Bayesian Data Analysis*, Second. ed. CRC Press.
- Ghiorso, M.S., Evans, B.W., 2008. Thermodynamics of Rhombohedral Oxide Solid Solutions and a Revision of the Fe-Ti Two-Oxide Geothermometer and Oxygen-Barometer. *Am. J. Sci.* 308, 957–1039.
- Ghiorso, M.S., Sack, R.O., 1995. Chemical mass transfer in magmatic processes IV. A revised and internally consistent thermodynamic model for the interpolation and extrapolation of liquid-solid equilibria in magmatic systems at elevated temperatures and pressures. *Contrib. to Mineral. Petrol.* 119, 197–212.
- Gomes, R., Levison, H.F., Tsiganis, K., Morbidelli, A., 2005. Origin of the cataclysmic Late Heavy Bombardment period of the terrestrial planets. *Nature* 435, 466–469.
- Grange, M.L., Nemchin, A.A., Pidgeon, R.T., Timms, N., Muhling, J.R., Kennedy, A.K., 2009. Thermal history recorded by the Apollo 17 impact melt breccia 73217. *Geochim. Cosmochim. Acta* 73, 3093–3107.
- Grange, M.L., Nemchin, A.A., Timms, N., Pidgeon, R.T., Meyer, C., 2011. Complex magmatic and impact history prior to 4.1 Ga recorded in zircon from Apollo 17 South Massif aphanitic breccia 73235. *Geochim. Cosmochim. Acta* 75, 2213–2232.
- Grimes, C.B., John, B.E., Cheadle, M.J., Mazdab, F.K., Wooden, J.L., Swapp, S., Schwartz, J.J., 2009. On the occurrence, trace element geochemistry, and crystallization history of zircon from in situ ocean lithosphere. *Contrib. to Mineral. Petrol.* 158, 757–783.

- Grimes, C.B., John, B.E., Cheadle, M.J., Wooden, J.L., 2008. Protracted construction of gabbroic crust at a slow spreading ridge: Constraints from  $^{206}\text{Pb}/^{238}\text{U}$  zircon ages from Atlantis Massif and IODP Hole U1309D (30°N, MAR). *Geochemistry Geophys. Geosystems* 9, 10.1029/2008GC002063
- Grimes, C.B., John, B.E., Kelemen, P.B., Mazdab, F.K., Wooden, J.L., Cheadle, M.J., Hanghøj, K., Schwartz, J.J., 2007. Trace element chemistry of zircons from oceanic crust: A method for distinguishing detrital zircon provenance. *Geology* 35, 643.
- Gromet, L.P., Silver, L.T., 1983. Rare earth element distributions among minerals in a granodiorite and their petrogenetic implications. *Geochim. Cosmochim. Acta* 47, 925–939.
- Hacker, B.R., Kelemen, P.B., Behn, M.D., 2011. Differentiation of the continental crust by relamination. *Earth Planet. Sci. Lett.* 307, 501–516.
- Harrison, T.M., 2009. The Hadean Crust: Evidence from >4 Ga Zircons. *Annu. Rev. Earth Planet. Sci.* 37, 479–505.
- Harrison, T.M., Bell, E.A., Boehnke, P., 2016. Hadean Zircon Petrochronology, in: *Reviews in Mineralogy and Geochemistry* (in review).
- Harrison, T.M., Blichert-Toft, J., Müller, W., Albarede, F., Holden, P., Mojzsis, S.J., 2005. Heterogeneous Hadean hafnium: evidence of continental crust at 4.4 to 4.5 ga. *Science* 310, 1947–1950.
- Harrison, T.M., Célérier, J., Aikman, A.B., Hermann, J., Heizler, M.T., 2009. Diffusion of  $^{40}\text{Ar}$  in muscovite. *Geochim. Cosmochim. Acta* 73, 1039–1051.
- Harrison, T.M., Duncan, I., McDougall, I., 1985. Diffusion of  $^{40}\text{Ar}$  in biotite: Temperature, pressure and compositional effects. *Geochim. Cosmochim. Acta* 49, 2461–2468.
- Harrison, T.M., Lovera, O.M., 2014. The multi-diffusion domain model: past, present and future, in: *Geological Society, London, Special Publications*. pp. 91–106.
- Harrison, T.M., Lovera, O.M., Heizler, M.T., 1991.  $^{40}\text{Ar}/^{39}\text{Ar}$  results for alkali feldspars containing diffusion domains with differing activation energy. *Geochim. Cosmochim. Acta* 55, 1435–1448.
- Harrison, T.M., McDougall, I., 1981. Excess  $^{40}\text{Ar}$  in metamorphic rocks from Broken Hill, New South Wales: implications for  $^{40}\text{Ar}/^{39}\text{Ar}$  age spectra and the thermal history of the region. *Earth Planet. Sci. Lett.* 55, 123–149.
- Harrison, T.M., Schmitt, A.K., 2007. High sensitivity mapping of Ti distributions in Hadean zircons. *Earth Planet. Sci. Lett.* 261, 9–19.
- Harrison, T.M., Schmitt, A.K., McCulloch, M.T., Lovera, O.M., 2008. Early ( $\geq 4.5$  Ga) formation of terrestrial crust: Lu–Hf,  $\delta^{18}\text{O}$ , and Ti thermometry results for Hadean zircons. *Earth Planet. Sci. Lett.* 268, 476–486.

- Harrison, T.M., Wang, S., 1981. Further  $^{40}\text{Ar}/^{39}\text{Ar}$  evidence for the multi-collisional heating of the Kirin chondrite. *Geochim. Cosmochim. Acta* 45, 2513–2517.
- Harrison, T.M., Watson, E.B., 1983. Kinetics of Zircon Dissolution and Zirconium Diffusion in Granitic Melts of Variable Water Content. *Contrib. to Mineral. Petrol.* 84, 66–72.
- Harrison, T.M., Watson, E.B., 1984. The behavior of apatite during crustal anatexis: Equilibrium and kinetic considerations. *Geochim. Cosmochim. Acta* 48, 1467–1477.
- Harrison, T.M., Watson, E.B., Aikman, A.B., 2007. Temperature spectra of zircon crystallization in plutonic rocks. *Geology* 35, 635.
- Harrison, T.M., Watson, E.B., Rapp, R.P., 1986. Does anatexis deplete the lower crust in heat producing elements?: Implications from experimental studies. *Trans. Am. Geophys. Union* 67, 386.
- Hartmann, W.K., 1975. Lunar “cataclysm”: A misconception? *Icarus* 24, 181–187.
- Heizler, M.T., Jicha, B.R., Koppers, A.A.P., Miggins, D.P., 2015.  $^{40}\text{Ar}/^{39}\text{Ar}$  Interlaboratory Calibration into the Holocene, in: AGU Abstract with Program V53H, 7.
- Heizler, M.T., Perry, F. V., Crowe, B.M., Peters, L., Appelt, R., 1999. The age of Lathrop Wells volcanic center: An  $^{40}\text{Ar}/^{39}\text{Ar}$  dating investigation. *J. Geophys. Res.* 104, 767–804.
- Hellebrand, E., Möller, A., Whitehouse, M., Cannat, M., 2007. Formation of oceanic zircons, in: Goldschmidt Conference Abstracts. p. A391.
- Holden, P., Lanc, P., Ireland, T.R., Harrison, T.M., Foster, J.J., Bruce, Z., 2009. Mass-spectrometric mining of Hadean zircons by automated SHRIMP multi-collector and single-collector U/Pb zircon age dating: The first 100,000 grains. *Int. J. Mass Spectrom.* 286, 53–63.
- Honda, M., Nishiizumi, K., Imamura, M., Takaoka, N., Nitoh, O., Horie, K., Komura, K., 1982. Cosmogenic nuclides in the Kirin chondrite. *Earth Planet. Sci. Lett.* 57, 101–109.
- Hopkins, M.D., Harrison, T.M., Manning, C.E., 2008. Low heat flow inferred from >4 Gyr zircons suggests Hadean plate boundary interactions. *Nature* 456, 493–496.
- Hopkins, M.D., Harrison, T.M., Manning, C.E., 2010. Constraints on Hadean geodynamics from mineral inclusions in >4Ga zircons. *Earth Planet. Sci. Lett.* 298, 367–376.
- Hopkins, M.D., Harrison, T.M., Manning, C.E., 2012. Metamorphic replacement of mineral inclusions in detrital zircon from Jack Hills, Australia: Implications for the Hadean Earth Comment. *Geology* 40, e281.
- Hoskin, P.W.O., 2005. Trace-element composition of hydrothermal zircon and the alteration of Hadean zircon from the Jack Hills, Australia. *Geochim. Cosmochim. Acta* 69, 637–648.
- Huang, W.L., Wyllie, P.J., 1981. Phase Relationships of S-Type Granite with  $\text{H}_2\text{O}$  to 35 kbar: Muscovite granite from Harney Peak, South Dakota. *J. Geophys. Res.* 86, 10515–10529.

- Huneke, J.C., 1976. Diffusion artifacts in dating by stepwise thermal release of rare gases. *Earth Planet. Sci. Lett.* 28, 407–417.
- Husain L. and Schaeffer O.A. 1973.  $^{40}\text{Ar}$ - $^{39}\text{Ar}$  crystallisation ages and  $^{38}\text{Ar}$ - $^{37}\text{Ar}$  cosmic ray exposure ages of samples from the vicinity of the Apollo 16 landing site. *Lunar Planet. Sci. Conf.* 4<sup>th</sup>, 406–408.
- Husain L., Schaeffer O.A., Funkhouser J. and Stutter J. 1972. The ages of lunar material from Fra Mauro, Hadley Rille, and Spur Crater. *Proc. Lunar Planet. Sci. Conf.* 3<sup>rd</sup>, Suppl. 3, *Geochim. Cosmochim. Acta*, 1557–1567.
- James, O.B., Lindstrom, M.M., Flohr, M.K., 1989. Ferroan anorthosite from lunar breccia 64435: Implications for the origin and history of lunar ferroan anorthosites. *Proc. 19th Lunar Planet. Sci. Conf.* 19, 219–243.
- Jeffery, P.M., Reynolds, J.H., 1961. Origin of excess  $\text{Xe}^{129}$  in stone meteorites. *J. Geophys. Res.* 66, 3582–3583.
- Jessberger E.K., Kirsten T. and Staudacher T. 1976. Argon-argon ages of consortium breccia 73215. *Proc. Lunar Planet. Sci. Conf.* 7<sup>th</sup>, 2201–2215.
- Jessberger E.K., Kirsten T. and Staudacher T. 1977. One rock and many ages – Further K-Ar data on consortium breccia 73215. *Proc. Lunar Planet. Sci. Conf.* 8<sup>th</sup>, 2567–2580.
- Jessberger E.K., Staudacher Th., Dominik B. and Kirsten T. 1978. Argon-argon ages of aphanite samples from consortium breccia 73255. *Proc. Lunar Planet. Sci. Conf.* 9<sup>th</sup>, 841–854.
- JIGKMS, 1977. A preliminary survey on the Kirin meteorite shower. *Sci. Sin.* 20, 502–512.
- Johnson, B.C., Bowling, T.J., 2014. Where have all the craters gone? Earth's bombardment history and the expected terrestrial cratering record. *Geology* 42, 587–590.
- Jones, J.H., Drake, M.J., 1986. Geochemical constraints on core formation in the Earth. *Nature* 322, 221–228.
- Jourdan, F., Verati, C., Féraud, G., 2006. Intercalibration of the Hb3gr  $^{40}\text{Ar}/^{39}\text{Ar}$  dating standard. *Chem. Geol.* 231, 177–189.
- Kaula, W.M., 1979. Thermal evolution of earth and moon growing by planetesimal impacts. *J. Geophys. Res.* 84, 999–1008.
- Keller, B., Boehnke, P., Schoene, B., 2016. Temporal variation in average zircon saturation temperature over the last 4 Gyr. In Prep.
- Kemp, A.I.S., Wilde, S.A., Hawkesworth, C.J., Coath, C.D., Nemchin, A., Pidgeon, R.T., Vervoort, J.D., DuFrane, S.A., 2010. Hadean crustal evolution revisited: New constraints from Pb-Hf isotope systematics of the Jack Hills zircons. *Earth Planet. Sci. Lett.* 296, 45–56.

- Kempton, P.D., Downes, H., Sharkov, E. V., Vetrin, V.R., Ionov, D.A., Carswell, D.A., Beard, A., 1995. Petrology and geochemistry of xenoliths from the Northern Baltic shield: evidence for partial melting and metasomatism in the lower crust beneath an Archaean terrane. *Lithos* 36, 157–184.
- Kennedy, J., Eberhart, R., 1995. Particle swarm optimization. *Proc. ICNN'95 - Int. Conf. Neural Networks* 4, 1942–1948.
- Kennedy, T., Jourdan, F., Bevan, A.W.R., Mary Gee, M.A., Frew, A., 2013. Impact history of the HED parent body(ies) clarified by new  $^{40}\text{Ar}/^{39}\text{Ar}$  analyses of four HED meteorites and one anomalous basaltic achondrite. *Geochim. Cosmochim. Acta* 115, 162–182.
- Kenny, G.G., Whitehouse, M.J., Kamber, B.S., 2016. Differentiated impact melt sheets may be a potential source of Hadean detrital zircon. *Geology* 44, G37898.1.
- Keppeler, H., 1993. Influence of fluorine on the enrichment of high field strength trace elements in granitic rocks. *Contrib. to Mineral. Petrol.* 114, 479–488.
- Kirsten T. and Horn P. 1974. Chronology of the Taurus-Littrow region III: Ages of mare basalts and highlands breccias and some remarks about the interpretation of lunar highland rock ages. *Proc. Lunar Planet. Sci. Conf. 5<sup>th</sup>, Suppl. 5*, *Geochim. Cosmochim. Acta*, 1451–1475.
- Korotev, R.L., 1994. Compositional variation in Apollo 16 impact-melt breccias and inferences for the geology and bombardment history of the Central Highlands of the Moon. *Geochim. Cosmochim. Acta* 58, 3931–3969.
- Kossert, K., Jörg, G., Nähle, O., v. Gostomski, C.L., 2009. High-precision measurement of the half-life of  $^{147}\text{Sm}$ . *Appl. Radiat. Isot.* 67, 1702–1706.
- Kossert, K., Jörg, G., v. Gostomski, C.L., 2013. Experimental half-life determination of  $^{176}\text{Lu}$ . *Appl. Radiat. Isot.* 81, 140–145.
- Kring, D.A., Cohen, B.A., 2002. Cataclysmic bombardment throughout the inner solar system 3.9–4.0 Ga. *J. Geophys. Res.* 107, 10.1029/2001JE001529.
- Lanphere, M.A., Dalrymple, G.B., 1971. A Test of the  $^{40}\text{Ar}/^{39}\text{Ar}$  Age Spectrum Technique on Some Terrestrial Materials. *Earth Planet. Sci. Lett.* 12, 359–372.
- Lee, J.K.W., 1995. Multipath diffusion in geochronology. *Contrib. to Mineral. Petrol.* 120, 60–82.
- Leich D.A., Kahl S.B., Kirschbaum A.R., Niemeyer S. and Phinney D. 1975. Rare gas constraints on the history of Boulder 1, Station 2, Apollo 17. *The Moon* 14, 407–444.
- Lissenberg, C.J., Rioux, M., Shimizu, N., Bowring, S.A., Mével, C., 2009. Zircon dating of oceanic crustal accretion. *Science* 323, 1048–1050.
- Lovera, O.M., 1992. Computer programs to model  $^{40}\text{Ar}/^{39}\text{Ar}$  diffusion data from multidomain samples. *Comput. Geosci.* 18, 789–813.

- Lovera, O.M., Heizler, M.T., Harrison, T.M., 1993. Argon diffusion domains in K-feldspar II: Kinetic properties of MH-10. *Contrib. to Mineral. Petrol.* 113, 381–393.
- Lovera, O.M., Richter, F.M., Harrison, T.M., 1989. The  $^{40}\text{Ar}/^{39}\text{Ar}$  thermochronometry for slowly cooled samples having a distribution of diffusion domain sizes. *J. Geophys. Res.* 94.
- Lovera, O.M., Richter, F.M., Harrison, T.M., 1991. Diffusion domains determined by  $^{39}\text{Ar}$  released during step heating. *J. Geophys. Res.* 96, 2057–2069.
- Mahon, K.I., 1996. The New “York” Regression: Application of an improved statistical method to geochemistry. *Int. Geol. Rev.* 38, 293–303.
- Maier, W.D., Barnes, S.J., Campbell, I.H., Fiorentini, M.L., Peltonen, P., Smithies, R.H., 2009. Progressive mixing of meteoritic veneer into the early Earth’s deep mantle. *Nature* 460, 620–623.
- Marchi, S., Bottke, W.F., Cohen, B.A., Wünnemann, K., Kring, D.A., McSween, H.Y., De Sanctis, M.C., O’Brien, D.P., Schenk, P., Raymond, C.A., Russell, C.T., 2013. High-velocity collisions from the lunar cataclysm recorded in asteroidal meteorites. *Nat. Geosci.* 6, 303–307.
- Marchi, S., Bottke, W.F., Elkins-Tanton, L.T., Bierhaus, M., Wünnemann, K., Morbidelli, A., Kring, D.A., 2014. Widespread mixing and burial of Earth’s Hadean crust by asteroid impacts. *Nature* 511, 578–582.
- Marvin U.B., Lindstrom M.M., Bernatowicz T.J., Podosek F.A. and Sugiura N. 1987. The composition and history of breccia 67015 from North Ray Crater. *Proc. 17th Lunar Planet. Sci. Conf., J. Geophys. Res.*, 92, B4, E471–E490.
- Maurer P., Eberhardt P., Geiss J., Grögler N., Stettler A., Brown G.M., Peckett A. and Krähenbühl U. 1978. Pre-imbrian craters and basins: ages, compositions and excavation depths of Apollo 16 breccias. *Geochim. Cosmochim. Acta* 42, 1687–1720.
- McDougall, I., Harrison, T.M., 1999. *Geochronology and Thermochronology by the  $^{40}\text{Ar}/^{39}\text{Ar}$  Method*, Second. ed. Oxford University Press.
- McGee, J.J., 1993. Lunar ferroan anorthosites’ mineralogy, compositional variations, and petrogenesis. *J. Geophys. Res.* 98, 9089–9105.
- Menneken, M., Nemchin, A.A., Geisler, T., Pidgeon, R.T., Wilde, S.A., 2007. Hadean diamonds in zircon from Jack Hills, Western Australia. *Nature* 448, 917–20.
- Mercer, C.M., Young, K.E., Weirich, J.R., Hodges, K. V., Jolliff, B.L., Wartho, J.A., Van Soest, M.C., 2015. Refining lunar impact chronology through high spatial resolution  $^{40}\text{Ar}/^{39}\text{Ar}$  dating of impact melts. *Sci. Adv.* 1, e1400050.
- Merrill, C., Turner, G., 1966. Potassium-argon dating by activation with fast neutrons. *J. Geophys. Res.* 71, 2852–2857.

- Miljkovic, K., Wieczorek, M.A., Collins, G.S., Laneuville, M., Neumann, G.A., Melosh, H.J., Solomon, S.C., Phillips, R.J., Smith, D.E., Zuber, M.T., 2013. Asymmetric distribution of lunar impact basins caused by variations in target properties. *Science* 342, 724–726.
- Minton, D.A., Jackson, A.P., Asphaug, E., Fassett, C.I., Richardson, J.E., 2015. Debris from Borealis basin formation as the primary impactor population of Late Heavy bombardment, in: *Early Solar System Impact Bombardment III*. 3033.
- Mojzsis, S.J., Arrhenius, G., McKeegan, K.D., Harrison, T.M., Nutman, A.P., Friend, C.R.L., 1996. Evidence for life on Earth before 3,800 million years ago. *Nature* 384, 55–59.
- Mojzsis, S.J., Harrison, T.M., Pidgeon, R.T., 2001. Oxygen-isotope evidence from ancient zircons for liquid water at the Earth's surface 4,300 Myr ago. *Nature* 409, 178–181.
- Morbidelli, A., Marchi, S., Bottke, W.F., Kring, D.A., 2012. A sawtooth-like timeline for the first billion years of lunar bombardment. *Earth Planet. Sci. Lett.* 355–356, 144–151.
- Müller, N., Jessberger, E.K., 1985. Dating Jilin and constraints on its temperature history. *Earth Planet. Sci. Lett.* 72, 276–285.
- Nemchin, A.A., Pidgeon, R.T., Whitehouse, M.J., Vaughan, J.P., Meyer, C., 2008. SIMS U-Pb study of zircon from Apollo 14 and 17 breccias: Implications for the evolution of lunar KREEP. *Geochim. Cosmochim. Acta* 72, 668–689.
- Neukum, G., Ivanov, B.A., Hartmann, W.K., 2001. Cratering Records In The Inner Solar System In Relation To The Lunar Reference System. *Chronol. Evol. Mars* 96, 55–86.
- Norman, M.D., Borg, L.E., Nyquist, L.E., Bogard, D.D., 2003. Chronology, geochemistry, and petrology of a ferroan noritic anorthosite clast from Descartes breccia 67215: Clues to the age, origin, structure, and impact history of the lunar crust. *Meteorit. Planet. Sci.* 38, 645–661.
- Norman, M.D., Duncan, R.A., Huard, J.J., 2006. Identifying impact events within the lunar cataclysm from  $^{40}\text{Ar}$ – $^{39}\text{Ar}$  ages and compositions of Apollo 16 impact melt rocks. *Geochim. Cosmochim. Acta* 70, 6032–6049.
- Norman, M.D., Duncan, R.A., Huard, J.J., 2010. Imbrium provenance for the Apollo 16 Descartes terrain: Argon ages and geochemistry of lunar breccias 67016 and 67455. *Geochim. Cosmochim. Acta* 74, 763–783.
- Palme, H., O'Neill, H.S.C., 2003. Cosmochemical estimates of mantle composition, in: *Treatise on Geochemistry*. pp. 1–38.
- Papanastassiou, D.A., Wasserburg, G.J., 1972. The Rb-Sr age of a crystalline rock from Apollo 16. *Earth Planet. Sci. Lett.* 16, 289–298.
- Patchett, P.J., 1983. Importance of the Lu-Hf isotopic system in studies of planetary chronology and chemical evolution. *Geochim. Cosmochim. Acta* 47, 81–91.

- Pearson, K., 1916. IX. Mathematical Contributions to the Theory of Evolution. -XIX. Second Supplement to a Memoir on Skew Variation. *Philos. Trans. R. Soc. A* 216, 429–457.
- Pollack, H.N., Hurter, S.J., Johnson, R., 1993. Heat flow from the Earth's interior: Analysis of the global data set. *Rev. Geophys.* 31, 267–280.
- Rapp, R.P., Watson, E.B., 1985. Solubility and dissolution behavior of monazite and LREE diffusion in a hydrous granitic melt. *EOS* 416.
- Rasmussen, B., Fletcher, I.R., Muhling, J.R., Gregory, C.J., Wilde, S.A., 2011. Metamorphic replacement of mineral inclusions in detrital zircon from Jack Hills, Australia: Implications for the Hadean Earth. *Geology* 39, 1143–1146.
- Reid, M.R., Coath, C.D., Harrison, T.M., Mckeegan, K.D., 1997. Prolonged residence times for the youngest rhyolites associated with Long Valley Caldera:  $^{230}\text{Th}$ - $^{238}\text{U}$  ion microprobe dating of young zircons. *Earth Planet. Sci. Lett.* 50, 27–39.
- Renne, P.R., Mundil, R., Balco, G., Min, K., Ludwig, K.R., 2010. Joint determination of  $^{40}\text{K}$  decay constants and  $^{40}\text{Ar}^*/^{40}\text{K}$  for the Fish Canyon sanidine standard, and improved accuracy for  $^{40}\text{Ar}/^{39}\text{Ar}$  geochronology. *Geochim. Cosmochim. Acta* 74, 5349–5367.
- Righter, K., 2003. Metal-silicate partitioning of siderophile elements and core formation in the early Earth. *Annu. Rev. Earth Planet. Sci.* 31, 135–174.
- Righter, K., 2015. Modeling siderophile elements during core formation and accretion, and the role of the deep mantle and volatiles. *Am. Mineral.* 100, 1098–1109.
- Righter, K., Danielson, L.R., Pando, K.M., Williams, J., Humayun, M., Hervig, R.L., Sharp, T.G., 2015. Highly siderophile element (HSE) abundances in the mantle of Mars are due to core formation at high pressure and temperature. *Meteorit. Planet. Sci.* 50, 604–631.
- Rollinson, H., 2008. Ophiolitic trondhjemites: A possible analogue for Hadean felsic “crust.” *Terra Nova* 20, 364–369.
- Rosing, M.T., 1999.  $^{13}\text{C}$ -Depleted carbon microparticles in >3700-Ma sea-floor sedimentary rocks from West Greenland. *Science* 283, 674–676.
- Rotenberg, E., Davis, D.W., Amelin, Y., Ghosh, S., Bergquist, B.A., 2012. Determination of the decay-constant of  $^{87}\text{Rb}$  by laboratory accumulation of  $^{87}\text{Sr}$ . *Geochim. Cosmochim. Acta* 85, 41–57.
- Rubatto, D., Hermann, J., 2007. Experimental zircon/melt and zircon/garnet trace element partitioning and implications for the geochronology of crustal rocks. *Chem. Geol.* 241, 38–61.
- Rudnick, R.L., Gao, S., 2003. Composition of the continental crust. *Treatise on geochemistry* 3, 1–64.
- Ryerson, F.J., Watson, E.B., 1987. Rutile saturation in magmas: implications for Ti-Nb-Ta depletion in island-arc basalts. *Earth Planet. Sci. Lett.* 86, 225–239.

- Sambridge, M., Bodin, T., Gallagher, K., Tkalcic, H., 2013. Transdimensional inference in the geosciences. *Philos. Trans. A. Math. Phys. Eng. Sci.* 371, 20110547.
- Savin, S.M., Epstein, S., 1970. The oxygen and hydrogen isotope geochemistry of clay minerals. *Geochim. Cosmochim. Acta* 34, 25–42.
- Schaeffer O.A. and Schaeffer G.A 1977.  $^{39}\text{Ar}$ - $^{40}\text{Ar}$  ages of lunar rocks. *Lunar Planet. Sci. Conf.* 8<sup>th</sup>, 840–842.
- Schaeffer O.A., Husain L. and Schaeffer G.A 1976. Ages of highland rocks: the chronology of lunar basin formation revisited. *Proc. Lunar Planet. Sci. Conf.* 7<sup>th</sup>, 2067–2092.
- Scherer, E.E., Munker, C., Mezger, K., 2001. Calibration of the lutetium-hafnium clock. *Science* 293, 683–687.
- Schmitt, A.K., 2011. Uranium series accessory crystal dating of magmatic processes. *Annu. Rev. Earth Planet. Sci.* 39, 321–349.
- Schmitt, A.K., Perfit, M.R., Rubin, K.H., Stockli, D.F., Smith, M.C., Cotsonika, L.A., Zellmer, G.F., Ridley, W.I., Lovera, O.M., 2011. Rapid cooling rates at an active mid-ocean ridge from zircon thermochronology. *Earth Planet. Sci. Lett.* 302, 349–358.
- Schoene, B., 2014. U–Th–Pb Geochronology, in: *Treatise On Geochemistry*. pp. 341–378.
- Schoene, B., Crowley, J.L., Condon, D.J., Schmitz, M.D., Bowring, S.A., 2006. Reassessing the uranium decay constants for geochronology using ID-TIMS U–Pb data. *Geochim. Cosmochim. Acta* 70, 426–445.
- Schopf, J.W., Kudryavtsev, A.B., 2014. Biogenicity of Earth's Earliest Fossils, in: *Evolution of Archean Crust and Early Life*. pp. 333–349.
- Seifert, K.E., Dymek, R.F., Whitney, P.R., Haskin, L.A., 2010. Geochemistry of massif anorthosite and associated rocks, Adirondack Mountains, New York. *Geosphere* 6, 855–899.
- Shea, E.K., Weiss, B.P., Cassata, W.S., Shuster, D.L., Tikoo, S.M., Gattacceca, J., Grove, T.L., Fuller, M.D., 2012. A long-lived lunar core dynamo. *Science* 335, 453–456.
- Shirey, S.B., Kamber, B.S., Whitehouse, M.J., Mueller, P.A., Basu, A.R., 2008. A review of the isotopic and trace element evidence for mantle and crustal processes in the Hadean and Archean: Implications for the onset of plate tectonic subduction. *Geol. Soc. Am. Spec. Pap.* 440, 1–29.
- Shuster, D.L., Balco, G., Cassata, W.S., Fernandes, V.A., Garrick-Bethell, I., Weiss, B.P., 2010. A record of impacts preserved in the lunar regolith. *Earth Planet. Sci. Lett.* 290, 155–165.
- Shuster, D.L., Cassata, W.S., 2015. Paleotemperatures at the lunar surfaces from open system behavior of cosmogenic  $^{38}\text{Ar}$  and radiogenic  $^{40}\text{Ar}$ . *Geochim. Cosmochim. Acta* 155, 154–171.

- Sleep, N.H., 2000. Evolution of the mode of convection within terrestrial planets. *J. Geophys. Res.* 105, 17563–17578.
- Sleep, N.H., Zahnle, K.J., Kasting, J.F., Morowitz, H.J., 1989. Annihilation of ecosystems by large asteroid impacts on the early Earth. *Nature* 342, 139–142.
- Smith, J. V., 1981. The first 800 million years of Earth's history. *Philos. Trans. R. Soc. A* 301, 401–422.
- Sneeringer, M., Hart, S.R., Shimizu, N., 1984. Strontium and samarium diffusion in diopside. *Geochim. Cosmochim. Acta* 48, 1589–1608.
- Staudacher Th., Dominik B., Jessberger E.K and Kirsten T. 1978. Consortium breccia 73255:  $^{40}\text{Ar}$ - $^{39}\text{Ar}$  dating. *Lunar Planet. Sci. Conf. 9<sup>th</sup>*, 1098–1100.
- Steiger, R.H., Jäger, E., 1977. Subcommittee on geochronology: convention on the use of decay constants in geochronology and cosmochronology. *Earth Planet. Sci. Lett.* 36, 359–362.
- Stettler A., Eberhardt P., Geiss J. and Grögler N. 1974.  $^{39}\text{Ar}$ - $^{40}\text{Ar}$  ages of samples from Apollo 17 Station 7 boulder and implications for its formation. *Earth Planet. Sci. Lett.* 23, 453–461.
- Stoffler, D., Keil, K., Scott, E.R.D., 1991. Shock metamorphism of ordinary chondrites. *Geochim. Cosmochim. Acta* 55, 3845–3867.
- Swindle, T.D., Kring, D.A., Weirich, J.R., 2013.  $^{40}\text{Ar}/^{39}\text{Ar}$  ages of impacts involving ordinary chondrite meteorites, in: Geological Society, London, Special Publications, 378, 333–347.
- Taylor, D.J., McKeegan, K.D., Harrison, T.M., 2009. Lu–Hf zircon evidence for rapid lunar differentiation. *Earth Planet. Sci. Lett.* 279, 157–164.
- Taylor, S.R., McLennan, S.M., 1985. The continental crust: Its composition and evolution. Blackwell, 312.
- Tera, F., Papanastassiou, D.A., Wasserburg, G.J., 1974. Isotopic evidence for a terminal lunar cataclysm. *Earth Planet. Sci. Lett.* 22, 1–21.
- Trail, D., Watson, E.B., Tailby, N.D., 2011. The oxidation state of Hadean magmas and implications for early Earth's atmosphere. *Nature* 480, 79–82.
- Trail, D., Watson, E.B., Tailby, N.D., 2012. Ce and Eu anomalies in zircon as proxies for the oxidation state of magmas. *Geochim. Cosmochim. Acta* 97, 70–87.
- Turner, G., 1968. The distribution of potassium and argon in chondrites, in: Ahrens, L.H. (Ed.), *Origin and Distribution of the Elements*, 387–398.
- Turner, G., 1970. Argon-40/Argon-39 dating of lunar rock samples. *Science* 167, 466–468.

- Turner, G., Cadogan, P.H., 1974. Possible effects of  $^{39}\text{Ar}$  recoil in  $^{40}\text{Ar}$ - $^{39}\text{Ar}$  dating, in: Proceedings of the Fifth Lunar Conference. 1601–1615.
- Turner G. and Cadogan P.H. 1975. The history of lunar basin formation inferred from  $^{40}\text{Ar}$ - $^{39}\text{Ar}$  dating of highland rocks. Lunar Planet. Sci. Conf. 6<sup>th</sup>.
- Turner, G., Enright, M.C., Cadogan, P.H., 1978. The early history of chondrite parent bodies inferred from  $^{40}\text{Ar}$ - $^{39}\text{Ar}$  ages, in: Proceedings of the Lunar and Planetary Science Conference. 989–1025.
- Turner G., Huneke J.C., Podosek, F.A. and Wasserburg J. 1971.  $^{40}\text{Ar}$ - $^{39}\text{Ar}$  ages and cosmic ray exposure ages of Apollo 14 samples. Earth Planet. Sci. Lett. 12, 19–35.
- Turner G., Cadogan P.H. and Yonge C.J. 1973. Argon selenochronology. Proc. Lunar Planet. Sci. Conf. 4<sup>th</sup>, Suppl. 4, Geochim. Cosmochim. Acta, 1889–1914.
- Turner, G., Miller, J.A., Grasty, R.L., 1966. The thermal history of the Bruderheim meteorite. Earth Planet. Sci. Lett. 1, 155–157.
- Valley, J.W., Kinny, P.D., Schulze, D.J., Spicuzza, M.J., 1998. Zircon megacrysts from kimberlite: oxygen isotope variability among mantle melts. Contrib. to Mineral. Petrol. 133, 1–11.
- Vervoort, J.D., Blichert-Toft, J., 1999. Evolution of the depleted mantle: Hf isotope evidence from juvenile rocks through time. Geochim. Cosmochim. Acta 63, 533–556.
- Walker, R.J., 2009. Highly siderophile elements in the Earth, Moon and Mars: Update and implications for planetary accretion and differentiation. Chemie der Erde - Geochemistry 69, 101–125.
- Wang, S., McDougall, I., Tetley, N., Harrison, T.M., 1980.  $^{40}\text{Ar}/^{39}\text{Ar}$  age and thermal history of the Kirin chondrite. Earth Planet. Sci. Lett. 49, 117–131.
- Warren, P.H., 1985. The magma ocean concept and lunar evolution. Annu. Rev. Earth Planet. Sci. 13, 201–240.
- Warren, P.H., 2003. The Moon, in: Treatise on Geochemistry. 559–599.
- Warren, P.H., Harrison, T.M., Isa, J., Boehnke, P., Heizler, M.T., 2013. Petrology and geochemistry of Apollo 16 North Ray Crater rocks: Precursor to an argon-thermochronologic investigation, in: 44<sup>th</sup> Lunar and Planetary Science Conference, 3107.
- Warren, P.H., Taylor, G.J., 2014. The Moon, in: Treatise on Geochemistry. Elsevier, 213–242.
- Warren, P.H., Wasson, J.T., 1979. The origin of KREEP. Rev. Geophys. Sp. Phys. 17, 73–88.
- Watson, E.B., 1979. Zircon saturation in felsic liquids: Experimental results and applications to trace element geochemistry. Contrib. Mineral. Petrol. 70, 407–419.

- Watson, E.B., Cherniak, D.J., 2013. Simple equations for diffusion in response to heating. *Chem. Geol.* 335, 93–104.
- Watson, E.B., Cherniak, D.J., Hanchar, J.M., Harrison, T.M., Wark, D.A., 1997. The incorporation of Pb into zircon. *Chem. Geol.* 141, 19–31.
- Watson, E.B., Harrison, T.M., 1983. Zircon saturation revisited: temperature and composition effects in a variety of crustal magma types. *Earth Planet. Sci. Lett.* 64, 295–304.
- Watson, E.B., Harrison, T.M., 1984a. Accessory minerals and the geochemical evolution of crustal magmatic systems: a summary and prospectus of experimental approaches. *Phys. Earth Planet. Inter.* 35, 19–30.
- Watson, E.B., Harrison, T.M., 1984b. What can accessory minerals tell us about felsic magma evolution? A framework for experimental study. *Proc. 27<sup>th</sup> Int. Geol. Congr.* 503–520.
- Watson, E.B., Harrison, T.M., 2005. Zircon Thermometer Reveals Minimum Melting Conditions on Earliest Earth. *Science* 308, 841–4.
- Wendt, I., 1993. Isochron or mixing line? *Chem. Geol.* 104, 301–305.
- Wetherill, G.W., 1980. Formation of the terrestrial planets. *Annu. Rev. Astron. Astrophys.* 18, 77–113.
- Wielicki, M.M., Harrison, T.M., Schmitt, A.K., 2012. Geochemical signatures and magmatic stability of terrestrial impact produced zircon. *Earth Planet. Sci. Lett.* 321–322, 20–31.
- Wilde, S.A., Valley, J.W., Peck, W.H., Graham, C.M., 2001. Evidence from detrital zircons for the existence of continental crust and oceans on the Earth 4.4 Gyr ago. *Nature* 409, 175–178.
- Wood, J.A., Dickey Jr, J.S., Marvin, U.B., Powell, B.N., 1970. Lunar Anorthosites. *Science* 167, 602–604.
- Yin, Q.Z., Jacobsen, S.B., Yamashita, K., Blichert-Toft, J., Télouk, P., Albarède, F., 2002. A short timescale for terrestrial planet formation from Hf-W chronometry of meteorites. *Nature* 418, 949–952.
- York D., Kenyon W.J. and Doyle R.J. 1972.  $^{40}\text{Ar}$ - $^{39}\text{Ar}$  ages of Apollo 14 and 15 samples. *Proc. Lunar Planet. Sci. Conf. 3<sup>rd</sup>*, *Geochim. Cosmochim. Acta*, 1613–1622.
- Zahnle, K., Arndt, N., Cockell, C., Halliday, A., Nisbet, E., Selsis, F., Sleep, N.H., 2007. Emergence of a habitable planet. *Space Sci. Rev.* 129, 35–78.
- Zhan, Z., Zhang, J., Li, Y., Chung, H.S., 2009. Adaptive particle swarm optimization. *IEEE Trans. Syst. man, Cybern. B Cybern.* 39, 1362–1381.